Numerical and analytical approaches to strongly correlated electron systems

Dissertation
zur Erlangung des Grades
"Doktor
der Naturwissenschaften"

am Fachbereich Physik
der Johannes Gutenberg-Universität
in Mainz

Carsten Lothar Knecht
geb. in Frankfurt am Main

Mainz, den 9.03.2006

Abstract

In this thesis we consider three different models for strongly correlated electrons, namely a multi-band Hubbard model as well as the spinless Falicov-Kimball model, both with a semi-elliptical density of states in the limit of infinite dimensions d, and the attractive Hubbard model on a square lattice in $d = 2$.

In the first part, we study a two-band Hubbard model with unequal bandwidths and anisotropic Hund's rule coupling (J_z-model) in the limit of infinite dimensions within the dynamical mean-field theory (DMFT). Here, the DMFT impurity problem is solved with the use of quantum Monte Carlo (QMC) simulations. Our main result is that the J_z-model describes the occurrence of an orbital-selective Mott transition (OSMT), in contrast to earlier findings. We investigate the model with a high-precision DMFT algorithm, which was developed as part of this thesis and which supplements QMC with a high-frequency expansion of the self-energy. The main advantage of this scheme is the extraordinary accuracy of the numerical solutions, which can be obtained already with moderate computational effort, so that studies of multi-orbital systems within the DMFT+QMC are strongly improved. We also found that a suitably defined Falicov-Kimball (FK) model exhibits an OSMT, revealing the close connection of the Falicov-Kimball physics to the J_z-model in the OSM phase.

In the second part of this thesis we study the attractive Hubbard model in two spatial dimensions within second-order self-consistent perturbation theory. This model is considered on a square lattice at finite doping and at low temperatures. Our main result is that the predictions of first-order perturbation theory (Hartree-Fock approximation) are renormalized by a factor of the order of unity even at arbitrarily weak interaction ($U \to 0$). The renormalization factor q can be evaluated as a function of the filling n for $0 < n < 1$. In the limit $n \to 0$, the q-factor vanishes, signaling the divergence of self-consistent perturbation theory in this limit. Thus we present the first asymptotically exact results at weak-coupling for the negative-U Hubbard model in $d = 2$ at finite doping.

Zusammenfassung

In dieser Arbeit werden drei verschiedene Modelle stark korrelierter Elektronensysteme betrachtet. Diese sind ein Mehrband-Hubbard-Modell sowie ein Falicov-Kimball-Modell, die beide mit halb-elliptischer Zustandsdichte und im Limes unendlicher Dimensionen behandelt werden. Außerdem wird das attraktive Hubbard-Modell auf dem Quadratgitter in zwei Dimensionen untersucht.

Im ersten Teil der Arbeit wird ein Zweiband-Hubbard-Modell mit unterschiedlichen Bandbreiten und anisotroper Hund'scher Kopplung (J_z-Modell) im Limes unendlicher Dimensionen im Rahmen der Dynamischen Molekularfeld-Theorie (DMFT) behandelt. Das DMFT-Störstellenproblem wird dabei mittels einer Quanten-Monte-Carlo-Simulation (QMC) gelöst. Als wichtigstes Resultat finden wir, daß das J_z-Modell das Phänomen des orbital-selektiven Mott-Übergangs (OSMT) beschreibt, im Gegensatz zu Ergebnissen früherer Arbeiten. Das Modell wird dabei mit einem hochpräzisen DMFT-Algorithmus untersucht, der als Teil dieser Arbeit entwickelt wurde und welcher die QMC-Ergebnisse um die Hochfrequenzentwicklung der Selbstenergie ergänzt. Der Hauptvorteil dieser Methode besteht in der außergewöhnlichen Genauigkeit der numerischen Lösungen, die schon mit moderatem numerischen Aufwand erhalten werden können. Die Untersuchung von Mehrband-Systemen wird dadurch stark verbessert. Das Phänomen des OSMT finden wir ebenfalls in einem Falicov-Kimball-Modell (FK), was die enge Verknüpfung der Physik des FK-Modells mit der orbital-selektiven Phase des J_z-Modells aufzeigt.

Im zweiten Teil dieser Arbeit wird das attraktive Hubbard-Modell in zweiter Ordnung selbstkonsistenter Störungstheorie in zwei räumlichen Dimensionen untersucht. Das Modell wird dabei auf dem Quadratgitter bei endlicher Dotierung und im Grenzwert niedriger Temperatur betrachtet. Als wichtigstes Resultat finden wir hier, daß die Ergebnisse der Störungstheorie erster Ordnung (Hartree-Fock Näherung) schon bei beliebig schwacher Wechselwirkung ($U \to 0$) um einen Faktor q der Ordnung eins renormiert werden. Der Renormierungsfaktor wird als Funktion der Füllung n, mit $0 < n < 1$, berechnet. Im Grenzwert $n \to 0$ finden wir, daß der q-Faktor verschwindet und folglich die Störungstheorie zusammenbricht. Damit haben wir die ersten aymptotisch exakten Ergebnisse für das attraktive Hubbard-Modell bei schwacher Kopplung und endlicher Dotierung in zwei Dimensionen erhalten.

Contents

Introduction

The subject of this thesis is the study of strongly correlated electron systems. A paradigm for such a system is the Hubbard model, which takes into account the quantum mechanical motion the electrons, H_t, and also a repulsive interaction, H_U, between them. With the reduction to these two contributions, the Hubbard model is truly a highly oversimplified model of the solid state. Nevertheless, it constains the key features of the many-body problem for fermions. Neither of the two parts alone favors any specific order. Their sum $H = H_t + H_U$, however, is known to exhibit a variety of nontrivial phenomena, including the correlation-driven metal-insulator transition (MIT), ferromagnetism, antiferromagnetism, ferrimagnetism, the Tomonaga-Luttinger liquid and even superconductivity.

The study of the MIT has a long history in solid state physics and much progress has been made, both experimentally and theoretically, in understanding strongly correlated electron systems and MITs (see, e.g., Gebhard, 1997; Imada et al., 1998). Among the most famous strongly correlated electron systems are the transition metal oxides, which are mainly degenerate d electron compounds. Of particular importance for the theoretical description of all of these systems are the strong coupling and the interplay of spin and orbital degrees of freedom (not to be confused with the usual spin-orbit coupling, even though it is also relevant in some cases), which constitute an unavoidable source of complicated behavior. Recently, the interest in these materials has been intensified by the observation of colossal magnetoresistance in the manganites and high-T_c superconductivity in the cuprates (Jin et al., 1994; Bednorz and Müller, 1986). Additionally, Nakatsuji and Maeno (2000*a*) found evidence for an orbital-selective metal-insulator transition (OSMT) in $Ca_{2-x}Sr_xRuO_4$, which introduces a new aspect to the theory of Mott transitions.

A very successful method to treat strongly correlated electron systems is given by the dynamical mean-field theory (DMFT; Metzner and Vollhardt, 1989). It is a nonperturbative theory that becomes exact in the limit of infinite dimensions d (or lattice coordination number Z) and is controlled in the parameter $\frac{1}{d}$. The DMFT is based on a mapping of the lattice model onto a quantum impurity model, subjected to a self-consistency condition. It thus fully retains local quantum mechanical fluctuations while spatial correlations are neglected.

For attractive on-site interaction (negative-U), the Hubbard model is one of the conceptually simplest models to describe superconductivity of two-dimensional systems with short-range, almost unretarded pairing. Consequently, it has been considered as an effective model of superconductivity in the family of cuprates, barium bismuthates, fullerids and Chevrel phases (Micnas et al., 1990). At weak coupling, the negative-U Hubbard model seems to be well described by a BCS picture of superconductivity. At strong coupling, however, the scenario of a Bose-Einstein condensate of preformed pairs appears to be more adequate. Of interest is also the study of the crossover from weak- to strong-coupling superconductivity, which is motivated in particular by experimental observations concerning unusual properties of high-T_c cuprate superconductors (Bednorz and Müller, 1986).

In low-dimensional quantum systems ($d = 1, 2$), fluctuations are known to be very strong, such that the results of a mean-field approximation are a priori questionable. For instance, in the BCS theory of superconductivity or in the antiferromagnetic Hartree-Fock theory of the Hubbard model, the order parameters (at weak-coupling) are exponentially small as a function of the interaction. In consideration of the fact that Hartree-Fock theory is equivalent to self-consistent first-order perturbation theory and consequently exact at most up to linear order in the interaction, it is of importance to know the relevance of these predictions. This issue can be studied by systematically calculating higher-order corrections to the mean-field results. An elegant method for this purpose is the self-consistent perturbation theory at fixed order parameters (PTFO; Georges and Yedidia, 1991). The method is based on the expansion of the free energy per site in powers of the interaction at a fixed value of the order parameter. Here, a Lagrange parameter is used to keep the order parameter fixed. Both order parameter and Lagrange parameter then have to be determined from a self-consistency condition to each order in the expansion.

In the first part of this thesis, we study the two-band Hubbard model with inequivalent bandwidths and isotropic Hund's rule coupling (J_z-model) within the DMFT for the occurrence of an OSMT. Here, the impurity problem of the DMFT is solved within a quantum Monte Carlo (QMC) simulation. The model is investigated with a high-precision DMFT algorithm that supplements QMC by a high-frequency expansion of the self-energy, and which is developed as part of this thesis. Included in this study are results from weak- and strong-coupling calculations. Finally, an OSMT-version of the Falicov-Kimball model, a simplified, spinless Hubbard model, is solved exactly in an "exact mean-field" study.

In the second part of this thesis, we consider the negative-U Hubbard model in two spatial dimensions at weak coupling and in the low-temperature limit. In particular, we study the relevance of the Hartree-Fock predictions for the model at finite doping by calculating the second-order corrections within self-consistent perturbation theory.

Structure of this Thesis

Chapter 1 introduces the Hubbard model, its extension to multiple bands as well as the negative-U Hubbard model. Thereafter, the DMFT is reviewed and it is shown how the impurity problem can be solved within an auxiliary-field QMC simulation. Subsequently, the analytical continuation of imaginary-time Green functions to the real axis within a maximum entropy method (MEM) is discussed. Finally, we discuss self-consistent perturbation theory at fixed order parameter, which is used to study the two-dimensional negative-U Hubbard model at weak coupling.

In chapter 2 we first study the consequences of the discretization of the imaginary time, introduced by the QMC method, for the solutions of the DMFT-equations. Then, a high-frequency corrected DMFT+QMC algorithm for the multi-band Hubbard model at half filling is developed, which is based on a large-energy expansion of the self-energy. The properties of this scheme as well as its applicability to the multi-orbital Hubbard model are then revealed in a comparison with schemes used in the literature. Finally, we test the applicability of this method also to the Hubbard model away from half filling.

Chapter 3, which is one of the central chapters of this thesis, concerns about orbital-selective Mott transitions. In the first part, the experimental observations and theoretical descriptions of the OSMT phenomenon are discussed. The two-band Hubbard model with inequivalent bandwidths and anisotropic Hund's rule coupling (J_z-model) is then examined for the occurrence of an OSMT in the second part. Using the high-precision DMFT+QMC scheme developed in chapter 2, we correct earlier QMC studies, in particular by Liebsch (2004) by proving the existence of two consecutive Mott transitions. Various observables are employed to study the OSM phase of the J_z-model. The critical interactions of the two consecutive transitions are determined as well as the critical temperature of the first transition. It is further found that the wide band exhibits non-Fermi-liquid behavior in the OSM phase and that it essentially displays the physics of the Falicov-Kimball model. The QMC results are also compared with the second-order weak-coupling expansion of the internal energy, which is calculated within this chapter. Afterwards, we determine the magnetic phase diagram of the J_z-model within the DMFT+QMC and compare our findings to weak- and strong-coupling results. Possible mechanisms of frustration are discussed subsequently. In the third part of chapter 3, a simplified Hubbard model, namely the spinless Falicov-Kimball (FK) model, is investigated for an OSMT. The model is solved exactly with the use of "exact mean-field theory". The close connection of the Falicov-Kimball physics and the J_z model in the OSM phase is confirmed by a comparison of observables. Finally, we study the influence of an additional hybridization to the FK Hamiltonian on the phase diagram.

In the last chapter (4), we consider the two-dimensional negative-U Hubbard model away from half-filling and at low temperatures within second-order self-

consistent (sc) perturbation theory at weak-coupling. The actual calculation is performed for the repulsive Hubbard model within a homogeneous magnetic field B, onto which the negative-U model can be mapped by a canonical transformation. First, we review the most important results from Hartree-Fock theory for $U \to 0$, such as the critical temperature, the order parameter and the free energy gain due to the symmetry breaking. We then calculate the second-order correction for small U. As a result we find that the HF order parameter (and similarly the critical temperature) is rescaled by a factor which is of the order of unity. The dependence of this renormalization factor on the field B is studied in detail.

Except for chapter 1, each chapter ends with a summary. Discussions and outlooks are given at the end of each relevant section. The main achievements are summarized at the end of the thesis.

Chapter 1

Models and Methods

1.1 Single-Band Hubbard Model

The Hubbard model is a tight-binding[1] lattice fermion model in which electrons are not only allowed to hop from one lattice site to another (kinetic energy) but also exhibit an on-site interaction (potential energy) that causes their motion to be correlated. The single band model with one electron per site is therefore also considered as the 'minimal' model for correlated electrons. Originally introduced independently by Hubbard (1963), Gutzwiller (1963), and Kanamori (1963) in order to describe itinerant ferromagnetism, the Hubbard model has been successfully used to explain a number of important phenomena in solid state physics, among which are the Mott-Hubbard metal-insulator transition (Mott, 1968; Brinkman and Rice, 1970; Gebhard, 1997), antiferromagnetism (Anderson, 1963), ferromagnetism (Müller-Hartmann, 1995; Hanisch et al., 1997; Tasaki, 1998*a*; Wahle et al., 1998; Ulmke, 1998), incommensurate phases (Schulz, 1990), phase separation (Visscher, 1974; van Dongen, 1995; van Dongen, 1996), and normal-state properties of high-T_c materials (Anderson, 1987; Lee and Nagaosa, 1992).

The grand canonical Hamiltonian of the Hubbard model is given [in second-quantized form[2]] by:

$$H = H_t + H_U + H_\mu \tag{1.1}$$

$$= -t \sum_{\langle ij \rangle \sigma} \left(c^\dagger_{i\sigma} c_{j\sigma} + \text{H.c.} \right) + U \sum_i n_{i\uparrow} n_{i\downarrow} - \mu \sum_{i\sigma} n_{i\sigma} \,, \tag{1.2}$$

with the creation and annihilation operators of a single-band electron at site i with

[1] For a discussion of the tight-binding approximation and its terminology, the reader is referred to textbooks of solid state physics, e.g., to Ashcroft and Mermin (1976).

[2] The formalism of the 'second quantization' is introduced, e.g., by Negele and Orland (1987).

spin σ, $c^\dagger_{i\sigma}$ and $c_{j\sigma}$, respectively, and the number operator $n_{i\sigma} \equiv c^\dagger_{i\sigma} c_{i\sigma}$. The kinetic energy is parameterized by t and the hopping is restricted to nearest-neighbor (NN) lattice sites, $\langle ij \rangle$.

The operator of the kinetic energy, H_t, is obtained from the overlap of two atomic Wannier orbitals $\psi_{i\sigma}(\boldsymbol{x})$ and $\psi_{j\sigma}(\boldsymbol{x})$ at sites i and j:

$$t = \int d\boldsymbol{x}\, \psi^\dagger_{i\sigma}(\boldsymbol{x}) \frac{\hbar^2}{2m} \Delta\, \psi_{j\sigma}(\boldsymbol{x})\,, \tag{1.3}$$

where the Planck constant $\hbar$ is set to unity henceforth and m is the mass of the electron. H_U denotes the contribution of the potential energy. The on-site Coulomb repulsion U of two electrons that occupy the same site is given by:

$$U = \int d\boldsymbol{x}\, d\boldsymbol{x'}\, \psi^\dagger_{i\sigma}(\boldsymbol{x}) \psi_{i\sigma}(\boldsymbol{x}) \frac{e^2}{|\boldsymbol{x} - \boldsymbol{x'}|} \psi^\dagger_{i\bar{\sigma}}(\boldsymbol{x'}) \psi_{i\bar{\sigma}}(\boldsymbol{x'})\,, \tag{1.4}$$

with $\bar{\sigma} = -\sigma$. Besides the hopping amplitude t and the Coulomb interaction U, the system is fully defined by the temperature T, the underlying lattice structure and its dimensions d as well as by the chemical potential μ.

It is important to note that a number of complications in real materials are ignored in this simplified electronic model. First, the Hubbard Hamiltonian neglects the intersite Coulomb force. This Coulomb repulsion, however, results in a (self)screening of the electrons, which limits the (infinite) range of the interaction. The coordinate-space screened interaction will be of shorter range with a characteristic screening length scale. In some cases it is justified to neglect the Coulomb interaction of electrons beyond the screening radius. Also, the hopping range of the electrons is restricted to nearest-neighbor sites. This is justified at least for $3d$ and $4f$ valence electrons for which the corresponding atomic orbitals barely overlap (compare, e.g., Ashcroft and Mermin, 1976). Consequently, the complexity of the model can be gradually enhanced by including intersite Coulomb interactions and by increasing the hopping range. A further simplification is the fact that the Hubbard model considers only electrons in a single orbit, e.g., the s orbital. This ideal case is justified if all other bands are energetically far away from the Fermi energy. Most systems of correlated electrons, like the transition metals, in contrast, are d-electron systems. In case the orbital degeneracy is lifted, the important low-energy excitations of such systems can be described by an effective single band close to the Fermi edge. This simplification is sometimes justified for materials where the bands are under the strong influence of an anisotropic crystal field. Another important class of materials that might well be described by an effective single-band model are the high-T_c cuprate superconductors (Bednorz and Müller, 1986; Anderson, 1987; Zhang and Rice, 1988).[3] As before,

[3]Here, the low-energy electronic structure of the copper oxide can be described well by taking

the Hubbard model can be extended to include multiple bands in order to make the description more realistic.

Despite its simplicity, the Hubbard Hamiltonian contains the full complexity of a many-body problem and the treatment of the single-band Hubbard model turns out to be extremely difficult. This is due to the fact that the hopping and interaction terms in (1.1) do not commute and, consequently, cannot be diagonalized in a simple manner. Exact solutions are therefore known only in few cases. In one dimension, the Hubbard model could be solved exactly with the Bethe ansatz method (Lieb and Wu, 1968; Essler et al., 1992). In dimensions $d \geq 2$, the few known exact results concern mainly the magnetic phase diagram. As a magnetically ordered state is excluded in one and two dimensions at finite temperature by the Mermin-Wagner theorem (Mermin and Wagner, 1966), symmetry breaking can possibly occur in the ground state only. Originally introduced as a model for itinerant ferromagnetism in transition metals, the occurrence of ferromagnetism in the Hubbard model is rather an exception. The generic magnetic phase of the half-filled single-band Hubbard model on bipartite lattices at low temperatures is antiferromagnetic (AF) for dimensions $d \geq 2$ (for $d = 2$ at $T = 0$ only). This is found by strong and weak-coupling calculations in dimensions $d > 2$ (Penn, 1966; Georges and Yedidia, 1991; van Dongen, 1991), and within renormalization group methods also for $d = 2$ (Halboth and Metzner, 2000; Honerkamp and Salmhofer, 2001).

Ferromagnetism is found for the Hubbard model for the case of one hole in an otherwise half-filled band in the limit $U \to \infty$ for dimensions $d \geq 2$ (Nagaoka, 1965). The extension of this rather pathological case to systems with finite interaction U or with a finite density of holes was not possible yet, at least not rigorously. In $d = 1$, ferromagnetism is excluded by the Lieb-Mattis theorem (Lieb and Mattis, 1962). Ferromagnetism is also found for so called 'flat-band systems', which are marked out by an idealized density of states with a flat and degenerate band (Mielke, 1991; Mielke and Tasaki, 1993). Ferrimagnetism is established for a half-filled band on bipartite lattices, where the sublattices have an unequal number of sites and the electrons can hop only between the sublattices (Lieb, 1989). Interestingly, the Hubbard model for this configuration displays superconducting correlations for an attractive interaction (Shen and Qiu, 1993). For a review on exact results, compare also Tasaki (1998*b*).

1.2 Multi-Band Hubbard Model

The class of materials that are reasonably well described by an effective single-band Hubbard model is small, high-T_c materials being a notable exception. Most materials

into account only the $d_{x^2-y^2}$ orbital, which is separated from the remaining d orbitals due to the crystal field. The $d_{x^2-y^2}$ orbital that further strongly hybridizes with the $2p_\sigma$ orbital forms an effective single antibonding band near the Fermi level.

with strongly correlated electrons are multi-orbital systems, where the orbital degeneracy plays an important role. In the case of Mn and Co compounds, for example, the relevant d electrons additionally favor high-spin states because of Hund's rule coupling. This exchange term was originally introduced to explain ferromagnetism (Slater, 1936; van Vleck, 1953). A multi-band Hubbard model that includes Hund's rule coupling is given by:

$$H = -\sum_{\langle ij\rangle\sigma\nu} t_\nu \left(c^\dagger_{i\nu\sigma} c_{j\nu\sigma} + \text{H.c.}\right) + U \sum_{i\nu} n_{i\nu\uparrow} n_{i\nu\downarrow} \tag{1.5}$$

$$+ \sum_{\substack{i\,\sigma\sigma' \\ \nu<\nu'}} \left(U' - \delta_{\sigma\sigma'} J_z\right) n_{i\nu\sigma} n_{i\nu'\sigma'} \tag{1.6}$$

$$+ J_\perp \sum_{i;\,\nu<\nu'} \left(c^\dagger_{i\nu\uparrow} c_{i\nu\downarrow} c^\dagger_{i\nu'\downarrow} c_{i\nu'\uparrow} + c^\dagger_{i\nu\uparrow} c^\dagger_{i\nu\downarrow} c_{i\nu'\uparrow} c_{i\nu'\downarrow} + \text{H.c.}\right), \tag{1.7}$$

with band index ν, interorbital Coulomb interaction U', and Hund's rule coupling constants J_z and $J_\perp$. Here, the J_z-term in (1.6) denotes the Ising component of the Hund's rule coupling, and (1.7) are the spin-flip and the pair-hopping terms, respectively. The two-band version of this Hamiltonian with distinct hopping amplitudes $t_2 = 2t_1$ is intensively studied in chapter 3 for the occurrence of an orbital-selective Mott transition, that was found in the ruthenate $Ca_{2-x}Sr_xRuO_4$ by Nakatsuji and Maeno ($2000a$). The same two-band Hamiltonian with equal hopping amplitudes $t_\nu = t$ exhibits ferromagnetism for one-dimensional systems at quarter filling, as found within exact diagonalization (ED) (Gill and Scalapino, 1987; Kuei and Scalettar, 1997; Hirsch, 1997), and in a broad range of electron fillings within DMFT+QMC[4] (Held and Vollhardt, 1998). The three-band version of (1.5) is in general expected to be relevant for the description of double perovskites, which are of particular interest, since they exhibit colossal magnetoresistance (Kobayashi et al., 1998; Petrone and Aligia, 2002).

1.3 Attractive Hubbard Model

The attractive (also negative-U) Hubbard model is one of the simplest models for the study of superconductivity through local pairing. The local attractive on-site density-density interaction term evidently favors double occupancy of sites and hence the formation of (s-symmetric) pairs below a critical temperature T_c. The model is therefore used to describe superconductivity of systems with short-range, almost unretarded pairing (Micnas et al., 1990), which are characterized by an extremely

[4] Due to a sign-problem within the DMFT+QMC, the Hund's rule coupling was restricted to the Ising component (1.6).

short coherence length[5], in contrast to conventional BCS superconductors (Bardeen et al., 1957). Thus the attractive Hubbard model has been considered as an effective model for the superconductivity that occurs in the cuprates, barium bismuthates ($Ba_{1-x}K_xBiO_3$ and $BaPb_xBi_{1-x}O_3$), the fullerides, as well as the Chevrel phases (Micnas et al., 1990).

The concept of pairing in real space, originally introduced by Anderson (1975) for the description of amorphous semiconductors, is also of interest in the context of the formation of charge-density waves (CDW) in narrow-band systems (Rice and Sneddon, 1970; Micnas et al., 1984). Amongst the microscopic mechanisms that can lead to an effective short-range attraction are strong electron-lattice couplings (Anderson, 1975; Robaszkiewicz et al., 1987) and couplings between electrons and quasibosonic excitations of electronic origin, such as excitations or plasmons (Little, 1964; Hirsch and Scalapino, 1985). The coupling mechanisms that can overscreen the local Coulomb repulsion, and the relevant materials are reviewed, e.g., by Micnas et al. (1990).

The attractive Hubbard model at arbitrary filling ($0 \leq n \leq 2$) can be mapped onto the half-filled repulsive Hubbard model in a homogeneous magnetic (Zeeman) field B by a canonical transformation. The Hamiltonian H^{R} of this (repulsive) Hubbard model in a homogeneous magnetic field is given by:

$$H^{\mathrm{R}} = H_t + H_U + H_\mu + H_B \tag{1.8}$$

$$= H_t + H_U + H_\mu - B \sum_{i\sigma} \sigma \, n_{i\sigma} \, . \tag{1.9}$$

Employing a particle-hole (ph) transformation [compare Appendix A] at half filling, H^{R} can be then mapped onto the attractive Hubbard model H^{A} away from half filling:

$$H^{\mathrm{A}} = H_{t'=t} + H_{U'=-U} + H_{\mu'=-(U/2+B)} \, . \tag{1.10}$$

The study of the attractive Hubbard model, H^{A}, is therefore equivalent to the study of the repulsive model H^{R}.

Exact solutions of the negative-U Hubbard model are known in $d = 1$ [for $n = 1$ by Shiba (1972), for general fillings compare Micnas et al. (1990) and references therein]. The ground state is strictly degenerate with CDW order and singlet-superconducting (SS) short range order. Furthermore, the single-electron spectrum has a gap for arbitrary n, in contrast to the case $U > 0$, where a gap exists only for $n = 1$ (Lieb and Wu, 1968). In the weak-coupling regime and at half filling, the negative-U Hubbard model exhibits conventional BCS-type superconductivity; the system undergoes a

[5] The coherence length of high-T_c superconductors is of the order of some lattice constants, which is very small compared to that of conventional superconductors, where it is of the order of several thousand Å.

transition from a normal metallic phase to a phase of coexisting CDW order and SS order. Long range pairing correlations occur only below T_c, which is exactly zero in dimensions $d \leq 2$. The transition is essentially mean-field in character (consistent with BCS theory) [compare, e.g., Singer et al. (1996) and references therein], with a Hartree critical temperature $k_B T_c \sim \sqrt{n(2-n)} \exp(-2W/|U|)$, for a square DOS with bandwidth W (Robaszkiewicz et al., 1982). In the strong-coupling limit (and at half filling), the model is adequately described by a Bose-Einstein condensate (BEC) of local, preformed pairs with a superconductor to insulator critical endpoint. Here, superconductivity occurs when the pairs condensate at a critical temperature that decreases as $t^2/|U|$ (Robaszkiewicz et al., 1981*a*; Robaszkiewicz et al., 1981*b*). The pairs exist, in contrast to the weak-coupling regime, already above this critical temperature. Away from half filling, the low-temperature phase is purely superconducting for $|U| > 0$, while T_c decreases with filling. In $d = 2$, there is evidence for a finite-temperature Kosterlitz-Thouless (Kosterlitz and Thouless, 1973) phase transition into the SS state with power-law decay of the pairing correlations (Scalettar, Loh, Gubernatis, Moreo, White, Scalapino, Sugar and Dagotto, 1989).

The attractive Hubbard model is of particular interest, because it allows for the study of the crossover from extended pairs in BCS-like superconductors to BEC superconductivity with its local pairs, just by tuning the interaction parameter U. The transition from weak- to strong-coupling superconductivity appears to be continuous (Nozières and Schmitt-Rink, 1985).

The degenerate ground state of the negative-U Hubbard model can be lifted by introducing an intersite electron density-density interaction V (extended Hubbard model). Then, at half-filling, the CDW is stable for $V > 0$, the SS phase for $V < 0$. Away from half filling, the ground state is always ordered, exhibiting either the SS or a mixed CDW-SS state (Robaszkiewicz et al., 1981*c*).

1.4 Dynamical Mean-Field Theory

As an exact solution for the Hubbard model is not known for dimensions $d > 1$, one can employ methods that give exact results in some limiting case [i.e., an approximation that is based on some controlled limit], methods that are based on uncontrolled approximations or apply direct numerical schemes. There exists a large number of both analytical methods and numerical approaches, all of which have their own limitations. Direct numerical solutions that apply to the Hubbard model using exact diagonalization and quantum Monte Carlo methods have been reviewed by Dagotto (1994).

Of particular interest is the limit of infinite dimensionality $d \to \infty$ [or the limit of infinite lattice coordination Z, which is the number of next neighbors of a lattice site], in which the coupling of one lattice site to the remaining lattice can be described by

an effective field: The lattice problem is reduced to a single-site problem in an effective medium. A self-consistency condition is then used to capture the translational invariance of the original lattice. It is well-known from classical statistical mechanics, that such a mean-field theory becomes exact in the limit $Z \to \infty$, where the inverse of the coordination number, $\frac{1}{Z}$, plays the role of the control parameter (Brout, 1960). In a pioneering work, Metzner and Vollhardt (1989) triggered the development of a mean-field theory that gets exact in the limit of large spatial dimensions also for strongly correlated fermion systems. This approach is now known as the dynamical mean-field theory (DMFT). Within the DMFT, local (time-dependent) quantum fluctuations are fully retained, while spatial fluctuations are neglected. Self-consistent functional equations for a mean-field theory of the Hubbard model, that can be solved essentially exactly, were then derived independently by Jarrell (1992), Janiš and Vollhardt (1992), and Georges and Kotliar (1992). Thus, an essentially exact solution exists for the Hubbard model also in $d = \infty$. The study of this limiting case is motivated by the fact that it can serve as a starting point for the investigation of finite-dimensional systems: The coordination number Z of an fcc lattice, for instance, is $Z = 12$, such that $\frac{1}{12}$ may be considered already as a small parameter. The DMFT and the limit of infinite dimensions are reviewed by Georges et al. (1996).

In the following, we provide a brief derivation of the self-consistency equations of the DMFT. More explicit derivations can be found, e.g., in Georges et al. (1996). The starting point for the development of a mean-field theory for many-body fermionic models that becomes exact in the limit of large spatial dimensions $Z \to \infty$, is the introduction of a proper scaling of the hopping amplitude (Economou, 1979; Zaitsev and Dushenat, 1983; Metzner and Vollhardt, 1989):

$$t = \frac{t^*}{\sqrt{Z}} \,. \tag{1.11}$$

This scaling ensures that the kinetic energy does not dominate the potential energy, which is independent of the coordination number in the limit $Z \to \infty$. The scaling (1.11) leads to a non-interacting density of states (DOS) for the hypercubic (hc) lattice, which is Gaussian:[6]

$$N^{\mathrm{hc}}(\epsilon) = \frac{1}{t^*\sqrt{2\pi}} e^{-\frac{\epsilon^2}{2t^{*2}}} \,. \tag{1.12}$$

Within the DMFT, one often uses a Bethe lattice (an infinite Cayley tree) which has no loops; it is completely characterized by the number of nearest neighbors Z or the connectivity $K = Z - 1$. A portion of a Bethe lattice with $Z = 3$ is depicted in

[6] Due to the fact that this DOS has (unphysical) tails up to infinite energies, the insulating phase is not expected to display a sharp gap (Georges et al., 1996).

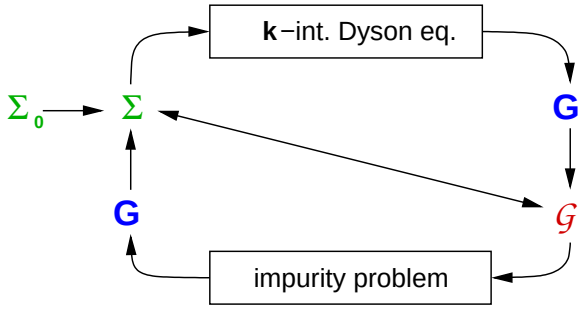

Figure 1.1: Self-consistency cycle of the DMFT [adapted from Blümer (2002)]. Starting with an initial guess for the self-energy $\Sigma = \Sigma_0$, the **k**-integrated Dyson equation is used to calculate the lattice Green function G. This estimate of G and the old self-energy Σ are used to obtain the bath Green function via the auxiliary equation $\mathcal{G}^{-1} = G^{-1} + \Sigma$. The impurity problem can then be evaluated with various methods (QMC, IPT, ED, NRG, etc.) to obtain a new estimate of G. The self-consistency cycle is finally closed by applying once more the auxiliary equation to yield a new estimate of Σ. Additional under or overrelaxation can be used to optimize the convergence.

Figure 1.2. The density of states is semi-elliptical:

$$N^{\mathrm{Bethe}}(\epsilon) = \frac{1}{2\pi t^{*2}} \sqrt{4t^{*2} - \epsilon^2}\,. \tag{1.13}$$

Here, the advantage of using a Bethe lattice within the DMFT is that its density of states has sharp band edges.

The most important observation for the development of the DMFT, however, is that perturbation theory becomes local in the limit $Z \to \infty$, which implies for the proper[7] self-energy:

$$\Sigma(\boldsymbol{k}, \omega) \xrightarrow{Z \to \infty} \Sigma(\omega)\,, \tag{1.14}$$

with momentum $\boldsymbol{k}$ and frequency ω. Within the DMFT, the Hubbard model is mapped to a single-impurity Anderson model (SIAM) embedded in an effective medium. A self-consistency condition then connects the effective medium with the original lattice. The self-consistency equations of the DMFT, written in terms of the

[7] A self-energy is defined to be proper when its external vertices are connected at least by three single Green function lines (compare, e.g., Economou, 1979).

Green function G and the self-energy Σ are given by:

$$G_{\nu\sigma n} = -\langle \psi_{\nu\sigma n} \psi^\dagger_{\nu\sigma n} \rangle_{\mathcal{A}} \tag{1.15}$$

$$G_{\nu\sigma n} = \int\limits_{-\infty}^{\infty} d\epsilon \, \frac{N(\epsilon)}{i\omega_n + \mu - \Sigma_{\nu\sigma n} - \epsilon} \, . \tag{1.16}$$

Here, $\omega_n = (2n+1)\pi T$ are the fermionic Matsubara frequencies (cf. Negele and Orland, 1987), ν and σ the spin and orbital index. Further, $G_{\nu\sigma n} \equiv G_{\nu\sigma}(i\omega_n)$ and $\Sigma_{\nu\sigma n} \equiv \Sigma_{\nu\sigma}(i\omega_n)$. The thermal average $\langle O \rangle_{\mathcal{A}}$ of an operator O is defined as the functional integral over Grassmann variables ψ and ψ^*:

$$\langle O \rangle_{\mathcal{A}} = \frac{1}{\mathcal{Z}} \int \mathcal{D}[\psi] \mathcal{D}[\psi^*] O(\psi\psi^*) e^{\mathcal{A}(\psi,\psi^*,\mathcal{G})} \, , \tag{1.17}$$

with the partition function

$$\mathcal{Z} = \int \mathcal{D}[\psi] \mathcal{D}[\psi^*] e^{\mathcal{A}(\psi,\psi^*,\mathcal{G})} \, , \tag{1.18}$$

and the effective local propagator $\mathcal{G}$, which is connected to the Green function and the self-energy via:

$$\mathcal{G}^{-1}_{\nu\sigma n} = G^{-1}_{\nu\sigma n} + \Sigma_{\nu\sigma n} \, . \tag{1.19}$$

The single-site action $\mathcal{A}(\psi, \psi^*, \mathcal{G})$ describes the dynamics of the impurity problem. For the multi-band Hubbard model that is restricted to the Ising component of the Hund's rule coupling (1.6), $\mathcal{A}$ reads:

$$\mathcal{A}(\psi, \psi^*, \mathcal{G}) \; = \; \mathcal{A}_0 + \mathcal{A}_U + \mathcal{A}_{U'} \, , \tag{1.20}$$

with

$$\mathcal{A}_0 \; = \; \sum_{\nu\sigma n} \psi_{\nu\sigma n} \mathcal{G}^{-1}_{\nu\sigma n} \psi^\dagger_{\nu\sigma n} \, , \tag{1.21}$$

$$\mathcal{A}_U \; = \; -U \sum_{\nu} \int\limits_0^\beta d\tau \, \psi^*_{\nu\uparrow}(\tau) \psi_{\nu\uparrow}(\tau) \psi^*_{\nu\downarrow}(\tau) \psi_{\nu\downarrow}(\tau) \, , \tag{1.22}$$

$$\mathcal{A}_{U'} \; = \; -\sum_{\substack{\sigma\sigma' \\ \nu<\nu'}} (U' - \delta_{\sigma\sigma'} J_z) \int\limits_0^\beta d\tau \, \psi^*_{\nu\sigma}(\tau) \psi_{\nu\sigma}(\tau) \psi^*_{\nu'\sigma'}(\tau) \psi_{\nu'\sigma'}(\tau) \, . \tag{1.23}$$

Here, τ denotes the imaginary time and $\beta = \frac{1}{k_{\mathrm{B}} T}$ is the inverse temperature (henceforth, $k_{\mathrm{B}} \equiv 1$). It is interesting to note that the lattice structure of the original

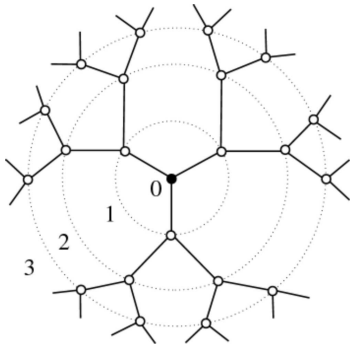

Figure 1.2: Part of the Bethe lattice (or Cayley tree) with $Z = 3$ nearest neighbors (taken from wikipedia). Included is also the distance n from a lattice site that is taken as the central site or the root.

problem enters the self-consistency equation only in the Dyson equation (1.16), in the form of an integration over the density of states.

The self-consistency equations (1.15) and (1.16) can be solved iteratively as illustrated in Fig. 1.1, by making use of (1.19) twice in each cycle. Here, the integration of the Dyson equation is unproblematic. The main difficulty, in contrast, poses the impurity problem (1.15). A variety of techniques have been developed for the solution of the single impurity Anderson model (SIAM), many of which can also be applied to solve (1.15), such as the exact diagonalization (ED) (Caffarel and Krauth, 1994), the numerical renormalization group (NRG) (Wilson, 1975), the non-crossing approximation (NCA) (Keiter and Kimball, 1970) or quantum Monte Carlo (QMC) simulations (Hirsch and Fye, 1986). Comparatively new QMC approaches to solve the impurity problem are the continuous time (CT) quantum Monte Carlo method (Rombouts et al., 1999; Rubtsov et al., 2005) and the projective quantum Monte Carlo method (Feldbacher et al., 2004) [compare also Sec. 1.5].

Despite its success, the DMFT suffers from fully neglecting nonlocal fluctuations. The DMFT is thus not able to capture dynamical effects[8] either in the charge channel (e.g., nearest-neighbor repulsion) nor in the spin channel (exchange). It is also impossible to describe pairing states with extended spatial symmetry such as d-wave superconductivity or localization in disordered systems (e.g., Anderson localization). There exist, however, various extentions of the DMFT that add nonlocal corrections. Most notably are the dynamical cluster approximation (DCA; Hettler et al., 1998; Hettler et al., 2000) and the cellular dynamical mean-field theory (CDMFT; Kotliar et al., 2001). Both methods, which are causal but not systematic in $1/Z$, reduce the

[8] As a matter of course, on-site dynamical effects are included.

lattice problem by mapping it onto a cluster of finite size, which is embedded self-consistently in a dynamical mean field. The effective cluster of the DCA is periodic and therefore translationally invariant. It is thus expected to give a good overall momentum resolution. The CDMFT, however, replaces the impurity by a cluster in real space and hence breaks the translational invariance of the lattice (which is due to the fact that the cluster has open boundary conditions implying that only the surface sites couple to the mean field). Short-range correlations are thus assumed to be resolved better within CDMFT. However, as shown by Aryanpour et al. (2005), DCA-results converge faster as a function of the cluster-size [compare also Biroli and Kotliar (2002)]. Other methods that introduce nonlocal correlations are the cluster perturbation theory (Pairault et al., 1998; Pairault et al., 2000; Gros and Valenti, 1994) or the self-energy-functional theory (Potthoff, 2003) [compare also the footnote 15 on page 98]. For a review of quantum cluster theories, see Maier et al. (2005).

1.5 Quantum Monte Carlo Algorithm

In this section we discuss how the impurity problem (1.15) can be solved within a quantum Monte Carlo simulation. We employ the Hirsch-Fey QMC method (Hirsch and Fye, 1986) for the solution of magnetic impurities, which was extended and applied to the solutions of the DMFT by Jarrell (1992), Georges and Krauth (1992), and Rozenberg et al. (1992). Before introducing the technical details of the QMC algorithm, it is useful to discuss its properties. First, the QMC method is written in imaginary time, such that Green functions and self-energies are obtained only for imaginary Matsubara frequencies. Dynamical information, e.g., the spectrum or the optical conductivity, is obtained only after an analytical continuation to the real axis. Next, Fourier transformations are needed twice in each DMFT iteration cycle to connect the impurity problem to the Dyson equation, which is formulated in frequency space, where it is diagonal. Finally, the QMC method is based on a discretization $\Delta\tau$ of the imaginary time τ. Therefore, results of the DMFT+QMC scheme correspond to physical quantities only after an extrapolation $\Delta\tau \to 0$. The discretization, however, not only restricts the application of the QMC method to comparatively high temperatures, but also complicates the Fourier transform. The problems that originate from the Fourier transforms within the DMFT+QMC simulations are studied in detail in chapter 2.

Trotter Discretization

The first step to solve the impurity problem (1.15) within a QMC simulation is to discretize the imaginary time τ into L time slices of the size $\Delta\tau = \frac{\beta}{L}$. The

imaginary time integrals of (1.22) and (1.23) are thus replaced by a finite sum over $\Delta\tau$. The noncommutative terms representing the kinetic and interaction energy can then be separated using the Trotter-Suzuki formula (Trotter, 1959; Suzuki, 1976), with operators A and B:

$$e^{-\beta(A+B)} = \left(e^{-\Delta\tau A}e^{-\Delta\tau B}\right)^L + \mathcal{O}(\Delta\tau^2)\,, \tag{1.24}$$

It is important to note, that the discretization error in $\Delta\tau$, introduced by the Trotter breakup, is the only systematic error within the QMC solution of the impurity problem.

Hubbard-Stratonovich Transformation

The interaction terms that appear in the effective single-site action [(1.22) and (1.23)] are decoupled by a Hubbard-Stratonovich transformation (Hirsch, 1983):

$$\exp\Big\{\frac{\Delta\tau}{2}V_{\nu\sigma;\nu'\sigma'}\left(\psi^*_{\nu\sigma l}\psi_{\nu\sigma l} - \psi^*_{\nu'\sigma' l}\psi_{\nu'\sigma' l}\right)^2\Big\} = \frac{1}{2}\sum_{s^l_{\nu\sigma;\nu'\sigma'}=\pm1} \exp\left\{\lambda_{\nu\sigma;\nu'\sigma'}s^l_{\nu\sigma;\nu'\sigma'}\left(\psi^*_{\nu\sigma l}\psi_{\nu\sigma l} - \psi^*_{\nu'\sigma' l}\psi_{\nu'\sigma' l}\right)\right\}, \tag{1.25}$$

with $\cosh(\lambda_{\nu\sigma;\nu'\sigma'}) = \exp\left(\frac{\Delta\tau V_{\nu\sigma;\nu'\sigma'}}{2}\right)$ and

$$V_{\nu\sigma;\nu'\sigma'} = \begin{cases} U & \text{for } \nu' = \nu \text{ and } \sigma' > \sigma \\ U' - J & \text{for } \nu' > \nu \text{ and } \sigma' = \sigma \\ U' & \text{for } \nu' > \nu \text{ and } \sigma' \neq \sigma \\ 0 & \text{otherwise} \end{cases}. \tag{1.26}$$

The integral in (1.15) is thereby replaced by a sum over $Lm(2m-1)$ auxiliary fields $s^l_{\nu\sigma;\nu'\sigma'}$. The functional integral for the Green function $G_{\nu\sigma ll'} \equiv G_{\nu\sigma}(l\Delta\tau - l'\Delta\tau)$ then reads:

$$G_{\nu\sigma ll'} = \frac{1}{\mathcal{Z}}\sum_{\{s\}}\int \mathcal{D}[\psi]\mathcal{D}[\psi^*]\psi^*_{\nu\sigma l}\psi_{\nu\sigma l'}\exp\Big\{\sum_{\nu\sigma;ll'}\psi^*_{\nu\sigma l}M^{\boldsymbol{s}}_{\nu\sigma ll'}\psi_{\nu\sigma l'}\Big\}, \tag{1.27}$$

with

$$M^{\boldsymbol{s}}_{\nu\sigma ll'} = \Delta\tau^2(\mathcal{G}^{-1}_{\nu\sigma})_{ll'} - \delta_{ll'}\sum_{\nu'\sigma'}\lambda_{\nu\sigma;\nu'\sigma'}\tilde{\sigma}_{\nu\sigma;\nu'\sigma'}s^l_{\nu\sigma;\nu'\sigma'}\,, \tag{1.28}$$

and $\tilde{\sigma}_{\nu\sigma;\nu'\sigma'} = 2\Theta(\sigma' - \sigma + \delta_{\sigma\sigma'}[\nu' - \nu]) - 1 = \pm1$. Here, $\boldsymbol{s}$ denotes the vector of the auxiliary field, and the sum in (1.27) is taken over all configurations of the

auxiliary spin field, with independent fermions in each term of the sum only. The form of the matrix $\boldsymbol{M}^{\boldsymbol{s}}_{\nu\sigma}$ can be improved by including corrections of $\mathcal{O}(\Delta\tau)$ (Georges et al., 1996; Held, 1999):

$$\boldsymbol{M}^{\boldsymbol{s}}_{\nu\sigma} = \Delta\tau^2 \mathcal{G}^{-1}_{\nu\sigma} e^{-\tilde{\lambda}^{\boldsymbol{s}}_{\nu\sigma}} + \mathbf{1} - e^{-\tilde{\lambda}^{\boldsymbol{s}}_{\nu\sigma}} , \tag{1.29}$$

with the matrix $\tilde{\lambda}^{\boldsymbol{s}}_{\nu\sigma}$:

$$\lambda^{\boldsymbol{s}}_{\nu\sigma ll'} = -\delta_{ll'} \sum_{\nu'\sigma'} \lambda_{\nu\sigma;\nu'\sigma'} \tilde{\sigma}_{\nu\sigma;\nu'\sigma'} s^{l}_{\nu\sigma;\nu'\sigma'} . \tag{1.30}$$

The latter form of the matrix $\tilde{\lambda}^{\boldsymbol{s}}_{\nu\sigma}$ is applied in the actual QMC algorithm.

Wick's Theorem

The functional integral of (1.27) is evaluated by applying Wick's theorem (cf. Negele and Orland, 1987):

$$G_{\nu\sigma ll'} = \frac{1}{\mathcal{Z}} \sum_{\{\boldsymbol{s}\}} \big(M^{\boldsymbol{s}}_{\nu\sigma}\big)^{-1}_{ll'} \prod_{\nu\sigma} \det \boldsymbol{M}^{\boldsymbol{s}}_{\nu\sigma} , \tag{1.31}$$

with the partition function

$$\mathcal{Z} = \sum_{\{\boldsymbol{s}\}} \prod_{\nu\sigma} \det \boldsymbol{M}^{\boldsymbol{s}}_{\nu\sigma} . \tag{1.32}$$

The evaluation of the functional integral (1.27) is thus reduced to a matrix problem. The sum in (1.31) is of exponential order ($2^{Lm(2m-1)}$ terms) and can be summed up exactly only for $Lm(2m-1) \lesssim 24$. A successful method to evaluate sums like (1.31) also for larger values of $Lm(2m-1)$ is the Monte Carlo simulation, which is discussed in the following section. It is further advisable to order the sum in (1.31) in such a way that successive spin-configurations $\{\boldsymbol{s}\}$ and $\{\boldsymbol{s'}\}$ differ only by a single component of the auxiliary spin field (single-spin flip). The computational cost of a single matrix calculation in (1.31) can be reduced from $\mathcal{O}(L^3)$ to $\mathcal{O}(L^2)$, when updating the matrix after a single-spin flip (Blankenbecler et al., 1981).

Quantum Monte Carlo Simulation

High-dimensional integrals or sums like the one in (1.31) can be approximated by a Monte Carlo simulation. Therefore, the full sum over a variable f is divided into a normalized probability distribution P and a remaining observable O:

$$\tfrac{1}{M} \sum_{k=1}^{M} f_k = \sum_{k=1}^{M} P(k) O_k \equiv \langle O \rangle_P . \tag{1.33}$$

Within a Monte Carlo simulation, (1.33) is then approximated by summing only over a subset N (with $N \ll M$), which is chosen randomly with the propability distribution $P(k)$ (importance sampling). The distribution $P(k)$, however, is not known a priori, but can be generated by a stochastic Markov process: Provided a configuration k_i is realized, then a new configuration k_j is accepted with the probability:

$$\mathcal{P}(i \to j) = \min\left\{1, \frac{P(i)}{P(j)}\right\}. \tag{1.34}$$

This choice of transition introduced by Metropolis et al. (1953) satisfies the detailed balance principle

$$P(k_i)\mathcal{P}(k_i \to k_j) = P(k_j)\mathcal{P}(k_j \to k_i)\,, \tag{1.35}$$

and thus creates configurations that correspond to the distribution P, provided the process is ergodic. It is important to note, that P remains unnormalized within the Markov process, implying that only ratios of observables are accessible. Another point is that the probability P associated with a starting configuration k_s might be extremely small, such that the head of the Markov chain has to be excluded from the average (because the length of the Markov chain will be finite in the actual calculation): The auxiliary spin field has to be thermalized.

For the evaluation of (1.31), the (unnormalized) probability distribution P is identified with

$$P\big(\{\boldsymbol{s}\}\big) = \Big|\prod_{\nu\sigma} \det \boldsymbol{M}^{\boldsymbol{s}}_{\nu\sigma}\Big|\,, \tag{1.36}$$

such that the Green function (1.31) is approximated by

$$G_{\nu\sigma ll'} = \frac{1}{\mathcal{Z}_s}\Big\langle \big(M^{\boldsymbol{s}}_{\nu\sigma}\big)^{-1}_{ll'} \operatorname{sign}\Big(\prod_{\nu\sigma} \det \boldsymbol{M}^{\boldsymbol{s}}_{\nu\sigma}\Big)\Big\rangle_s\,, \tag{1.37}$$

with

$$\mathcal{Z}_s = \Big\langle \operatorname{sign}\Big(\prod_{\nu\sigma} \det \boldsymbol{M}^{\boldsymbol{s}}_{\nu\sigma}\Big)\Big\rangle_s\,. \tag{1.38}$$

Here, the average $\langle\cdots\rangle_s$ denotes the spin configuration which is sampled according to (1.36). Note, that the full partition function $\mathcal{Z}$ cannot be calculated within the Monte Carlo simulation (this is due to the importance sampling).

The standard error ΔO of the observable O is given by:

$$\Delta O = \frac{1}{\sqrt{N}}\sqrt{\langle O^2\rangle_P - \langle O\rangle_P^2}\,, \tag{1.39}$$

where the average is taken over a statistical independent configuration N. In case the sample N is within a part of the phase space, where positive and negative values

of the observable O nearly cancel each other, the error ΔO can become larger than the value of the observable, $\langle O \rangle$. This effect is known as the 'minus-sign problem'.[9]

The number of independent measurements is reduced due to the finite autocorrelation of successive configurations visited in the Markov chain. Thus, the true error of the measurement is enhanced compared to (1.39).[10] The influence of a finite autocorrelation on the errors and the convergence of (quantum) Monte Carlo simulations is reviewed by Evertz (2003).

Further QMC Methods

The problems that arise by discretizing the imaginary time is addressed by the continuous time (CT) quantum monte Carlo method (Rombouts et al., 1999; Rubtsov et al., 2005). Here, the decomposition is exact and results in a sum over exponentials of one-body operators. Thus, the error is only statistically and stems from the Monte Carlo sampling of the terms in the decomposition. Advantages of the CT QMC method in comparison to the Hirsch-Fye QMC scheme are expected for multiband, time-dependent correlations since no Hubbard-Stratonovich transformation has to be employed. The computational costs of the CT scheme, however, are of the same order. Furthermore, the sign problem is found to be similar (Rubtsov et al., 2005).

A method to solve the impurity problem of the DMFT within a QMC simulation at zero temperature is given by the projective quantum Monte Carlo method (PQMC; Feldbacher et al., 2004). It is based on the idea that ground state properties can be obtained by filtering out the ground state wave function from a set of trial wave functions (here, the filtering is performed by a projection along the imaginary axis). The convergence to ground state properties is thereby improved compared to the Hirsch-Fye QMC method. Within the limit $\beta \to \infty$, the Green function is only accessible on the interval $[0, \theta]$ (with a finite θ), which is discretized into L time steps with $\Delta\tau = \theta/L$. In order to close the self-consistency cycle of the DMFT, a MEM method has to be employed to obtain $G(i\omega_n)$ via the spectral function $G(i\omega_n) = \int d\omega [A(\omega)/(i\omega_n - \omega)]$. The PQMC method, however, has difficulties to treat insulating solutions with a narrow charge gap, for which θ has to be very large in order to project the trial wave function (which is always metallic) to the insulating ground state solution. As a consequence, the statistical errors become very large even at intermediate values of τ, and the extrapolation with the MEM method results in substantial noise in the charge gap of the spectrum.

[9] This problem arises within the DMFT+QMC, e.g., for a multi-band Hubbard model with isotropic Hund's rule coupling, but not for the anisotropic case.

[10] The effect of a finite correlation time is not considered in the determination of errors within this thesis.

1.6 Maximum Entropy Method

Within the quantum Monte Carlo simulation, Green functions G and self-energies Σ are accessible only for imaginary times τ or imaginary Matsubara frequencies ω_n. Real-time data is therefore only obtained after an analytical extrapolation to the real axis. Of particular interest is the local spectral function

$$A(\omega) = -\frac{1}{\pi}\mathrm{Im}G(\omega + i0^+)\,, \tag{1.40}$$

which, when multiplied with the Fermi function, can be identified with the photoemission spectrum (cf. the review by Damascelli et al., 2003). It is also used to compute transport properties like the optical conductivity (Pruschke et al., 1993).

In this thesis, the imaginary-time QMC data is extrapolated by use of the maximum entropy method (MEM) (Silver et al., 1990). Other approaches, like the Padé approximation of the Green function $G(i\omega_n)$ with a subsequent replacement $i\omega_n \to \omega$, require extremely accurate data which the QMC method cannot provide due to the statistical errors and the finite correlation length (oversampled data). A review of the analytic continuation of imaginary-time quantum Monte Carlo data is given by Jarrell and Gubernatis (1996).

The starting point of the MEM is the spectral representation of the Green function $G(\tau)$, from which the spectral function $A(\omega)$ can, in principle, be obtained by inversion:

$$G(\tau) = \int_{-\infty}^{\infty} d\omega\, \frac{e^{\tau(\mu-\omega)}}{1+e^{\beta(\mu-\omega)}} A(\omega)\,. \tag{1.41}$$

The inversion, however, is an ill-conditioned problem since the weighting of the spectrum $A(\omega)$ is exponentially small for large frequencies ω, and the Green function is measured on a finite grid $\Delta\tau$ only. This results in large errors of the spectral function at high frequencies. The low-frequency results of $A(\omega)$, in contrast, can be determined with high accuracy.

As the spectral function $A(\omega)$ is normalizable and positive semidefinite, it can be taken as probability density. The conditional probability distribution of $\widetilde{G}$ for a given spectrum A is given by:

$$P(\widetilde{G}|A) \propto e^{\frac{1}{2}\chi^2}\,, \tag{1.42}$$

where the distribution of the statistical error is assumed to be Gaussian with variance χ. In order to find the most probable spectrum A for some given data $\widetilde{G}$, one has to invert the conditional probability function $P(\widetilde{G}|A)$ from (1.42). This is possible using Bayes theorem of conditional probability: $P(A|\widetilde{G})P(\widetilde{G}) = P(\widetilde{G}|A)P(A)$. Here, $P(\widetilde{G})$ is constant and can therefore be neglected. According to the principle of maximum

entropy,[11] the probability function $A(\omega)$ is also obtained by maximizing the following entropy expression:

$$P(A) = e^{\alpha S[A(\omega),m(\omega)]}\,, \tag{1.43}$$

with the entropy

$$S = \int d\omega \left[A(\omega) - m(\omega) - A(\omega) \ln\left(\frac{A(\omega)}{m(\omega)}\right)\right]. \tag{1.44}$$

Here, α is a Lagrange parameter, and $m(\omega)$ a default model that can be used to incorporate prior knowledge. The posterior probability is then given by:

$$P(A|\widetilde{G}) = e^{\alpha S[A,m]-\frac{1}{2}\chi^2}\,. \tag{1.45}$$

This posterior probability is finally maximized within the MEM to obtain the spectrum that most probably corresponds to the measured data $\widetilde{G}$. The Lagrange parameter α is used to balance between a good match of the data and a high probability. For further aspects of the MEM compare also Ref. (Gubernatis et al., 1991). The issue of oversampled data is discussed in Ref. (Bryan, 1990), the influence of covariance, non-Gaussian distribution of statistical errors, and systematic errors of QMC data is studied by Blümer (2002).

Within this thesis, spectra are obtained by a program based on the scheme of Sandvik and Scalapino (1995), which assumes that the components of the imaginary time Green function $\widetilde{G}(l\Delta\tau)$ are uncorrelated.[12]

1.7 Self-Consistent Perturbation Theory

Within weak-coupling perturbation theory of an interacting quantum many-body systems, one usually expands the free energy f in powers of the interaction strength. Restricting the series to terms up to first order and determining the order parameters self-consistently, corresponds to Hartree-Fock theory, which is the classical mean-field theory for interacting many-particle systems at weak coupling. Its results are asymptotically exact in the weak-coupling limit, at least up to linear order in the interaction and are well suited to describe non-symmetry broken phases. At weak-coupling, however, the Hartree-Fock predictions for order parameters or critical temperatures that involve the symmetry broken phase are much smaller than linear in the interaction. A prominent example is the BCS theory of superconductivity (Bardeen et al., 1957).

[11] For a definition compare also Ref. (Jarrell and Gubernatis, 1996) and references therein.

[12] Successive elements of the Green function $G(\Delta\tau)$, in contrast, are correlated; more advanced codes that take these correlations into account, however, need QMC data with very small statistical errors (Blümer, 2002). The accuracy of the obtained spectra, as obtained with the Sandvik scheme, however, was sufficient for the conclusions made within this thesis.

Here, the energy difference due to the formation of Cooper pairs is exponentially small at weak interaction: $E_s - E_n \propto -\exp(-\frac{1}{U})$. A similar behavior is found within mean-field theory of antiferromagnetism for the Hubbard model (Langer et al., 1969). Especially in low dimensions ($d = 1$ and $d = 2$), however, fluctuations are known to be large [such that long-range order is explicitly excluded for $T > 0$ (Mermin and Wagner, 1966)]. As a consequence, Hartree-Fock theory, which completely neglects fluctuations, overestimates order-parameters of a symmetry-broken phase or even yields results that are qualitatively incorrect in the limit $U \to 0$. As an example, the Hartree-Fock results overestimate the Néel temperature and the order parameter of the Hubbard model by a factor of the order of four in $d = 3$, even in the extreme weak-coupling limit, as is known from $1/d$-expansions (van Dongen, 1991; van Dongen, 1994*a*), from the local approximation (Tahvildar-Zadeh et al., 1997) and from fully three-dimensional calculations (Schauerte and van Dongen, 2002). Hence, the thermodynamics at small interaction has to be determined self-consistently from the Hartree contributions and the fluctuations together.

There exist various equivalent methods to impose self-consistency, such as the method of conserving approximations (Baym and Kadanoff, 1961; Baym, 1962), the self-consistent perturbation scheme of Bickers and Scalapino (1989) and Bickers and White (1991). A comparatively new method is the self-consistent perturbation theory at fixed order parameters (PTFO), which was originally developed for the ground state of the Hubbard model by Georges and Yedidia (1991)[13] and was extended to finite temperatures and nearest neighbor interactions by van Dongen (1991).

Within the self-consistent perturbation theory at fixed order parameter,[14] the free energy per site $f(U, m)$ is expanded in powers of the interaction at a fixed order parameter m (Georges and Yedidia, 1991):

$$\begin{aligned} f(U,m) &= \tilde{f}_0(m) + U\tilde{f}_1(m) + U^2\tilde{f}_2(m) + \cdots \\ &\equiv f_0 + f_1 + f_2 + \cdots . \end{aligned} \tag{1.46}$$

Here, the functions $\tilde{f}_i(m)$ depend implicitly on U and T. The first two terms of this expansion reproduce the Hartree-Fock approximation, higher-order terms give corrections to the mean-field theory. The order parameter m is kept fixed by introducing a Lagrange parameter $h(U)$, which couples linearly to m. The Lagrange parameter has also to be expanded in powers of the interaction at constant order parameter:

$$h(U) = h_0(m) + h_1(m)U + h_2(m)U^2 + \cdots . \tag{1.47}$$

[13] Within PTFO, the second-order correction to the mean-field theory (of the expansion of the free energy) is also referred to as the Onsager reaction term, in allusion to the terminology of spin-glass theory (Onsager, 1936; Brout and Thomas, 1967).

[14] Working at fixed order parameter effectively resums an infinite number of diagrams calculated at fixed field, which becomes evident in the calculation of the inverse susceptibility within PTFO: $\chi^{-1} = \chi_0^{-1} - \frac{U}{2} + \mathcal{O}(U^2)$. This result coincides with the one of the standard random-phase approximation (RPA) (see, e.g., Doniach and Sondheimer, 1998).

As an example, let us consider the Hamiltonian of the Hubbard model (1.1) at half filling, implying a chemical potential $\mu = \frac{U}{2}$. A staggered magnetization m_{st} in the z direction is assumed. The field $h(U)$ keeps the staggered magnetization per site at a fixed value $m_{st} > 0$. The perturbation expansion of the Hamiltonian is then performed in the usual manner by splitting off the U-dependent terms from the exactly solvable noninteracting part:

$$K = K_0 + K_1 \tag{1.48}$$

$$= H_t + H_U + h(U)\Big[\mathcal{N} m_{st} - \sum_{\boldsymbol{i}} (-1)^{\boldsymbol{i}} S^z_{\boldsymbol{i}}\Big]\,, \tag{1.49}$$

with $S^z_{\boldsymbol{i}} = n_{\boldsymbol{i}\uparrow} - n_{\boldsymbol{i}\downarrow}$. Employing (1.47), one obtains for K_0:

$$K_0 = H_t + h_0\Big[\mathcal{N} m_{st} - \sum_{\boldsymbol{i}} (-1)^{\boldsymbol{i}} S^z_{\boldsymbol{i}}\Big]\,, \tag{1.50}$$

while the perturbation K_1 is given by:

$$K_1 = H_U + (h(U) - h_0)\Big[\mathcal{N} m_{st} - \sum_{\boldsymbol{i}} (-1)^{\boldsymbol{i}} S^z_{\boldsymbol{i}}\Big]\,. \tag{1.51}$$

The perturbation expansion of the free energy in powers of K_1 is

$$\begin{aligned} f =& f_0 - \frac{1}{\beta\mathcal{N}} \int_0^\beta d\tau\, \langle K_1(\tau)\rangle_0^c \\ & - \frac{1}{2\beta\mathcal{N}} \int_0^\beta \int_0^\beta d\tau_1 d\tau_2 \langle K_1(\tau_1) K_1(\tau_2)\rangle_0^c + \cdots\,. \end{aligned} \tag{1.52}$$

Here, $\langle \cdots \rangle_0^c$ signifies that only connected diagrams are taken into account, according to the linked cluster theorem (compare, e.g., Negele and Orland, 1987). The optimal value of m_{st} is determined by minimization of the free energy at fixed values of U and T at each order of the expansion:

$$\frac{df}{dm_{st}} = 0\,. \tag{1.53}$$

The optimized order parameter is then used to determine the next order in perturbation theory. Truncating the free energy at $\mathcal{O}(U)$ yields the Hartree-Fock free energy.

Chapter 2

High-Frequency corrected QMC Simulations within the DMFT

The most successful QMC method[1] to solve the DMFT impurity problem, due to Hirsch and Fye (1986), is based on a discretization of the imaginary time. It is a nonperturbative method which is numerically exact, i.e., the solution of the impurity problem is exact in the limit of vanishing discretization. First DMFT+QMC simulations using this method were performed independently by Jarrell (1992), Rozenberg et al. (1992), and Georges and Kotliar (1992) and allowed, among other things, for the confirmation of the metal-insulator transition in the half-filled Hubbard model in infinite dimensions.

The introduction of the imaginary time, however, implies that Fourier transformations are needed twice in each DMFT iteration cycle, in order to connect the impurity problem (1.15) to the Dyson equation (1.16), which is formulated and diagonal in frequency space. One has to go beyond naive Fourier transforms in order to maintain causality beyond the Nyquist frequency. This important issue has been addressed in various ways. Most of the methods are based on the interpolation of the discretized Green function with cubic splines, but unconventional ones like Ulmke's scheme (Ulmke, 1995), which is based on a transformation of the discretized Green function, also exist.

Of equal importance is the dependence of the QMC estimates on the discretization $\Delta\tau$. As physical quantities are obtained only after an extrapolation $\Delta\tau \to 0$ and the numerical effort of the QMC simulations scales like $2m(m-1)/\Delta\tau^3$ (with the number of orbitals m), it is essential to develop methods with a well controlled[2] $\Delta\tau$ dependence in order to study systems like the Hubbard model at low tempera-

[1] Schemes that are based on the original method for performing QMC calculations for lattice fermions which is due to Blankenbecler et al. (1981) encountered severe numerical instabilities [cf. Ref. Georges et al. (1996) and references therein].

[2] The optimum would be a scheme without $\Delta\tau$ dependence.

tures or multi-band systems ($m > 1$). The error due to the Trotter breakup is of order $\Delta\tau^2$, but the Fourier transform used (more explicitly, the implementation of the DMFT+QMC scheme) adds significantly to this $\Delta\tau$ error. The optimization of DMFT+QMC algorithms is in this respect still an active field [compare also (Joo and Oudovenko, 2001), and (Oudovenko et al., 2005)].

This chapter introduces a method that supplements the QMC Green functions and self-energies with the physically correct high-frequency behavior for arbitrarily large frequencies. This innovation is important, since one finds, apart from obvious improvements at large frequencies, that this method also reduces the inevitable discretization error of the DMFT+QMC scheme to the Trotter error even for comparatively large values of the discretization.

The structure of this section is as follows. First, the effects of the discretization of the imaginary time are discussed and methods that are used in the literature to cure the emerging problems are presented. It is then shown how the DMFT+QMC method can be supplemented with high-frequency corrections. This method, henceforth called QMC+$\frac{1}{\omega}$ scheme, is valid for the single-band and for the multi-band Hubbard model. The scheme is finally compared to competing methods for the following characteristic cases:

- The single-band Hubbard model at half filling,
- the two-band Hubbard model as an example of a multi-band model at half filling,
- the single-band Hubbard model away from half filling.

Because of symmetry, the single-band Hubbard model at half filling is the easiest case for the application of high-frequency corrections. The asymptotic behavior to first order is fully determined by exactly known parameters. This changes in the multi-band case, where already the first order coefficient is explicitly dependent upon density-density correlation functions, which have to be determined self-consistently. The Hubbard model away from half filling turned out to be considerably more difficult. The symmetry of the imaginary time Green function is reduced, resulting in Green functions $G(i\omega)$ with both imaginary and real part. It will be shown, that the developed scheme does not yet correctly account for this asymmetry.

2.1 Methods

2.1.1 Fourier Transform

The application of a QMC simulation within the DMFT requires Fourier transformations twice in each iteration cycle. This is due to the fact that the impurity problem

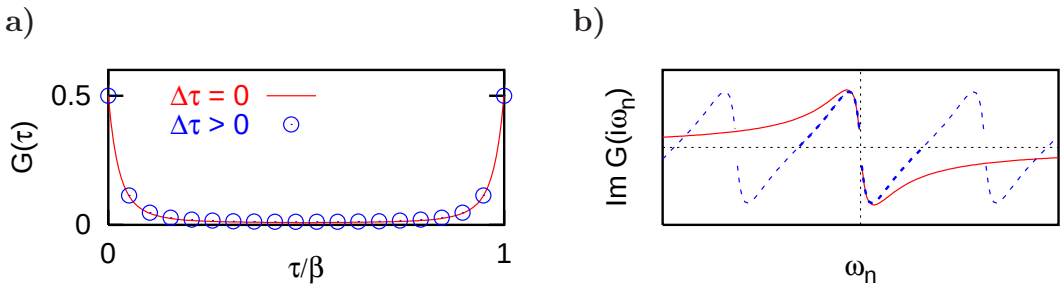

Figure 2.1: Example of a simple discrete Fourier transform: The discretized ($\Delta\tau > 0$) Green function $G(\Delta\tau)$ **(a)** will be mapped on a Green function $G(i\omega_n)$ **(b)** that oscillates instead of showing the correct physical behavior ($\Delta\tau = 0$): $G(i\omega_n) \xrightarrow{\omega_n \to \infty} \frac{1}{\omega_n}$.

(1.15) is formulated in imaginary time representation when solved within the QMC method, whereas the Dyson equation (1.16) is most easily written in terms of Matsubara frequencies. Those two representations are connected by the following Fourier and inverse Fourier transformations:

$$G(i\omega_n) = \int_0^\beta e^{i\omega_n \tau} G(\tau) \mathrm{d}\tau \,, \tag{2.1}$$

$$G(\tau) = \frac{1}{\beta} \sum_{n=-\infty}^{\infty} e^{-i\omega_n \tau} G(i\omega_n) \,, \tag{2.2}$$

with $\omega_n = (2n+1)\pi T$. The Fourier representation takes proper account of the fact that the Green function is antiperiodic for translations β: $G(\tau) = -G(\tau + \beta)$, since $e^{i\omega_n \beta} = -1$. The Green function $G(\tau)$ can further be discontinuous at $\tau = 0$, since the number of terms is infinite in (2.2). From the spectral representation of a Green function it is known that $G(\omega) \approx 1/\omega$ for $\omega \to \infty$ (Negele and Orland, 1987). At half filling, $G(i\omega_n)$ is purely imaginary, which is equivalent to the Green function for imaginary times being symmetric: $G(\tau) = G(\beta - \tau)$. The Green function away from half filling, in contrast, lacks this symmetry, as can be seen from Fig. 2.17.

2.1.2 Discretization, Nyquist Theorem

The discretization of the imaginary time τ into L time slices $\Delta\tau = \frac{\beta}{L}$ implies that the integral in (2.1) has to be approximated by a sum. A simple discretized version

of the Fourier transformation would read:

$$\tilde{G}(i\omega_n) = \Delta\tau \left(\frac{G(0) - G(\beta)}{2} + \sum_{l=1}^{L-1} e^{i\omega_n l\Delta\tau} G(l\Delta\tau) \right) \tag{2.3}$$

$$\tilde{G}(l\Delta\tau) = \frac{1}{\beta} \sum_{n=-L/2}^{L/2-1} e^{-i\omega_n l\Delta\tau} G(i\omega_n)\,. \tag{2.4}$$

Now, the Fourier transform (2.3) of $G(l\Delta\tau)$ has an important implication which is also known as the sampling or Nyquist theorem (Press et al., 1992): Sampling the continuous function $G(\tau)$ at an interval $\Delta\tau$ results in a Fourier transform $\tilde{G}(i\omega_n)$ which is restricted to the frequency range $-\omega_c < \omega_n < \omega_c$, with the Nyquist frequency $\omega_c = \frac{\pi}{\Delta\tau}$. Furthermore, if $G(\tau)$ is not bandwidth limited (e.g., its real Fourier transform $G(i\omega_n) \neq 0$ for $|\omega| \geqslant \omega_c$) and sampled at an interval $\Delta\tau$, the spectrum that lies outside the frequency range $-\omega_c < \omega_n < \omega_c$ will be incorrectly mapped into this range. This effect is also called aliasing. Thus, essentially no information about the Green function $G(i\omega_n)$ above the Nyquist frequency is available directly from a QMC simulation. The result of the finite sum in (2.3) is that $\tilde{G}(i\omega_n)$ does not show the correct analytic behavior for $\omega_n \to \infty$ (e.g., $\frac{1}{\omega_n}$-decay), but drops off to zero at ω_c. The naive Fourier transform further oscillates with period $2\,\omega_c$, as is illustrated in Fig. 2.1b. Especially the large error at the Nyquist frequency makes the solution of the self-consistency equation impossible. A related effect arises from the finite sum in (2.4) which implies that $\tilde{G}(l\Delta\tau)$ is not discontinuous at $\tau = 0$. This is, however, needed for the Green function to be analytic. Furthermore, the discrete Fourier transform (2.4) creates Green functions $\tilde{G}(l\Delta\tau)$ that oscillate around the real physical Green function.

Thus, in summary, the following problem has to be overcome: The Green function in the frequency domain should not vanish at the critical frequency in order to ensure a solution of the DMFT self-consistency equation. This holds especially for a rather coarse grid $\Delta\tau$, where the critical frequency ω_c is small and the relative error at ω_c large. On the other hand, calculations at smaller and smaller values of $\Delta\tau$, that would push the critical frequency to larger and larger values and that would, therefore, also decrease the relative error at ω_c, result in a rapidly increasing numerical effort: The costs of a QMC simulation scale like $m(2m-1)L^3$, with $L = \frac{\beta}{\Delta\tau}$ and the number of orbitals m. At present, e.g., single-band calculations are restricted to $L \lesssim 400$ for supercomputers and to $L \lesssim 250$ for workstations.

2.1.3 Splining

Another important issue is to lift the restriction that is imposed by the discretized Fourier transform (2.3) that implies the number of Matsubara frequencies to equal

the number of time slices. From its spectral representation, $G(\tau)$ is known to be a smooth and discontinuous function. Its Fourier transform $G(i\omega_n)$ thus consists of an infinite number of Matsubara frequencies. The usual method to increase the frequency-range of a continuous function which is known only at discrete points is to interpolate between neighboring data points with cubic polynomials. This procedure is called spline interpolation. The splined Green function can then be either oversampled or directly piecewise Fourier transformed [as in Krauth's code (Georges et al., 1996)] to obtain $G(i\omega_n)$ for arbitrary frequencies. By increasing the range of Matsubara frequencies one can further correctly reproduce the discontinuity of the Green function $G(\tau)$ via (2.4): The rounding errors at the boundaries $\tau = 0^+$ and $\tau = \beta^-$ can be exactly accounted for by adding a constant $\frac{1}{2}$. The errors away from the boundaries become very small and are negligible. The main difficulty in splining the discretized Green function is due to its boundary conditions. The boundary conditions are necessary for closing the set of linear equations that determine the interpolation function. A natural cubic spline is defined to have a zero second derivative at its boundary. The m-th derivatives of the Green function, instead, are in general non-zero, and given by the moments of the spectral density (2.7). A natural cubic spline therefore oscillates around the correct function in order to compensate for the wrong boundary condition. This effect is illustrated in Fig. 2.2, showing the difference of an exact Green function $G(\tau)$ and different spline interpolations from its discretized version $G(\Delta\tau)$. The oscillations can be reduced significantly using an Akima spline, that allows to have discontinuous second derivatives at the data points but still has a zero second derivative at its boundary. As a side effect, the frequency of the resulting oscillations are doubled. Akima-splines are used, e.g., in the QMC code by Jarrell (the frequency-range is thereby increased to up to 800 Matsubara frequencies) (Jarrell, 1992). It is of course also possible to account for the boundary conditions of the Green function already in the spline: This is the case for the 'optimal spline' in Fig. 2.2, for which $G^{(2)}(0)$ was estimated by minimizing the following functional:

$$F(G^{(2)}(0)) = \sum_{j=1}^{L-1} \left(\frac{G^{(2)}((j+1)\Delta\tau)}{G((j+1)\Delta\tau)^2} - \frac{G^{(2)}(j\Delta\tau)}{G(j\Delta\tau)^2} \right)^2 . \tag{2.5}$$

The oscillations can thereby be reduced by a factor of 10. A cubic spline interpolation supplemented with the correct boundary conditions as imposed by the moments of the spectral density (2.7) is used, e.g., by Joo and Oudovenko (2001).

Directly splining the QMC estimate of the Green function does not account for fourth and higher order derivatives of $G(\tau)$, which are especially large at the boundary. This is, however, possible by splining only the *difference* of the QMC estimate of the Green function and a good model Green function, G_{model}, which should, in particular, reproduce the boundaries of the QMC estimate. A method that uses this approach is implemented in Jarrell's code: The reference Green function is obtained

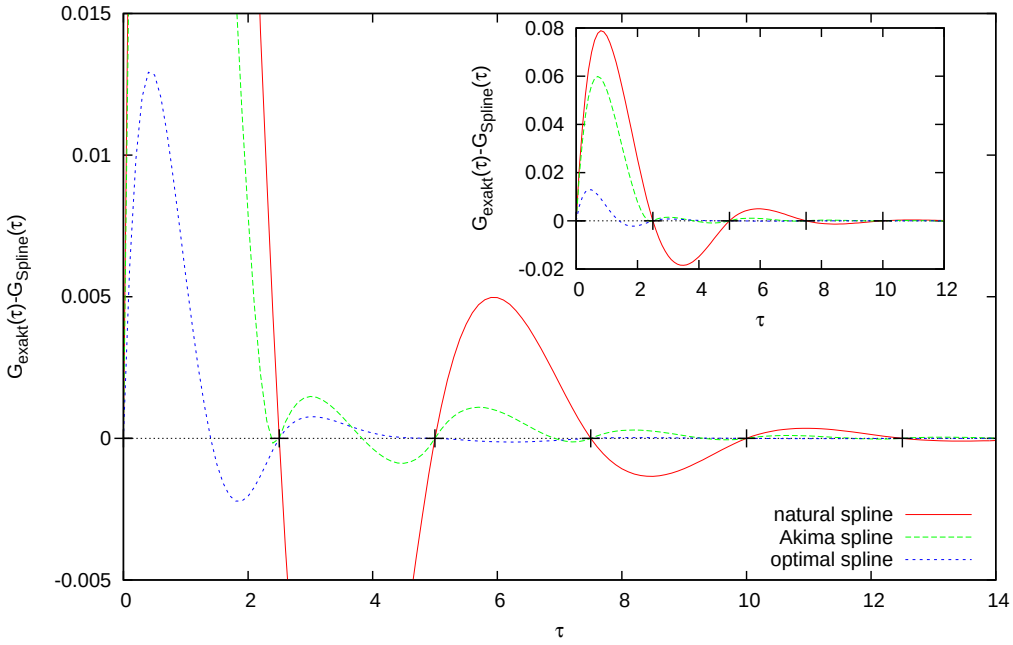

Figure 2.2: Difference between the exact noninteracting Green function for the Bethe lattice ($\beta = 100$) and different cubic spline interpolations of the discretized Green function for $L = 40$ (black crosses). The natural spline and the Akima spline show strong oscillations close to the boundary $\tau = 0$ (and similarly at $\tau = \beta$). This behavior is caused by their vanishing second derivative, which is in contrast to the exact Green function. Using optimal boundary conditions, as they can be obtained, e.g., by a minimizing functional, reduces the oscillations by an order of magnitude. The inset shows the results on a different vertical scale.

from plain second order perturbation theory. This scheme, however, does not account for terms of $\mathcal{O}\left(\frac{1}{\omega^2}\right)$ or higher. Another way to create a good model Green function of the QMC estimate, which is based on the moments of the spectral density, is presented in the Sec. 2.2.

2.1.4 Other Methods

A rather unconventional method to cure the problem of a vanishing Green function at ω_c was presented by Ulmke (1995). A naive asymmetric Fourier transform (2.3) of the QMC estimate $G(\Delta\tau)$ is combined with an approximation scheme, that is asymptotically exact for $\Delta\tau \to 0$, namely:

$$G(i\omega_n) = \frac{\Delta\tau}{\ln\left[1 + \Delta\tau/\tilde{G}(i\omega_n)\right]} \,. \tag{2.6}$$

The transformed Green function then approximately exhibits a $\frac{1}{\omega_n}$-fall off for large frequencies. The transformation is inverted before Fourier transforming the Green function back to the imaginary time representation. Unfortunately, the approximation also slightly modifies the low frequency regime, resulting in a better treatment of the metallic phase than of the insulating one (Blümer, 2002). The deficiency of the transformation (2.6) can be overcome when using a modified version as implemented by Blümer (2002): The discretization $\Delta\tau$ in (2.6) is explicity made dependent upon the frequency: $\Delta\tau \to \left[1-(\omega_n\Delta\tau/\pi-1)^8\right]\Delta\tau$. This modification ensures that low frequencies are less affected [to $\mathcal{O}(\Delta\tau^2)$ instead of to $\mathcal{O}(\Delta\tau)$, as in (2.6)] and that the smoothing trick works normally for $\omega \approx \omega_c$. A comprehensive analysis of Ulmke's method and also of the modified version of it, that will be called corrected Ulmke scheme henceforth, can be found in Ref. Blümer (2002).

2.2 High-Frequency corrected QMC Simulation

In this part, a scheme is presented that supplements the DMFT+QMC Green functions with the physically correct high-frequency behavior up to $\mathcal{O}\left(\frac{1}{\omega^2}\right)$. The large frequency behavior of the self-energies is thereby correctly produced up to $\mathcal{O}\left(\frac{1}{\omega}\right)$. For simplicity, the scheme will henceforth also be referred to as the QMC+$\frac{1}{\omega}$ method. The scheme makes use of the fact that the difference of the QMC estimate of the Green function $G(\Delta\tau)$ and a good model Green function G_{model}, which has physically correct derivatives at its boundaries at least up to second order, can be interpolated safely with a natural cubic spline. The constructed model of the Green function is based on the high-frequency expansion of the self-energy (Potthoff et al., 1997). This method, already presented in Ref. Knecht (2002) for the single-band Hubbard model at half filling, will be expanded to the multi-band case at half filling.

2.2.1 Model Green Function

In order to successfully make use of a cubic spline interpolation of the discretized Green function $G(\Delta\tau)$, it is necessary to correctly account for the boundary conditions. One possibility is to directly impose the correct boundary conditions on the spline, which was done for the single-band Hubbard model at half filling, e.g., by Joo and Oudovenko (2001). The second derivatives of the Green function, $G^{(2)}(0^+,\beta^-)$, can be obtained from the moments of the spectral density:

$$(-1)^m G^{(m)}(0^+) + G^{(m)}(\beta^-) \;=\; \langle(\omega-\mu)^m\rangle_{A(w)}\,. \tag{2.7}$$

Using the symmetry property of the Green function at half filling

$$G^{(m)}(0^+) = (-1)^m G^{(m)}(\beta^-)\,, \tag{2.8}$$

and the value of the second moment for $\mu = 0$ which is given in Appendix B, one finds: $G^{(2)}(0^+) = G^{(2)}(\beta^-) = \frac{U^2}{8}$. Directly splining the full Green function, however, cannot account for derivatives of fourth and higher order because those derivatives vanish on segments of the cubic spline. These higher order derivatives are, however, especially large at the boundaries $\tau = 0$ and $\tau = \beta$. A possibility to consider them is not to spline the full Green function but only the difference to a good estimate of $G(\Delta\tau)$ which incorporates the correct boundary conditions and for which the exact Fourier transform is known. The missing part can then be added in frequency space to obtain the full Green function $G(i\omega_n)$.

The construction of a model Green function can be based on an exact high-frequency expansion of the self-energy, which was presented by Potthoff et al. (1997) for the single-band Hubbard model:

$$\Sigma_\sigma(\omega) = U \langle \hat{n}_{-\sigma} \rangle + \frac{1}{\omega} U^2 \langle \hat{n}_{-\sigma} \rangle (1 - \langle \hat{n}_{-\sigma} \rangle) + \mathcal{O}(\omega^{-2}) \,. \tag{2.9}$$

The derivation of this expansion for the single-band case as well as for the general case of multiple bands is given in Appendix B. A model self-energy which has this asymptotic behavior can be used to generate a model Green function in frequency space, $G_{\mathrm{model}}(i\omega_n)$, with the help of the $\boldsymbol{k}$-integrated Dyson equation (1.16). This model Green function is then available for arbitrary high frequencies and therefore easily Fourier transformed to obtain the corresponding model Green function $G_{\mathrm{model}}(\tau)$ in the imaginary time representation. The m-th coefficient of the self-energy expansion (2.9) is determined by the $(m+1)$-th moment of the spectral density (2.7). It is therefore assured that the boundary conditions of $G^{(2)}_{\mathrm{model}}(0^+)$ and $G^{(2)}_{\mathrm{model}}(\beta^-)$ exactly reproduce the ones of the true Green function. Higher order coefficients of the self-energy expansion then account for the corresponding higher order derivatives at the boundaries.

The extension to the general case of multiple bands, as obtained independently by Knecht (2002) and Oudovenko et al. (2005), is given by:

$$\Sigma_\gamma(\omega) = \sum_{\beta \neq \gamma} U_{\beta\gamma} \langle n_\beta \rangle + \frac{1}{\omega} \sum_{\alpha,\beta \neq \gamma} U_{\alpha\gamma} U_{\beta\gamma} (\langle n_\alpha n_\beta \rangle - \langle n_\alpha \rangle \langle n_\beta \rangle) + \mathcal{O}(\frac{1}{\omega^2}) \,. \tag{2.10}$$

Here α, β and γ are multi-indices, combining spin and orbital degrees of freedom: $\alpha \equiv (m, \sigma)$; the interaction matrix is defined by $U_{m\sigma,m\bar{\sigma}} = U$, $U_{m\sigma,\bar{m}\sigma'} = U' - J_z \delta_{\sigma\sigma'}$. Equating the indices α and β reproduces (2.9). In contrast to the single-band case, higher-order correlation functions of the form $\langle n_\alpha n_\beta \rangle$ enter the expansion of the self-energy. They have to be computed self-consistently within the QMC part of the DMFT iteration scheme.

2.2.2 Choice of the Model Self-Energy

For the single-band Hubbard model at half filling, the choice of the exact form of the model self-energy is not very critical. One possibility is to use a two-pole expansion:

$$\Sigma_\sigma(\omega) = \Sigma_\sigma^{\mathrm{HF}} + \frac{A_1}{\omega - \omega_1} + \frac{A_2}{\omega - \omega_2}\,. \tag{2.11}$$

The coefficients A_i of the pole expansion determine the high-frequency behavior. $\Sigma_\sigma^{\mathrm{HF}}$ is the Hartree Fock value of the self-energy which is frequency independent because it acts instantaneously. The values of the parameters ω_i are not too important at half filling, as long as they are not much larger than the bandwidth. They can be used to adjust the low-frequency part. As the self-energy of the Hubbard model at half filling is purely imaginary, it is useful to choose the poles to be symmetric with respect to zero, $\omega_1 = -\omega_2$, and to have equally distributed weights: $A_1 = A_2$. This choice ensures that the self-energy is purely imaginary on the imaginary axis. One then obtains the following form of a model self-energy, which will henceforth be labeled PE1 (where PE stands for 'pole expansion'):

$$\Sigma_{\mathrm{PE1},\sigma}(\omega) = U\left(\langle \hat{n}_{-\sigma}\rangle - \tfrac{1}{2}\right) + \tfrac{1}{2}U^2\,\langle \hat{n}_{-\sigma}\rangle(1 - \langle \hat{n}_{-\sigma}\rangle)\Big(\frac{1}{\omega + \omega_0} + \frac{1}{\omega - \omega_0}\Big)\,. \tag{2.12}$$

A model self-energy with two poles is motivated by the fact that it is already able to describe a 3-peak structure comprising a quasiparticle peak in the spectrum of single-electron excitations. This corresponds to a simplified picture of the basic structure of the Hubbard model with the upper and lower Hubbard bands and a quasiparticle peak.

Another possible form of the model self-energy is a continued fraction expansion:

$$\Sigma_\sigma(\omega) = \Sigma_\sigma^{\mathrm{HF}} + \cfrac{A_\sigma}{\omega - B_\sigma - \cfrac{C_\sigma}{\omega - D_\sigma - \cdots}}\,. \tag{2.13}$$

Both representations of the self-energy, (2.11) and (2.13) are causal, their coefficients related non-linearly. The latter representation, however, has an advantage that can be seen when expanding both representations in a $\frac{1}{\omega}$ series. For the pole expansion (2.11) one gets:

$$\Sigma_{\mathrm{pole}}(\omega) = \Sigma^{\mathrm{HF}} + \frac{A_1 + A_2}{\omega} + \frac{A_1\omega_1 - A_2\omega_2}{\omega^2} + \frac{A_1\omega_1^2 + A_2\omega_2^2}{\omega^3} + \mathcal{O}(\omega^{-4})\,. \tag{2.14}$$

For the continued fraction expansion (2.13) one finds:

$$\Sigma_{\mathrm{cf}}(\omega) = \Sigma^{\mathrm{HF}} + \frac{A}{\omega} - \frac{AB}{\omega^2} + \frac{AB^2 - AC}{\omega^3} + \mathcal{O}(\omega^{-4})\,, \tag{2.15}$$

with $B = 0$ at half filling and symmetric DOS. Now, there is one fundamental difference in the dependence of the $\frac{1}{\omega}$-coefficients of the pole expansion and of the continued fraction expansion: Only the first n coefficients of the continued fraction expansion determine the n-th order of the $\frac{1}{\omega}$-expansion. Including a term of the order $n+1$ in the continued fraction expansion leaves the coefficients of the $\frac{1}{\omega}$-expansion up to $\mathcal{O}\left(\frac{1}{\omega^n}\right)$ untouched. This is not the case in the pole expansion. There, already the term of $\mathcal{O}\left(\frac{1}{\omega^2}\right)$ is dependent upon all coefficients of all poles. The inclusion of an additional pole affects the coefficients of any order in $\frac{1}{\omega}$. This difference in the behavior of the two representations for the self-energy upon its coefficients is reflected in the ability to find a high-quality model self-energy for the multi-band case: It turned out that the model self-energy must also be a good estimate in the intermediate frequency regime to create a model Green function that connects smoothly to the QMC estimate near the Nyquist critical frequency. This intermediate regime is controlled by the coefficients of $\mathcal{O}\left(\frac{1}{\omega^2}\right)$ and higher. In principle, higher order coefficients can be computed analytically, but they will depend also upon higher order correlation functions that need to be calculated within the QMC part, which itself is an extremely time-consuming task. It is, therefore, easier to fit higher order coefficients to the data. How this is done in detail will be discussed in the following section. The advantage of the continued fraction expansion for the model self-energy is, therefore, that the quality of the model self-energy can be increased by successively taking higher order moments into account without affecting the already optimized coefficients of lower order. A minimization scheme based upon such a model self-energy is much more stable than the one using a pole representation for Σ_{model}.

The model self-energies discussed above are of 'metallic' nature. It is therefore interesting, to also study the QMC+$\frac{1}{\omega}$ scheme by using an 'insulating' model self-energy:

$$\Sigma_{\text{PE2}}(i\omega_n) = -i\,\frac{U^2\,\text{sign}(\omega_n)}{4(|\omega_n| + \omega_r)}\,. \tag{2.16}$$

This model self-energy develops a pole for $\omega_r \to 0^+$ at $\omega = 0$ and therefore exhibits an 'insulating' nature in this limit. Although this model self-energy does not, strictly speaking, contain actual poles, it will, nevertheless, be referred to as a pole expansion, labeled by PE2, just to simplify matters. Note that this model self-energy is not causal and, hence, does not obey a Kramers-Kronig relation. Nevertheless, as is shown below, this deficiency alone has no influence on the results of the QMC+$\frac{1}{\omega}$ scheme for single-band systems at half filling.

2.3 Comparison of DMFT+QMC Schemes for the Single-Band Hubbard Model at half Filling

A fundamental criterion for the comparison of DMFT+QMC schemes is the dependence of the data upon the discretization $\Delta\tau$. As physical quantities are only obtained after an extrapolation $\Delta\tau \to 0$, a scheme with a small and well-controlled dependence upon the discretization is favorable. Another important point is the quality of predictions for the Green function or the self-energy beyond the Nyquist frequency. The frequency range of some schemes used in the literature up to now is even restricted to the Nyquist frequency (e.g., Krauth's or Ulmke's scheme).

In this section, the developed QMC+$\frac{1}{\omega}$ scheme will be compared to the scheme due to Ulmke (1995) and to its corrected version by Blümer (2002) for the single-band model. Although the applicability of the QMC+$\frac{1}{\omega}$ scheme [in combination with the pole expansion of the form (2.12) for the model self-energy] was already demonstrated for the single-band Hubbard model by Knecht (2002), the comparison is instructive because the features of the QMC+$\frac{1}{\omega}$ splining scheme are best illustrated for the single-band case. A comparison of the multi-band scheme is then given in Sec. 2.4.

The Ulmke scheme was already verified by Held (1999) by the following tests, which were applied to both, the single-band and the multi-band case:

- Reproduction of the Green function in the atomic limit ($t = 0$),
- reproduction of the susceptibilities and Green functions in the Fermi gas limit ($U = 0$),
- reproduction of results obtained by Rozenberg (1997) and by Wahle et al. (1998).

These and further comprehensive tests (which were performed by Blümer (2002) and are related to the study of the MIT in the 1-band Hubbard model with Bethe DOS) qualify the corrected Ulmke scheme and, with restrictions[3], also Ulmke's original scheme as reference systems.

2.3.1 Observables

The observables that will be used in this and in the following comparisons are, on the one hand, the Green function and the self-energy, which are the solutions of the

[3]The restriction concerns the difference of the Ulmke scheme in treating metallic and insulating phases, as mentioned in 2.1.4.

DMFT self-consistency cycle, and, on the other hand, the Eliashberg estimate of the quasiparticle weight Z as well as the double occupancy D.

As a matter of course, the self-energy and Green function are naturally considered in the context of high-frequency corrections. The behavior of the self-energy at the lowest frequency is closely related to the quasiparticle weight Z or mass renormalization factor:[4]

$$Z = \frac{m}{m^*} = \frac{1}{1 - \frac{\partial \mathrm{Re}\Sigma(\omega)|_{\omega=0}}{\partial \omega}} \,. \tag{2.17}$$

Within a QMC simulation, this quantity is normally approximated by the Eliashberg estimate:

$$Z \approx \frac{1}{1 - \frac{\mathrm{Im}\Sigma(i\omega_1)}{\pi T}} \,. \tag{2.18}$$

The double occupancy D, finally, is an example of a correlation function, which also determines the lowest order coefficient of the large frequency expansion in the multi-band case. It is directly calculated within the QMC simulation by employing Wick's theorem.

2.3.2 Results

When comparing different QMC schemes, it is not too instructive to consider the Green function directly, as is illustrated in Fig. 2.3. The small differences at low frequencies are due to the different $\Delta\tau$ error of the schemes, while a discrepancy at large frequencies is not detectable. The estimates of all schemes correctly exhibit a $\frac{1}{\omega}$-decay (inset), while the QMC+$\frac{1}{\omega}$ scheme is not restricted to frequencies below the Nyquist critical frequency. The differences of splining methods are better studied by considering the self-energy. At half filling, it suffices to examine only the imaginary part, $\mathrm{Im}\Sigma(i\omega_n)$, because the real part of $\Sigma(i\omega_n)$ vanishes exactly. Figure 2.4 shows predictions of the self-energy of the single-band Hubbard model with semi-circular DOS at $T = 0.1$ for the correlated metallic phase at $U = 4$, and Fig. 2.6 for the insulating phase at $U = 5$ for various discretizations $\Delta\tau$, as obtained from Ulmke's smoothing method. The self-energies are restricted to below and vanish at the Nyquist frequency. The dependence upon the discretization is significant for all frequencies. Furthermore, within the insulating solution, the low-frequency behavior is qualitatively wrong for large values of $\Delta\tau$ (e.g., for $\Delta\tau = 0.4$). The inset shows the relative deviation from the asymptotic large-frequency behavior $-U^2/(4\omega_n)$. An approximately correct behavior can be obtained only for very small discretizations ($\Delta\tau < 0.1$) at intermediate frequencies.

The self-energies obtained from the QMC+$\frac{1}{\omega}$ scheme are shown in Fig. 2.5 and Fig. 2.7. The correct asymptotic behavior is obtained for all discretizations at large

[4] The reader is referred to 3.2.1 for a more detailed discussion of the quasiparticle weight.

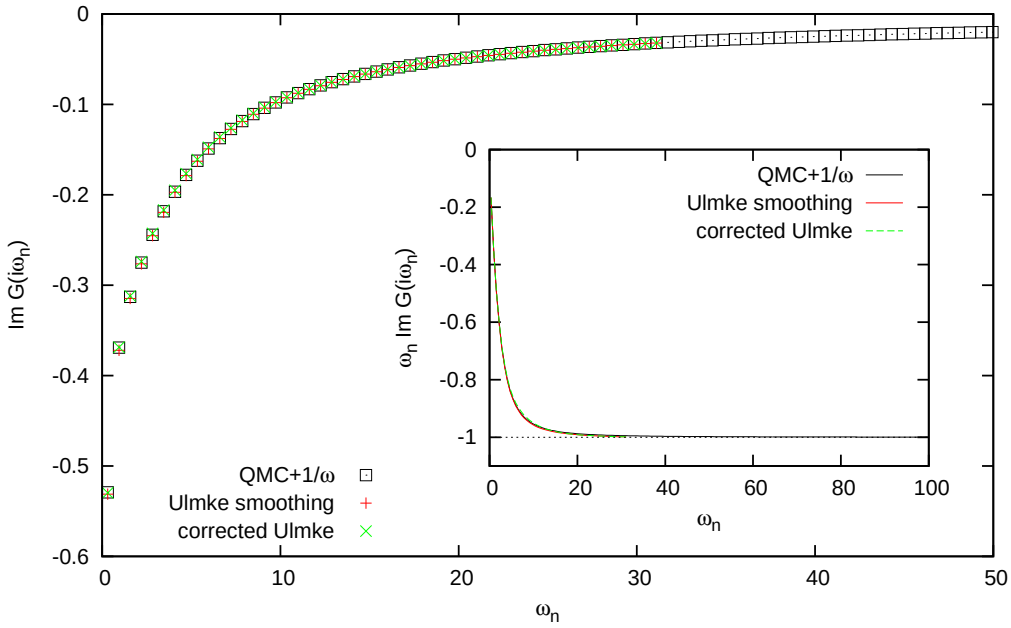

Figure 2.3: Imaginary part of the Green function at $T = 0.1$ and $U = 4$ for semi-elliptic DOS with $\Delta\tau = 0.1$ as obtained by different splining schemes. The inset shows the product $\omega_n \mathrm{Im}G(i\omega_n)$ and its exact asymptotic value -1.

frequencies. Oscillations around the asymptote are significant only at intermediate frequencies (cf. insets) for very large discretizations ($\Delta\tau \gtrsim 0.4$). Furthermore, the dependence upon the discretization in the most important low-frequency region is very small: differences in $\mathrm{Im}\Sigma(\omega_1)$ for discretizations $\Delta\tau = 0.125$ and $\Delta\tau = 0.10$ cannot be seen on this scale.

The convergence upon the discretization is illustrated in Fig. 2.8 for the Eliashberg estimate of the quasiparticle weight Z as a function of $\Delta\tau^2$. The quasiparticle weight obtained by the QMC+$\frac{1}{\omega}$ scheme shows the smallest $\Delta\tau$ dependence and is quadratic in $\Delta\tau$ for discretizations $\Delta\tau \lesssim 0.4$. The results from the corrected Ulmke smoothing method show a similar behavior. The dependence upon $\Delta\tau$ is significantly larger for the Ulmke scheme: its estimates are not purely quadratic in $\Delta\tau$, but also depend on terms of $\mathcal{O}(\Delta\tau^4)$ for $\Delta\tau \lesssim 0.4$.

Figure 2.9 shows the dependence of the double-occupancy D upon $\Delta\tau^2$ for $T = \frac{1}{15}$ within the Mott insulating regime at $U = 6$, as obtained by various DMFT+QMC schemes used in the literature. The correct value for D at $T = 0$ is calculated by the 'extended perturbation theory' (ePT), a method of Blümer and Kalinowski (2005). Only the estimates obtained by the QMC+$\frac{1}{\omega}$ scheme are quadratic in $\Delta\tau$ for $\Delta\tau \lesssim 0.3$.

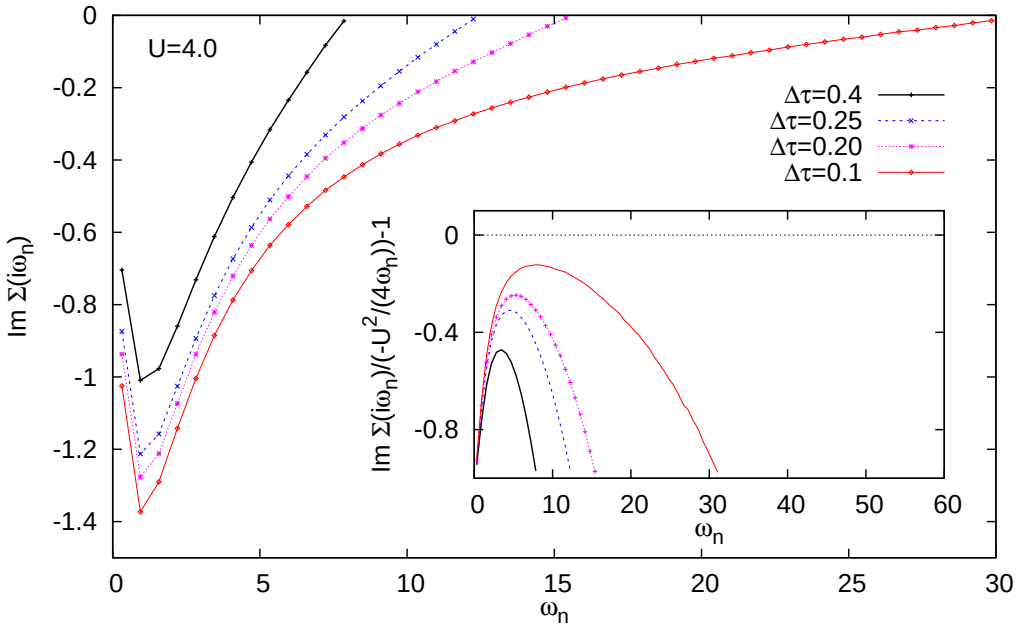

Figure 2.4: Imaginary part of the self-energy for $U = 4$ and $T = 0.1$ obtained with Ulmke's smoothing scheme for various discretizations $\Delta\tau$. The inset shows the relative deviation from the asymptotic large-frequency behavior $-U^2/(4\omega_n)$. Adapted from Ref. (Knecht, 2002).

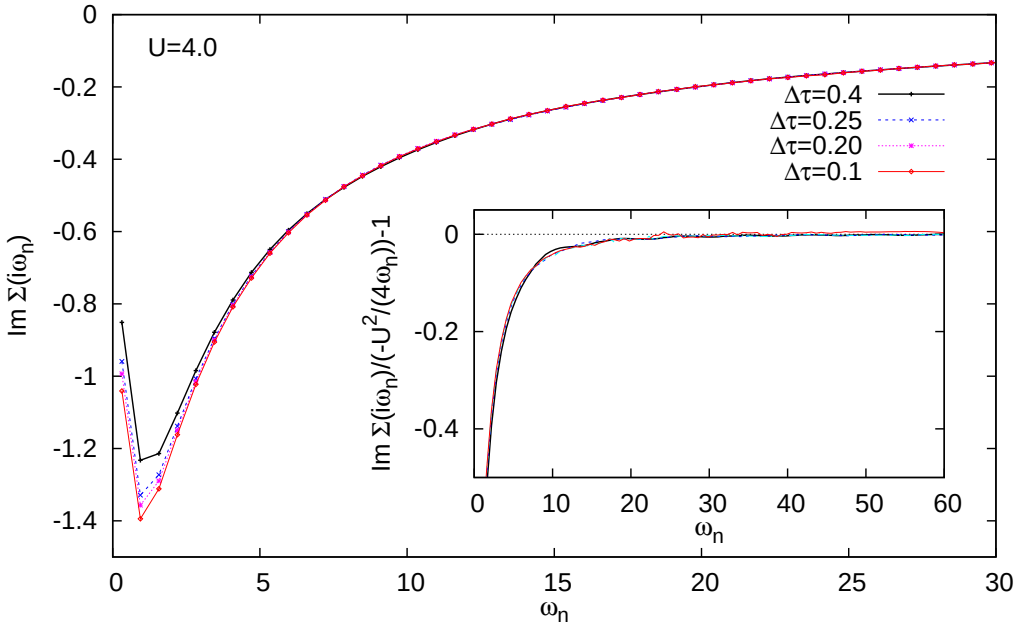

Figure 2.5: Imaginary part of the self-energy for $U = 4$ and $T = 0.1$ obtained with the QMC+$\frac{1}{\omega}$ scheme for various discretizations $\Delta\tau$. The inset shows the relative deviation from the asymptotic large-frequency behavior $-U^2/(4\omega_n)$. Adapted from Ref. (Knecht, 2002).

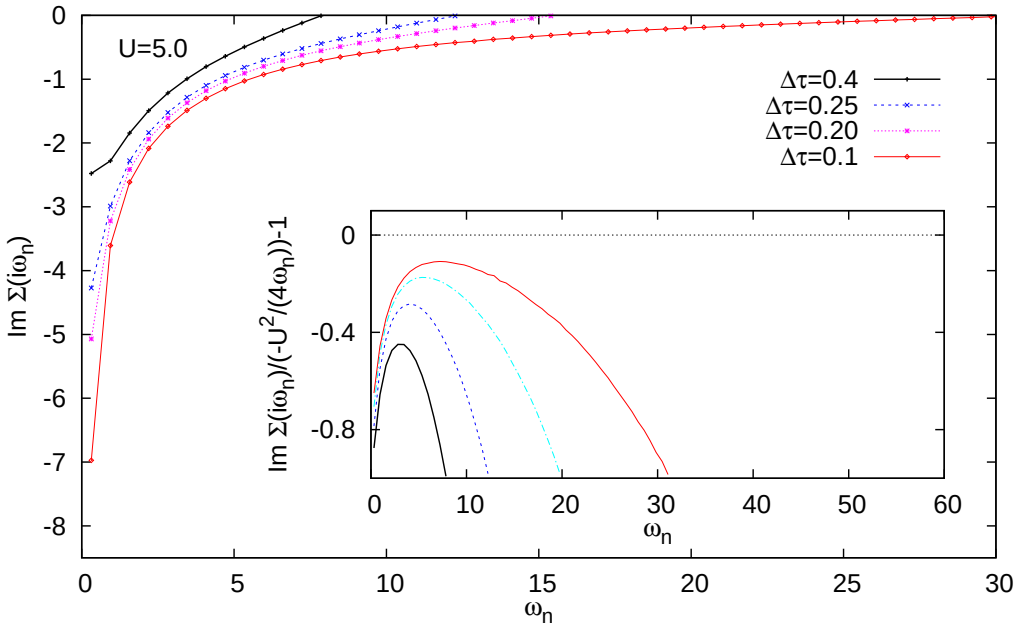

Figure 2.6: Imaginary part of the self-energy for $U = 5$ and $T = 0.1$ obtained with Ulmke's smoothing scheme for various discretizations $\Delta\tau$. The inset shows the relative deviation from the asymptotic large-frequency behavior $-U^2/(4\omega_n)$. Adapted from Ref. (Knecht, 2002).

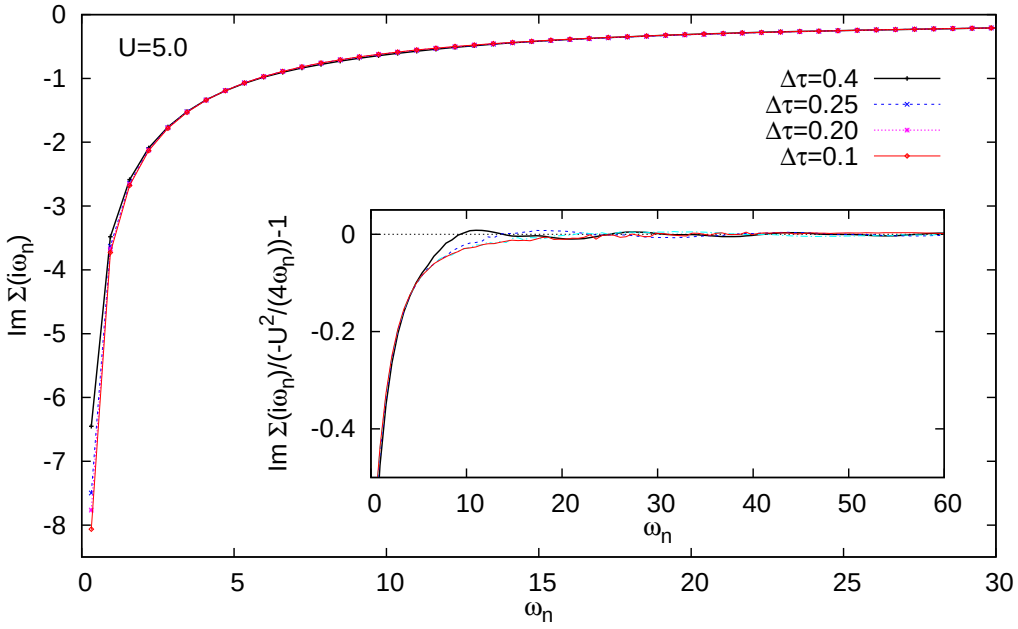

Figure 2.7: Imaginary part of the self-energy for $U = 5$ and $T = 0.1$ obtained with the QMC+$\frac{1}{\omega}$ scheme for various discretizations $\Delta\tau$. The inset shows the relative deviation from the asymptotic large-frequency behavior $-U^2/(4\omega_n)$. Adapted from Ref. (Knecht, 2002).

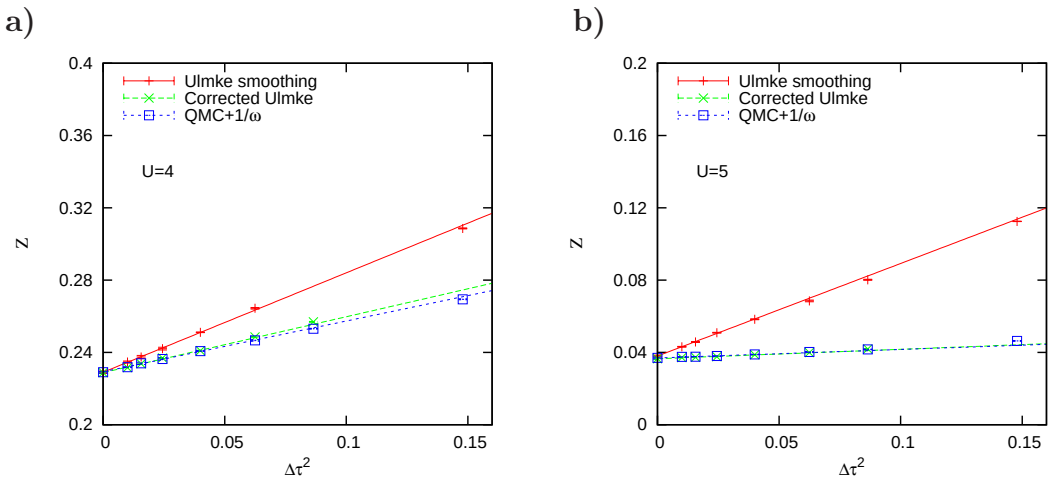

Figure 2.8: Quasiparticle weights Z for semi-elliptic DOS at $T = 0.1$ and $U = 4$ (**a**) and $U = 5$ (**b**) as a function of $\Delta\tau^2$. Adapted from Ref. (Knecht, 2002).

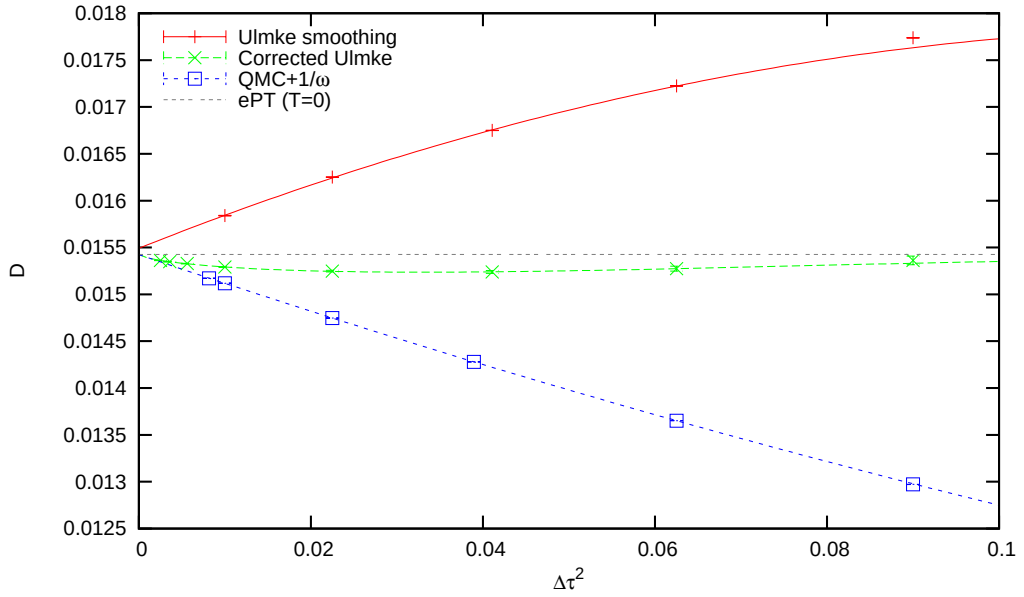

Figure 2.9: Double occupancy D as a function of $\Delta\tau^2$ at $T = \frac{1}{15}$ and $U = 6$ for different DMFT+QMC implementations. The correct value at $T = 0$ is calculated by ePT.

Having discussed the main features of the QMC+$\frac{1}{\omega}$ scheme, it is instructive to study the influence of the model self-energy on the resulting self-energy or Green function, respectively. This is illustrated in Fig. 2.10 which shows the imaginary part of the self-energies $\mathrm{Im}\Sigma(i\omega_n)$ (points) and the corresponding model self-energies (lines) in the main panel. CF denotes a continued fraction expansion for the model self-energy of the form (2.13). The coefficients of the expansion are determined as described below. The free parameter ω_0 of the symmetric pole expansion PE1 (2.12) is fixed to $\omega_0 = 1$. The free parameter ω_r of the model self-energy PE2 (2.16) was adjusted by hand such that the model self-energy connects as smoothly as possible to the QMC estimate of the self-energy around the Nyquist critical frequency. The different choices for the model self-energy have obviously no influence on the low frequency behavior of the self-energy; discrepancies are observed only for $\omega_n > 10$, especially within the high-frequency regime. This is illustrated in the inset of Fig. 2.10, showing the relative deviation from the asymptotic behavior. Solutions obtained from the continued fraction expansion and from the pole expansion PE1 approach the asymptotic behavior quickly and then oscillate with twice the Nyquist critical frequency $\omega_c = \frac{\pi}{\Delta\tau}$. The amplitude of the oscillations for the CF scheme are reduced by a factor of approximately 2 compared to the ones of the pole expansions (PE1 and PE2, at least for $\omega_n \lesssim 50$) . In summary, the highest quality of the self-energy (with respect to the correct asymptotic behavior and the vanishing of the oscillations) is achieved by an optimal choice of the free parameters of the model self-energy.

The free parameters are in principle determined by higher order correlation functions. They are, however, hardly computable within the QMC simulation with a reasonable effort. It is more advisable to estimate the free parameters numerically by a minimization scheme. One possibility to approximate the free parameters is to minimize the difference of the Green function $G(\Delta\tau)$ and the model Green function $G_{\mathrm{model}}(\Delta\tau)$ at the first n time steps $\tau = n\Delta\tau$ ($n = 0, 1, \dots$). At half filling, it turned out that it suffices to take the first three coefficients [besides A, also B and C in (2.13)] into account and to minimize the sum F of the differences up to $n = 1$:

$$F = \sum_{k=0}^{n} |G(k\Delta\tau) - G_{\mathrm{M}}(k\Delta\tau)| \,. \tag{2.19}$$

The resulting Green function and the model based on the results of the minimization is shown in the lower part of Fig. 2.11, while the upper part shows the difference Green functions $G_{\mathrm{D}} = G - G_{\mathrm{model}}$ also for the pole expansions PE1 and PE2. The deviation of the QMC estimate for G from the model Green function, based upon the continued fraction expansion obtained by minimizing (2.19), is very small at $\tau = \Delta\tau$ compared to the results from the pole expansions PE1 and PE2 and nearly vanishes at $\tau = 2\Delta\tau$. This ensures that the second order derivatives (and of higher order)

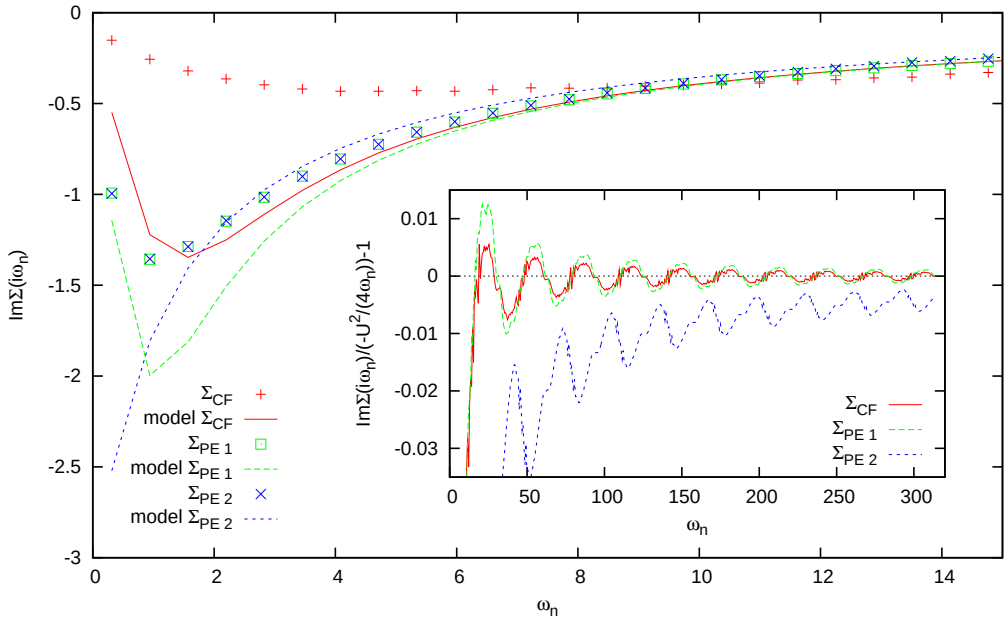

Figure 2.10: Imaginary part of the self-energy obtained with different model self-energies $\mathrm{Im}\Sigma(i\omega_n)$ for $U = 4$, $T = 0.1$ and $\Delta\tau = 0.2$ for a semi-elliptic DOS. CF denotes a continued fraction expansion, PE1 (PE2) pole expansions for the model self-energy. PE1 is an expansion of the form (2.12) with free parameter $\omega_0 = 1$, PE2 an expansion of the form (2.16). Inset: Relative deviation of $\mathrm{Im}\Sigma(i\omega_n)$ from the asymptotic high-frequency form $-\frac{U^2}{4\omega_n}$. The relative deviations shows oscillations around the asymptote with a period of twice the Nyquist critical frequency $\omega_c = \frac{\pi}{\Delta\tau} \approx 15.7$.

are very small at the boundaries $\tau = 0^+, \beta^-$ and thus already well incorporated in the model Green function G_{model}. The difference Green function G_{D} can, therefore, be splined with a natural cubic spline which is defined to have a vanishing second derivative at its boundaries.

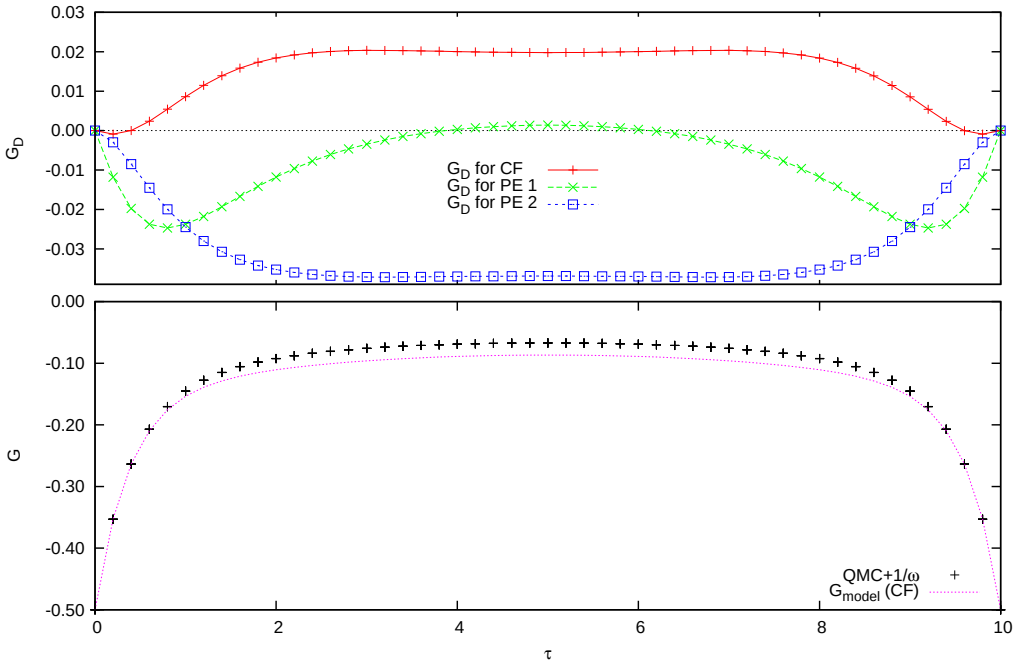

Figure 2.11: Lower panel: QMC estimate of the Green function $G(\Delta\tau)$ for semicircular DOS, $U = 4$, $T = 0.1$ and $\Delta\tau = 0.2$. The model Green function is based on the continued fraction expansion (2.13), restricted to the first 2 coefficients, which were obtained by minimizing (2.19). Upper panel: Corresponding difference Green function $G_{\mathrm{D}} = G - G_{\mathrm{M}}$ for the continued fraction expansion and the pole expansions PE1 and PE2.

2.4 Comparison of DMFT+QMC Schemes for the Multi-Band Hubbard Model at Half Filling

The generalization of the asymptotic expansion of the self-energy to the multi-band case does not only involve expectation values of the densities $\langle n_\sigma \rangle$, but also of pairwise double occupancies $\langle n_\alpha n_\beta \rangle$, which appear already in the terms of $\mathcal{O}\left(\frac{1}{\omega}\right)$. These correlation functions are not known a priori but have to be calculated self-consistently within the DMFT iteration scheme. Hence, in contrast to the single band case, also the high-frequency behavior is determined self-consistently. The calculation of the pairwise double occupancies, however, does not come along with additional costs, because they are computed by default within the QMC simulation.

In the following, the influence of the form of the model self-energy on the results of the QMC+$\frac{1}{\omega}$ method is studied in the two-band Hubbard model with parameters $U = 2U' = 4J_z$ and equal bandwidths $t_1 = t_2$, as an example of a multi-band system. The results are also compared to the predictions of the Ulmke scheme and its corrected version. The two-band model is motivated by the fact that it contains already all possible couplings occurring in the general anisotropic multi-band Hubbard model. The choice of parameters ensures on the one hand that the extension to the multi-band case is nontrivial (the model does not decouple into an effective system of two independent single-band models) and on the other hand corresponds to the parameter set which is used in chapter 3, with the exception of having equal bandwidths.

Estimates for the imaginary part of the self-energy for the two-band Hubbard model at half filling with semi-elliptic DOS at $T = 0.1$ are shown in Fig. 2.12 for $U = 2$ and in Fig. 2.13 for $U = 4$. Similar to the single-band case, an influence of the form of the model self-energy on the low-frequency behavior of the QMC estimates for $\mathrm{Im}\Sigma$ is not found. The estimates from the Ulmke scheme are in accord with the QMC+$\frac{1}{\omega}$ results at low frequencies within the metallic phase, but still underestimate the value of $\mathrm{Im}\Sigma(\omega_1)$ by more than 30% within the insulating phase. The predictions of the corrected Ulmke scheme are in exceptionally good agreement with the results of the refined QMC scheme at low frequencies. At intermediate values of ω_n, however, one observes an overshooting of the QMC estimates of the corrected Ulmke scheme. The large frequency behavior within both the metallic and insulating phase is shown in the insets of Fig. 2.12 and Fig. 2.13. The asymptotic behavior of the self-energy within the metallic phase is approached in almost the same manner as for the single-band model: Results from the pole expansion PE2 (2.16) (with adjusted coefficient) converge slowly to the correct behavior, while results from the pole expansion PE1 (2.12) approach the correct behavior quickly and then oscillate again with period $2\,\omega_c$. A detailed analysis of the occurring oscillations is depicted in Fig. 2.14, showing the relative deviation from the asymptotic behavior C_1 (B.19) for $U = 2$ (a) and for $U = 4$

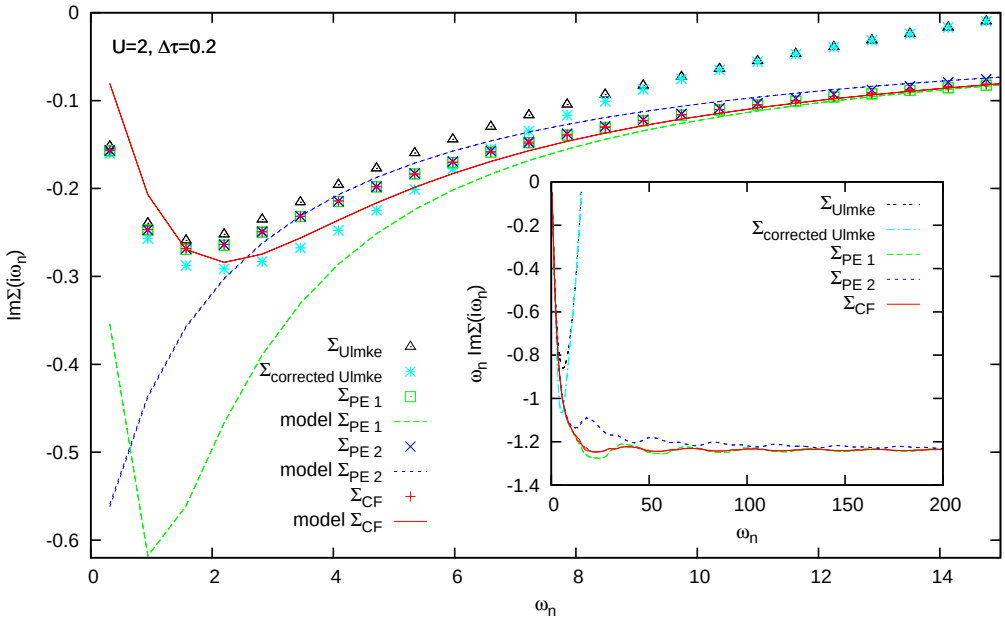

Figure 2.12: Estimates of the imaginary part of the self-energy for the two-band Hubbard model at $T = 0.1$, $U = 2U' = 4J_z = 2$ and $\Delta\tau = 0.2$. The inset shows the product $\omega_n \mathrm{Im}\Sigma(i\omega_n)$ which reveals the asymptotic high-frequency behavior. Lines are guides to the eye only.

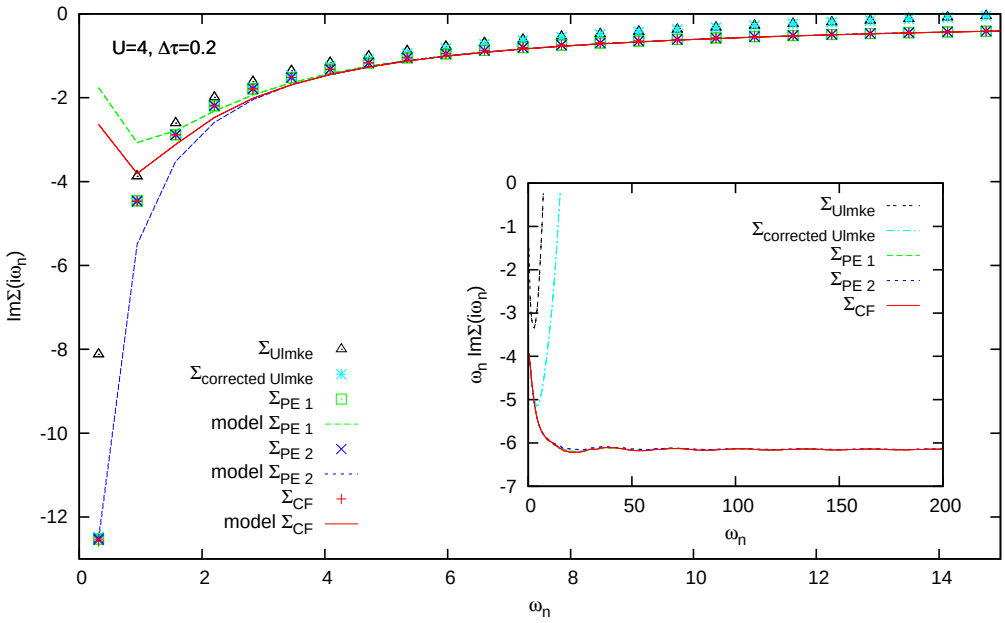

Figure 2.13: Estimates of the imaginary part of the self-energy for the two-band Hubbard model at $T = 0.1$, $U = 2U' = 4J_z = 4$ and $\Delta\tau = 0.3$. The inset shows shows the product $\omega_n \mathrm{Im}\Sigma(i\omega_n)$. Lines are guides to the eye only.

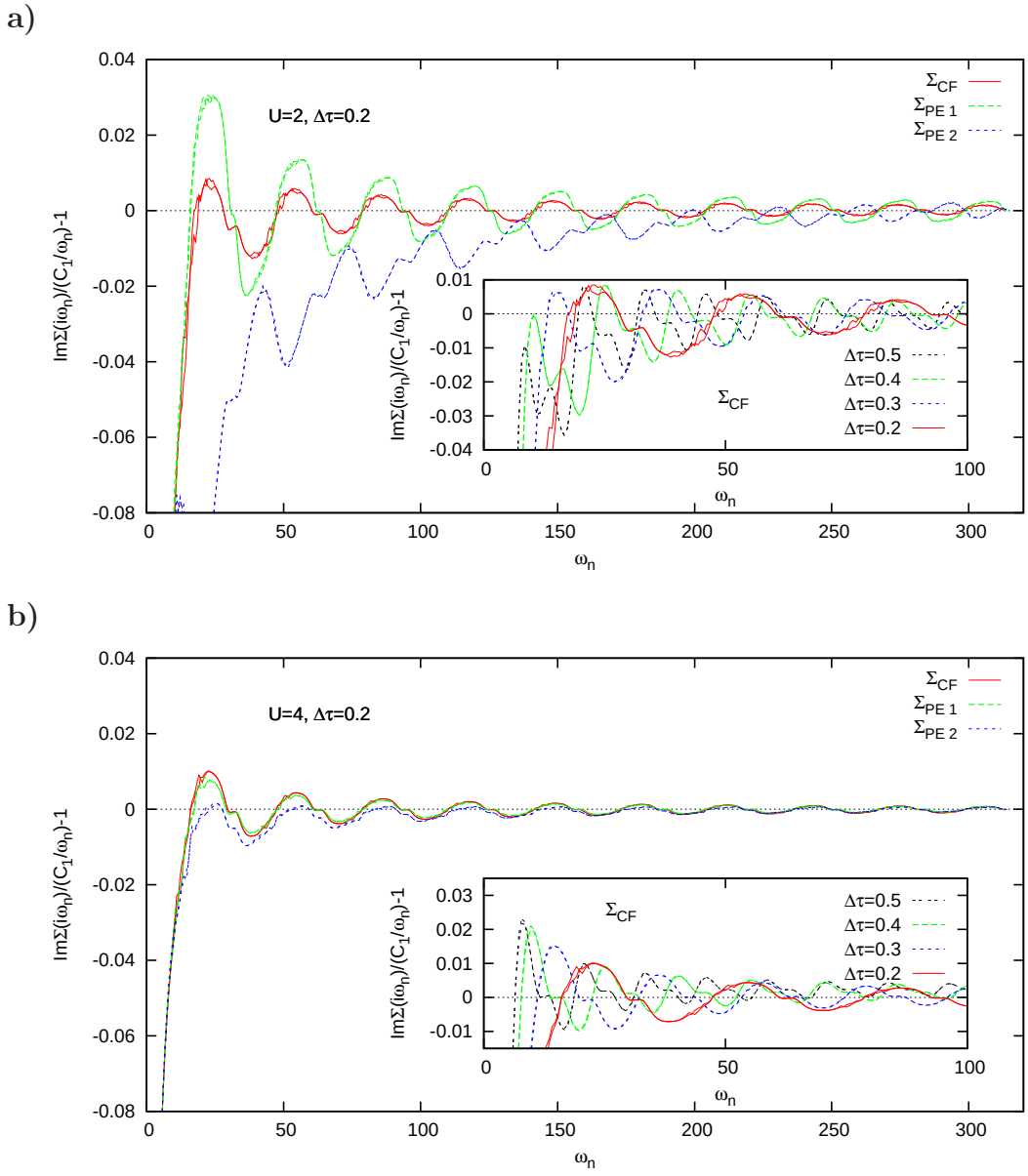

Figure 2.14: Relative deviation of $\mathrm{Im}\Sigma(i\omega_n)$ from the asymptotic high-frequency behavior, given by the coefficient C_1 (B.19) in the high-frequency expansion of the self-energy for the two-band Hubbard model with semi-elliptic DOS at $T = 0.1$, $\Delta\tau = 0.2$ and $U = 2U' = 4J_z = 2$ in **(a)** and $U = 2U' = 4J_z = 4$ in **(b)**. The inset shows the same relative deviation from the asymptotic behavior as obtained from the continued fraction expansion for the model self-energy, but now for different values of the discretization $\Delta\tau$.

(b). The occurring oscillations are minimal for the continued fraction expansion: An optimal choice for the multi-band case is achieved by including coefficients up to fourth order. The functional (2.19) is then minimized for $n = 3$. The oscillations within the insulating phase are much less strongly dependent on the form of the model self-energy. The insets show the $\Delta\tau$ dependence of the oscillations for the continued fraction expansion of the model self-energy. The initial overshooting is shifted towards larger frequencies as the discretization gets smaller, resulting in a smoother crossover to the large frequency behavior. The amplitude of the oscillations, however, is not decreased but rather independent of $\Delta\tau$.

The dependence of observables upon the discretization $\Delta\tau$ is depicted in Fig. 2.15 for the quasiparticle weight Z and in Fig. 2.16 for the total double occupancy $D = \frac{1}{2}\sum_{\alpha\neq\beta}\langle n_\alpha n_\beta\rangle$. One important observation is that the results of the QMC+$\frac{1}{\omega}$ scheme are essentially equivalent for all three types of model self-energy used. As expected, differences in the oscillatory behavior at large frequencies (as observed above) are not reflected in the observables that are mainly determined by the low-frequency behavior (e.g., Z is a function of $\mathrm{Im}\Sigma(\omega_1)$ only). It therefore suffices to compare the results of different QMC schemes, namely the Ulmke scheme, its corrected version and the QMC+$\frac{1}{\omega}$ scheme. For the estimates of the quasiparticle weight Z, the QMC+$\frac{1}{\omega}$ scheme yields the smallest errors, which are nearly perfectly quadratic in $\Delta\tau$ in the metallic phase and quasi-independent of the discretization within the insulating phase. The results from the Ulmke scheme and also from its corrected version clearly depend also on terms of $\mathcal{O}(\Delta\tau^4)$ [the corrected Ulmke scheme additionally on terms of $\mathcal{O}(\Delta\tau)$], while the estimates from the Ulmke scheme in the insulating phase even disagree after an extrapolation $\Delta\tau \to 0$. The strong $\Delta\tau$-dependence of the Ulmke scheme obviously requires QMC simulations with much smaller discretization, in order to achieve correct results. This is a rather severe deficiency, because of the numerical effort, which scales at least like $\Delta\tau^{-3}$.

The $\Delta\tau$ error of the double occupancy, calculated within the QMC+$\frac{1}{\omega}$ scheme, is of the same order and again nearly quadratic in $\Delta\tau$ within both the metallic and the insulating phase. Estimates from the corrected Ulmke scheme show a similar behavior within the metallic phase, while the results from the Ulmke scheme are again not purely quadratic in the discretization. Interestingly, results from the corrected Ulmke scheme are quasi-independent of $\Delta\tau$ within the insulating phase. Estimates obtained by the Ulmke scheme show again the largest $\Delta\tau$ errors. Remarks made concerning the quasiparticle weight in this respect apply to the double occupancy as well.

In summary, it could be shown that the results of the QMC+$\frac{1}{\omega}$ scheme and the reference schemes agree in the limit $\Delta\tau \to 0$ for the two-band Hubbard model. The chosen example Hamiltonian strongly suggests that the agreement holds also

for the more generic case of a multi-band Hamiltonian at half filling with arbitrary[5] interaction matrix $U_{\alpha\beta}$. Moreover, the inevitable discretization error of the QMC+$\frac{1}{\omega}$ scheme is quadratic in $\Delta\tau$ at least for $\Delta\tau < 0.5$ at $T = \frac{1}{10}$. It is further found that the large-frequency behavior of the self energy (and, accordingly, of the Green function) is best controlled by a model self energy of the form of a continued fraction expansion. The free parameters of this expansion can easily be determined with the use of a minimization routine.

[5]Here, the interaction strength is restricted by the usual working rule for a QMC simulation, namely $\Delta\tau U < 2$. This estimate is due to the Trotter breakup and ensures that the systematic error, introduced by the parameter λ in $\cosh(\lambda) = \exp\left(\frac{\Delta\tau U}{2}\right)$, is kept under control (by not allowing the argument of the exponential to be too large).

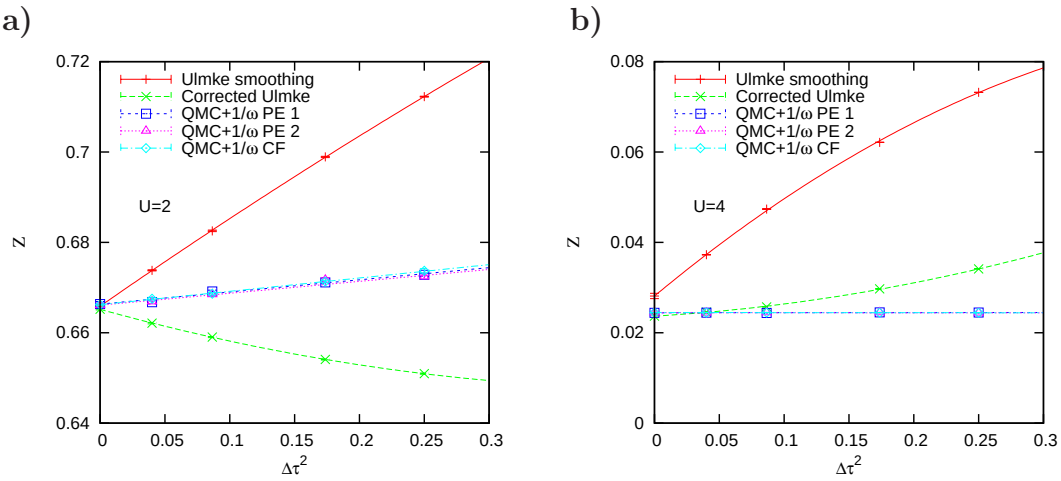

Figure 2.15: Quasiparticle weights Z for the two-band Hubbard model for semi-elliptic DOS at $T = 0.1$ and $U = 2U' = 4J_z = 2$ (**a**) and $U = 2U' = 4J_z = 4$ (**b**) as a function of $\Delta\tau^2$.

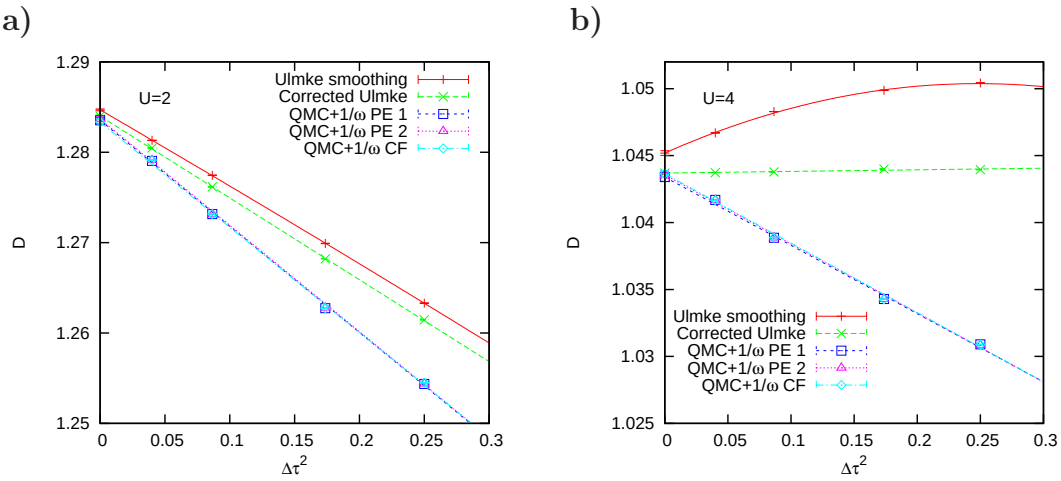

Figure 2.16: Total double occupancy $D = \frac{1}{2}\sum_{\alpha\neq\beta} n_\alpha n_\beta$ for the two-band Hubbard model for semi-elliptic DOS at $T = 0.1$ and $U = 2U' = 4J_z = 2$ (**a**) and $U = 2U' = 4J_z = 4$ (**b**) as a function of $\Delta\tau^2$.

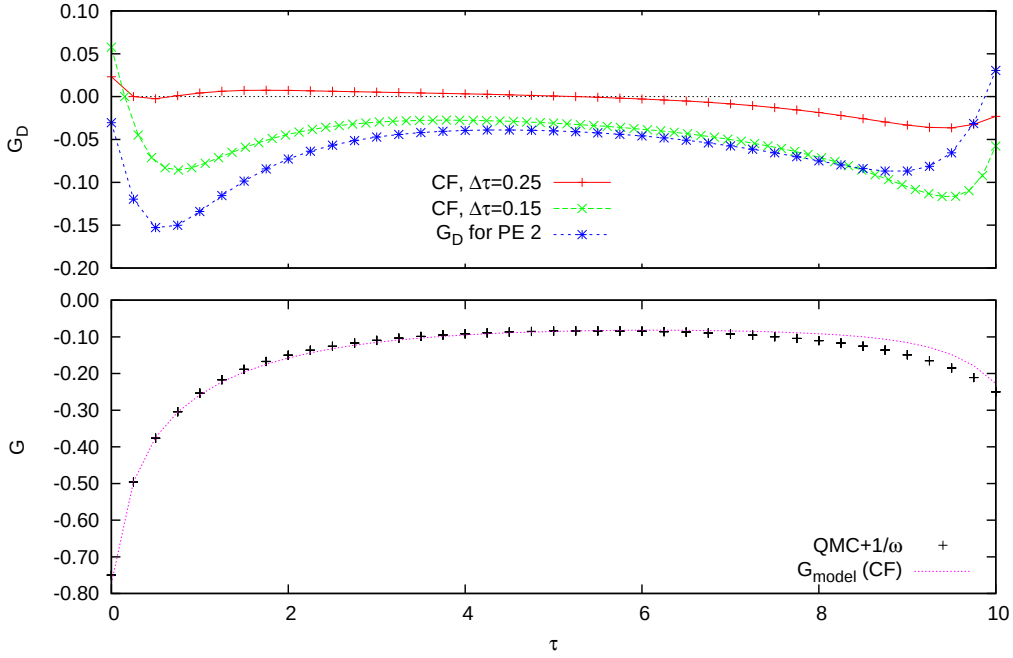

Figure 2.17: Lower panel: QMC estimates for the Green function $G(\Delta\tau)$ for the quarter filled single-band Hubbard model with semi-elliptic DOS at $T = 0.1$ and for $U = 5$. Upper panel: Difference Green function G_{D} as obtained with two distinct model self-energies and for different discretizations $\Delta\tau$ for the continued fraction expansion (CF). The form of G_{D} is independent upon $\Delta\tau$ for the pole expansion (PE2).

2.5 QMC+$\frac{1}{\omega}$ Scheme away from Half Filling

Systems at half filling are the exception rather than the general case. Many interesting materials, like the manganites or the perovskites, can be described by multi-band Hubbard models away from half filling (Petrone and Aligia, 2002). A DMFT+QMC simulation[6] of multi-band systems substantially benefits from a scheme producing reliable results already for a rather coarse grid $\Delta\tau$ [recall the numerical effort, that scales like $m(m-1)L^3$]. It would therefore be desirable to apply the QMC+$\frac{1}{\omega}$ scheme also to single-(multi-)band models with arbitrary filling.

It turns out, however, that the asymmetry[7] of the Green function, which arises

[6]The DMFT would additionally be supplemented by the LDA density of states. This method is then usually referred to as LDA+DMFT. An introduction to the LDA+DMFT method is given by Held, Nekrasov, Blümer, Anisimov and Vollhardt (2001).

[7]The asymmetry of the imaginary time Green function away from half filling also implies that

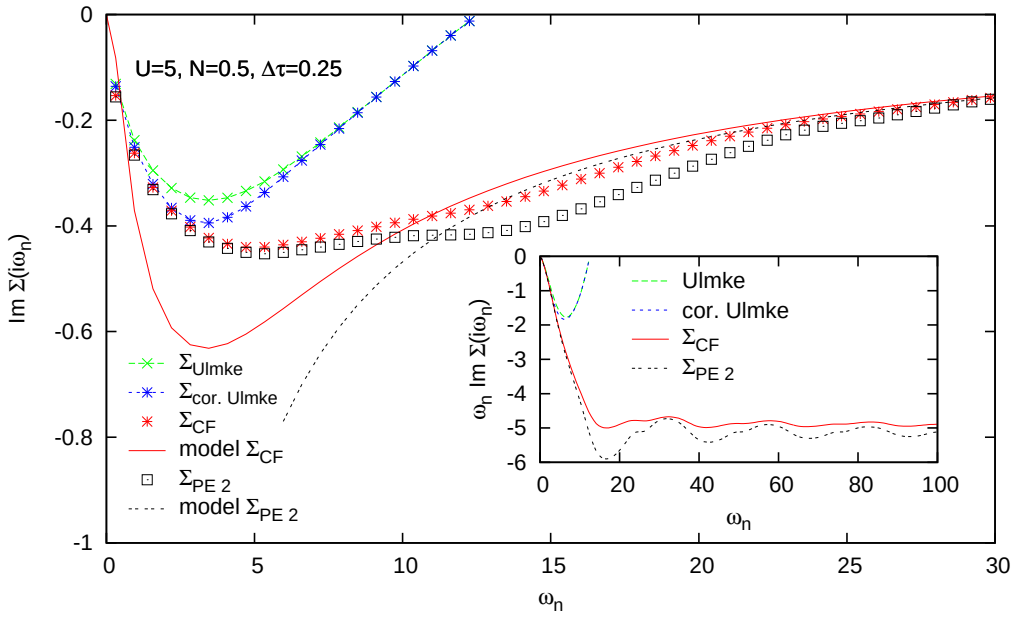

Figure 2.18: Estimates of the imaginary part of the self-energy for the single-band Hubbard model at quarter filling, $T = 0.1$ and $\Delta\tau = 0.25$. The inset shows the product $\omega_n \mathrm{Im}\Sigma(i\omega_n)$ which reveals the asymptotic high-frequency behavior. Lines are guides to the eye only.

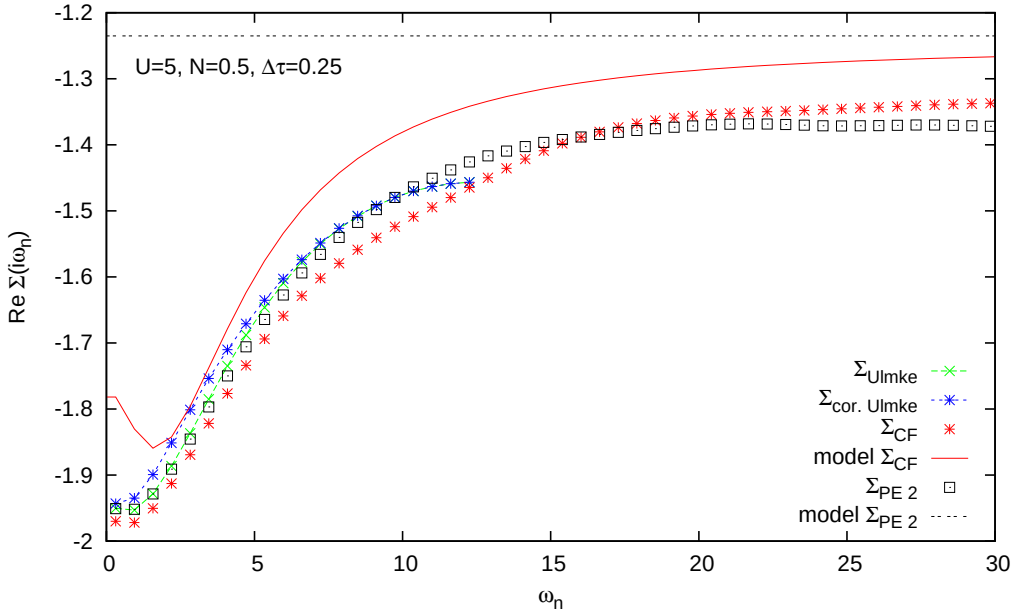

Figure 2.19: Estimates of the real part of the self-energy at quarter filling, $T = 0.1$ and $\Delta\tau = 0.25$. Lines are guides to the eye only.

away from half filling, cannot be accounted for in a satisfactory manner by the model self-energies that work very successfully for the half-filled case. In the following, the applicability of the QMC+$1/\omega$ scheme away from half filling is studied in detail for the test case of a the single-band Hubbard model at quarter filling and $U = 5$. The Ulmke scheme and its corrected version serve again as reference systems.

The estimates for the imaginary-time Green function $G(\Delta\tau)$ and a model Green function (CF) are shown in the lower panel of Fig. 2.17. The upper panel shows the difference Green functions G_{D} as obtained for different model Green functions. The discrepancy of G_{D} at the boundary $\tau = 0^+, \beta^-$ decreases as the discretization is reduced for the case of the continued fraction expansion, but is quasi independent of $\Delta\tau$ for Σ_{PE2} (therefore, only results for $\Delta\tau = 0.25$ are included). The finite offset of G_{D} at both $\tau = 0^+$ and $\tau = \beta^-$ reflects the fact that the correct boundary conditions can be reproduced neither by a 2-pole expansion of the model self-energy nor by a continued fraction expansion of the order 4.[8]

Now, the discrete Fourier transform expects the input data to be periodic, and the first sample is expected to follow the last samples. The difference between the amplitude of the first and last sample creates a ringing known as Gibb's phenomenon. This ringing distorts the spectral information in the frequency domain [as is observed in Fig. 2.18]. The width of the ringing can be reduced by increasing the number of data samples, thus by decreasing $\Delta\tau$. This will, however, not reduce the amplitude of the ringing, which is a function of the difference between the amplitude of the first and last samples. The Fourier transformation of this discontinuity (which corresponds to a sawtooth-like function) requires an infinite number of frequencies and essentially results in the $\frac{1}{\omega^2}$-contribution to the real part of the Green function that in turn accounts for the offset in the real part of the self-energy, as observed in Fig. 2.19 (see below). Within signal or image processing, a discontinuity of this type is reduced by multiplying the data by a windowing function (sometimes called window weighting functions) before the Fourier transform is performed. Windowing, however, cannot be applied in our case without loosing an essential part of the Green function.

The estimates of the imaginary part of the self-energies at $T = 0.1$ and $\Delta\tau = 0.25$ are shown in Fig. 2.18. Results from the QMC+$\frac{1}{\omega}$ scheme apparently exhibit stronger kinks in the crossover region at the Nyquist critical frequency than at half filling. This 'ringing' can be minimized by tuning the free parameters of the model self-energy, similar to the case of the continued fraction expansion. The inset shows the large-frequency behavior revealing the characteristic oscillations. The real part of the self-energy is plotted in Fig. 2.19. It consists only of the constant Hartree contribution for the pole expansion PE2; higher order terms were neglected in the

the Matsubara frequency Green function and the self-energy have a non-zero real part.

[8] The offset also remains (selectively at $\tau = \beta^-$, only) when forcing $G_{\mathrm{D}}(\tau = 0) \stackrel{!}{=} 0$ by applying a different weight in (2.19).

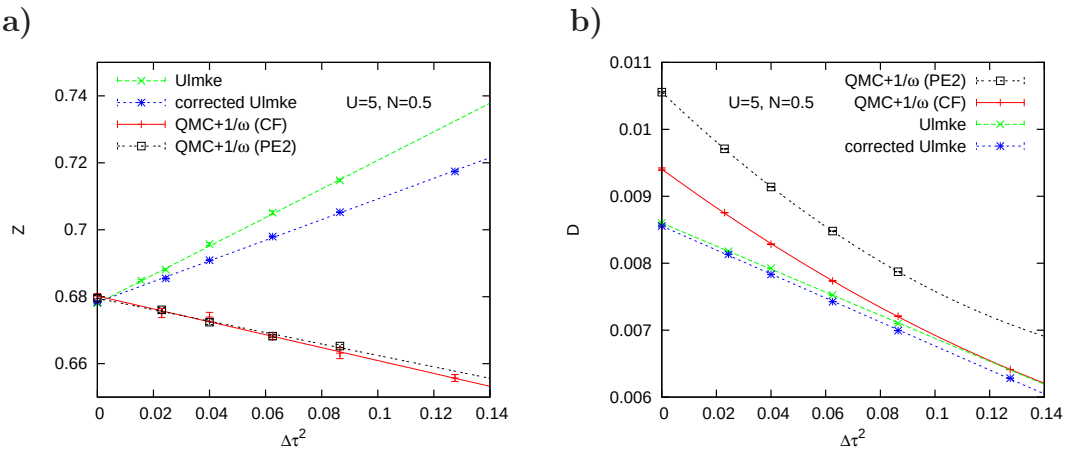

Figure 2.20: QMC estimates for the quasiparticle weight Z **(a)** and the total double occupancy D **(b)** as a function of $\Delta\tau^2$ for the single-band Hubbard model at quarter filling and $T = 0.1$. The QMC+$\frac{1}{\omega}$ scheme clearly generates different results for D, depending on the model self-energy, uncovering problems in the implementation.

definition of PE2. The model self-energy CF already contains $\frac{1}{\omega^2}$-corrections. The discrepancy in the real part of the resulting self-energy and its model is due to a finite ($\Delta\tau$-dependent) offset in the $\frac{1}{\omega^2}$-term of the Green function $G(i\omega_n)$ at large frequencies, which in turn stems from the discrepancy of the QMC estimate $G(\Delta\tau)$ and its model Green function $G_{\text{model}}(\Delta\tau)$ at the boundaries ($\tau = 0^+$, β^-) as shown below (cf. Fig. 2.17). This $\frac{1}{\omega^2}$-contribution of $G(i\omega_n)$ brings about an offset in the real part of the self-energy, which can be seen, e.g., by employing the Dyson equation for the Bethe lattice: $\Sigma = i\omega_n + \mu - (W/4)^2 G - \frac{1}{G}$.

The problems of the QMC+$\frac{1}{\omega}$ implementation are reflected in the $\Delta\tau$ error of the observables, as can be seen, e.g., in Fig. 2.20a for the quasiparticle weight Z and in Fig. 2.20b for the total double occupancy $D = \frac{1}{2}\sum_{\alpha\neq\beta}\langle n_\alpha n_\beta\rangle$. While the extrapolated values of Z ($\Delta\tau \to 0$) from the compared schemes still agree within the errors, they do not in the case of the total double occupancy D. Also, the purely quadratic dependence of D upon $\Delta\tau$, which was observed at half filling, is lifted for the results of the QMC+$\frac{1}{\omega}$ scheme. Needless to say, the observed discrepancies persist for multi-band systems away from half filling. The observed difference of the extrapolated observables between the QMC+$\frac{1}{\omega}$ scheme and the reference schemes is severe: As the only systematic error of the QMC simulation is introduced by the discretization of the imaginary time, results from different DMFT+QMC schemes must yield identical results in the limit of vanishing discretization. Therefore, the QMC+$\frac{1}{\omega}$ scheme is so far applicable only to systems at half filling.

2.6 Implementation of the QMC+$\frac{1}{\omega}$ Method

One part of this thesis was the implementation of the QMC+$\frac{1}{\omega}$ scheme for the general case of multiple bands at half filling into an existing multi-band DMFT+QMC code by Held and Keller, which was parallelized by Blümer (2002) using the Message Passing Interface (MPI). Routines for the spline interpolation of the Green function and the creation of a model self-energy on the base of a pole expansion for the single-band case were already implemented by Knecht (2002). The optimal parameters of the continued fraction expansion for the model self-energy are determined by Powell's direction set method (Press et al., 1992). To ensure convergence, the number of coefficients is increased stepwise, using the results of the previous run as input for the new minimization.

Calculations at low temperatures or at high precision (e.g., for $L > 150$ and more than one band) can only be performed efficiently on computers with a very fast memory access (supercomputers). As the calculation time on supercomputers is usually limited (as in the case of the IBM p690, on which some of the calculation of this thesis were performed), the QMC code was constructed such as to be restartable. For this purpose, all data of the parallelized QMC routine, including Ising spin fields, Green functions and self-energies from the iteration cycle are stored at constant rate. An integrated timer automatically stops the QMC simulation before the allocated time runs out. Both implemented actions allow the calculations to be resumed at any time, such that calculations can be performed for multi-band models also for large number of sweeps.

2.7 Summary

In this chapter, a scheme to include high-frequency corrections into the DMFT+QMC method for multi-band Hubbard models was developed. The method is based on the large-frequency expansion of the self-energy, which can be derived rigorously by the moments of the spectral density. The first-order coefficients of the expansion comprise expectation values of densities in the single-band case and additionally of pairwise double occupancies in the multi-band case. Correlation functions up to second order can easily be determined self-consistently within the DMFT iteration cycle. Higher order coefficients of the expansion, however, also include correlation functions of higher and higher order, the calculation of which is very time-consuming within a QMC simulation and thus not practicable. It could be shown in this chapter, that the scheme works most satisfactorily for both the single-band and the multi-band case when employing the exactly known coefficients up to $\mathcal{O}\left(\frac{1}{\omega}\right)$. The observed artificial oscillations of the large-frequency behavior can be minimized by adjusting higher order coefficients to the QMC estimates at intermediate frequencies.

The developed DMFT+QMC scheme (QMC+$\frac{1}{\omega}$) was compared to reference schemes by Ulmke and Blümer (corrected Ulmke) for the single and the multi-band case. It could be shown that all methods produce equivalent physical observables within the limit $\Delta\tau \to 0$. Moreover, the analysis of this chapter demonstrated, that the systematic error of the developed DMFT+QMC scheme is virtually reduced to the inevitable Trotter error, which is quadratic in the discretization $\Delta\tau$. Thus, the error associated with the discrete Fourier transformations, that are performed twice in each DMFT iteration cycle, could essentially be eliminated.

It was further shown, that the quality of the scheme concerning the behavior at intermediate to large frequencies, is optimal when employing a continued fraction expansion for a model self-energy. This analytical form of the self-energy allows best for a reliable fitting of higher order coefficients of the large frequency expansion to the QMC data.

In the last part of this chapter it was pointed out, that the QMC+$\frac{1}{\omega}$ scheme is not yet applicable to systems away from half filling: The extrapolated observables ($\Delta\tau \to 0$) do not agree with the results of the reference schemes. The reason for this deficiency is expected to be the asymmetry of the imaginary time Green function $G(\tau)$ away from half filling. The key point to establish the developed scheme also for systems away from half filling is therefore to produce a model self-energy that correctly accounts for the asymmetric boundary conditions at both $\tau = 0^+$ and $\tau = \beta^-$. The successful application of the QMC+$\frac{1}{\omega}$ scheme to half-filled systems in this chapter suggests that the construction of an appropriate model self-energy for doped systems should have high priority in future QMC work.

Chapter 3

Orbital-Selective Mott Transitions

3.1 Introduction

The interaction-induced Mott metal-insulator transition of strongly correlated electron systems has been a subject of intense study in solid state physics for decades (Gebhard, 1997; Imada et al., 1998). Introduced by Mott in 1968, it is a perfect example of a quantum phase transition where the electron-electron interaction leads to a transition from a correlated paramagnetic metal to an insulator (Mott, 1968). If the local moments in the insulating phase do not show long-range order, the transition is called Mott-Hubbard transition, otherwise Mott-Heisenberg transition (Gebhard, 1997). The Mott transition is not to be confused with filling-induced transitions because it cannot be explained in terms of an effective non-interacting electron theory. To reveal the basic phenomenon of the transition, Mott originally considered only the single-band case.

The Hubbard model is probably the most prominent example of a system exhibiting a Mott-Hubbard transition. It describes itinerant electrons that interact locally via a Coulomb interaction U, forcing the electrons' motion to be correlated. At half filling, its ground state is metallic for $U = 0$ and insulating for $U \gg W$, where W is the band width. The Hubbard model is expected to exhibit a Mott metal-insulator transition at a critical interaction $U_c \approx W$ for all dimensions $d > 1$.[1] The exact value of the critical interaction U_c, is, depending on the lattice dimension, known only for rather special cases, e.g., at strong magnetic fields (van Dongen, 1994*b*). Of particular interest is the limit of infinite dimensions, for which Mott-Hubbard behavior was first found for a hyper-cubic lattice at half filling by Jarrell (1992). Since then, the nature of the Mott transition in the $d = \infty$ Hubbard model has been a subject of

[1] The metallic region of the Hubbard model in one dimension is restricted to the singular point $U = 0$. In the narrower sense, the one-dimensional Hubbard model therefore does not describe a Mott transition, because the range of the metallic phase is not finite (Gebhard, 1997).

intense study [compare also the review by Georges et al. (1996)].

A new aspect was brought into the theory of Mott transitions by Nakatsuji and Maeno (2000*a*), who found evidence for two consecutive orbital-selective metal-insulator transitions (OSMT) in $Ca_{2-x}Sr_xRuO_4$. The crystal structure of this compound, which is a quasi two-dimensional degenerate d-electron system, is shown in Fig. 3.1 a, the phase diagram in Fig. 3.1 b. The end-member Ca_2RuO_4 is a Mott insulator while Sr_2RuO_4 is a p-wave superconductor. Upon doping x, the system undergoes complex phase transitions from an antiferromagnetic insulator for $0 \leq x \leq 0.2$, via an antiferromagnetically correlated metal for $0.2 \leq x \leq 0.5$, towards a paramagnetic metal for $x \geq 0.5$. Furthermore, there is an increase of the low-temperature (uniform) susceptibility for $x \geq 0.5$ with a peak at the boundary $x \approx 0.5$, corresponding to the formation of a localized spin $S = \frac{1}{2}$. This nearly ferromagnetic state at $x \approx 0.5$ vanishes upon decreasing x towards the antiferromagnetic ordered state at $x \approx 0.2$.

The nature of this complex evolution is debated lively in literature [cf. subsections 3.1.1 and 3.1.2]. A very promising explanation is to assume that some orbitals exhibit localized spin and orbital degrees of freedom while others retain itinerant. Various theoretical calculations strongly suggest [LDA (Fang and Terakura, 2001; Fang et al., 2004), LDA+DMFT (Anisimov et al., 2002), strong-coupling calculations (Sigrist and Troyer, 2004)] that the occurrence of the orbital-selective metal-insulator transition is a correlation induced effect in a system with inequivalent bands. The OSMT would thus generalize the classical Mott transition to the multi-orbital case with inequivalent bands.

Up to recently, studies of multi-band systems concentrated on the special 'isotropic' case of identical orbitals. In these models, the metal-insulator transition occurs at the same critical Coulomb interaction U_c in all bands. However, it is a priori not clear how this picture evolves in general. The transition obviously occurs at different critical interactions if the inequivalent bands are uncoupled.

The chapter is organized as follows. Section 3.1.1 gives an experimental motivation of the OSMTs. A likely microscopic model for OSMTs, namely the two-band Hubbard model, is discussed in 3.1.2, followed by a short summary of the recent work in that field in Sec. 3.1.3. In section 3.2, the anisotropic two-band Hubbard model is studied within the DMFT+QMC. Using the high-frequency corrected QMC algorithm developed as part of this thesis, the anisotropic Hubbard model is established as the minimal model for the OSMT in the paramagnetic phase. The orbital-selective Mott (OSM) phase is further studied within a simplified multi-band Hubbard model, which has the general structure of a Falicov-Kimball model, in section 3.3. A detailed comparison shows that the physics of the OSM phase is closely related to the Falicov-Kimball model. The results are discussed at the end of each section [3.2.11 and 3.3.6, respectively], and summarized at the end of this chapter in Sec. 3.4.

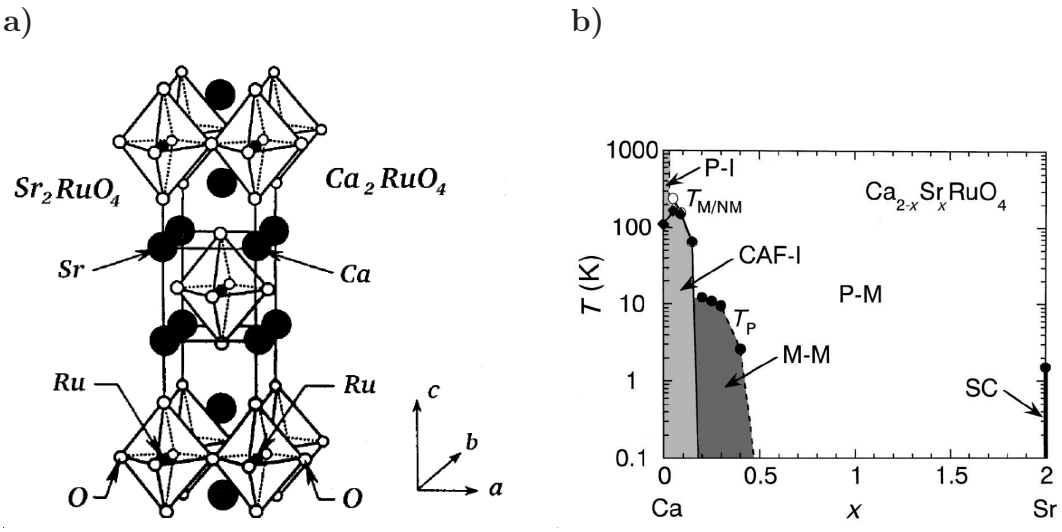

Figure 3.1: **a)** Basic crystal structure of $Ca_{2-x}Sr_xRuO_4$ (reproduced from Anisimov et al., 2002). **b)** Phase diagram of $Ca_{2-x}Sr_xRuO_4$ with abbreviations: P for paramagnetic, CAF for canted anti-ferromagnetic, M for magnetic, SC for superconducting phase, -M for metallic phase, and -I for insulating phase (Nakatsuji and Maeno, 2000*a*).

3.1.1 Experiment

One of the most famous materials to exhibit a Mott transition is the transition metal oxide V_2O_3 (Rice and McWhan, 1970). The transition is induced upon pressure which directly distorts the lattice structure and thus changes the overlap integral of the relevant orbitals. This can be identified with a variation of the bandwidth, hence the transition is also called bandwidth-controlled. The Mott transition in V_2O_3 is well described by a half-filled single-band Hubbard model even though orbital effects certainly play an important role (Held, Keller, Eyert, Vollhardt and Anisimov, 2001).

The microscopic mechanism that leads to the orbital-selective Mott transition in the ruthenate $Ca_{2-x}Sr_xRuO_4$ turned out to be fairly complex (Nakatsuji and Maeno, 2000*a*; Nakatsuji and Maeno, 2000*b*; Anisimov et al., 2002; Fang and Terakura, 2001; Fang et al., 2004; Sigrist and Troyer, 2004). The 4*d* transition metal oxide belongs to the group of perovskites and crystallizes in a single-layered structure (cf. Fig. 3.1). The end member Sr_2RuO_4 was found to be an unconventional superconductor (Maeno et al., 1994) with spin-triplet Cooper pairing (Ishida et al., 1998). It is iso-structural to the well known high-T_c superconductor $La_{2-x}Sr_xCuO_4$. The normal state of Sr_2RuO_4 is a good metal, forming a 3-dimensional but anisotropic Landau-Fermi-liquid at low temperatures (Oguchi, 1995; Singh, 1995; Mackenzie et al., 1996).

The electronic band structure is dominated by the $4d$ t_{2g} orbitals (d_{xy}, d_{yz}, d_{xz}) of the Ru ion. The d_{xy} orbitals π-hybridize with the $2p$ orbitals of all 4 in-plane O-neighbors, while the $d_{xz}(d_{yz})$ orbitals hybridize only with the 2 O-neighbors along the $x(y)$-axis (Anisimov et al., 2002). This results in a d_{xy} bandwidth that is approximately twice the d_{xz},d_{yz} bandwidths. The t_{2g} bands are occupied as follows: The d_{xz},d_{yz} absorb 3 electrons generating a localized spin $\frac{1}{2}$ and an orbital isospin $\frac{1}{2}$ and the d_{xy} band is filled with one electron. The crystal structure of Ca_2RuO_4 (for $x = 0$) is orthorhombic. The bandwidth of the t_{2g}-orbitals is smaller than the one in Sr_2RuO_4 and, additionally, the energy splitting between d_{xy} and (d_{xz},d_{yz})-orbitals is changed. The d_{xy}-orbital is thus fully filled and the 2 remaining electrons occupy the (d_{xz},d_{yz})-orbitals.

The evolution between the two end members, for which the phase diagram is shown in Fig. 3.1 b, is quite complex. Substituting the smaller ion Ca for Sr leads to a contraction of the crystal volume due to a rotation of the RuO_6-octahedra around the c-axis. This distortion reduces the bandwidth of the t_{2g}-orbitals and also changes the energy splitting between d_{xy} and (d_{xz},d_{yz})-orbitals. For doping $x > 0.5$, the system is in a paramagnetic metallic phase. Down to $x = 0.5$, the crystal remains tetragonal but is characterized by an increase of the uniform susceptibility. Also, at $x = 0.5$, the susceptibility becomes Curie-like with a Curie constant corresponding to the formation of a localized spin $S = \frac{1}{2}$. From $x = 0.5$ downward to $x = 0.2$, an additional rotation of the RuO_6-octahedra takes place, emerging in the orthorhombic structure of Ca_2RuO_4. The system remains metallic, but antiferromagnetic ordering sets in. According to Anisimov et al. (2002), decreasing the doping x in this regime leads to a progressive narrowing of the three distinct bands; the orbital-selective Mott transition is then caused by electronic correlations. Finally, at $x \approx 0.2$, a first-order phase transition to the antiferromagnetic insulating phase of Ca_2RuO_4 takes place.

The microscopic mechanism, which leads to the rich phase diagram of $Ca_{2-x}Sr_xRuO_4$ is still discussed lively in literature [cf. also Sec. 3.1.3]. As the compound is assumed to be a strongly-correlated electron system, it is especially important whether electronic correlations alone are responsible for the OSMT or whether other effects, like lattice-distortion or spin-orbit coupling, which is not negligible for the Ru-ion (Ng and Sigrist, 2000; Sigrist and Troyer, 2004), must also be taken into account. This leads to the question of whether Mott transitions in a purely electronic multi-orbital model take place in sequence or simultaneously. Interestingly, experimental observations that contradict the assumption of a correlation-induced transition also exist: Optical spectroscopy data, e.g., denote that the observed change of carrier concentration at $x \approx 0.5$ is smaller than an orbital-selective Mott transition would suggest (Lee et al., 2002).

3.1.2 Theory

A microscopic model able to describe the OSMT must contain at least 2 bands. The actual number of relevant bands in $Ca_{2-x}Sr_xRuO_4$, however, is larger. These are the 3 t_{2g}-orbitals of the Ru-ions as well as the $2p$-orbitals of the O-ions, if one restricts oneself to only the low-energy-contributions. The complexity can be reduced by integrating out the intermediate O-orbitals, yielding an effective[2] three-band Hubbard model. Similar effective models were derived, e.g., for the cuprates yielding an effective single-band model (Zhang and Rice, 1988) or for double perovskites yielding an effective three-band model (Petrone and Aligia, 2002).

The essence of the OSMT, however, should already be captured by a two-band model. One usually considers the following half-filled two-band Hubbard model

$$H = H_1 + H_2\,, \tag{3.1}$$

where

$$H_1 = -\sum_{\langle ij\rangle m\sigma} t_m c^\dagger_{im\sigma} c_{jm\sigma} + U\sum_{im} n_{im\uparrow} n_{im\downarrow} \tag{3.2}$$

$$+\sum_{i\sigma\sigma'} (U' - \delta_{\sigma\sigma'} J_z) n_{i1\sigma} n_{i2\sigma'} \tag{3.3}$$

includes hopping between nearest-neighbor sites i, j with amplitude t_m for orbital $m \in \{1, 2\}$, *intra-* and *inter*orbital Coulomb repulsion parameterized by U and U', respectively, and Ising-type Hund's exchange coupling J_z; $n_{im\sigma} = c^\dagger_{im\sigma} c_{im\sigma}$ for spin $\sigma \in \{\uparrow, \downarrow\}$. In addition,

$$H_2 = \tfrac{1}{2} J_\perp \sum_{im\sigma} c^\dagger_{im\sigma} \left(c^\dagger_{i\bar{m}\bar{\sigma}} c_{im\bar{\sigma}} + c^\dagger_{im\bar{\sigma}} c_{i\bar{m}\bar{\sigma}} \right) c_{i\bar{m}\sigma} \tag{3.4}$$

contains spin-flip and pair-hopping terms (with $\bar{1} \equiv 2$, $\bar{\uparrow} \equiv \downarrow$ etc.). In the following, $H_1 + H_2$ is referred to as the J-model and the simplified Hamiltonian H_1 as the J_z-model. For the further study of the OSMT it is instructive to discuss the symmetry of the Hamiltonian in more detail. The terms in H_2 were first discussed by Castellani et al. (1978), who showed that both terms are generated by a spherically symmetric two-particle potential (in particular therefore by a screened Coulomb interaction). The authors further noted that the Hamiltonian is rotationally symmetric if and only if the following relation between the interaction parameters holds:

$$U = U' + 2J\,, \tag{3.5}$$

[2] The advantage of such an effective model is the reduced Hilbert space, e.g., for numerical diagonalization of finite system and that the largest interactions (mostly the on-site Coulomb interaction) are treated exactly inside an effective cell. This makes approximations give better results when applied to an effective model rather than to the original complex one.

provided that $J_z = J_\perp \equiv J$. In this case, the Hamiltonian is SU(2)-symmetric in the spin sector and SO(2)-symmetric in the band sector [here, the restriction is due to the pair hopping term]. Precisely the relation (3.5) is usually employed (for simplicity) in the context of OSMT studies, presuming a rotational invariance. In contrast to this assumption, the symmetry of the experimental system, $Ca_{2-x}Sr_xRuO_4$, is lower and at the most rotationally invariant in the xy plane. The study of the Néel temperature in Sec. 3.2.8 shows that scaling the interaction parameters according to (3.5) is problematic and should eventually be lifted. The model 3.1 is investigated (see Sec. 3.1.3) in the paramagnetic (PM) phase only, where one finds two transitions. The experimental system, however, is antiferromagnetic for $x \leq 0.2$; the influence of long-range order (LRO) on the phase diagram is 'under investigation'.

3.1.3 Recent Work

In the context of the OSMT scenario, the J_z-model was originally investigated by Liebsch (Liebsch, 2003*a*; Liebsch, 2003*b*; Liebsch, 2004) using the dynamical mean-field theory (DMFT) in combination with finite-temperature quantum Monte Carlo (QMC) calculations. For simplicity, a semi-elliptical DOS with bandwidth ratio $W_2/W_1 = 2$ was considered, motivated by the fact that the MIT, occurring in the corresponding single-band model, is already well understood. The interorbital interactions were assumed to scale with the on-site Coulomb interaction like $U' = \frac{U}{2}$ and $J_z = \frac{U}{4}$, which fulfills the condition (3.5) for spherically symmetric screened Coulomb interactions (Castellani et al., 1978). Liebsch claimed that both bands undergo a single first-order transition at the same critical Coulomb interaction $U_c \approx 2.1$ eV. Also, the critical temperature was estimated by $T_c \approx 0.038$ eV (Liebsch, 2004). The results were mainly achieved by considering the quasiparticle weight Z [for a definition, see (3.7)], which is shown in Fig. 3.2a for $T = 0.031$. The curve 11 (22) denotes the results for two narrow (wide) orbitals and 12 labels the solutions for orbitals with bandwidth ratio $W_2 = 2W1$. The change in slope of Z for both bands at $U_c \approx 2.1$ was taken as an indicator for the occurrence of one single Mott transition.[3]

It was subsequently found by Koga et al. (2004) using exact diagonalization (ED) that an OSMT takes place in the full J-model but not in the J_z-model. Thus the OSMT was attributed to spin-flip and pair-hopping processes. Figure 3.2b shows their results for the quasiparticle weight. In contrast to the QMC estimate of Z [cf. Sec. 3.2.1] the quasiparticle weight calculated within ED is exactly zero at the MIT, due to the fact that the calculations are performed at zero temperature.

The existence of an OSMT in the J-model was confirmed by calculations based on the Gutzwiller variational approach at zero temperature by Ferrero et al. (2005),

[3] Liebsch explicitly stated that, regardless the order, there was no evidence for a second transition in the wider band at larger interaction U (Liebsch, 2004).

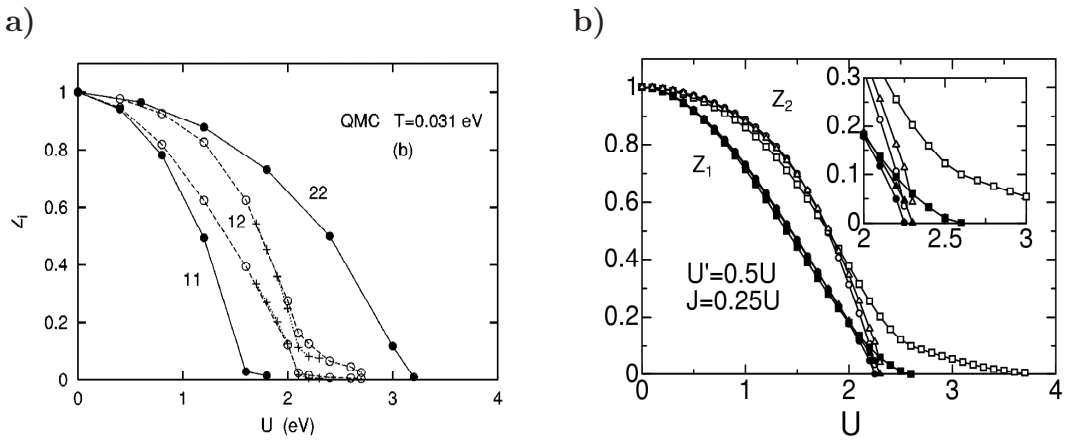

Figure 3.2: **a)** Quasiparticle weight Z (taken from Liebsch, 2004) for the J_z-model at $T = 0.031$ eV, calculated within DMFT+QMC. The change in slope of Z_2 at $U = 2.1$ is taken as an indicator for a single Mott transition. **b)** Results from DMFT+ED (Koga et al., 2005*a*) for Z at zero temperature for the full J-model (squares), the J_z-model (circles) and an intermediate coupling $J_\perp/J_z = 0.5$ (triangles).

provided that the ratio W_2/W_1 of the two bandwidths is sufficiently small.[4] Similar results were obtained by Arita and Held (2005) who used the projective QMC (PQMC) method (Feldbacher et al., 2004) to investigate the J-model at $T = 0$ and who demonstrated a first[5] OSMT for $J = \frac{U}{4}$ and $U = 2.6$ (in units of half the width of the narrow band). Finally, Koga et al. (2005*b*) used QMC to characterize the OSMT for the J-model at finite T on the basis of spin, charge and orbital susceptibilities as well as spectral functions; they further showed that an additional hybridization between the bands smears out the OSMT at $T = 0$.

The scenario of a single Mott transition was then challenged in 2005 by de' Medici et al. (2005) and Knecht et al. (2005). Using a slave-spin mean field theory (which is closely related to the Gutzwiller method), de' Medici et al. (2005) found an OSMT at $T = 0$ for the J_z-model with $U' = U - 2J_z$, in contradiction to Liebsch's and Koga's earlier findings. This result, however, can not be taken as a clear evidence, since the slave-spin method is essentially uncontrolled. The issue could be clarified using the high-precision QMC-algorithm developed as a part of this work: It turned out that

[4] Interestingly, Ferrero et al. (2005) also find, within a DMFT+ED study, existence of small spectral weight near the Fermi level of the narrow-band subsystem in the orbital-selective Mott phase, favoring the existence of a single Mott transition only.

[5] Only the Mott transition of the narrow band could be observed, while the wide band remains itinerant. The PQMC method is stable only for $U \lesssim W$ due to a dramatic increase of the statistical error that comes along with the spin flip terms of the Hund's rule coupling (Arita and Held, 2005).

the J_z-model, indeed, is the minimal model for the OSMT at finite temperatures (Knecht et al., 2005).

3.2 OSMTs in the Anisotropic Two-Band Hubbard Model

In this section, the J_z-model with $U' = \frac{U}{2}$, $J_z = \frac{U}{4}$ and semi-elliptic densities of states with full bandwidths $W_1 = 2$, $W_2 = 4$, for the 'narrow' and 'wide' band, respectively, is treated within the DMFT. The calculations are performed using the QMC+$\frac{1}{\omega}$ method developed in chapter 2.

3.2.1 Quasiparticle Weight

A traditional criterion for metal-insulator transitions is the quasiparticle weight or mass renormalization factor Z, which can be expressed in terms of the real part of the self-energy $\Sigma(\omega)$:

$$Z = \frac{m}{m^*} = \frac{1}{1 - d\mathrm{Re}\,\Sigma/d\omega|_{\omega=0}}\,. \tag{3.6}$$

In the context of QMC simulations, it is usually estimated in a secant approximation by the discrete Eliashberg estimate

$$Z \approx \frac{1}{1 - \mathrm{Im}\,\Sigma(i\pi T)/(\pi T)}\,. \tag{3.7}$$

Evidently, both definitions recover the limit $Z \to 1$ in the absence of interactions (when $\Sigma \equiv 0$), however, in the insulating regime the discrete approximation necessarily remains finite, whereas the true Z vanishes exactly. As a consequence, metal-insulator transitions are expected to appear washed-out at finite temperatures. It is important to note, that Z is a physical observable only within the Fermi-liquid phase; the value of the discrete estimate for Z has no physical meaning in the insulating regime.

Figure 3.3 shows Z as a function of the interaction U for temperatures $T = \frac{1}{32}$ and $T = \frac{1}{50}$. The quasiparticle weight of the narrow band, Z_{narrow}, drops from its non-interacting value $Z_{\mathrm{narrow}}(U=0) = 1$ as the interaction is increased. The MIT of the narrow band is indicated by a drastic change in slope (for $T = \frac{1}{32}$) of Z_{narrow} at $U_{c1} \approx 2.0$ and occurs within the coexistence region ($T \lesssim \frac{1}{50}$). The behavior of Z_{wide} is different: At U_{c1}, it also shows a transition but the drop is smaller compared to the one of Z_{narrow}. This drop is a signature of the Mott transition of the narrow band, and reflects the fact that phase transitions usually leave traces in every observable. The value of Z_{wide} in the interval $2.0 \lesssim U \lesssim 2.5$, however, is still large which indicates

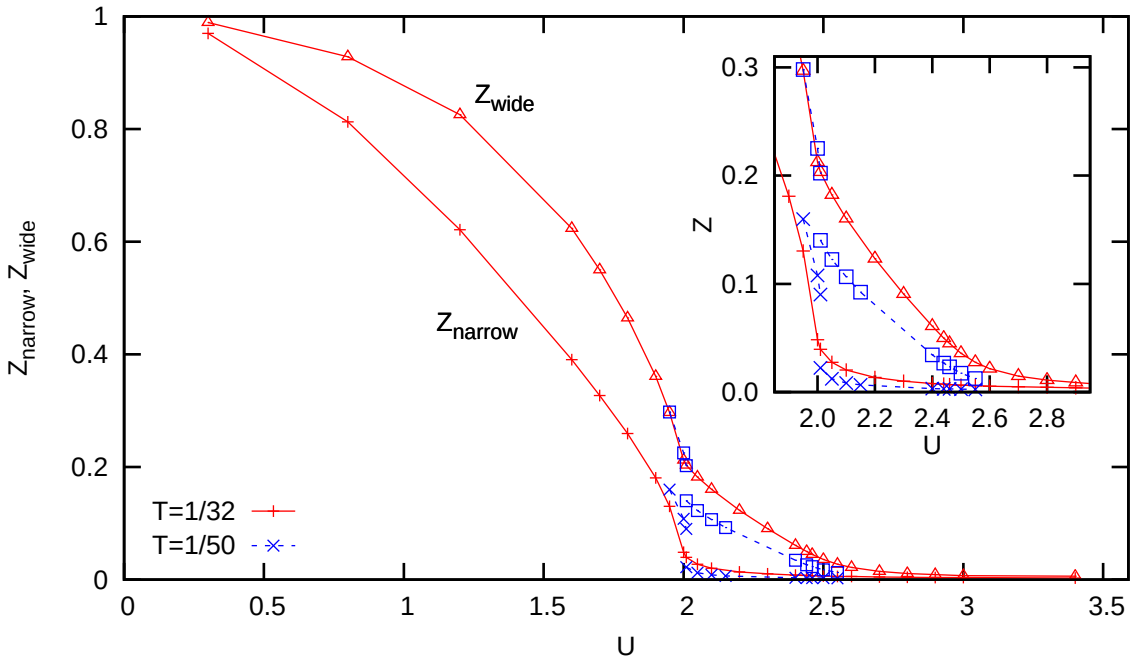

Figure 3.3: $Z_{\text{narrow}}, Z_{\text{wide}}$ of the discrete QMC estimates of the quasiparticle weights of both bands versus interaction U for $T = \frac{1}{32}$ ($\Delta\tau = 0.32$) and $T = \frac{1}{50}$ ($\Delta\tau = 0.35$). The inset shows a magnified view of the transition region. For $T = \frac{1}{50}$, two solutions coexist at $U = 2.01$. A second transition for the wider band is not visible at this scale. Lines are guides to the eye only.

that the second band is still metallic. For increasing interaction, Z_{wide} seems to diminish smoothly. The slight change in slope near $U \approx 2.6$ cannot be identified as a second transition on this scale. The fact that the phase transition as indicated by the discrete estimate of the quasiparticle weight, indeed, looks 'washed-out', can be seen from the inset of Fig. 3.3: Z_{narrow} drops only by about 60% when the band becomes insulating at $U \approx 2.0$.

Another important point concerns the order of the transition at U_{c1}. A first-order transition can only take place within a region of coexisting metallic and insulating solutions. This issue can be studied in Fig. 3.4, which shows a magnified view of the first transition region for various temperatures. The quasiparticle weight of both bands is a smooth function of U for high temperatures ($T \geq \frac{1}{40}$); the transition region can only be identified by a change in slope of Z (e.g., for $T = \frac{1}{32}$). The first coexisting metallic and insulating solutions are found for $T = \frac{1}{50}$ at $U = 2.01$. As no coexistent solutions could be detected for higher temperatures, the estimate of the critical temperature, below which the transition is of first order, is $T_c \approx \frac{1}{50} = 0.02$.

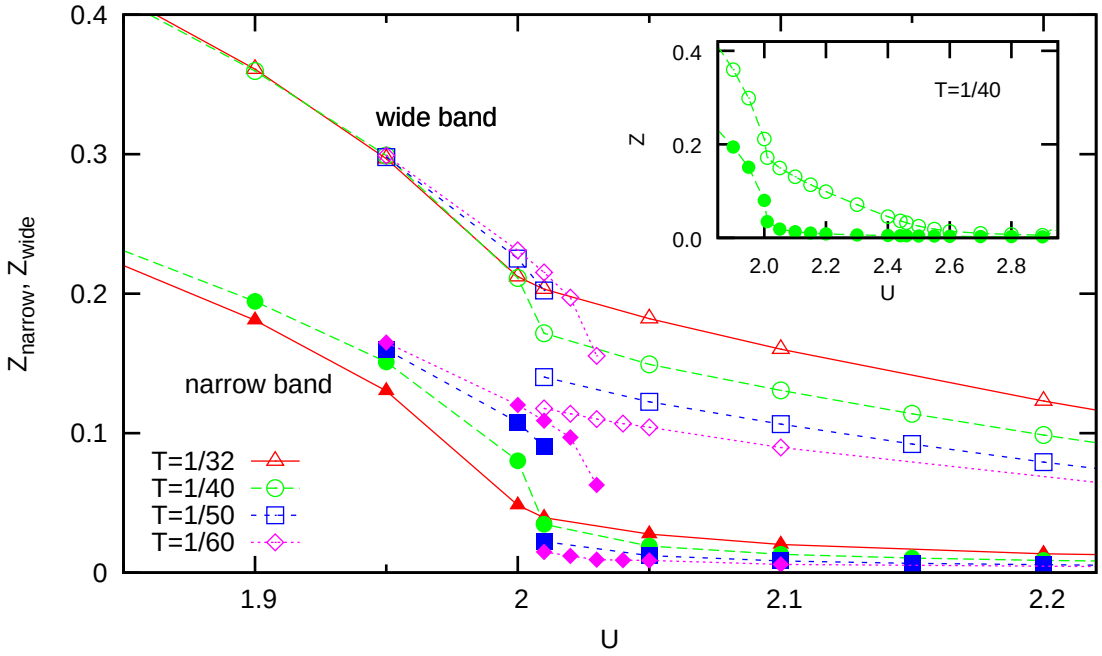

Figure 3.4: Magnified view of the first transition of Fig. 3.3 for various temperatures T and $0.32 \leq \Delta\tau \leq 0.4$. The inset shows the full region of the OSMT.

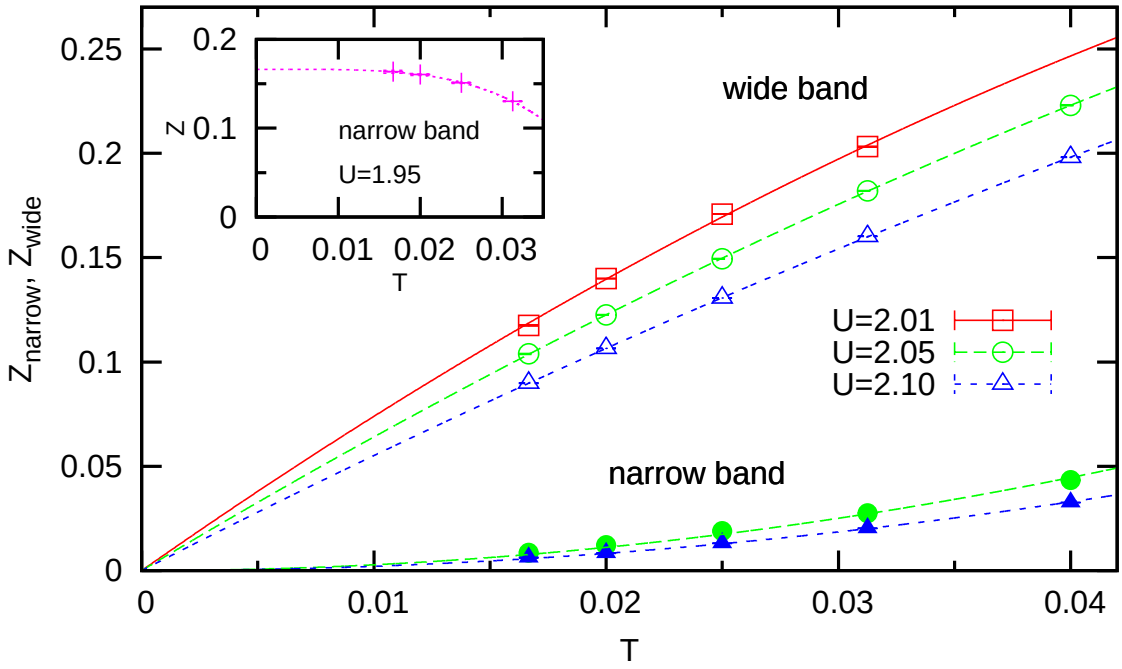

Figure 3.5: Temperature dependence of the quasiparticle weights Z_{narrow} and Z_{wide} ($0.32 \leq \Delta\tau \leq 0.4$). The lines are polynomials in T resulting from least square fits. Z_{narrow} is purely quadratic in T, whereas Z_{wide} is best described when additionally considering a term linear in T. The inset shows the extrapolation of Z_{narrow} in the metallic phase. In this case Z_{narrow} is best fitted by $Z_{\text{narrow}} = a + bT^2 + cT^4$.

The coexistence region that is found at $T = \frac{1}{60}$ spans from $U = 2.01$ to $U = 2.03$. These findings are to be contrasted with earlier results by Liebsch who reported a critical temperature of $T_c = 0.038$ and a coexistence region of width $\Delta U = 0.3$ at $T = \frac{1}{50}$ (Liebsch, 2004).

Next compare the behavior of the quasiparticle weights at the first transition (Fig. 3.4). Both bands exhibit a discontinuity of Z for $T = \frac{1}{50}$, whereas the jump of Z_{narrow} is much larger compared to the one of Z_{wide} [about 75% (30%) for Z_{narrow} (Z_{wide})]. The values of Z_{wide} right after the transition, e.g., at $U = 2.01$, are even larger than Z_{narrow} right before the transition [at least for temperatures $T > \frac{1}{60}$]. This finding suggests that the wide band is still metallic after the narrow band became insulating.

It is also instructive to consider the temperature dependence of the quasiparticle weights. Z_{narrow} shows, in contrast to Z_{wide}, a strong dependence upon T in the metallic phase right before the transition (compare, e.g., the solutions at $U = 1.95$ and at $U = 2.0$). The dependence on the temperature for $U > U_{c1}$ is inverted compared to the metallic phase: Both Z_{narrow} and Z_{wide} decrease as the temperature is lowered, whereas the absolute change of Z_{wide} upon T is larger. A detailed analysis of this temperature dependence is given in Fig. 3.5. In the OSM phase, e.g., at $U = 2.1$, Z_{narrow} is proportional to T^2 as $T \to 0$. Making use of the definition (3.7) of Z, this behavior implies the following relation:

$$Z^{-1} \sim -\frac{\mathrm{Im}\Sigma(i\omega_1)}{T} \overset{!}{\sim} \frac{1}{T^2} \quad \longrightarrow \quad \mathrm{Im}\Sigma(i\omega_1) \sim -\frac{1}{T} \qquad (T \to 0). \tag{3.8}$$

Thus the imaginary part of the self-energy, $\mathrm{Im}\Sigma(i\omega_1)$, diverges for $T \to 0$ within the insulating phase. If the self-energy is not directly dependent upon T, (3.8) implies that the limit $T \to 0$ is solely determined by $\omega_1 = \pi T \to 0$. This behavior would correspond to the development of a pole at $\omega = 0$. The condition (3.8) is however also fulfilled when the self-energy diverges for any low frequency. This demonstrates that the behavior of the self-energy at low frequencies cannot be inferred from the quasiparticle weight. This issue is studied in more detail below. Next, consider the inset of Fig. 3.5, which shows the temperature dependence of Z_{narrow} for $U = 1.95$ where the narrow band is still metallic. For $T \to 0$, the quasiparticle weight is best described by $Z_{\text{narrow}} = a + bT^2 + \mathcal{O}(T^4)$. Employing the same considerations as in (3.8), one finds, that $\mathrm{Im}\Sigma(i\omega_1) \sim T$ for $T \to 0$. Thus $\mathrm{Im}\Sigma(i0^+)$ of the narrow band vanishes in the metallic phase at zero temperature, consistent with Fermi-liquid behavior. The behavior of Z_{wide} after the narrow band became insulating is quite different. The leading term of Z_{wide} in the extrapolation $T \to 0$ is of $\mathcal{O}(T)$, implying that $\mathrm{Im}\Sigma(i\omega_1) \sim \mathcal{O}(1)$ for $T \to 0$. Neither does $\mathrm{Im}\Sigma(i0^+)$ develop a pole for $T \to 0$, indicating an insulating phase, nor does it vanish, as in the metallic phase of a Fermi-liquid.[6] It is also interesting to note, that the prefactor in the term quadratic in T

[6] Compare also the discussion of Fig. 3.8.

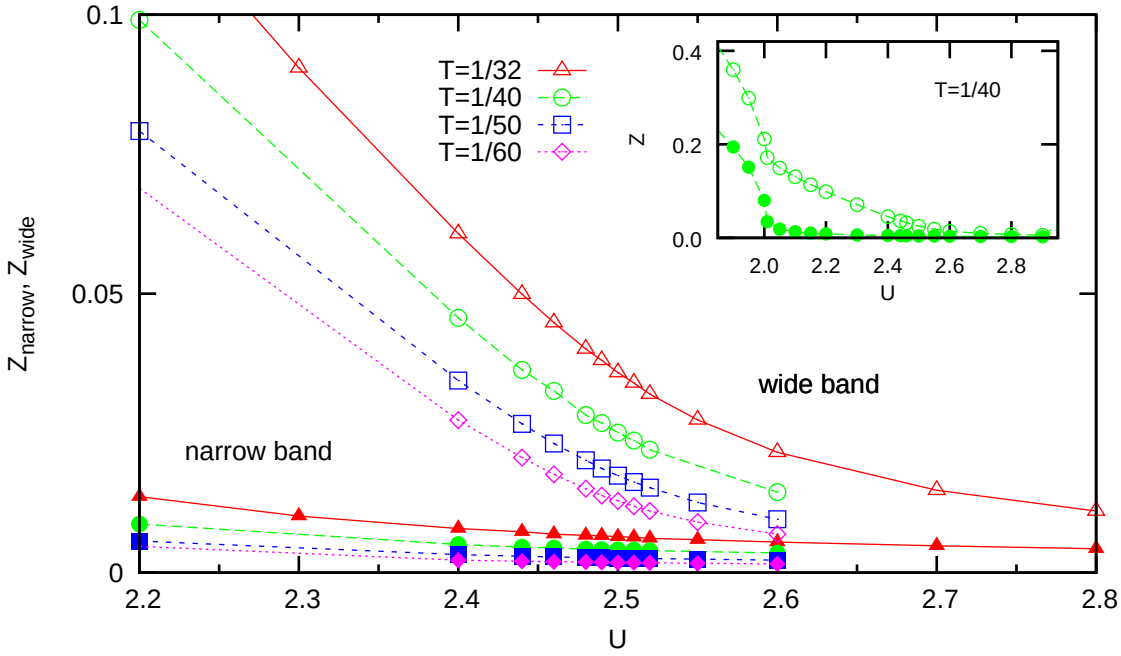

Figure 3.6: Magnified view of the second transition region of Fig. 3.3 for various temperatures. The inset shows the full region of the OSMT. Lines are guides to the eye only.

has opposite sign for Z_{narrow} and Z_{wide}, which results in the opposite curvature. The main conclusion of this part is, therefore, that the wide band is still metallic after the narrow band became insulating but does not show Fermi-liquid behavior anymore.

Let us now focus on the region in which the wide band becomes insulating. This is shown in Fig. 3.6, again for the quasiparticle weight for various temperatures. Z_{wide} seems to undergo a smooth transition from a quasi linear fall-off starting from U_{c1} towards the insulating phase, which is indicated by a slight change in slope at about $U \approx 2.55$. Additionally, the dependence upon the temperature reduces gradually as the interaction is increased. The analysis of the temperature dependence of Z_{wide}, similar to the one of Z_{narrow} in (3.8), is depicted in Fig. 3.7. Z_{wide} is again a smooth function of T, best described by $Z_{\text{wide}}(T) = aT + bT^2 + \mathcal{O}(T^3)$. The lines are results of least square fits. For $U = 2.4$, Z_{wide} shows a similar behavior as for smaller interactions (cf. also Z_{wide} in Fig. 3.5); the leading contribution in the limit $T \to 0$ is the term linear in T. Thus the wide band is still within the metallic non-Fermi-liquid phase. Upon increasing interaction U, the term linear in T diminishes and the quadratic contribution is more and more pronounced: The wide band becomes insulating. It is interesting to take a look at the behavior of the coefficients a and b

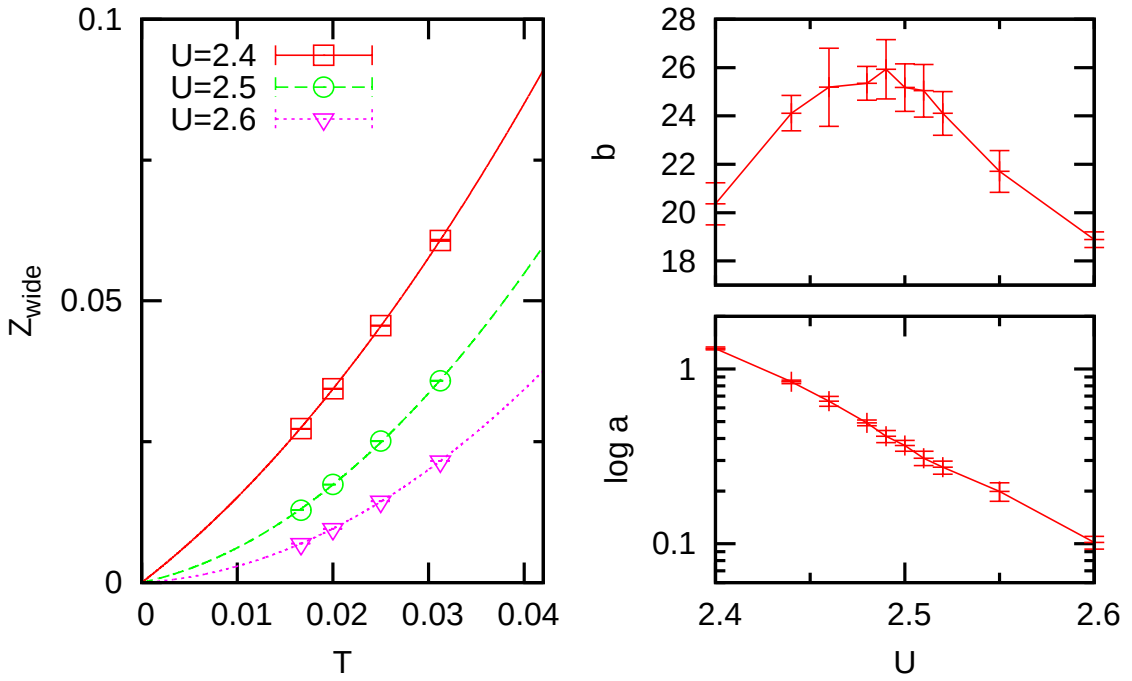

Figure 3.7: Left side: Temperature dependence of Z_{wide}. The lines are polynomials in T resulting from least square fits of the form $Z(T) = aT + bT^2$. Right side: Results from least square fits with errors for the parameters a and b as a function of the interaction U. While a is well described by an exponential decay (lower panel), b exhibits a maximum at about $U \approx 2.5$ (upper panel). Lines are guides to the eye only.

as the interaction is increased, which is shown in the insets of Fig. 3.7. The linear coefficient a decreases approximately exponentially while b exhibits a sharp maximum at $U \approx 2.5$. This extremum in b is a first indicator for a metal insulator transition of the wide band. Henceforth, the associated critical interaction will be labeled U_{c2}.

For the study of the OSM phase, it is instructive to resume the discussion of how the estimate of the quasiparticle weight Z is connected to the self-energy. Within the QMC method, Z is approximated by the Eliashberg estimate (3.7), which is derived using the rules of complex derivatives:

$$\left.\frac{\partial \mathrm{Re}\Sigma(\omega)}{\partial \omega}\right|_{\omega=0} = \left.\frac{\partial \mathrm{Im}\Sigma(i\omega_n)}{\partial \omega_n}\right|_{\omega_n\to 0} \stackrel{!}{=} \lim_{\omega_1\to 0} \frac{\mathrm{Im}\Sigma(i\omega_1)}{\omega_1}\,. \tag{3.9}$$

The definitions agree in the limit $T \to 0$ as long as the Luttinger theorem [i.e., $\mathrm{Im}\Sigma(\omega = 0) = 0$] is fulfilled. The imaginary part of the self-energy, $\mathrm{Im}\Sigma(i\omega_n)$, of the wide band is shown in Fig. 3.8 for different temperatures T and interactions U. For small frequencies, $\mathrm{Im}\Sigma(i\omega_n)$ is well described by the function $a/(\omega_n - b) + c$ (dashed

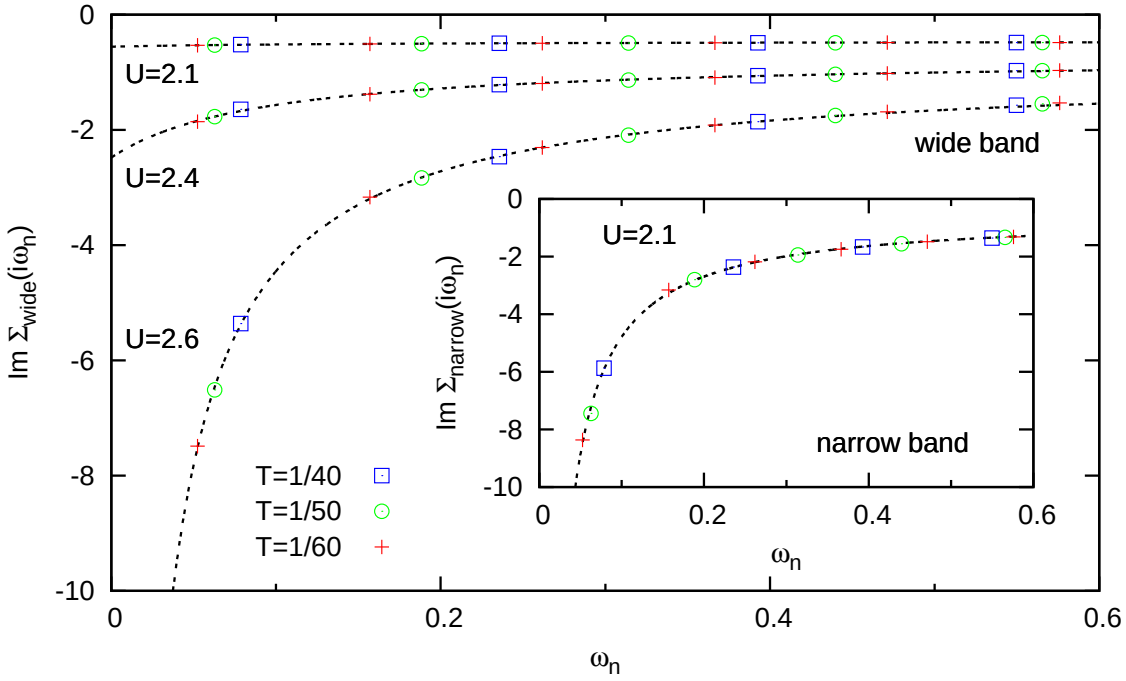

Figure 3.8: QMC estimates of the imaginary part of the self-energy, $\mathrm{Im}\Sigma$, of the wide band for different temperatures T and interactions U. The self-energy is essentially independent of the temperature T. $\mathrm{Im}\Sigma(i\omega_n)$ is well described by $a/(\omega_n + b) + c$ in the limit $\omega_1 \to 0$ (dashed black line) and extrapolates to a finite value at zero frequency for $U = 2.1$ and $U = 2.4$, but diverges for $U = 2.6$. The inset shows results for the narrow band for $U = 2.1$, for which $\mathrm{Im}\Sigma(i\omega_n)$ diverges for $\omega_n \to 0$, as expected within an insulating phase.

black lines), for which the coefficients are determined with a least square fit. The imaginary part of the self-energy extrapolates linearly (in first order) to a finite value Γ_{wide} for $U = 2.1$ and $U = 2.4$. For $U = 2.6$, the imaginary part of the self-energy diverges as $1/\omega_n$ for $\omega_n \to 0$, implying that the wide band is insulating. An equivalent behavior is found for $\mathrm{Im}\Sigma(i\omega_n)$ of the narrow band already for $U = 2.1$ (inset). Moreover, the self-energy of the wide band turns out to be essentially independent of the temperature for interactions $U > U_{c1}$. This behavior is expected at least for the narrow band, which becomes insulating at U_{c1}. The strong dependence on T in the metallic phase of the narrow band stems (only) from the temperature dependence of the quasiparticle peak, which develops as the temperature is lowered [this can be inferred, e.g., from Fig. 3.13]. Thus, the absence of a quasiparticle peak in the spectrum of the wide band in the OSM phase and the already insulating nature of the narrow band (its quasiparticle peak is already fully destroyed), are expected to be the reason for the observed T-independence of the wide band.

Two important conclusions follow from this observation: First, the wide band is not a Fermi-liquid within the OSM phase because $\mathrm{Im}\Sigma(\omega_1)$ extrapolates to a finite value Γ_{wide}, i.e., the conditions required for Luttinger's theorem to apply do not hold anymore. Secondly, the temperature dependence of the Eliashberg estimate of Z for a single Coulomb interaction U [as observed, e.g., in Fig. 3.7] results from the approximation used in the definition (3.7) and therefore does not apply for the quasiparticle weight itself. The genuine quasiparticle weight Z, is seemingly independent of T and can be approximated in a better way, e.g., by taking the difference quotient in the middle of equation (3.9).

It should be noted, however, that these observations do not disqualify the Eliashberg estimate of the quasiparticle weight, $Z_{\mathrm{Eliashberg}}$, for being used as an indicator for the OSMT at finite temperatures. The vanishing of $Z_{\mathrm{Eliashberg}}$ within the OSM phase in the limit $T \to 0$, however, is an artifact due to its definition (3.7), because it is applied outside its domain (i.e., because the preconditions for Luttinger's theorem to hold are not fulfilled).[7]

3.2.2 Ratio of the Quasiparticle Weights

The analysis of the quasiparticle weight not only shows that the wide band still exhibits metallic properties above U_{c1}, but also indicated a second transition at a critical interaction $U_{c2} \approx 2.5 > U_{c1}$. Now consider the ratio $r \equiv Z_{\mathrm{narrow}}/Z_{\mathrm{wide}}$ of the quasiparticle weights, which is shown in the lower panel of Fig. 3.9. Clearly, three different regions can be distinguished: In region I ($U \lesssim 2.0$), r is of the order of unity with a sharp decrease near the boundary, in region II ($2.0 \lesssim U \lesssim 2.5$), r is nearly constant and of $\mathcal{O}(0.1)$, and in region III ($U \gtrsim 2.5$), r increases with nearly constant slope. In order to analyze the boundary between region II and III, piecewise quadratic fits to the QMC data are performed for both regions separately (lines for $U > 2.1$ in Fig. 3.9).

The kinks at the boundary are resolved better after subtracting a linear offset, as seen in the upper panel of Fig. 3.9. The transition is getting sharper as the temperature is lowered and for $T \leq \frac{1}{32}$, all QMC data falls on the fit curve. The transition of the wide band at U_{c2} is thus better resolved in the ratio r (in particular when subtracting a linear term) than in the quasiparticle weight itself, indicating the subtle nature of the second transition.

[7] The difference quotient in (3.9) is consistently applied for the calculation of the quasiparticle weight in Ref. Blümer and Požgajčić (2005), in which the order of the OSMTs in the J_z-model are studied for interaction parameters that are parameterized like $U' = \alpha\frac{U}{2}$, $J_z = \alpha\frac{U}{4}$, with $0 \leq \alpha \leq 1$. The order of the MIT of the wide band is studied as a function of α, which is obviously of first order for $\alpha = 0$ (and $T > 0$).

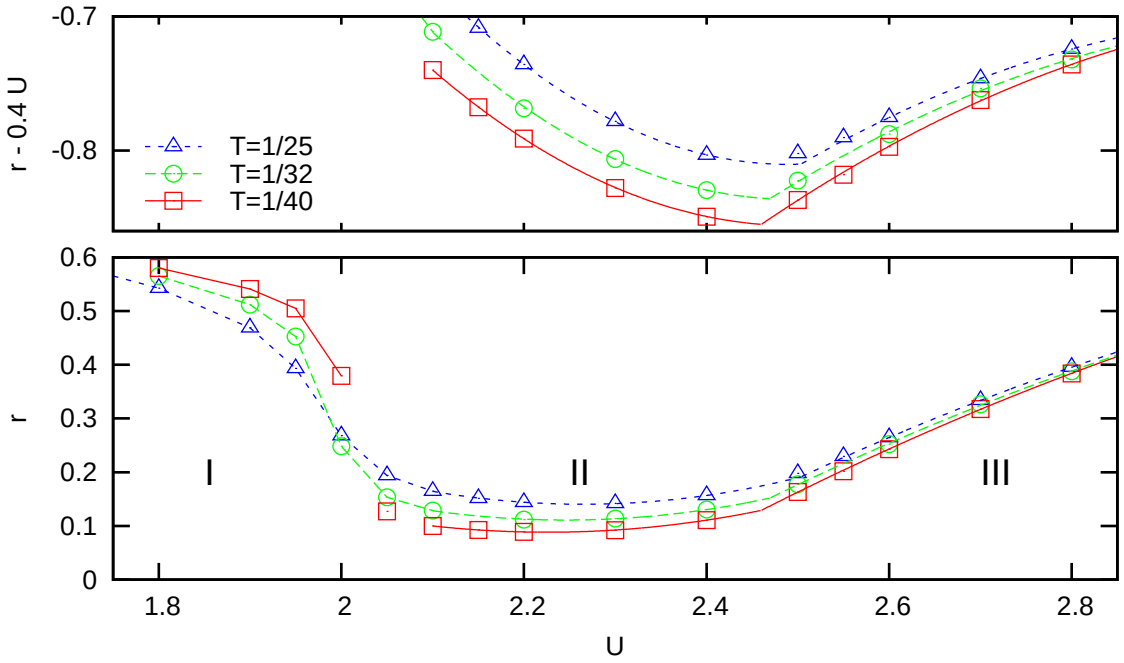

Figure 3.9: Lower panel: Ratio $r = Z_{\mathrm{narrow}}/Z_{\mathrm{wide}}$ of the discrete QMC estimates of the quasiparticle weights of both bands versus interaction U for various temperatures T; lines for $U > 2.1$ represent piecewise quadratic fits. $\Delta\tau = 0.4$. Upper panel: Same data with linear offset.

3.2.3 Low-Frequency Analysis of the Self-Energy

The intrinsic ambiguities associated with the discrete estimate for Z can be overcome when analyzing the low-frequency behavior of the self-energy as is shown in Fig. 3.10. The data points represent QMC estimates of the product $\omega\Sigma(\omega)$ at the Matsubara frequencies $i\omega_n$. These products are real-valued since the self-energy is purely imaginary on the imaginary axis due to particle-hole symmetry. The lines, given by cubic polynomials in ω, are expected to extrapolate to 0 at least linearly within a metallic phase (where Σ is regular) and to a finite value within an insulating phase. By this criterion, the narrow band (cf. upper panel of Fig. 3.10) becomes insulating for $U \gtrsim 2.0$ while the wide band (cf. lower panel of Fig. 3.10) remains metallic up to $U = 2.4$.

The extrapolated product $\lambda \equiv \omega\Sigma(\omega)|_{\omega=i0^+}$, a measure of the singularity in the self-energy and roughly proportional to the expected gap,[8] is shown at better resolu-

[8] This can be inferred from by splitting up $G_\epsilon(\omega) = 1/[\omega - \epsilon - \Sigma(\omega)]$ into real and imaginary part and employing $A(\omega) = -\frac{1}{\pi}\mathrm{Im}G(\omega + i0^+)$. The width Δ of the gap is then approximately given

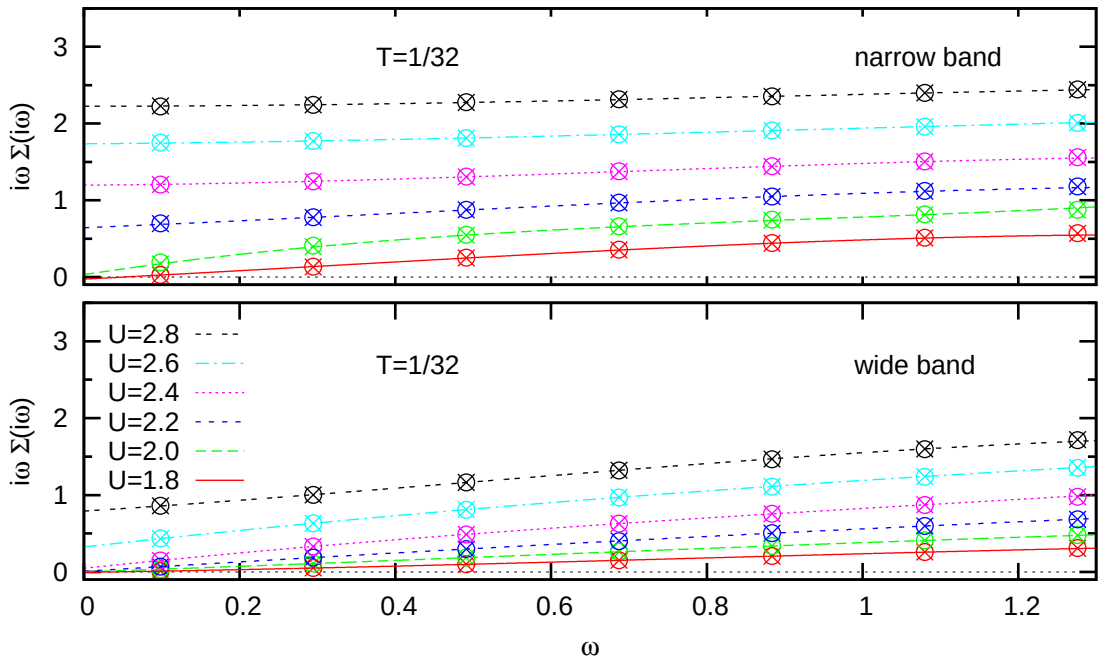

Figure 3.10: Low-frequency analysis of the self-energy for $T = \frac{1}{32}$: QMC data (crosses: for $\Delta\tau = 0.40$, circles: for $\Delta\tau = 0.32$) for the product of frequency ω and self-energy Σ at the Matsubara frequencies is extrapolated by cubic polynomials in ω for the narrow/wide band (upper/lower panel).

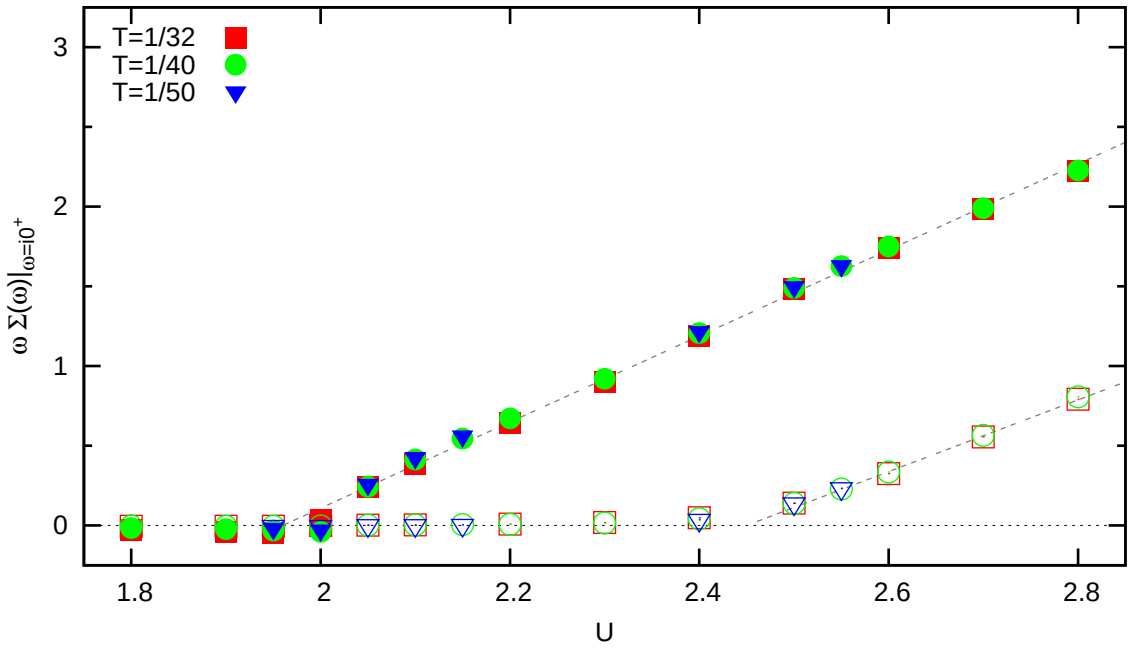

Figure 3.11: Low-frequency analysis of the self-energy for various temperatures: Extrapolated value of $\omega\Sigma(\omega)$ for $\omega \to i0^+$ for the narrow/wide band (solid/open symbols).

tion as a function of U in Fig. 3.11. Clearly, two distinct transitions for the narrow and wide band can be seen at $U = U_{c1} \approx 2.0$ and at $U = U_{c2} \approx 2.5$, respectively. Once the bands become insulating, λ is linear in U (within the errors) which is represented by the dotted (black) line. In contrast to the kink in λ of the first band (which is quite sharp and becomes a discontinuity below T_c), the transition of λ for the wide band is slightly softened. This 'smoothness' is probably an artifact of the extrapolation. Another important point is that λ is rather independent of the temperature. Data for lower temperatures ($T = \frac{1}{40}$ and $T = \frac{1}{50}$) is distinguishable only right at the first transition U_{c1}. This result strongly suggests, that the character (including the order) of the two transitions remains unchanged at finite temperatures $T > 0$. The transition of the narrow band, however, can become of second order at $T = 0$, similar to the behavior of the MIT of the single-band Hubbard model (Georges et al., 1996).

3.2.4 Spectral Function

The two distinct transitions can also be observed in the spectral function

$$N(\omega) = -\frac{1}{\pi}\mathrm{Im}\, G(\omega + i0^+), \tag{3.10}$$

which is obtained from QMC by analytic continuation using the maximum-entropy method (MEM). Results for $T = \frac{1}{40}$ are depicted in Fig. 3.12. For $U = 0$, one obtains the non-interacting semi-elliptic density of states of the Bethe lattice. Up to the interaction $U = 1.8$, the density of states at the Fermi energy, $N(\omega = 0)$, is pinned at its noninteracting value $\frac{1}{2\pi}$ for the wide band (lower panel) and nearly pinned for the narrow band (upper panel). The behavior of the two bands then evolves quite differently as the interaction is increased. The spectrum of the narrow band shows a clear quasiparticle peak, e.g., at $U = 1.8$. The reduction of the peak-height as the interaction is increased, reflects the destruction of the Fermi-liquid, while spectral weight is shifted towards the Hubbard shoulder. A gap opens for $U \gtrsim 2.05$ and the narrow band becomes insulating. The behavior of the spectrum is therefore similar to the one of the single-band case [compare, e.g., Blümer (2002)]. The spectrum of the wide band, N_{wide}, shows a quite different behavior. It remains flat near $\omega \approx 0$ up to $U \approx 2.05$, then develops a dip upon further increase of the interaction, until $N_{\mathrm{wide}}(0)$ vanishes at $U \approx 2.5$. The absence of a quasiparticle peak is another indicator for that the wide band cannot be described as a Fermi-liquid within the orbital-selective Mott (OSM) phase. The reduced height of $N_{\mathrm{wide}}(0)$ [the spectrum of the wide band is obviously not pinned to its noninteracting value within the OSM phase] is consistent with the results obtained directly from the study of the quasiparticle weight in section

by $\Delta = 2\omega_0 \sim \mathrm{Re}\Sigma(\omega_0)$. Assuming the simplest form of a one-pole self-energy, $\Sigma = \frac{a}{\omega}$, implies for frequencies on the imaginary axis $i\omega_n \mathrm{Im}\Sigma(i\omega_n) \to a$ with $\omega_0 = \sqrt{a}$.

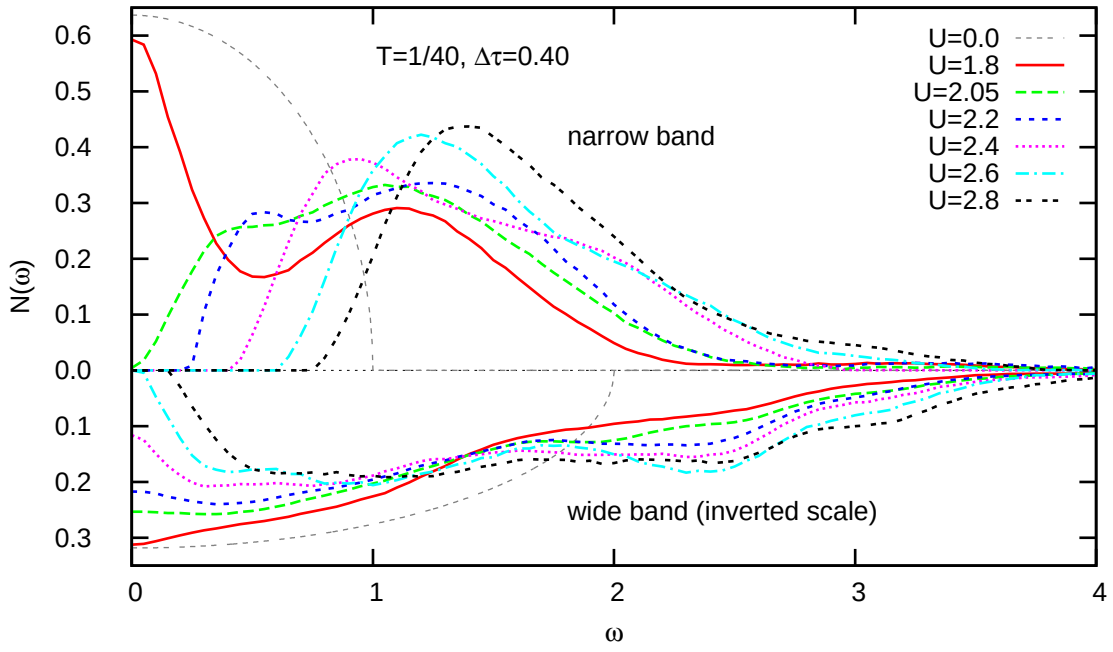

Figure 3.12: Spectral function of the narrow/wide band (upper/lower panel) from QMC + MEM for $T = \frac{1}{40}$.

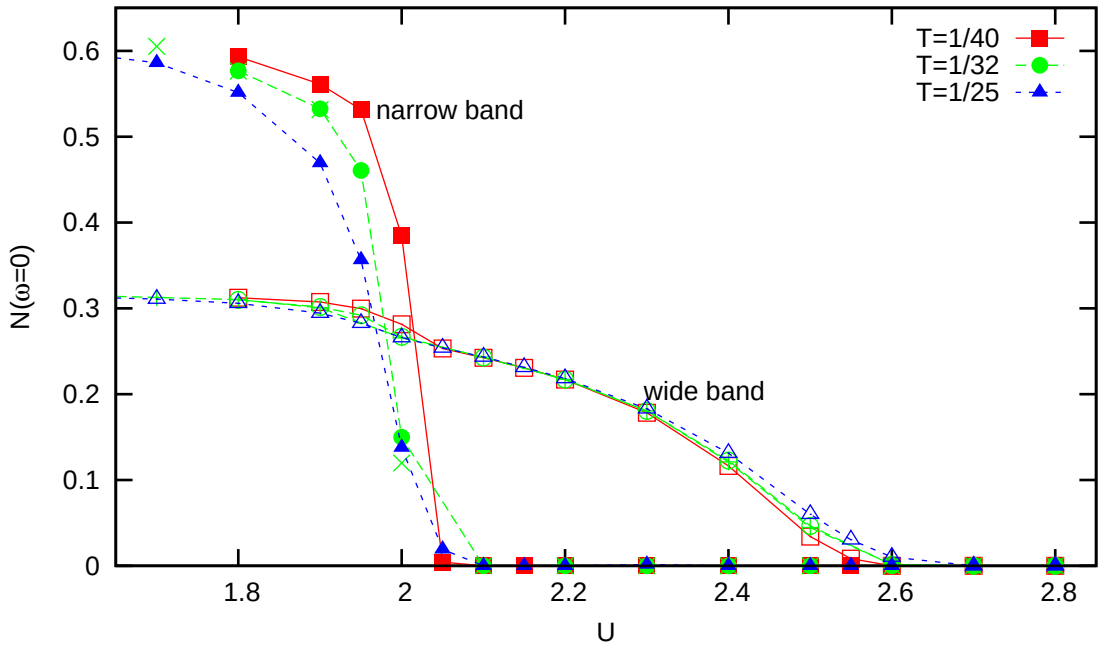

Figure 3.13: QMC estimates for the value $N(0)$ of the spectral function at the Fermi energy versus the interaction. Full/open symbols correspond to the narrow/wide band at $\Delta\tau = 0.4$; crosses to results for $\Delta\tau = 0.32$ at $T = \frac{1}{32}$.

3.2.1: The violation of the Luttinger sum rule $N_{\mathrm{wide}}(0) = N_0(0)$ [with $N_0(0)$ being the non-interacting DOS at the Fermi edge] is due to the finite value Γ_{wide}, to which the imaginary part of the self-energy extrapolates in the limit $\omega_1 \to 0$. This is seen as follows. The local Green function is related to the self-energy by the Dyson equation: $G(i\omega_n) = \int d\epsilon\, N_0(\epsilon)/(i\omega_n - \Sigma(i\omega_n) - \epsilon)$. Employing this relation in the definition 3.10 and evaluating at $\omega = 0$ implies:

$$N_{\mathrm{wide}}(0) = \int d\epsilon\, \frac{N_0(\epsilon)\Gamma_{\mathrm{wide}}}{\pi(\epsilon^2 + \Gamma_{\mathrm{wide}}^2)} < N_0(0)\,. \tag{3.11}$$

For $U = 2.6$, a gap appears also for the wide band. At this interaction, the size of the gap of the narrow band is already larger than half the bandwidth. Also, the shape of the corresponding curve is very similar to the narrow-band spectrum for $U = 2.05$. The behavior of the spectrum of the wide band close to $\omega \approx 0$ resembles the one of the Falicov-Kimball model (compare also Fig. 3.25), which describes spinless electrons coupled to local charges. In the case of the J_z-model within the OSM phase, the itinerant electrons of the wide band are coupled to the electrons of the narrow band which are already local. The essence of the physics in the region of the OSMT might be captured already by the Falicov-Kimball model, which will be discussed in section 3.3, although the leading contribution to the interaction (the on-site Coulomb repulsion for electrons in the same orbital) will be neglected.

The dependence of $N(\omega{=}0)$ upon the interaction and the temperature is resolved in Fig. 3.13, which exposes the orbital-selective Mott transition quite clearly: At U_{c1} a sudden decay to 0 is observed only for the narrow band, while the wide band value is reduced only by about 20%. The second band becomes insulating only for $U_{c2} \approx 2.5$. Both transitions become sharper at lower temperatures. It is of further interest, that $N(\omega = 0)$ of the wide band is practically independent of T right after the narrow band becomes insulating. This is again a strong indicator for the OSMT scenario to remain valid also in the limit $T \to 0$.

The local spectral functions of this section were computed with the MEM procedure as implemented by Sandvik and Scalapino (1995) [cf. also 1.6] with a Gaussian default model. They are based on a minimum of 24 measurements for each parameter set. In order to gain reliable results within the MEM, it is important to ensure systematic errors to be much smaller than statistical errors. First of all, the finite discretization (here, $\Delta\tau = 0.4$) contributes to the systematic error. Another contribution stems from unconverged solutions. The latter source of errors was kept small by iterating a stable solution for at least 16 more iterations. In this context it is important to note the rapid decay of the spectra at high frequencies, which proves that the quality of the data has kept artificial broadening to a minimum.

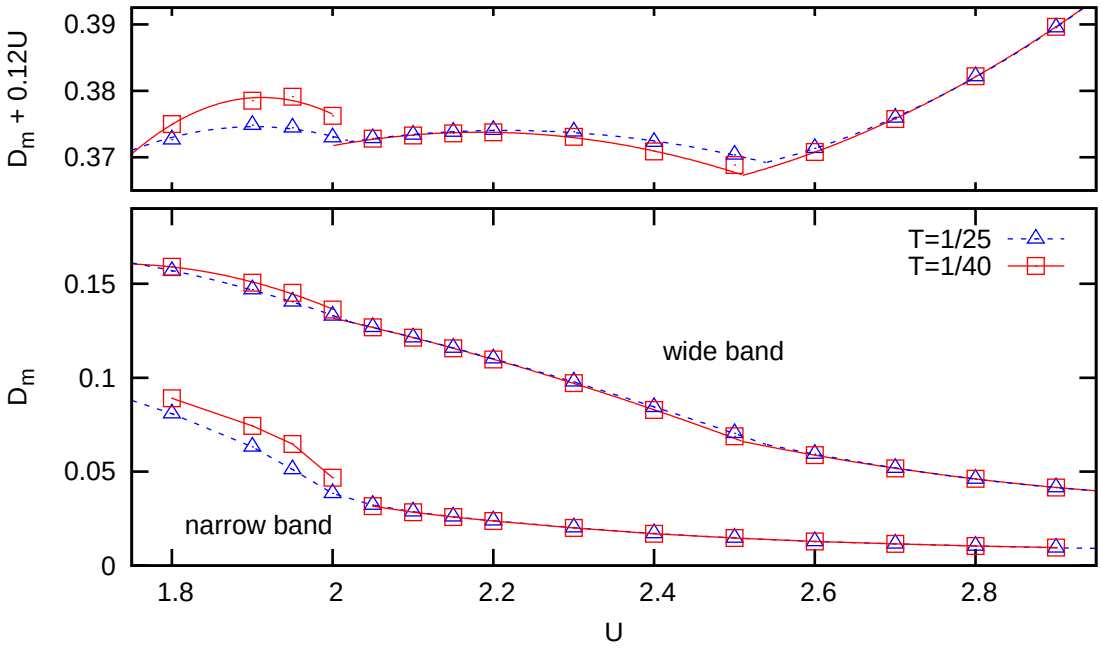

Figure 3.14: Lower panel: Intra-orbital double occupancy $D_m = \langle n_{m\uparrow} n_{m\downarrow} \rangle$. Lines indicate piecewise quadratic fits for the wide band and guides to the eye for the narrow band. Upper panel: A linear offset exposes the features of the wide band.

3.2.5 Double Occupancy

Another observable that is useful in the study of Mott transitions, and which can be directly computed in the QMC routine, is the double occupancy. Of special interest for the study of the OSMT is the intra-orbital double occupancy $D_m = \langle n_{m\uparrow} n_{m\downarrow} \rangle$, where m denotes the orbital. As seen in the lower panel of Fig. 3.14, D_{wide} barely shows any features near U_{c1}, while D_{narrow} is reduced by about 50% from $U = 1.9$ to $U = 2.1$. In the insulating phase, D_{narrow} is quasi independent of the temperature. The wide orbital, however, remains itinerant in a regime where the narrow orbital is already fully localized. At $U \approx 2.5$, the wide band exhibits again an enhanced temperature dependence as well as a change in slope. This transition can be emphasized by adding a suitable linear term as shown in the upper panel of Fig. 3.14. Here, both transitions appear as kinks and as regions of enhanced temperature dependence. For high temperatures, e.g., for $T = \frac{1}{25}$, the kink is even more pronounced at U_{c2} than at U_{c1}. For lower temperatures ($T \leq T_c$), the kink at U_{c1} will be replaced by a discontinuity, due to the coexistence of metallic and insulating solutions (not shown here). The behavior of D_{wide} in the insulating phase

is eventually similar to the corresponding behavior of D_{narrow}.

In conclusion, the study of the double occupancy also reveals two consecutive phase transitions, each of which can be associated with a Mott transition of one orbital.

3.2.6 Internal Energy within Second-Order Perturbation Theory

The observable that turned out to be most precise in the determination of the phase boundary of the Mott transition in the one band Hubbard model is the internal energy, i.e., the energy per lattice site (Blümer, 2002). It is therefore expected, that the OSMT is also detectable in this observable. In the following, the internal energy is first calculated within the weak-coupling limit up to second order [2nd order perturbation theory (2OPT)] at zero temperature and $d = \infty$ in order to verify if the QMC results for the anisotropic two-band model reproduce known exact results.[9] The calculation is performed in analogy to the one by van Dongen (2005) for the single-band model.

The grand canonical Hamiltonian of the J_z-model reads:

$$H = \sum_{k\alpha} \epsilon_k d^\dagger_{k\alpha} d_{k\alpha} + \tfrac{1}{2} \sum_{i\alpha\gamma} U_{\alpha\gamma} n_{i\alpha} n_{i\gamma} - \mu \sum_{i\alpha} n_{i\alpha} \,, \tag{3.12}$$

with the momentum k, the band-index ν, and the combined spin-band indices $\alpha, \gamma = (\nu, \sigma)$. The usual Hartree decoupling: $n_\alpha n_\gamma \to \langle n_\alpha \rangle\, n_\gamma + n_\alpha \langle n_\gamma \rangle - \langle n_\alpha \rangle \langle n_\gamma \rangle$ gives the following contribution to the chemical potential $\mu = \mu_\alpha = \frac{1}{2} \sum_\gamma U_{\alpha\gamma}$ and yields the first-order contribution to the ground state energy at half filling:

$$E^{\mathrm{HF}} = -2 \sum_\nu \int_0^\infty d\epsilon\, \epsilon N_\nu(\epsilon) + \frac{1}{4} \sum_{\alpha > \gamma} U_{\alpha\gamma} \,. \tag{3.13}$$

The second-order contribution to the energy is easiest calculated when considering the following Hamiltonian, where averages are already subtracted:

$$K = H_t + V(\tau) = H_t + \frac{1}{2} \sum_{i\alpha\gamma} U_{\alpha\gamma} \left(n_{i\alpha} - \langle n_{i\alpha} \rangle \right) \left(n_{i\gamma} - \langle n_{i\gamma} \rangle \right) \,. \tag{3.14}$$

The second-order term is then:

$$e_2 N = -\frac{1}{2\beta} \int_0^\beta d\tau_1 \int_0^\beta d\tau_2 \, \langle V(\tau_1) V(\tau_2) \rangle_0^c \,, \tag{3.15}$$

[9] The calculation of the energy in the strong-coupling limit is omitted, because it is not expected to coincide with the QMC results, in analogy to the discrepancy of the QMC estimates of the Néel temperature and the results of the strong-coupling expansion in Sec. 3.2.8.

where the upper index c signifies that only connected diagrams contribute, according to the linked-cluster theorem. As only the z-component of Hund's coupling is considered, inter-orbital propagators do not need to be taken into account. In $d = \infty$, e_2 can be expressed in terms of the local propagator G_0^α only:

$$e_2 = -\frac{1}{2}\sum_{\alpha\gamma} U_{\alpha\gamma}^2 \int_0^{\beta/2} d\tau\, G_0^\alpha(\tau) G_0^\alpha(-\tau) G_0^\gamma(\tau) G_0^\gamma(-\tau)\,, \tag{3.16}$$

with

$$G_0^\gamma(\tau) = \mathrm{sign}(\tau) \int_0^\infty d\epsilon\, N_\gamma(\epsilon) e^{-|\tau|\epsilon} = \mathrm{sign}(\tau)\hat{N}_\gamma(\tau)\,. \tag{3.17}$$

For the semi-elliptic density of states $N_\gamma = \frac{4}{W_\gamma \pi}\sqrt{1 - \left(\frac{2\epsilon}{W_\gamma}\right)^2}$ with bandwidth W_γ, the Laplace transform $\hat{N}_\gamma$ can be expressed in terms of the modified Bessel function of the first kind, $I_1(x)$, and the modified Struve function, $L_1(x)$:

$$\hat{N}_\gamma(\tau) = \frac{I_1\left(\frac{W_\gamma \tau}{2}\right) - L_1\left(\frac{W_\gamma \tau}{2}\right)}{\frac{W_\gamma \tau}{2}}\,. \tag{3.18}$$

The integral in (3.16) can then be evaluated easily and is a function of the bandwidth W_γ only:

$$e_2 = -\frac{1}{2}\sum_{\alpha\gamma} U_{\alpha\gamma}^2 I(W_\alpha, W_\gamma)\,, \tag{3.19}$$

with

$$I(W_\alpha, W_\gamma) = \int_0^\infty d\tau\, \hat{N}_\alpha(\tau)^2 \hat{N}_\gamma(\tau)^2\,. \tag{3.20}$$

Thus the total energy in 2nd order perturbation theory reads:

$$E_{\mathrm{2OPT}} = -\frac{2}{3\pi}\sum_m W_m + \frac{1}{4}\sum_{\alpha>\gamma} U_{\alpha\gamma} - \sum_{\alpha>\gamma} U_{\alpha\gamma}^2 I(W_\alpha, W_\gamma)\,, \tag{3.21}$$

where the sum in the first term is only over the bands. The bandwidths considered in this chapter are $W_1 = 2eV$ and $W_2 = 4eV$. For $I(W_1, W_2)$, which is symmetric in the bands m, one finds:

$$I(W_1, W_1) = 0.0417324 \tag{3.22}$$
$$I(W_1, W_2) = 0.0282504 \tag{3.23}$$
$$I(W_2, W_2) = 0.0208662\,, \tag{3.24}$$

with all digits significant.

3.2.7 Internal Energy within QMC

Within the DMFT, the internal energy per orbital ν is given by (Fetter and Walecka, 1971; Georges et al., 1996):

$$E_\nu = \lim_{\eta\to 0^+} T\sum_{n,\sigma}\int_{-\infty}^{\infty} d\epsilon \frac{e^{i\omega_n\eta}\epsilon\rho_\nu(\epsilon)}{i\omega_n+\mu-\Sigma_{\nu\sigma}(i\omega_n)-\epsilon} + \frac{1}{2}T\sum_{n,\sigma}\Sigma_{\nu\sigma}(i\omega_n)G_{\nu\sigma}(i\omega_n)\,. \quad (3.25)$$

Here, $e^{i\omega_n\eta}$ is a convergence factor and thus difficult to control numerically. In actual calculations, the limit $\eta\to 0^+$ can be either replaced by setting η equal to the discretization $\Delta\tau$, which determines the frequency cutoff in the infinite sum, or by evaluating the noninteracting part separately. In the latter case, the kinetic energy per orbital reads:

$$E_{\mathrm{kin},\nu} = \lim_{\eta\to 0^+} 2T\sum_{n,\sigma} e^{i\omega_n\eta}\int_{-\infty}^{\infty} d\epsilon \frac{\epsilon\rho_\nu(\epsilon)}{i\omega_n+\mu-\Sigma_{\nu\sigma}(i\omega_n)-\epsilon} \quad (3.26)$$

$$= 2\int_{-\infty}^{\infty} d\epsilon \frac{\epsilon\rho_\nu(\epsilon)}{e^{\beta(\epsilon-\mu)}+1} + 2T\sum_{n=-\infty}^{\infty}\int_{-\infty}^{\infty} d\epsilon\rho_\nu(\epsilon)(G_{\nu\epsilon}(i\omega_n)-G^0\nu_\epsilon(i\omega_n)) \quad (3.27)$$

$$\approx 2\int_{-\infty}^{\infty} d\epsilon \frac{\epsilon\rho_\nu(\epsilon)}{e^{\beta(\epsilon-\mu)}+1} + 2T\sum_{n=-\frac{L}{2}+1}^{\frac{L}{2}}\int_{-\infty}^{\infty} d\epsilon\rho_\nu(\epsilon)(G_{\nu\epsilon}(i\omega_n)-G^0_{\nu\epsilon}(i\omega_n))\,, \quad (3.28)$$

where the paramagnetic case is assumed and $G_{\nu\epsilon}(i\omega_n)$ $[G^0_{\nu\epsilon}(i\omega_n)]$ denotes the [non-] interacting Green function for the orbital ν. The truncation error leading to the finite sum in (3.28) is very small, because, on the one hand, the difference of the Green functions in the Matsubara frequency sum falls off at least as $\frac{1}{\omega^2}$, and, on the other hand, the splining routine allows, in principle, for an arbitrarily large number of Matsubara frequencies. In the current implementation of the QMC algorithm, frequency dependent quantities are represented with 1000 Matsubara frequencies by default. The internal energy per orbital is then given by $E_\nu = E_{\mathrm{kin},\nu} + E_{\mathrm{pot},\nu}$, with the potential energy per orbital calculated by the double occupancy via:

$$E_{\mathrm{pot},\nu} = \frac{1}{2}\sum_{\sigma\sigma'\nu'}\langle n_{\nu\sigma}n_{\nu'\sigma'}\rangle U_{\alpha=\nu\sigma;\gamma=\nu'\sigma'}\,, \quad (3.29)$$

with the multi-indices α,γ combining spin and band index and the Coulomb interaction matrix, which is given in (B.14). In the QMC method, the double occupancy is calculated, according to Wick's theorem, by averaging over the Ising spin configurations.

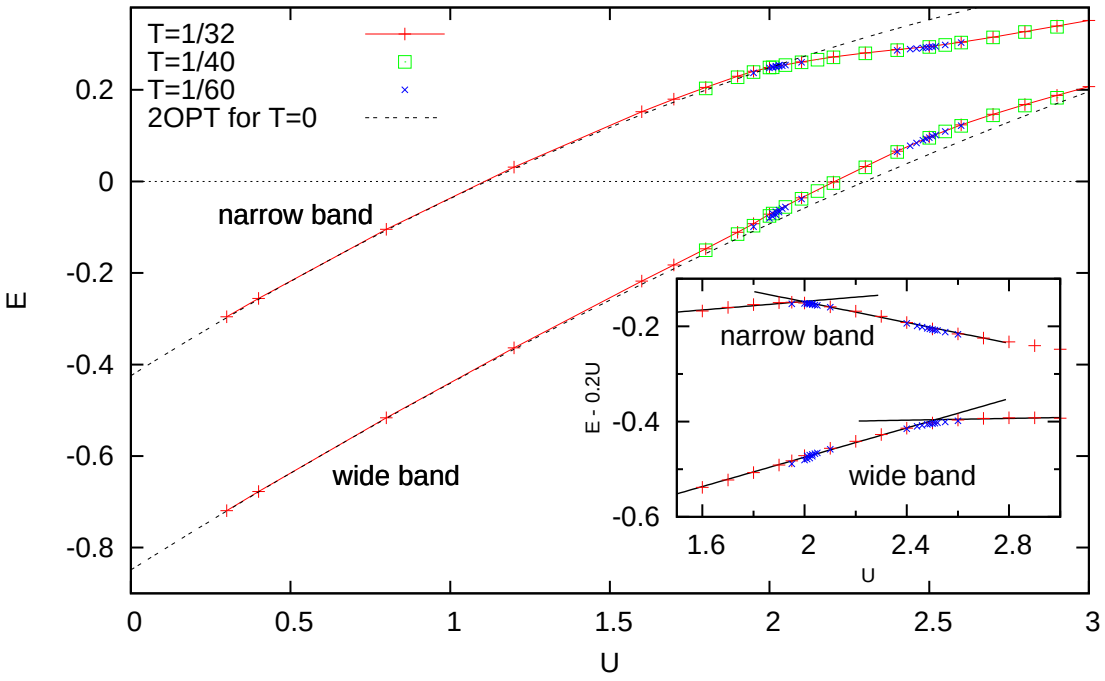

Figure 3.15: QMC estimates and the result from 2OPT for the internal energy per orbital of the two-band Hubbard model at half filling, $U - 2J_z = U'$ and bandwidth ratio $\frac{W_2}{W_1} = 2$. Inset: Transitions in both bands are seen clearly when subtracting a linear term $0.2U$. Lines (black) indicate piecewise linear fits.

The QMC estimates for the internal energy and also the results from 2OPT are shown in Fig. 3.15. The predictions for small interactions $U < 0.5$ agree extremely well with the results of the 2OPT for both bands, even for the relative high temperature of $T = \frac{1}{32}$. The QMC results therefore recover well the weak-coupling limit. The fact that the results from 2OPT are in exceptional accordance with the QMC results until the first transition of the narrow band at $U_{c1} \approx 2$, should not be overestimated: Within the perturbation theory at weak coupling, the internal energy is represented as an asymptotic series with zero radius of convergence only (Guillou and Zinn-Justin, 1990). As usual in asymptotic expansions, higher order corrections will change the results noticeably, in particular at intermediate-to-large coupling, demonstrating that high-order perturbation theory at such large U-values is pointless. Another important point is the fact that the internal energy also shows two distinct transitions, one for each band, which are both characterized by a change in slope: The coexisting solutions of the internal energy at $T = \frac{1}{60}$ are not seen on this scale. The transition of the wide band at $U_{c2} \approx 2.5$ is more pronounced when

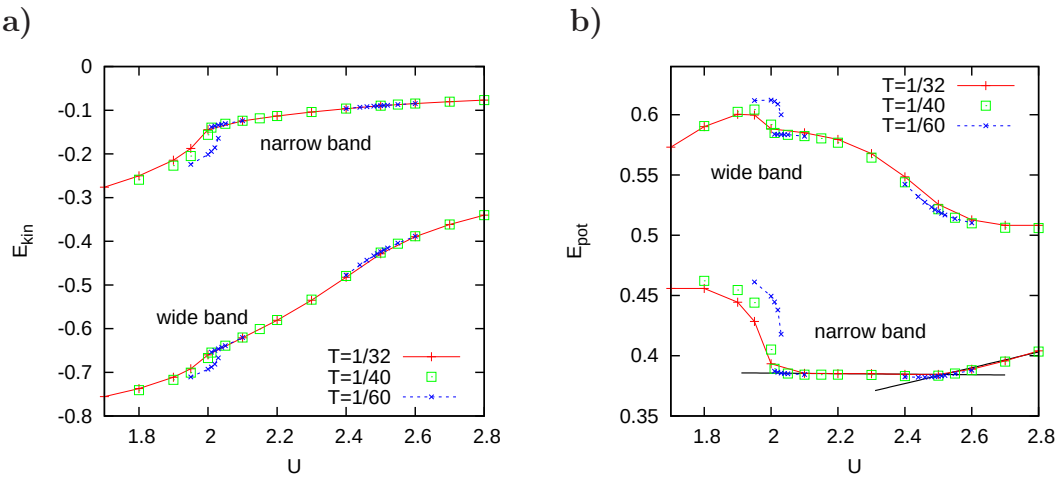

Figure 3.16: a) QMC estimates for the kinetic energy, **b)** for the potential energy. Lines are guides to the eye. Lines (black) indicate piecewise linear fits.

subtracting a term linear in U as is shown in the inset of Fig. 3.15. The transition is then clearly seen as a kink. An important observation is that the internal energy is quasi independent of the temperature within the insulating phase of each band on this scale. This changes only in the vicinity of the transitions. A similar behavior is also found for the single-band case (Blümer, 2002) and is expected in general in the insulating low-temperature phase with a well-developed gap in the spectrum. The reduced dependence of the energy upon T compared to the metallic phase comes along with a reduction of the specific heat right above the Mott transition. The estimates for the kinetic and potential energy in the transition region of the OSMT are shown in Fig. 3.16. The transition of the narrow band is seen in both observables as a kink for temperatures above T_c and as a discontinuity with coexisting solutions for $T = \frac{1}{60}$. In each case, the transition is reflected in the wide band. Once again, the transition in the wide band at U_{c2} is characterized by a change in slope. The itinerant character of the electrons can be studied well by means of the kinetic energy: The mobility decreases quickly in the metallic phase as the Coulomb interaction is increased. The influence of the on-site interaction on the mobility of the already local electrons in the insulating phase, however, is small. This is reflected in the reduced dependence of E_{kin} upon U above U_{c1} and U_{c2}. The observed temperature dependence of the internal energy originates from the one of the kinetic and potential energy. Both show a dependence only for metallic solutions. The general remarks about the shape and the temperature dependence of the double occupancy in 3.2.5 obviously apply also to the potential energy.

As expected, the OSMT scenario is also observed in the internal energy as well as in its components, the kinetic and the potential energy. Coexisting solutions are found for the transition in the narrow band and kinks in the observables for the transition in the wide band, corresponding to first and second-order transitions, respectively. A remarkable observation is the extremely small dependence of the insulating solutions on the temperature, already right above the transitions. This behavior is usually expected only deep inside the insulating low-temperature phase.

3.2.8 Magnetic Phase Diagram of the J_z-Model

One important aspect in the context of the study of the OSMT that has not been discussed in the literature up to now concerns the magnetic ground state of the two-band Hubbard model. The Mott-Hubbard transition in the single-band Hubbard model in $d = \infty$ occurs only in the fully frustrated phase: The critical temperature $T^* \approx 0.055$ of the MIT is below the Néel temperature, which is about $T_N \approx 0.2$. The MIT is therefore completely hidden in the antiferromagnetic ground state. Consequently, it is advisable to also determine the magnetic phase diagram for the J_z-model. In the following, the Néel temparature is calculated within the QMC method and compared to results of weak-coupling and strong-coupling approaches. It is found, that the OSM phase is also hidden deep inside the symmetry-broken phase of the J_z-model. The section therefore ends with a discussion of microscopic mechanisms for frustration.

Néel Temperature within QMC

The magnetic phase diagram of the half-filled single-band Hubbard model in infinite dimensions actually consists only of the phase boundary of the antiferromagnetic ground state and the paramagnetic high-temperature phase as a function of the on-site interaction. Other magnetically ordered phases, like ferromagnetism, which occur for instance in 'flat band systems' (Mielke, 1991; Mielke and Tasaki, 1993), are not relevant for the case of interest, which is lattices with AB-structure, like the hypercubic or the Bethe lattice. The antiferromagnetic (AF) ground state for half-filled and bipartite lattices is found for small interactions for dimensions $d \geq 2$ within Hartree-Fock theory and also by variational calculations (Penn, 1966; Langer et al., 1969). The inclusion of higher order corrections usually leads to a renormalization of the Hartree results (Georges and Yedidia, 1991; van Dongen, 1991). In the strong-interaction limit, the Hubbard model maps onto the Heisenberg model which also exhibits an antiferromagnetic state with a Néel temperature proportional to $\frac{1}{U}$. Results for the Néel temperature at intermediate coupling were obtained with the QMC-method for a hypercubic lattice by Jarrell (1992) and Georges and Krauth (1993).

The Néel temperature can be calculated from the antiferromagnetic susceptibility

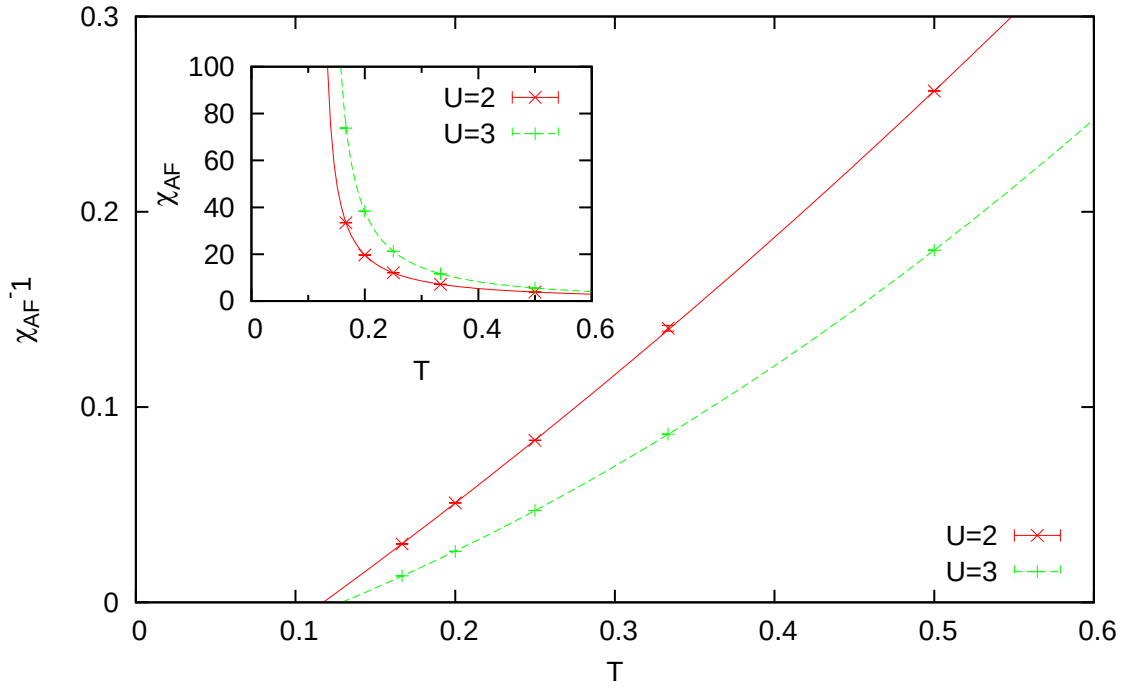

Figure 3.17: QMC estimates for the inverse of the antiferromagnetic susceptibility χ_{AF} as a function of T for the two-band Hubbard model with semi-elliptic DOS. Included are the results from a least square fit. The inset shows directly χ_{AF} with the results from the fit.

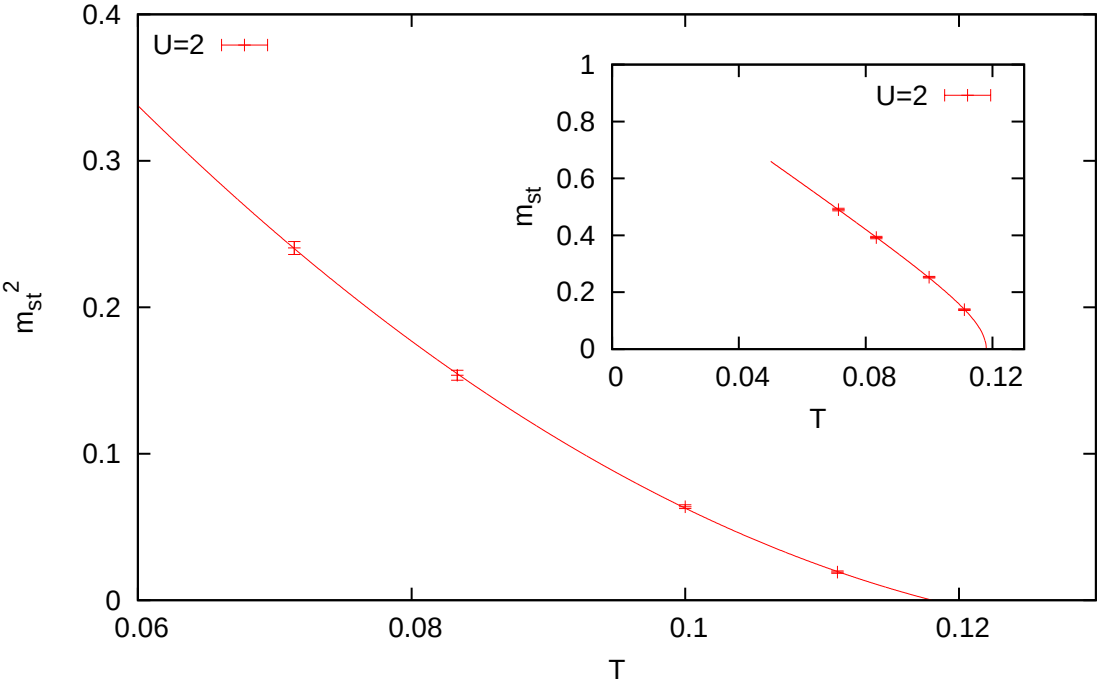

Figure 3.18: QMC estimates for the square of the staggered magnetization m_{st} as a function of the temperature, calculated in the symmetry-broken phase for $U = 2$. Included is the result of a least square fit. Inset: Plain staggered magnetization with the fit result.

χ_{AF} in the high-temperature phase, which is expected to show Curie-Weiss mean-field behavior right above the Néel temperature:

$$\chi_{\mathrm{AF}} \propto \frac{1}{T - T_{\mathrm{N}}}\,, \tag{3.30}$$

corresponding to a critical exponent $\gamma = 1$. It is also possible to compute T_{N} via the staggered magnetization m_{st} within the antiferromagnetically ordered phase:

$$m_{\mathrm{st}} = \frac{1}{2}\sum_{\alpha\sigma} \alpha\sigma n_{\alpha\sigma}\,. \tag{3.31}$$

Here, α denotes the sublattice: $\alpha = \pm 1$. The staggered magnetization of the single-band model shows a square-root behavior close to the transition temperature, corresponding to a critical exponent $\beta = \frac{1}{2}$.

The Néel temperature for the two-band model was calculated for various interactions U from the antiferromagnetic susceptibility.[10] Results from this approach are shown in Fig. 3.17 for the inverse susceptibility χ_{AF}^{-1} for $U = 2$ and $U = 3$ and discretization $\Delta\tau = 0.2$. The transition is signalled by the divergence of χ_{AF}, which is shown in the inset. The QMC results for χ_{AF}^{-1} are well described by a polynomial quadratic in T, corresponding to the Curie-Weiss form (3.30) close to the transition temperature. The transition temperature for $U = 2$ is found to be $T_N = 0.117 \pm 0.005$. The uncertainty does not include the discretization error yet, which is found to alter the results by about 1-2%, depending on the interaction U. The results of this approach were verified by predictions from the staggered magnetization for selected interactions. QMC estimates for m_{st} are presented in Fig. 3.18 for $U = 2$ and $\Delta\tau = 0.2$. The main panel shows m_{st}^2 as a function of T. The data fits well a polynomial form of second order in T, for which the coefficients are determined by a least square fit. This corresponds to a square root behavior of m_{st} close to the critical temperature as shown in the inset. The magnetization m_{st} thus shows mean-field behavior and the transition is of second-order; both in analogy to the single-band model. The QMC estimate of the critical temperature at $U = 2$ is $T_N = 0.115 \pm 0.01$. The results of both schemes therefore coincide within the error. The determination of the phase boundary using the susceptibility, however, is numerically less expensive, as the calculations are performed at higher temperature within the paramagnetic phase.

[10] The determination of response functions like susceptibilities, is based on the calculation of vertex functions such as $\langle T c_\sigma^\dagger(\tau_1) c_\sigma(\tau_2) c_\sigma^\dagger(\tau_3) c_\sigma(\tau_4)\rangle_A$, with the effective action A and the time-ordering operator T. Within the QMC scheme, those local correlators are computed by employing Wick's theorem and subsequently averaging over the auxiliary spin field. Compare also Ref. Georges et al. (1996) for a comprehensive review of how to calculate response function and transport properties within the DMFT and Held (1999) for details of the implementation in a multi-orbital context.

T_N within the Weak-Coupling Limit

The Néel temperature of the Hubbard model in infinite dimensions and at half filling can also be calculated within the weak and strong-coupling limit. At weak coupling, however, standard perturbation theory yields wrong results within a symmetry broken phase: The 2nd order correction of standard perturbation theory around the Hartree result is found to be of the same order of magnitude as the Hartree contribution itself (van Dongen, 1994*a*). The thermodynamics at weak coupling is therefore determined by the Hartree contribution and the fluctuation together. The reason for this failure is that the energy correction of the symmetry broken phase is exponentially small as a function of the coupling constant and can therefore not be addressed by the Hartree term which is of linear order. A similar behavior is found for the order parameter of the superconducting phase in the BCS theory (Bardeen et al., 1957). A method that correctly accounts for the fluctuations is the perturbation theory at fixed order parameter (Georges and Yedidia, 1991), which is discussed in detail in chapter 4. The calculation of the Néel temperature for the two-band Hubbard model (3.2) within the weak-coupling limit is due to van Dongen (2005) and performed in analogy to the single-band case (van Dongen, 1991; van Dongen, 1996).

In order to allow for a possible phase transition to an antiferromagnetically ordered state, one has to impose a staggered magnetization Δ_m for each band m, separately:

$$\langle n_{im\sigma}\rangle = \frac{1}{2}(1 + \lambda\sigma\Delta_m)\,, \quad \lambda \equiv (-1)^i\,. \tag{3.32}$$

In a next step, the free energy is expanded in powers of the interaction at constant staggered magnetization and density. Here, Lagrange multipliers are used to fix the order parameters. The expansion of the free energy is then truncated at stepwise increasing powers of U and minimized as a function of the order parameters at each step. Truncating at $\mathcal{O}(U)$ is thereby equivalent to the Hartree free energy. The order parameters are then determined self-consistently in any order of the perturbation expansion. A quicker way to obtain the first-order contribution, however, is to directly apply the usual Hartree decoupling scheme $\langle nn\rangle \xrightarrow{\text{HF}} n\langle n\rangle + \langle n\rangle n - \langle n\rangle\langle n\rangle$ to each density-density interaction of (3.2). A canonical transformation can then be used to diagonalize the Hamiltonian, resulting in:

$$H^{\text{HF}} = \sum_{km\sigma} \eta_{km} n_{km\sigma} - C\mathcal{N}\,, \tag{3.33}$$

with

$$C = \frac{1}{4}U\sum_m(1-\Delta_m^2) + U' - \frac{1}{2}J_z(1+\Delta_1\Delta_2) \tag{3.34}$$

$$\eta_{km} = \mathrm{sign}(\epsilon_{km})\sqrt{\epsilon_{km}^2 + (\mu_{m\uparrow}^+)^2} \tag{3.35}$$

$$\mu_{m\uparrow}^+ = \frac{1}{2}(U\Delta_m + J_z\Delta_{\overline{m}})\,. \tag{3.36}$$

The grand canonical potential per lattice site, Ω, is given by:

$$\Omega^{\mathrm{HF}} = -C - \frac{4}{\beta}\sum_m\int_0^\infty d\epsilon\,\nu_m(\epsilon)\ln\left[2\cosh(\tfrac{1}{2}\beta\eta_{\epsilon m})\right]\,. \tag{3.37}$$

The consistency relations for the order parameters then follow from the requirement $\frac{\partial\Omega^{\mathrm{HF}}}{\partial\Delta_m} = 0$. The resulting self-consistency equations are also the defining equations for the critical temperature, for which the staggered magnetization vanishes: $\Delta_1(T_c) = \Delta_2(T_c) = 0$. The Hartree solution for T_c is then found to be (van Dongen, 2005):

$$k_BT_c^{\mathrm{HF}} = t_1^*\exp\left[I_\infty + \frac{t_1^*}{t_2^*}\ln\left(\frac{t_2^*}{t_1^*}\right)b_1^{(1)} - \frac{t_1^*b_1^{(0)}}{U\nu(0)}\right]\,, \tag{3.38}$$

with

$$b_1^{(0)} \equiv \frac{\left(1+\frac{t_1^*}{t_2^*}\right) - \sqrt{\left(1-\frac{t_1^*}{t_2^*}\right)^2 + 4j_3^2\,\frac{t_1^*}{t_2^*}}}{2\,(1-j_3^2)\,\frac{t_1^*}{t_2^*}}\,, \quad b_1^{(1)} \equiv \frac{1-(1-j_3^2)\,b_1^{(0)}}{\left(1+\frac{t_1^*}{t_2^*}\right) - 2\,(1-j_3^2)\,b_1^{(0)}\,\frac{t_1^*}{t_2^*}}\,, \tag{3.39}$$

and $j_3 = \frac{J_z}{U}$. It is interesting to note, that the only result at Hartree level that depends on the lattice is the constant I_∞. All other results are lattice-independent or depend only on $\nu(0)$. For the Bethe lattice one has $\nu(0) = \frac{1}{\pi}$ and $I_\infty = 3\ln 2 - \ln\pi - \gamma - 1$, with Euler's constant γ.

By applying perturbation theory at constant order parameter up to second-order, one finds, that the general form of the Hartree results is preserved, but renormalized by a factor of q, which is of the order of unity for the model under consideration (van Dongen, 2005). The renormalization effect due to the quantum fluctuations is given by:

$$T_c = T_c^{\mathrm{HF}}\exp\left[-\frac{t_1^*\,b'}{\nu(0)}\right] \equiv q\,T_c^{\mathrm{HF}}\,. \tag{3.40}$$

were the constant b' is explicitly dependent upon the lattice and the interactions of the Hamiltonian. The critical temperature for the two-band Hubbard model (3.2) is

then given by (van Dongen, 2005):

$$T_c \sim 0.889\, e^{-\frac{1.4875}{U}}\,, \tag{3.41}$$

with a renormalization factor of $q = 0.272$. The Hartree results are renormalized already for arbitrary small interactions U. Quantum fluctuations can therefore not be neglected in high dimensions. They are however small compared to low dimensions ($d \leq 2$), where long-range order is completely suppressed.

T_N within the Strong-Coupling Limit

The calculation of the critical temperature within the strong-coupling limit $U \gg W$ is comparatively easy: In second order, the Hubbard model at half filling can be mapped to the antiferromagnetic Heisenberg model with the exchange coupling $J = \frac{4t^2}{U}$ (Anderson, 1959):

$$H_{\text{Heisenberg}} = \frac{J}{2} \sum_{\langle ij \rangle} \mathbf{S}_i \cdot \mathbf{S}_j\,, \tag{3.42}$$

with the spins $S_i^x = \frac{1}{2}(c_{i\uparrow}c_{i\downarrow}^\dagger + c_{i\downarrow}c_{i\uparrow}^\dagger)$, $S_i^y = -\frac{i}{2}(c_{i\uparrow}c_{i\downarrow}^\dagger - c_{i\downarrow}c_{i\uparrow}^\dagger)$ and $S_i^z = \frac{1}{2}(n_{i\uparrow} - n_{i\downarrow})$. In the limit of infinite dimensionality, the effective Heisenberg model is exactly described by the Weiss mean-field theory. A further simplification occurs due to the anisotropic coupling in the two-band Hubbard model (3.2), in which spin flips do not occur. In this case, the effective Heisenberg model is reduced to the Ising model:

$$H_{\text{Ising}} = J_{\text{Is}} \sum_{\langle ij \rangle} S_{i3} S_{j3}\,, \tag{3.43}$$

where the effective interaction for the anisotropic two-band Hubbard model is given by $J_{\text{IS}} = \frac{t_1^2 + t_2^2}{U + J_z}$ for $J_z > 0$ (van Dongen, 2005). The critical temperature of the Ising model is $k_B T_c = \mathcal{Z} J_{\text{Is}}$, with $\mathcal{Z}$ the number of nearest neighbors of each lattice site of an AB-lattice. Hence:

$$k_B T_c = \mathcal{Z}\, \frac{t_1^2 + t_2^2}{U + J_z} = \frac{(t_1^*)^2 + (t_2^*)^2}{U + J_z}\,. \tag{3.44}$$

Note, that the first-order term in the strong-coupling expansion depends only upon the on-site Coulomb interaction U and the Hund coupling J_z, but not upon the interorbital Coulomb interaction U'. For the parameters considered in this chapter, $J_z = \frac{U}{4}$ and $2t_1^* = t_2^* = 1$, one gets the following estimate for the Néel temperature:

$$k_B T_c = \frac{1}{U}\,, \tag{3.45}$$

which is identical to the asymptotic behavior of T_c of the single-band Hubbard model with $t^* = 1$.

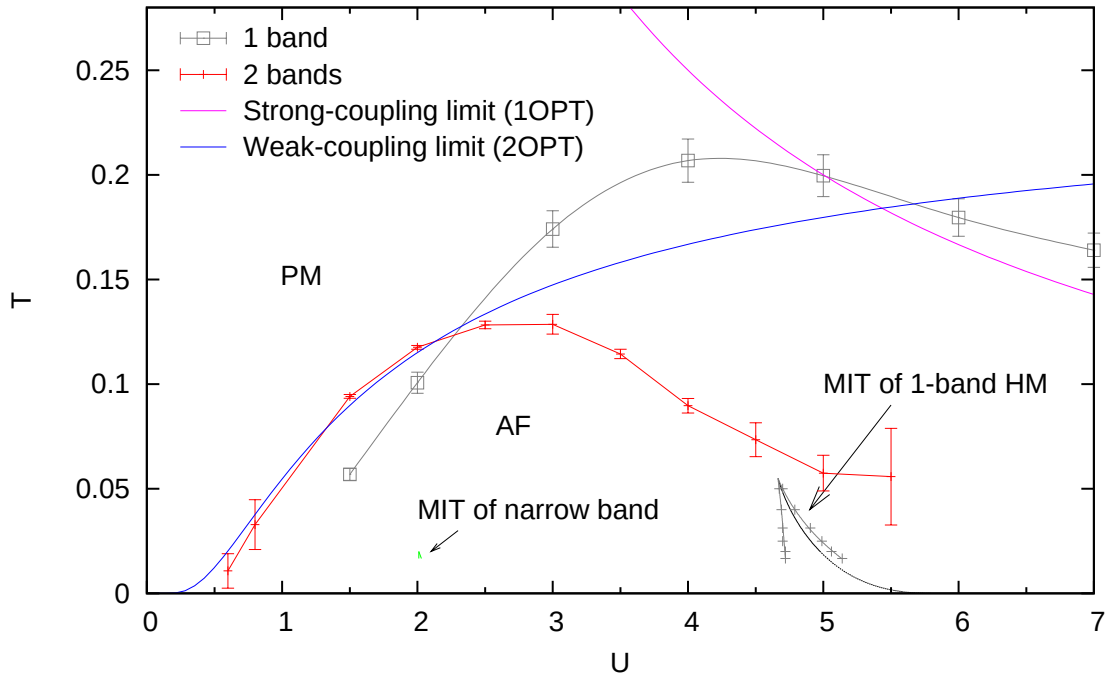

Figure 3.19: Magnetic phase diagram of the two-band anisotropic Hubbard model with $U - 2J_z = U'$ and semi-elliptic DOS: QMC estimates and exact results from the weak and strong-coupling limit for the Néel temperature T_N. Included is the MIT phase diagram for the narrow band with critical temperature $T_c \approx 0.02$ at $U_{c1} \approx 2.01$. PM and AF denote the paramagnetic and antiferromagnetic phase, respectively. Also included are QMC estimates for the Néel temperature for the single-band model as well as the corresponding MIT phase diagram, as obtained using QMC by Blümer (2002). Lines connecting the QMC data are guides to the eye.

Discussion of the Phase Diagram

The magnetic phase diagram of the anisotropic ($J_\perp = 0$) two-band Hubbard model (3.2) is presented in Fig. 3.19, containing QMC estimates for the Néel temperature T_N, which were calculated in this work, as well as results for the strong and weak-coupling limit as obtained by van Dongen (2005). The position of the MIT of the narrow band occurring in the fully frustrated model is also plotted. For comparison to the single-band Hubbard model, QMC estimates for the Néel temperature for the semi-elliptic DOS with bandwidth $W = 4$ are reproduced and inserted together with the corresponding MIT phase diagram as obtained by Blümer (2002).

The study of the phase diagram reveals a number of interesting points. The most important one concerns the critical temperature $T_{c1} \approx 0.02$ of the OSMT: It is about

6 times smaller than the corresponding QMC estimate for the Néel temperature of $T_N \approx 0.12$. The OSMT found in the fully frustrated paramagnetic phase is therefore hidden deep inside the antiferromagnetic ground state of the J_z-model. This is a rather severe issue, implying that the J_z-model with the selected choice of parameters is not able to explain the OSMT of $Ca_{2-x}Sr_xRuO_4$, which occurs in the AF phase. In order to find an appropriate model one has to either consider more complicated Hamiltonians or introduce microscopic mechanisms for frustration. The latter point is discussed in Sec. 3.2.9.

Nevertheless, it is instructive to further discuss the phase diagram. Comparing the asymptotic results to the QMC predictions, one finds a very good agreement of the QMC data with the results of the 2OPT at weak coupling for $U \lesssim 2$. Similar to the findings of the internal energy in Sec. 3.2.7, this accordance should not be overestimated: As in all asymptotic expansions, one expects that higher order corrections will alter the results strongly, in particular at intermediate-to-strong interaction values. When comparing the QMC results to the strong-coupling limit, one observes a striking disagreement between the data. The results of the strong-coupling approach [which includes terms up to order of $\mathcal{O}(\frac{1}{U})$] overestimate the Néel temperature by a factor of more than 2. This result is in strong contrast to the single-band case, in which the Néel temperature deviates by less than 10% from the asymptotic behavior already for interactions of $U \approx \frac{3}{2}W$. It would therefore be instructive to calculate the contribution of the next order (which is of the order of $\frac{1}{U^3}$) in the strong-coupling expansion. Accordingly, the magnetic order of the J_z-model seems to be governed by the weak-coupling regime.

It is also interesting to compare the Néel temperatures of the two-band model and the single-band model. The maximum $T_N^{\max,1} \approx 0.2$ for the single-band model is reached for $U \approx W$. The Néel temperature of the two-band model reaches its maximum of $T_{\mathrm{N}}^{\max,2} \approx 0.13$ for $U \approx 3$, which corresponds to about the average of the bandwidths $W_{\mathrm{narrow}} = 2$ and $W_{\mathrm{wide}} = 4$. T_N of the coupled two-band system is therefore strongly influenced by the narrow band. This scenario is also supported by the fact that $T_{\mathrm{N}}^{\max,2}$ is just slightly larger than the maximum of the Néel temperature of a single-band model with bandwidth $W = 2$, which would be about $T_N^{\max,1} \approx 0.1$.

3.2.9 Microscopic Mechanisms for Frustration

The results of the previous part showed that the OSM phase is hidden in the AF ground state of the J_z-model.[11] It is therefore essential to study microscopic mechanism that suppress the symmetry-broken phase. In the following, the influence of the interaction parameters of the J_z-model on the Néel temperature is studied within 2OPT. The variation of these parameters, however, is also expected to influence the

[11] This is true only for ordered bipartite lattices.

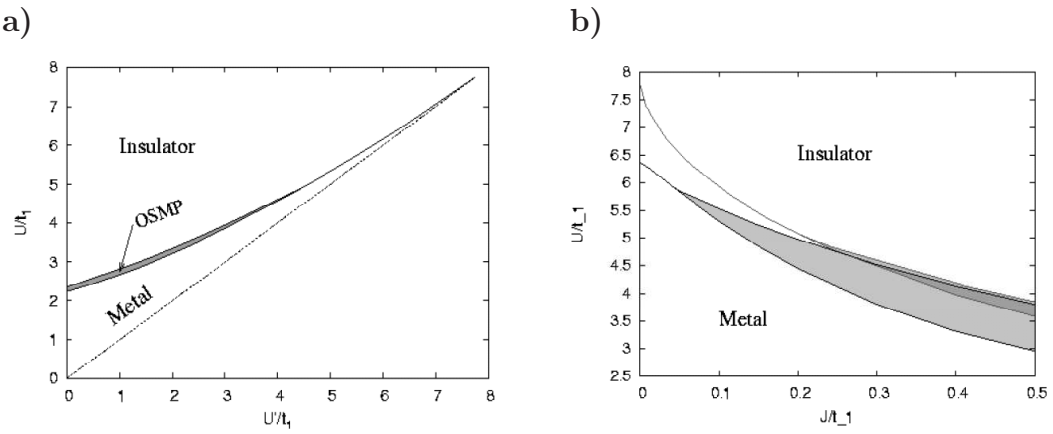

Figure 3.20: Phase diagrams of the anisotropic two-band Hubbard model ($J_\perp = 0$) with $\frac{W_2}{W_1} = 2$ for the anisotropic case within slave-spin mean-field theory (de' Medici et al., 2005). **(a)** for U vs U' at $T = 0$, and **(b)** for U vs J_z at $T = 0$ (narrow stripe) and at $T = \frac{1}{40}$.

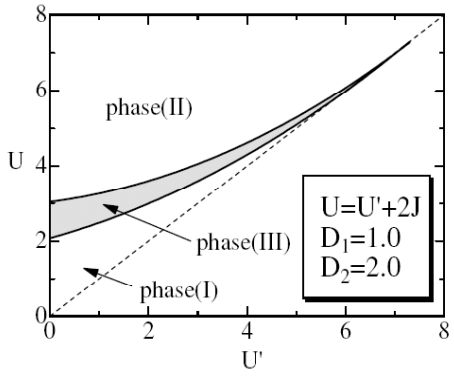

Figure 3.21: Phase diagrams of the isotropic two-band Hubbard model with $\frac{W_2}{W_1} = 2$ as obtained within ED+DMFT (Koga et al., 2004). In phase I (II), both bands are in the metallic (insulating) state, phase III labels the OSM phase.

OSM phase. For this reason, the known results concerning this issue are reviewed beforehand. Other relevant microscopic mechanisms for frustration, like disorder or the influence of the dimensionality, are discussed at the end of this part.

Dependence of the OSM Phase upon the Interaction Parameters

The parameter space of the anisotropic two-band model (3.2) is already too large to study the dependence of the OSM phase within a QMC simulation within a reasonable effort. A more promising approach is to study first the effect of the parameters within 2OPT at weak coupling and to eventually verify the predictions at larger interactions within a QMC simulation. This approach is supported by the good agreement of the results of 2OPT to the QMC data in the weak-coupling regime. Changing the parameters, however, will also influence the position of the OSM phase or, in the worst case, lead to its destruction. The position of the OSM phase as a function of the interaction parameters was studied for the isotropic two-band Hubbard model within exact diagonalization (DMFT+ED) by Koga et al. (2004), and for both the isotropic and the anisotropic model by means of a slave spin mean-field study [which is similar to the Gutzwiller approximation of variational wave functions] by Ferrero et al. (2005) and de' Medici et al. (2005). The resulting slave spin mean-field phase diagrams of the OSMT region in the $U-U'$-plane as well as in the $U-J_z$ plane are shown in Fig. 3.20 for $T=0$ and $T=\frac{1}{40}$ and bandwidth ratio $\frac{W_2}{W_1}=2$. The OSMT phase resides only within a small stripe in the upper half ($U>U'$) of the $U-U'$ plane. Increasing interorbital interaction U' narrows the OSM phase which is broadest for $U'=0$, while it is at the same time shifted towards stronger interactions U before vanishing when $U \gtrsim W$. The behavior of the OSM phase upon the Hund's rule coupling J_z is different: The width is increased upon raising J_z while the OSM phase shifts towards lower interactions U. It is also interesting to note, that the OSM phase is enlarged at finite temperature. Even though the results of the slave spin mean-field study are intrinsically uncontrolled, they point out the direction in which the parameters of the anisotropic two-band model should be tuned: The phase boundary for T_N drops quickly for $U \to 0$, such that the OSM phase can be driven into the paramagnetic phase of the Hubbard model by increasing J_z. The phase diagram of the isotropic two-band model as obtained within DMFT+ED (Koga et al., 2004) is shown in Fig. 3.21. Here, the OSM phase shows a similar behavior upon U', but is enlarged compared to the previous results for the anisotropic case. Results for the $U-J$-plane are not known up to the completion of this work.

Dependence of T_N upon the Interaction Parameters within 2OPT

Next, it is important to discuss how the symmetry broken phase can be suppressed by varying the interaction parameters. In this context, it is of interest to examine the solution of the two-band Hubbard model in 2OPT; its predictions are expected to give a first hint of how T_N changes [at least at weak coupling].

Within 2OPT, the Néel temperature is governed by the factor q, which renormalizes the Hartree results. The prefactor that controls the exponential decay of the

order parameter, in contrast, is only weakly dependent upon the lattice structure or the model parameters. A qualitative picture of how T_N changes as a function of the interaction parameters therefore emerges already when considering the factor q, only. Compared to the parameter set that is considered throughout this section ($U' = U - 2J_z\,, q \approx 0.272$), q is significantly reduced only for the following configurations (van Dongen, 2005):

(i) $q \to 0$ for $u' \to \infty$ (strong interband coupling),

(ii) $q \approx 0.0695$ for $J = 0,\ u' = 1$ and $\frac{W_2}{W_1} = 2$ (rotationally invariant case without Hund coupling),

with $\frac{U'}{U} \equiv u' \geq 0\,,\ J_\perp = 0 = J_z$ and a Bethe DOS. The first case, (i), disqualifies because the OSM phase vanishes simultaneously according to 3.2.9. Case (ii) is the only promising candidate, for which q is decreased by about a factor 4. The OSM phase, however, ceases to exist for vanishing Hund coupling J. Rotationally invariant configurations that additionally consider spin flip and pair hopping terms ($J_\perp \neq 0$) do not lead to a significant reduction of the renormalization factor. These findings point out, that the antiferromagnetic phase cannot be suppressed sufficiently by varying the interaction parameters of the two-band Hubbard model, as long as one assumes the Hamiltonian to be rotational invariant, implying $U = U' - 2J$. This condition, however, was imposed for simplicity only. In contrast, the experimental system displaying an OSMT, $Ca_{2-x}Sr_xRuO_4$, is not rotationally invariant but as most SO(2)-invariant, due to its planar structure. The most important result of the above considerations is the fact that, eventually, rotational invariance of the Hamiltonian has to be abandoned for a deeper understanding of the OSMT.

The Effects of Disorder and Dimensionality on T_N

The AF phase of the Hubbard model in infinite dimensions is also known to be suppressed by other microscopic mechanisms such as disorder or the fluctuations that arise in lower dimensions.

There exists various types of disorder in crystals, starting from impurities (magnetic or non-magnetic) and defects of the lattice structure to the limit of strong disorder of glass or alloy structures. Of particular interest for the case at hand is the binary alloy disorder, in which two sorts of atoms randomly occupy the lattice sites of a crystal structure. Important concepts in this field are Anderson localization for strong disorder (Anderson, 1958) and the coherent potential approximation (CPA) (Soven, 1967; Taylor, 1967). Reviews on the field of disorder are given, e.g., in Ref. Elliott et al. (1974) and Ref. Lee and Ramakrishnan (1985). A phenomenon like Anderson localization, however, cannot be described within the DMFT due to the purely local nature of the theory. Electrons in infinite dimensions are thus delocalized

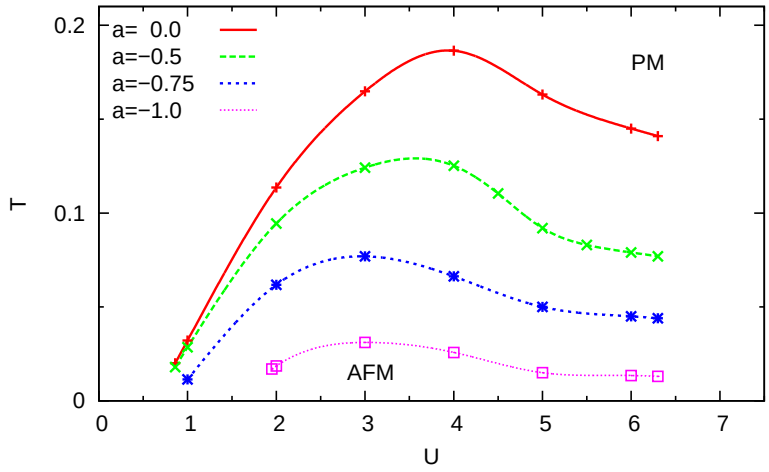

Figure 3.22: Magnetic phase diagram of the single-band Hubbard model for the hypercubic lattice with NN and NNN hopping in $d = \infty$ (Schlipf, 1998). The Néel temperature is suppressed as the frustration parameter $a = \frac{t'^*}{t^*}$ is decreased.

even for arbitrarily strong disorder. Nevertheless, the introduction of disorder (e.g., binary alloy disorder) has several effects. Of importance in this respect is the suppression of the antiferromagnetic long-range order, especially for small interactions in the metallic regime of the phase diagram [i.e., $\frac{U}{W} < u_c \simeq 0.6$ for a single-band model with bandwidth W]. This was shown, e.g., for diagonal disorder[12] for an Anderson-Hubbard model in infinite dimensions (Ulmke et al., 1995). Similar results were obtained for a two-dimensional Hubbard model using a finite-temperature quantum Monte Carlo method (Ulmke et al., 1999). Interestingly, the AF phase is found to be enhanced for the same configurations at large values of the interaction.

The AF phase is also known to be suppressed upon introducing longer-range hopping (for hypercubic lattice, Müller-Hartmann, 1989). In general, one has to distinguish between frustration at constant DOS and frustration, which leads to an asymmetry of the DOS. In the first case, the MIT is expected to remain unchanged. The influence of next-neighbor (NN) and next-nearest-neighbor (NNN) hopping on the Néel temperature of the single-band Hubbard model in $d = \infty$ was investigated by Schlipf (1998) within a DMFT+QMC study as an example of frustration that leads to an asymmetry of the DOS; the results are shown in Fig. 3.22. The Néel temperature T_N is suppressed as a function of the frustration parameter $a = \frac{t'^*}{t^*}$,

[12] Diagonal disorder assumes the hopping elements to be independent of the randomness, while the atomic potentials are chosen at random.

with NN and NNN hopping amplitude t^* and t'^*, respectively. There is, however, evidence that the critical temperature T_c^* of the MIT drops quicker than T_N upon decreasing a (Knecht, 2002). The relationship between lattice types, densities of states, and magnetic frustration, especially in large dimensions, is studied in detail in Ref. Blümer (2002).

Another important aspect in the context of frustration is the influence of the dimensionality d. This question was addressed in various approaches to calculate the Néel temperature such as QMC simulations (Hirsch, 1987; Scalettar, Scalapino, Sugar and Toussaint, 1989; Ulmke et al., 1996; Staudt et al., 2000), analytical approaches like the weak-coupling perturbation theory (van Dongen, 1991; van Dongen, 1994*a*) or strong-coupling calculations (Szczech et al., 1995), DMFT studies (Jarrell, 1992; Georges and Krauth, 1993; Ulmke et al., 1995) and the two-particle self-consistent formalism (Daré and Albinet, 2000). The spatial fluctuations of finite-dimensional systems are expected to reduce the critical temperature compared to the purely local theory in $d = \infty$. In low dimensions ($d = 1, 2$), fluctuations even completely suppress long range order at finite temperatures (Mermin and Wagner, 1966). The effect of finite dimensionality can be studied, e.g., within a $\frac{1}{d}$-expansion. At weak coupling, the renormalization factor q [which renormalizes the Hartree results in 2nd order perturbation theory, cf. 3.2.8] is further reduced in finite dimensions, implying that the Néel temperature is lowered compared to the one in $d = \infty$ (van Dongen, 1994*a*). Direct studies of the Hubbard model in three dimensions, e.g., using QMC simulations, yield Néel temperatures that are in accord with the results of the weak-coupling expansion for small interactions. In addition, T_N is also reduced within the intermediate and large interaction-regime (Staudt et al., 2000).

3.2.10 Comparison with earlier QMC Results

In the following, the QMC data of this work is compared to earlier results by Liebsch (Liebsch, 2003*a*; Liebsch, 2003*b*; Liebsch, 2004), which explains why the OSMT of the J_z-model was not found before.

The quasiparticle weights of the OSM phase of this work for discretizations $\Delta\tau = 0.4$ and $\Delta\tau = 0.32$ are compared to results from (Liebsch, 2004)[13] for $T = \frac{1}{32}$ in the lower panel of Fig. 3.23 a.

Differences in the two data sets are significant especially in the vicinity of the first and second transition, at U_{c1} and U_{c2} respectively. The first transition is much more pronounced in the data of this work than in Liebsch's data [which is not only due to the denser grid of data points but also because of the reduced error (see below)]. The differences in the data are exposed in a better way when adding a linear term to Z_{wide} as shown in the upper panel of Fig. 3.23 a. In this case, the transition of the

[13] The value of the discretization is not stated in the Ref. Liebsch (2004).

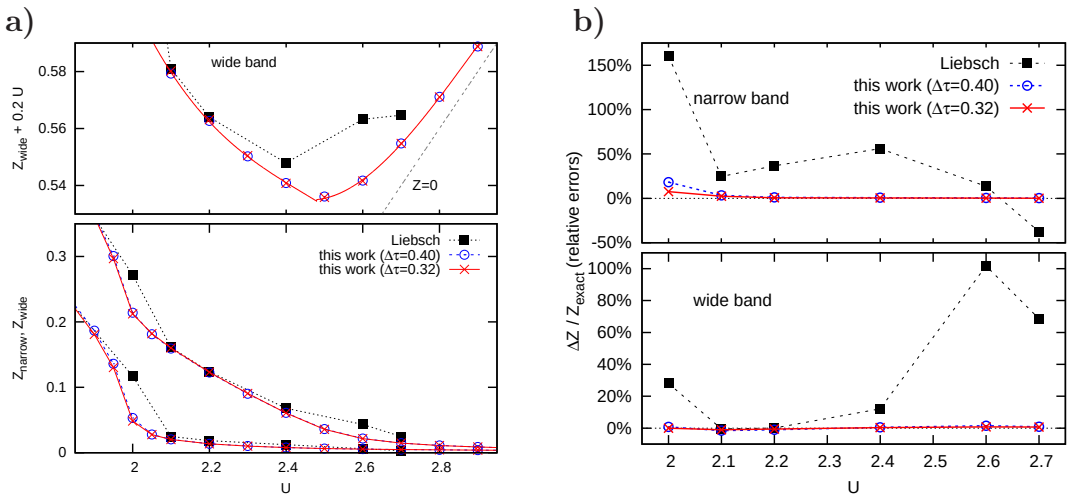

Figure 3.23: **a)** Comparison of discrete quasiparticle weights Z at $T = \frac{1}{32}$ of QMC data of this work and by Liebsch (Liebsch, 2004). Upper panel: Added linear term to Z_{wide} indicates the second transition visible as a kink. **b)** Estimate of relative errors in Z at $T = \frac{1}{32}$: The QMC data for discretizations $\Delta\tau = 0.4$ and $\Delta\tau = 0.32$ (this work) is accurate within about 1% (except for Z_{narrow} at $U = 2.0$). Liebsch's data deviates by more than 100% near transitions.

wide orbital is clearly indicated by a kink only for the data of this work. Liebsch's data, in contrast, does not provide evidence for a second transition of the wide band. Moreover, the behavior of Z_{wide} near the second transition differs even qualitatively: The change in slope is opposite in direction.

As physical observables are obtained from the QMC data only after an extrapolation $\Delta\tau \to 0$ it is important to also discuss the $\Delta\tau$ error of the QMC data. As can be seen from Fig. 3.23 [**a)** and **b)**], the QMC estimates of this work for different discretization $\Delta\tau$ are practically on top of each other. Deviations can be seen on this scale only in the vicinity of the transition U_{c1}. The relative error of the QMC data with respect to the extrapolated values is plotted in Fig. 3.23 b. A significant dependence upon the discretization is found only for the narrow band (upper panel) close to the first transition. Throughout the rest of the OSMT region, the relative error is less than 1%. The relative errors of Liebsch's QMC estimates, in contrast, deviates by more than 100% from the exact values, in particular within the important region in the vicinity of the critical interactions U_{c1} and U_{c2}. Both the study of the OSM phase by means of the quasiparticle weight as well as the comparison of the QMC errors explain why the two distinct transitions are only visible in high-quality QMC data and were missed before.

3.2.11 Discussion

In this section, the anisotropic two-band Hubbard model (J_z-model) with distinct bandwidths $W_2 = 2W_1$ was considered within the DMFT at finite temperatures. Using the high-precision QMC simulation developed as part of this thesis (cf. chapter 2), it was shown, that the J_z-model contains two successive metal-insulator transitions and can therefore be considered as a minimal model for the OSMT phenomenon, as observed experimentally, e.g., in $Ca_{2-x}Sr_xRuO_4$.

The transition of the first (narrow) band, is found to be of first order with a critical interaction $U_{c1} \approx 2.01$ and a critical temperature of $T_{c1} \approx 0.02$. This value revises the previous result of $T_c \approx 0.038$ (Liebsch, 2004). The transition of the wide band turned out to be more subtle. It is reflected in a change of slope in observables like the quasiparticle weight or the intraorbital double occupancy, but is clearly revealed by the low-frequency behavior of the self-energy and the spectral function. The second transition of the wide band therefore shows evidence to be of second order. This finding is not only in contrast to earlier QMC studies, which reported only a single Mott transition (Liebsch, 2003*a*; Liebsch, 2003*b*; Liebsch, 2004), but also contradicts early ED results (Koga et al., 2005*a*). The finite energy-resolution of the ED may be the reason that the transition cannot be seen there. On the other hand, the results are in qualitative agreement with a recent slave-spin mean-field phase diagram for the J_z-model by de' Medici et al. (2005), which also contains an orbital-selective Mott phase, albeit at slightly larger values of the interaction U (at $T = 0$). The quantitative differences may be due to the approximate nature of the slave-spin mean-field theory and also to the finite temperatures used within the QMC method. The OSMT found in the fully frustrated J_z-model implies that the isotropy of the Hund's rule exchange is not a prerequisite for the existence of OSMTs, as was suggested by Koga et al. (2005*a*) on the basis of ED calculations.

Another important point concerns the value of the critical temperature T_{c1} of the OSMT compared to the critical temperature T^* of the single-band model: T_{c1} is decreased by a factor of $\frac{T^*}{T_{c1}} \approx \frac{0.055}{0.02} = 2.75$, which is larger than one would suggest at first sight by simply considering the ratio of the bandwidths. The critical interaction U_{c1} shows a similar behavior: it is of the size of the bandwidth W_{narrow}, compared to the critical interaction $U^* \approx 4.66$ for T^* of the single-band model with bandwidth $W = 4$. This decrease of the critical interaction as well as of the critical temperature of the Mott transition is therefore clearly an effect of the interorbital coupling. It is however not a priori clear, whether the interorbital Coulomb coupling U' or the anisotropic Hund's rule coupling J_z, or both couplings together, are responsible for the observed effect.

It is further found, that the wide band exhibits non-Fermi-liquid behavior in the OSM phase, in contradiction to the findings of Liebsch (2004). Non-Fermi-liquid behavior is seen, e.g., in the low-frequency behavior of the self-energy, which extrap-

olates to a finite imaginary part for $w_n \to 0$, independent of the temperature. In this context, the vanishing of the Eliashberg estimate of the quasiparticle weight Z of the wide band in the limit $T \to 0$ could be revealed as an artifact,[14] which has its origin in the definition of the Eliashberg estimate of Z. The Eliashberg estimate is often used to approximate the genuine Z within a QMC simulation, but looses its validity outside the Fermi-liquid regime. Non-Fermi-liquid behavior is also observed in the behavior of the spectral function near the Fermi edge. Similar results were found by Biermann et al. (2005) for an effective Falicov-Kimball model for each spin species, valid at low energies in the orbital-selective regime (cf. also Sec. 3.3.6). On the basis of the Falicov-Kimball analogy, it is thus physically plausible that the transition of the wide orbital at U_{c2} is of second order. The first-order transition at U_{c1} of the narrow band, however, is exactly what one expects on the basis of experience with the Mott transition in the single-band Hubbard model (Gebhard, 1997; Rozenberg et al., 1999; Blümer, 2002).

Nevertheless, the question of the order of the second transition of the wide band is still a matter of controversy. For the full J-model, recent ED+DMFT results suggest that both OSMTs are of first order for $T > 0$ (Liebsch, 2005). This is supported by results from Inaba et al. (2005), who find that the OSMTs are of first order at finite temperatures but of second order at $T = 0$, in accordance with the scenario of the single-band Hubbard model. The authors applied the recently introduced self-energy functional approach[15] (SFA) (Potthoff, 2003). In contrast, a first-order scenario of the transition of the first (narrow) band at $T = 0$ is found by Arita and Held (2005) using PQMC. For the J_z-model, DMFT+QMC results (this work) suggest, that the transition of the narrow band remains of first order, while the second transition of the wide band is of second order (at least for $T > \frac{1}{60}$). This scenario is supported by results from ED+DMFT (Liebsch, 2005). In this context, it is interesting to note, that the MITs of a decoupled two-band Hubbard model are of first order at finite T and eventually become of second order at $T = 0$.[16] When scaling the interaction parameters like $U' = \alpha\frac{U}{2}$, $J_z = \alpha\frac{U}{4}$, the second-order transition of the wide band in

[14] This vanishing of the Eliashberg estimate of Z was incorrectly taken as an indicator for a single Mott transition to persist also in the limit $T \to 0$ (Liebsch, 2004).

[15] This approach is based on the fact, that the Luttinger-Ward functional (Luttinger and Ward, 1960; Baym and Kadanoff, 1961) is independent of one-particle contributions (e.g., the kinetic energy) (Potthoff, 2003). The grand canonical functional $\Omega = \Omega(\Sigma)$ can then be evaluated rigorously on a restricted set of self-energies of a reference system, which shares the same interaction with the original system. A suitable reference system for the Hubbard model is obtained, e.g., by adding to each correlated site i a number of $n_s - 1$ uncorrelated ('bath') sites, which are disconnected from the rest of the lattice but hybridize with the correlated site i. This mapping recovers the DMFT in the limit $n_s \to \infty$. The special case of a reference system with a local self-energy is also referred to as the 'dynamical impurity approximation' (DIA).

[16] A two-band model without interorbital coupling corresponds to two single-band Hubbard models, for which the order of the MIT is as stated. Compare, e.g., (Georges et al., 1996).

the J_z-model for $T > 0$, should therefore become a first-order transition for $\alpha \to 0$. This scenario is studied by Blümer and Požgajčić (2005).

In future work it will be of interest to investigate also the effect of other terms in the Hamiltonian, such as hybridization terms of various symmetry; first results in this direction have already been reported by Koga et al. (2005*b*) and by de' Medici et al. (2005). It is also of interest to extend the calculations to the more realistic three-band case since the experimental system $Ca_{2-x}Sr_xRuO_4$ has three bands, two of which are physically equivalent. Since the experimental system is an antiferromagnetic insulator for small doping ($x \lesssim 0.2$), it is further important to include also magnetic phases. Finally, as suggested by the study of the magnetic phase diagram, it seems favorable to abandon the restriction that is imposed on the interaction parameters (viz. $U = U' + 2J$) by assuming rotational invariance of the Hamiltonian.

3.3 OSMTs in the Two-Band Falicov-Kimball Model

The Falicov-Kimball (FK) model was initially introduced in 1969 for the study of metal-insulator transitions in rare-earth and transition metal oxides (Falicov and Kimball, 1969). It is a simplified version of the Hubbard model in which only the spin-down electrons can move. The concept appeared already in Hubbard's earlier work (Hubbard, 1963) and the model is also referred to as the simplified Hubbard model (Kennedy and Lieb, 1986).

When it was realized, that the FK model is the simplest model of correlated electrons to display long-range order for dimensions greater than one at low temperatures (Brandt and Schmidt, 1986; Brandt and Schmidt, 1987; Kennedy and Lieb, 1986; Lieb, 1986), it became subject of intense study.[17] A new aspect was brought to the physics of the Falicov-Kimball model by the pioneering work on the limit of large dimensions for strongly correlated fermion models by Metzner and Vollhardt (1989): The FK model could be solved exactly in the limit of infinite dimensions (Brandt and Mielsch, 1989). Among the following work, the exact solution in $d = \infty$ also for the Bethe lattice (van Dongen and Vollhardt, 1990), the study of the breakdown of Fermi-liquid behavior (Si et al., 1992), and the study of the Mott-like metal-insulator transition (van Dongen and Leinung, 1997) are of particular interest for the study of the OSMT. Subsequently, the FK model was applied, among other things, to systems exhibiting a metal-insulator transition upon doping [Ta_xN (Freericks et al., 2001)]. A review of the physics of the Falicov-Kimball model in $d = \infty$ is given by Ref. Freericks and Zlatic (2003).

The FK model describes itinerant electrons of one spin species (e.g., the spin-down electrons) that interact only on-site with a localized charge. Recall, that the OSM phase of the J_z-Hubbard model is marked out by itinerant electrons of the wide band interacting with the already localized electrons of the narrow band. Therefore, a two-band FK model could give insight into the physics of the J_z-Hubbard model particularly in this regime. The existence of an OSMT in a two-band FK model would therefore support the understanding of the OSMT in the anisotropic Hubbard model.

The structure of this section is as follows. In the first part, an extension of the FK model to two bands is introduced and discussed. The model is then solved analytically in $d = \infty$ within an exact mean-field theory, obtaining an implicit equation for the Green function. This equation is then solved numerically for different sets of parameters. The results are discussed and compared to the J_z-model.

[17] For a list of results in low dimensions compare Ref. Freericks and Zlatic (2003) and references therein.

3.3.1 Model

In this section, the following two-band Falicov-Kimball model is considered:

$$H = -\frac{1}{\sqrt{Z}} \sum_{\langle ij\rangle;m} t_m d^\dagger_{im} d_{jm} + \sum_{imm'} U_{mm'} \left(n^d_{im} - \frac{1}{2}\right)\left(n^f_{im'} - \frac{1}{2}\right) - \sum_{imm'} V_{mm'} d^\dagger_{im} d_{im'} \,. \tag{3.46}$$

Here, $d^\dagger_{im}$ and d_{im} create and annihilate the itinerant electrons at site i with hopping amplitude t_m for orbital $m \in \{1,2\}$, and $\langle ij\rangle$ signifies that the hopping is restricted to nearest neighbors. Furthermore, $n^d_{im} \equiv d^\dagger_{im} d_{im}$ is the number operator and the index f labels the localized electrons. The d-electrons may be identified with the spin-down ($\downarrow$) electrons of the Hubbard model. The f-electrons can be considered as localized charges such as ions or as immobile spin-up ($\uparrow$) electrons at site i. For the calculation of thermodynamic properties, all possible configurations of the $\uparrow$ electrons are averaged over at the level of the partition function, so that the position of the $\uparrow$-electrons are treated as annealed disorder.

The first term of (3.46) is the kinetic energy of the conducting electrons. The hopping amplitude is scaled with the inverse square root of the coordination number Z to yield a nontrivial result in the limit of infinite dimensions. The second term is the interaction term which represents the local Coulomb interaction $U_{mm'}$, when itinerant and localized electrons occupy the same orbital ($m = m'$) as well as the inter-orbital interaction for electrons in different bands ($m \neq m'$). The third term introduces a possible on-site hybridization of strength $V_{mm'}$. Note that the Hamiltonian (3.46) [for $V_{mm'} = 0$] is indeed a simplified model of the anisotropic two-band Hubbard model in which the spin down electrons of both orbitals are immobile [taken to be fully localized] and identified with the f-electrons of the FK model. The spin up electrons are itinerant and mapped to the d-electrons of the FK model with hopping amplitudes $t_2 = 2t_1$; the intra-orbital Coulomb interaction, however, is neglected. The analogy is further justified by the fact that the spins are conserved quantities because of the absence of spin-flip terms in the J_z-model.

Symmetries of the Hamiltonian

The Hamiltonian (3.46) exhibits a number of symmetries that turn out to be useful in solving the FK model. In analogy to the J_z-model, we consider the half-filled case. Thus, the Hamiltonian (3.46) is written in a particle-hole symmetric manner, implying $\langle n^d_{im}\rangle = \langle n^f_{im}\rangle = 1/2$ for $\mu = 0$.

Let (t_1, t_2, U, V) denote the FK model (3.46) with interaction and hybridization matrices $U \equiv U_{mm'}$ and $V \equiv V_{mm'}$, respectively. Then, the special particle-hole transformation

$$d_{i1} \to d^\dagger_{i1} e^{i\alpha/2}, \quad d_{i2} \to d^\dagger_{i2} e^{i\alpha/2}, \quad f_{im} \to f_{im}\,, \quad \text{with} \quad \alpha \in \mathbb{R}, \tag{3.47}$$

changes the model (t_1, t_2, U, V) at half filling into the canonically equivalent model $(-t_1, -t_2, -U, -V)$. Hence, the transformation changes the sign of the Hamiltonian, implying that each energy eigenvalue has a counterpart with opposite sign. Therefore, the density of states (DOS) is symmetric. This is true not only for the global DOS (the sum of the DOS of both bands) but also for the DOS of each band, separately.

The Hamiltonian (3.46) also has to be hermitian, implying the following relation for the hybridization V:

$$t_m \in \mathbb{R}, \quad U_{mm'} \in \mathbb{R}, \tag{3.48}$$

$$V = V^\dagger \quad \Longleftrightarrow \quad V_{mm'} = V^*_{m'm}\,. \tag{3.49}$$

Using the special particle-hole transformation

$$d_{i1} \to d^\dagger_{i1}(-1)^i e^{i\alpha/2}, \quad d_{i2} \to d^\dagger_{i2}(-1)^i e^{-i\alpha/2}, \quad f_{im} \to f^\dagger_{im}(-1)^i\,, \quad \text{with} \quad \alpha \in \mathbb{R}\,, \tag{3.50}$$

it can further be shown, that

$$V = \begin{pmatrix} 0 & v \\ v & 0 \end{pmatrix}, \quad (v > 0)\,. \tag{3.51}$$

The details of the calculation are described in Appendix C. The above relations imply that the hybridization V is symmetric and a function of one variable only.

3.3.2 Exact Mean-Field Theory

In the following, the FK model (3.46) is solved within the exact mean-field theory (van Dongen and Vollhardt, 1990; van Dongen, 1992) for the Bethe lattice in the high-temperature phase. This method is particularly well suited for the calculation of the density of states. The analytical part of the calculation is due to van Dongen (2005).

Within the exact mean-field theory for the Falicov-Kimball model, the dynamics of a lattice site is described in terms of collective or mean-field variables. The Hamiltonian (3.46) of the full FK model on a Bethe lattice in $d = \infty$ can then be mapped on a Bethe lattice with coordination number $Z^{\mathrm{MF}} = 5$ by defining collective fermions:

$$\Psi_{\boldsymbol{X}} = \begin{pmatrix} d_{\boldsymbol{X}1} \\ d_{\boldsymbol{X}2} \end{pmatrix} = Z^{-\frac{n}{2}} \sum_{[j_1, j_2, \ldots, j_n]} \left[\prod_{l=1}^{n} \alpha(j_l, x_l) \right] \begin{pmatrix} d_{j_n 1} \\ d_{j_n 2} \end{pmatrix}, \tag{3.52}$$

with

$$\boldsymbol{X} = (x_1, x_2, \ldots, x_n)\,, \quad n \in \{0, 1, 2, 3\}\,, \tag{3.53}$$

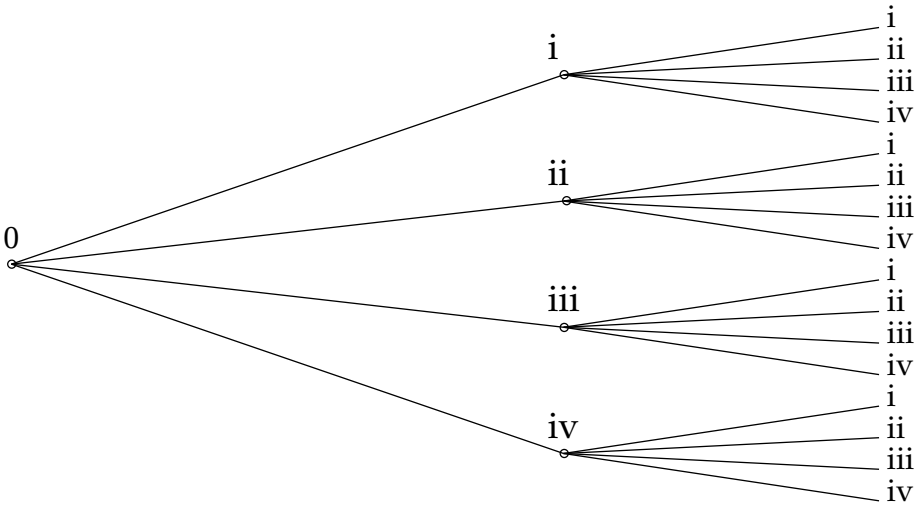

Figure 3.24: Effective Bethe lattice of the exact mean-field Hamiltonian with coordination number $Z^{\mathrm{MF}} = 5$; only the central site **0** has $Z^{\mathrm{MF}} = 4$. Here, the labels (i, ii, ...) denote the presence or absence of electrons on the f-sites according to (3.3.2).

and

$$\alpha(j_l, x_l) = \begin{cases} (1-n^f_{j_l 1})(1-n^f_{j_l 2})/\sqrt{(1-\rho^f_{l_1})(1-\rho^f_{l_2})} & \text{if } x_l = 0 \\ n^f_{j_l 1}(1-n^f_{j_l 2})/\sqrt{\rho^f_{l_1}(1-\rho^f_{l_2})} & \text{if } x_l = 1 \\ (1-n^f_{j_l 1})n^f_{j_l 2}/\sqrt{(1-\rho^f_{l_1})\rho^f_{l_2}} & \text{if } x_l = 2 \\ n^f_{j_l 1}n^f_{j_l 2}/\sqrt{\rho^f_{l_1}\rho^f_{l_2}} & \text{if } x_l = 3 \end{cases}, \tag{3.54}$$

with the density of the f-electrons ρ_l. The sum in (3.52) runs over all nearest-neighbor pairs (j_l, j_{l+1}), with j_l in the lth shell of the Bethe lattice around an arbitrary site **0**, which is defined to be the origin. The collective fermions in (3.52) are then operators that annihilate a $\downarrow$ electron in the nth shell for a given path $\boldsymbol{X}$ with respect to the site **0** [cf. also Fig. 3.24] The atomic configuration of this nth shell further specifies the form of the annihilation operator, as given by (3.54). At half filling, i.e., for $\rho_l = \frac{1}{2}$ for all l, this implies a mapping of the kinetic energy to the following mean-field Hamiltonian:

$$H^{\mathrm{MF}} = \tfrac{1}{2} \sum_{l(\boldsymbol{X})\geq 0} \left(\Psi^\dagger_{\boldsymbol{X}} \Theta \Psi_{\boldsymbol{X}} + \mathrm{H.c.} \right), \quad \Theta \equiv \begin{pmatrix} t_1 & 0 \\ 0 & t_2 \end{pmatrix}. \tag{3.55}$$

The mean-field variables of H^{MF} are, however, operators, in contrast to Hartree-Fock theory. The effective Hamiltonian (3.55) can then be solved using the renormalized perturbation expansion (RPE)(Economou, 1979), which is a perturbation expansion in the hopping amplitude.

In order to calculate the density of states of the FK model, it is useful to define the following matrix Green function:

$$G_{ij}(\tau) \equiv -\begin{pmatrix} \langle T_\tau d_{i1}(\tau) d_{j1}^\dagger(0)\rangle & \langle T_\tau d_{i1}(\tau) d_{j2}^\dagger(0)\rangle \\ \\ \langle T_\tau d_{i2}(\tau) d_{j1}^\dagger(0)\rangle & \langle T_\tau d_{i2}(\tau) d_{j2}^\dagger(0)\rangle \end{pmatrix} . \tag{3.56}$$

Of particular interest is only the on-site Green function ($i = j$). It is further useful to distinguish between the full on-site Green function $G(\tau)$, which includes hopping processes and the atomic Green function $G_0(\tau)$, which does not include hopping processes. There are four atomic environments that have to be averaged over:

(i) 0 f-electrons on the site,

(ii) 1 f-electron in band 1,

(iii) 1 f-electron in band 2,

(iv) 2 f-electrons, one in each band.

With the Fourier transform

$$G(z) \equiv \int_0^\beta d\tau\, e^{z\tau} G(\tau)\,, \tag{3.57}$$

the corresponding atomic Green functions (label by the upper indices: $G^{(1..4)}$) are given in terms of frequency by:

$$\begin{aligned} G_0^{(1)}(z) &= \begin{pmatrix} z+U_{1+} & V \\ V & z+U_{2+} \end{pmatrix}^{-1} & G_0^{(2)}(z) &= \begin{pmatrix} z-U_{1-} & V \\ V & z-U_{2-} \end{pmatrix}^{-1} \\ G_0^{(3)}(z) &= \begin{pmatrix} z+U_{1-} & V \\ V & z+U_{2-} \end{pmatrix}^{-1} & G_0^{(4)}(z) &= \begin{pmatrix} z-U_{1+} & V \\ V & z-U_{2+} \end{pmatrix}^{-1} , \end{aligned} \tag{3.58}$$

with $U_{m\pm} \equiv \frac{1}{2}(U_{m,1} \pm U_{m,2})$. When mapping the full FK model on a Bethe latice with $Z^{\mathrm{MF}} = \infty$ to a Bethe lattice with $Z = 5$ by defining collective fermions, one can make use of the renormalized perturbation expansion (RPE), to get the following expression for the Green function:

$$G^{(b)} = \left[\mathbf{1} - G_0^{(b)} \Theta G \Theta\right]^{-1} G_0^{(b)} . \tag{3.59}$$

Here, $\mathbf{1}$ denotes the unit matrix in 2 dimensions and $\Theta \equiv \left(\begin{smallmatrix} t_1 & 0 \\ 0 & t_2 \end{smallmatrix}\right)$. The full Green function G is also defined as the average over the Green functions of the atomic configurations: $G \equiv \frac{1}{4}\sum_{b'} G^{(b')}$. One therefore obtains the following consistency relation for G:

$$G(z) = \frac{1}{4}\sum_{b}\left[G_0^{(b)}(z)^{-1} - \Theta G(z)\Theta\right]^{-1} . \tag{3.60}$$

In this matrix equation, $G(z)$ is the only unknown.

Symmetries of G

The matrix equation (3.60) implies the following symmetries of the Green function, which turn out to be useful:

- $G(z) = G(z^*)^*$; since both $G(z)$ and $G(z^*)^*$, separately, are solutions of (3.60) and coincide for $\Theta = 0$.
- $G(z) = G(z^*)^\dagger$; same argument as above. Combining the first two relations yields: $G(z) = [G(z^*)^*]^T = G(z)^T$. Thus $G(z)$ is an analytic symmetric function.
- $G_V(z) = -\sigma_3\,[G_V(-z^*)]^\dagger\,\sigma_3$;
  with $G_V(z)$ a solution for hybridization V and the Pauli matrix $\sigma_3 = \left(\begin{smallmatrix} 1 & 0 \\ 0 & -1 \end{smallmatrix}\right)$. The proof can be found in Appendix C. Both solutions (left and right-hand side of the equation, separately) coincide for $\Theta = 0$ and are identical also for $\Theta \neq 0$.

The Green function G can generally be written as:

$$G(z) \equiv \begin{pmatrix} g_1(z) & g_2(z) \\ g_2(z) & g_3(z) \end{pmatrix} . \tag{3.61}$$

Then, the implications of the last identity are as follows. For $z = i\omega_n \in i\mathbb{R}$ one gets:

$$G(i\omega_n) = \begin{pmatrix} g_1(i\omega_n) & g_2(i\omega_n) \\ g_2(i\omega_n) & g_3(i\omega_n) \end{pmatrix} = \begin{pmatrix} -g_1(i\omega_n)^* & g_2(i\omega_n)^* \\ g_2(i\omega_n)^* & -g_3(i\omega_n)^* \end{pmatrix} = -\sigma_3\,[G_V(-i\omega_n)^*]^\dagger\,\sigma_3\,. \tag{3.62}$$

Therefore,

$$g_1(i\omega_n),\ g_3(i\omega_n) \in i\mathbb{R}\,, \qquad g_2(i\omega_n) \in \mathbb{R}\,. \tag{3.63}$$

For real frequencies $z = E + i0^+$ one gets:

$$\begin{pmatrix} g_1(E+i0^+) & g_2(E+i0^+) \\ g_2(E+i0^+) & g_3(E+i0^+) \end{pmatrix} = \begin{pmatrix} -g_1(-E+i0^+)^* & g_2(-E+i0^+)^* \\ g_2(-E+i0^+)^* & -g_3(-E+i0^+)^* \end{pmatrix} . \tag{3.64}$$

Thus the real parts of g_1, g_3 and the imaginary part of g_2 are antisymmetric under the transformation $E \leftrightarrow (-E)$, while the imaginary parts of $g_1\,, g_3$ and the real part of g_2 are symmetric. This implies that the DOS of both bands is symmetric,

$$\nu_m(E) = \nu_m(-E) \qquad (m = 1, 2)\,, \tag{3.65}$$

in agreement with the previous result (3.47).

The implicit equation (3.60) for the full Green function $G(z)$ cannot be solved analytically for all frequencies. A common method to solve implicit equations is to employ a numerical complex root finding algorithm. The explicit equations that need to be solved are obtained by expanding (3.60). For simplicity, the atomic Green functions (3.58) are written as:

$$G_0^{(b)}(z)^{-1} = \begin{pmatrix} z + U_1^{(b)} & V \\ V & z + U_2^{(b)} \end{pmatrix}, \tag{3.66}$$

with $U_{1,2}^{(1)} \equiv U_{1,2+} \equiv -U_{1,2}^{(4)}$ and $U_{1,2}^{(3)} \equiv U_{1,2-} \equiv -U_{1,2}^{(2)}$. Then, (3.60) yields:

$$\begin{aligned} G = \begin{pmatrix} g_1 & g_2 \\ g_2 & g_3 \end{pmatrix} &= \frac{1}{4} \sum_b \begin{pmatrix} z + U_1^{(b)} - t_1^2 g_1 & V - t_1 t_2 g_2 \\ V - t_1 t_2 g_2 & z + U_2^{(b)} - t_2^2 g_3 \end{pmatrix}^{-1} \\ &= \frac{1}{4} \sum_b \frac{1}{D_b} \begin{pmatrix} z + U_2^{(b)} - t_2^2 g_3 & t_1 t_2 g_2 - V \\ t_1 t_2 g_2 - V & z + U_1^{(b)} - t_1^2 g_1 \end{pmatrix}, \end{aligned} \tag{3.67}$$

with the determinants D_b:

$$D_b = \big(z + U_1^{(b)} - t_1^2 g_1\big)\big(z + U_2^{(b)} - t_2^2 g_2\big) - \big(V - t_1 t_2 g_2\big)\,, \quad b \in (1 \ldots 4)\,. \tag{3.68}$$

The three coupled equations for g_1, g_2 and g_3 have to be solved simultaneously. As the Green function is analytic in the upper half of the complex plane, one needs the root, that behaves as

$$G(z) \sim \frac{1}{z} \begin{pmatrix} 1 & 0 \\ 0 & 1 \end{pmatrix}, \tag{3.69}$$

or

$$g_1(z),\, g_3(z) \sim \tfrac{1}{z}, \quad |g_2(z)| < \mathcal{O}\big(\tfrac{1}{z}\big) \qquad (z \to \infty)\,. \tag{3.70}$$

These criteria are used to single out the correct Green function in the numerical solution of (3.67). This procedure is described in the following section.

3.3.3 Numerical Solution

The coupled equations (3.67) for the Green functions g_1, g_2 and g_3 can be solved using a complex root finding algorithm. As the three Green functions are complex, finding a simultaneous solution is equivalent to finding a root in a 6 dimensional space, which is a difficult task. Normally, root finding mechanisms such as the secant method or the Newton method work sufficiently well only in 1 dimension. Finding the root x_0 of a function $f(x)$ in the region $a-\epsilon \leq x_0 \leq a+\epsilon$ is, however, equivalent to finding the minimum of the function $f(x)^2$ [the value of which is zero].

The Green functions g_1, g_2, and g_3 are computed by minimizing the following functional F:

$$F = F(g_1, g_2, g_3, z; U, V, t) = f_1^2 + f_2^2 + f_3^2 \,. \tag{3.71}$$

Here, f_i is the difference of the left and right site of (3.67) for each g_i; e.g., for $i = 1$:

$$f_1(g_1, g_2, g_3, z; U, V, t) = g_1 - \frac{1}{4}\sum_b \frac{1}{D_b}\big(z + U_2^{(b)} - t_2^2 g_3\big) \,. \tag{3.72}$$

The actual minimization is performed using Powell's direction set method (Press et al., 1992).
Of particular interest is the determination of the local density of states ν_m of the $\downarrow$ electrons in bands $m = (1, 2)$, which are given by:

$$\nu_1(E) = -\frac{1}{\pi}\mathrm{Im}\, g_1(E + i0^+) \,, \quad \text{and} \quad \nu_2(E) = -\frac{1}{\pi}\mathrm{Im}\, g_3(E + i0^+) \,. \tag{3.73}$$

The limit of a vanishing imaginary part $z = x + i0^+$ in the arguments of the Green functions is performed in the following manner for the solution (g_1, g_2, g_3) with interactions (U, V, t):

1. Minimize F for $z = x+iy$ and $y > 0$ (with initial value $y \approx 10$) with the atomic Green function (3.66) for interaction $U_a = 0$ as starting value for (g_1, g_2, g_3).

2. Use the solution of the previous step as input and repeat the minimization, while adiabatically increasing U_a, until $U_a = U$.

3. Decrease the imaginary part y adiabatically, while using the result (g_1, g_2, g_3) of the previous step as input for the new step, until $y = 0$.

By this procedure, the analytic requirement (3.70) for the Green functions can be verified easily for every frequency. A solution (g_1, g_2, g_3) was accepted when the numerical value of F was of the size of the machine-precision.

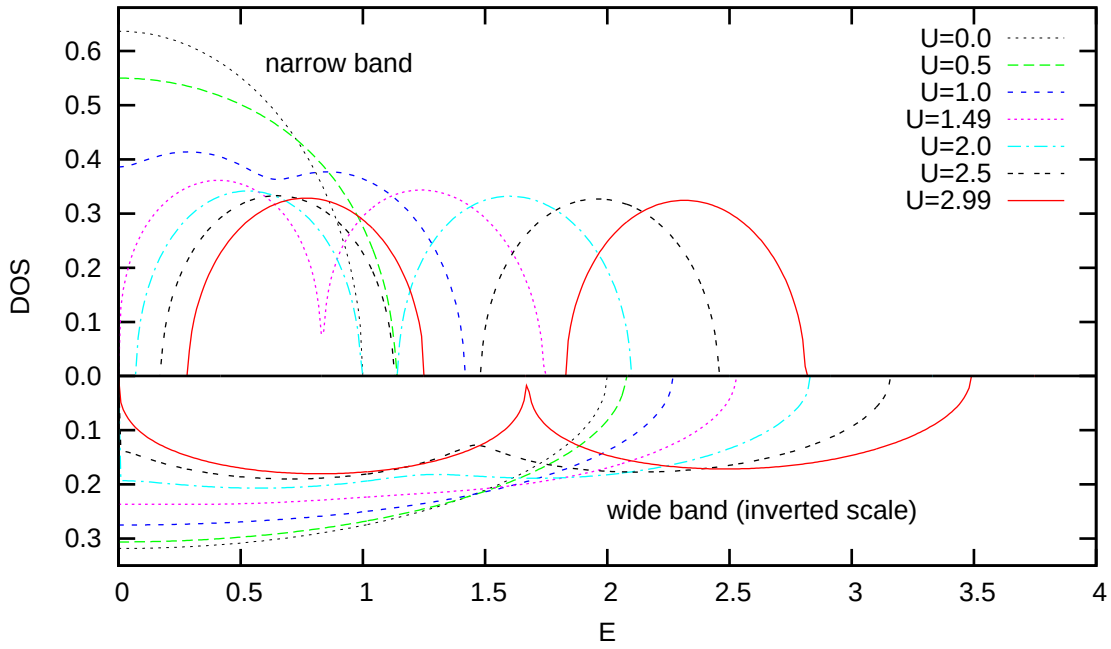

Figure 3.25: Density of states of the two-band Falicov-Kimball model in the high-temperature phase for $U' = \frac{1}{2}U$ and zero hybridization ($V = 0$) for various interactions U. Only positive energies are plotted, since the DOS is symmetric.

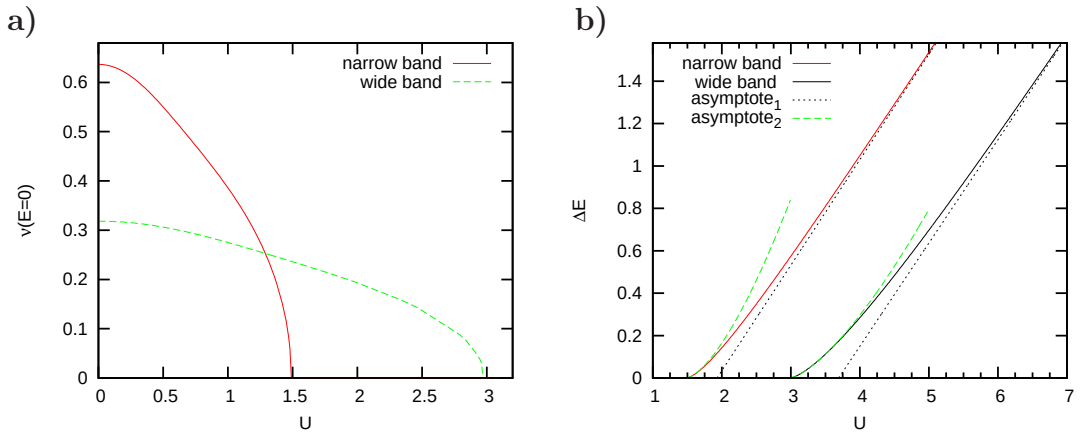

Figure 3.26: a) Density of states at the Fermi edge of the two-band Falicov-Kimball model for $U' = \frac{1}{2}U$ and $V = 0$. **b)** Width of the gap Δ of the narrow and wide band. The line labeled by asymptote$_1$ represents the asymptotic behavior for $U \to \infty$, asymptote$_2$ the behavior for $U \to U_c$. [The small difference in the slope of the asymptote between the narrow and wide orbital is due to finite ΔU-effects when determined from the numerical data.]

3.3.4 Results: FK Model without Hybridization

In this part, the results for the two-band FK model are discussed for different parameters. The ratio of the bandwidth is chosen in analogy to the two-band Hubbard model: $\frac{t_1}{t_2} = 0.5$. The Coulomb interaction between the itinerant $\downarrow$ electrons (d) and the local f-electrons in the same band is set to be equal for the narrow and wide band, thus $U_{1,1} = U_{2,2} \equiv U$. The interorbital Coulomb interaction is scaled in the same way as in the two-band Hubbard model: $U_{1,2} = U_{2,1} \equiv U'$. The hybridization is neglected ($V = 0$) in this section but scaled like $V = \frac{U}{4}$ in Sec. 3.3.5.

The density of states for the two-band FK model without hybridization and for $U' = \frac{1}{2}U$ are shown in Fig. 3.25 for various interactions. For the non-interacting case ($U = 0$), the semi-elliptic density of states of the Bethe lattice is obtained with values $\nu(E=0) = \frac{2}{\pi}\,(\frac{1}{\pi})$ for the narrow (wide) orbital at the Fermi edge ($E = 0$). Upon increasing interaction, the densities of states at the Fermi edge, $\nu(E = 0)$, of both bands start to decrease while the band edges move outward. At the Fermi edge, the DOS remains flat, no quasi-particle peak develops. As expected, the two-band FK model does not exhibit Fermi-liquid behavior, in full analogy to the single-band case.[18] For $U > U_{c1} \approx 1.49$,[19] a gap develops for the narrow orbital: The DOS splits into an upper and lower band. The DOS of the wide orbital, however, is still nonzero at $E = 0$. For $U > U_{c2} \approx 2.99$, a gap also opens for the wide orbital, while the gap of the narrow orbital is already well developed. In summary, the two-band FK model shows for this choice of parameters an OSMT.

Another effect of the interaction is the splitting of the upper and lower band of each orbital: Already for $U = 1$, a dip is clearly seen in the DOS of the narrow orbital. This dip further develops until the band splits into 2 parts at about the same critical interaction $U \approx 1.5$. The upper band of the wide orbital shows the same behavior and splits for $U \approx 3$. Upon further increase of the interaction, the band edges move apart, while the shape of the parts of the DOS remains the same. The splitting of the bands does not occur in the single-band FK model[20] and is therefore attributed to the additional orbital degree of freedom in the two-band model. The fact that the DOS of the narrow (wide) orbital splits into 4 subbands can be explained when

[18] In fact, the two-band FK model with $V = 0$ considered in this section effectively 'is' a single-band FK model. Cf. footnote (19).

[19] The critical interaction can be calculated analytically, provided one assumes that $g_2 = 0$, which indeed yields a consistent solution, but could not be proven rigorously, and, in fact, emerged as a byproduct from the numerical solution in section 3.3.3. It then follows, that $U_{c1} = \frac{2}{3}\sqrt{5} \simeq 1.49$ (van Dongen, 2005). Employing the scaling behavior of the Green functions, $g_3(0;U) = \frac{t_1}{t_2}\, g_1(0;\frac{t_1}{t_2}U)$ (which also follows when assuming $g_2 = 0$), the critical interaction of the wide orbital is determined as $U_{c2} = \frac{t_2}{t_1}U_{c1} = \frac{4}{3}\sqrt{5} \simeq 2.98$. The numerical results are therefore in good agreement with these exact results.

[20] A splitting of the Hubbard bands occurs in the single-band FK model only when also taking nearest-neighbor Coulomb repulsion into account (van Dongen, 1992).

considering the energy that corresponds to hopping processes between singly and doubly occupied sites.[21] The following hopping processes are possible for each, the narrow and the wide orbital, separately:

$$\binom{0}{0} \overset{\frac{1}{2}U}{\longleftrightarrow} \binom{0}{1}, \qquad \binom{0}{0} \overset{U}{\longleftrightarrow} \binom{1}{0}, \qquad \binom{0}{0} \overset{\frac{3}{2}U}{\longleftrightarrow} \binom{1}{1}; \tag{3.74}$$

$$\binom{0}{1} \overset{\frac{1}{2}U}{\longleftrightarrow} \binom{1}{0}, \qquad \binom{0}{1} \overset{U}{\longleftrightarrow} \binom{1}{1}, \qquad \binom{1}{0} \overset{\frac{1}{2}U}{\longleftrightarrow} \binom{1}{1}. \tag{3.75}$$

The upper label in $\binom{1}{0}$ counts the double occupancies in the same orbital (in this case, one site is occupied by one d-electron and one f-electron) and the lower label counts the double-occupancies for different orbitals. The energy-costs of the hopping process is stated in each case. For each band, there are 4 possible configurations for doubly-occupied states, thus the DOS splits into 4 parts for sufficiently large interaction. The centers of the sub-bands are separated by the energy $\frac{1}{2}U$ and as the DOS is symmetric, positioned at $\frac{1}{4}U\,, \frac{3}{4}U$ as well as $-\frac{1}{4}U\,, -\frac{3}{4}U$ for $U \to \infty$. This conclusion is supported by the numerical data: The sub-bands are found to be centered at $E = \pm 0.25U$ and $E = \pm 0.75U$ with constant width 1(2) and height $\frac{1}{\pi}(\frac{1}{2\pi})$ for the narrow (wide) band. The shape is always semi-elliptical. Thus, in the limit $U \to \infty$, the behavior of each sub-band is very similar to the behavior of the Hubbard bands of the single-band FK model. There, it was found, that the Hubbard bands are semi-elliptical and centered at $E = \pm\frac{U}{2}$ with constant width (van Dongen, 1992).

The behavior of the DOS at the Fermi edge, $\nu(E = 0)$, is shown in Fig. 3.26 a. The decrease of $\nu(E = 0)$ is very small as the interaction is gradually turned on and reaches its maximum when the gap opens at the critical interactions $U_{c1} = 1.49 \pm 0.01$ ($U_{c2} = 2.99 \pm 0.01$) for the narrow (wide) orbital. The OSMT is clearly exposed. A criterion that can be used to determine the order of the metal-insulator transition is the width ΔE of the gap centered at $E = 0$. The width ΔE is plotted in Fig. 3.26 b for the narrow and wide orbital. The numerical data indicates that the gap vanishes continuously as a function of U for both orbitals. The functional dependence for $U \to U_c$ is well described by the function $\Delta \sim d\,(U - U_c)^\alpha$ with a critical exponent $\alpha = 1.50 \pm 0.11$ (1.44 ± 0.07) of the narrow (wide) band and with constant $d = 0.45 \pm 0.12$ (0.28 ± 0.04). The critical exponent is therefore equivalent to the single-band case, which exhibits a second-order transition at U_c with $\Delta \sim \frac{4}{3\sqrt{3}}(U - U_c)^{3/2}$ for $U \to U_c$ (van Dongen, 1992). For $U \to \infty$, the width ΔE of the gap is linear in the interaction: $\Delta E(U) \sim 0.5\,U$, for both bands, in analogy to the single-band case (van Dongen, 1992).

[21] This scenario corresponds to taking the strong-coupling limit.

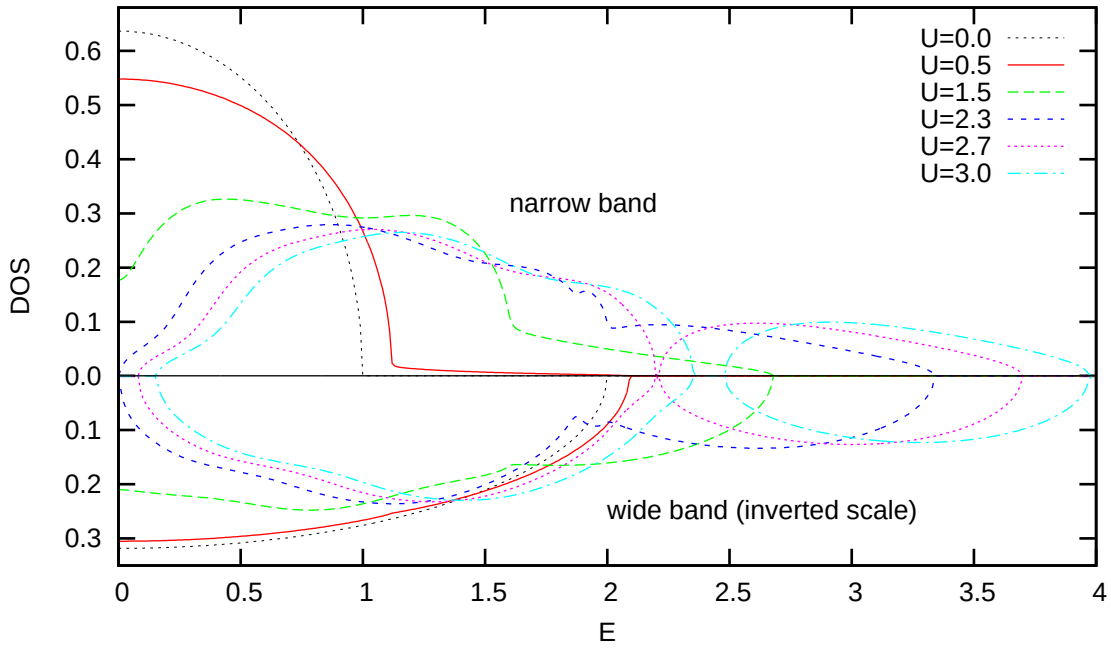

Figure 3.27: Density of states of the two-band Falicov-Kimball model in the high-temperature phase for $U' = \frac{1}{2}U$ and hybridization $V = \frac{1}{4}U$ for various interactions U.

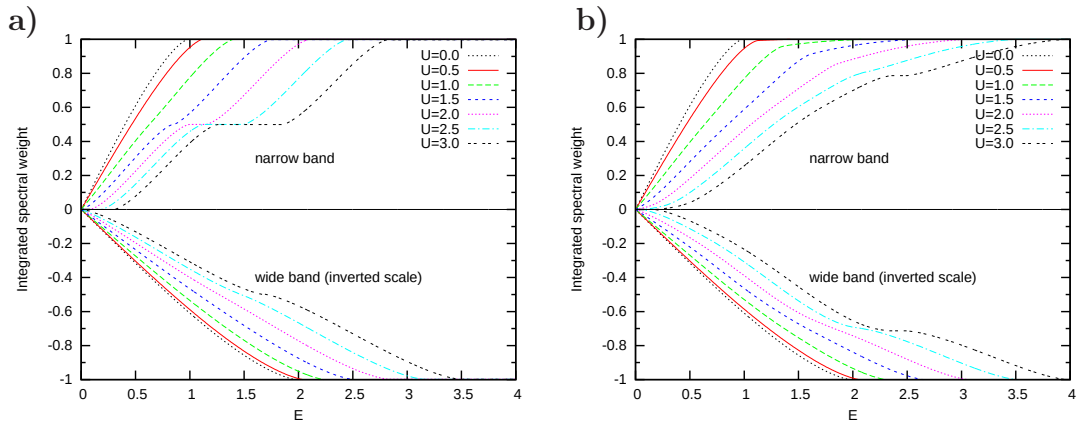

Figure 3.28: **a)** Integrated spectral weight for $U' = \frac{1}{2}U$, and $V = 0$. **b)** Integrated spectral weight for $U' = \frac{1}{2}U$ and hybridization $V = \frac{1}{4}U$.

3.3.5 Results: FK Model with Hybridization

The DOS of the two-band FK model for parameters $U' = \frac{1}{2}U$ and hybridization $V = \frac{1}{4}U$ is plotted in Fig. 3.27. The DOS at the Fermi edge, $\nu(E=0)$, decreases as the interaction is turned on, but stays flat at the Fermi edge. This behavior is similar to the FK model with vanishing hybridization. The influence of the hybridization, however, can be seen already for $U = 0.5$: The singularity at the band edge of the narrow orbital is lifted and the band edge stretches out, up to the band edge of the wide orbital. This effect is more pronounced for larger interactions. Furthermore, the gap of both bands develops for the same interaction $U_c \approx 2.3$; thus, only a single Mott transition takes place. The numerical results suggest a transition of second order, similar to the case with vanishing hybridization. The bands of both orbitals also split. The critical interaction of the splitting, however, does not coincide with U_c anymore, but is increased: $U_{c2} \approx 2.7$. Additionally, the shape of the upper and lower part of the split DOS is not the same (or similar) anymore. More spectral weight remains in the lower part.

The influence of the hybridization on the distribution of the spectral weight $\int_{-E}^{E} \nu(E')\,dE'$ is depicted in Fig. 3.28. For simplicity, the parts of the DOS are referred to as the lower and upper subband with respect to the energy of their center. For $V = 0$ **(a)**, the spectral weight is equally distributed between the lower and upper subband for all interactions. The splitting of the DOS is indicated by the flat part, which appears for $U > U_c$ always at a spectral weight of 0.5. For finite hybridization **(b)**, about 80% (70%) of the spectral weight of the narrow (wide) orbital is located in the lower subband. Once the DOS has split, the distribution of the spectral weights remains constant (at least within the numerical precision).

3.3.6 Discussion

In this section, a simplified two-band Hubbard model (Falicov-Kimball model) with bandwidth ratio $\frac{W_2}{W_1} = 2$, where only the spin-down electrons of each band can move, was considered on a Bethe lattice in high dimensions ($Z \to \infty$). The model was solved in the high-temperature phase in analogy to the single-band Falicov-Kimball model using an exact mean-field theory (van Dongen and Vollhardt, 1990). The main result of this part is that the two-band FK model exhibits an OSMT for $V = 0$ [and for parameters that are scaled similar to the ones used for the J_z-model in the first part of this chapter]. In this case, the Green functions of the two orbitals (g_1 and g_2) are scaled, such that the two-band FK model reduces to an effective single-band model. As expected, the OSM phase ceases to exist for finite hybridization ($V > 0$).

It is instructive to compare the OSM phase of the two-band FK model and the J_z-model. The critical interaction of the FK model, $U_{c1}^{\mathrm{FK}} \simeq 1.49$, for which the narrow band becomes insulating is smaller than the critical interaction $U_{c1}^{J_z} \simeq 2.01$

of the J_z-model. This is, however, not the case for the transition of the wide band: $U_{c2}^{\mathrm{FK}} \simeq 2.99 \longleftrightarrow U_{c2}^{J_z} \simeq 2.5$. The width of the OSM phase is therefore of about a factor 3 larger in the simplified model, whereas the position of the center of the OSM phases is similar and about at $U \approx 2.25$. Also, the behavior of the spectral density of the wide bands close to the Fermi edge [Fig. 3.25 for the FK model and Fig. 3.12 for the J_z-model] is similar, emphasizing the fact that the wide band in the OSM phase of the J_z-model is metallic, but not a Fermi-liquid.[22] A similar behavior was found by Biermann et al. (2005) for a simplified two-band Hubbard model where the interorbital Coulomb interaction U' is neglected in order to retain the intraorbital interaction U of the itinerant electrons of the wide band. The itinerant electrons further couple to the localized electrons in the narrow band through Ising terms only. The resulting effective single-band Hubbard model was then solved within the DMFT+QMC, by additionally averaging over the Ising spin configurations of the localized electrons. The authors observed non-Fermi-liquid behavior similar to the one of the single-band Falicov-Kimball model (Si et al., 1992), namely the following low-frequency form of the self-energy: $\Sigma(\omega + i0^+) = -i\Gamma + (1 - \frac{1}{Z})\,\omega$, with $\Gamma > 0$. It is interesting to note, that a similar behavior was found for the self-energy Σ_{wide} of the J_z-model in section 3.2.1 within the OSM phase.

Another important issue concerns the order of the metal-insulator transitions in the FK model. Within both the numerical solution and the exact solution (van Dongen, 2005) one observes a smooth vanishing of the width of the gap as a function of U (for $V = 0$), corresponding to a second-order transition and in analogy to the single-band FK model. A similar behavior is found for the wide band of the J_z-model [at least within the examined parameter set of the first part of this chapter and for high temperatures].

A major difference in the spectra of the FK model and the J_z-model, however, is the behavior at intermediate to large couplings, namely the splitting of the DOS of each orbital of the two-band FK model into 4 parts which exactly occurs at the critical interaction $U_{c1,2}$.[23] Even though the spectrum of the wide band of the J_z-model shows indications of a splitting for $U \approx U_{c2}$ [cf. Fig. 3.12], the Hubbard shoulders retain a semi-elliptic shape in the strong-coupling limit, similar to the single-band model (van Dongen, 2005).

The above findings support, that essential features of the paramagnetic OSM phase of the anisotropic two-band Hubbard model are already captured by a Falicov-Kimball model. This observation is encouraging: The FK model might also give insight into the physics of the OSM regime of the J_z-model in the important low-temperature limit $T \to 0$ and also for lower spatial dimensions, e.g., in $d = 2$.

[22] Note, that the FK model shows non-Fermi-liquid behavior in $d = \infty$ (Si et al., 1992).

[23] In the limit $U \to \infty$, the centers of the 4 semi-elliptic parts are located near $U = \pm\frac{1}{2}(U_{11} \pm U_{12})$ for the first orbital and near $U = \pm\frac{1}{2}(U_{21} \pm U_{22})$ for the second orbital.

Both models have the same magnetically ordered ground state (AF), but numerical calculations are much easier performed in the FK model.

3.4 Summary

In the first part of this chapter, the anisotropic two-band Hubbard model (J_z-model) with distinct band widths $W_2 = 2W_1$ was studied within the DMFT+QMC in the fully frustrated phase at finite temperatures. The interaction parameters were scaled as $U = U' + 2J_z$, implying rotational invariance of the Hamiltonian (Castellani et al., 1978). Using the high-precision QMC algorithm, which was developed as part of this thesis, it was shown, that the J_z-model contains two successive metal-insulator transitions. This finding revises earlier QMC results (Liebsch, 2003*b*; Liebsch, 2004) that reported the existence of only one single Mott transition at low temperatures in the J_z-model, i.e., that the transitions which occur in the separate orbitals merge upon unison. Thus, the additional spin-flip and pair hopping terms that arise in the J-model, which clearly exhibits an OSMT (Koga et al., 2004; Koga et al., 2005*a*; Ferrero et al., 2005; de' Medici et al., 2005; Arita and Held, 2005; Koga et al., 2005*b*), are not a prerequisite for the existence of two distinct transitions as suggested in Ref. Koga et al. (2005*a*). Hence, the J_z-model can be considered as a minimal model for the OSMT phenomenon. The transitions at $U_{c1} \approx 2.01$ and $U_{c2} \approx 2.5$ were revealed by the low-frequency behavior of the self-energy, but are also visible in the spectral functions, the intra-orbital double occupancies, the quasiparticle weights and their temperature dependence as well as in the internal energy and its composites the kinetic and potential energy.

The transition of the first (narrow) band of the J_z-model is found to be of first order at U_{c1} with a critical temperature $T_{c1} \approx 0.02$. The physical observables like the quasiparticle weight or the double occupancy of the second (wide) band, in contrast, are continuous at U_{c2}, as expected for a second-order transition. The order of the second transition, however, cannot be determined definitely within this work. This is due to the fact that the QMC calculations are at present difficult to perform in the relevant low-temperature regime [recall, that the computational costs scale like $m(2m-1)L^3$] and also because it is numerically difficult to distinguish a real second-order transition at $T > 0$ from a narrow cross-over, possibly eradiating from a $T = 0$ quantum critical point.

It was further found, that the wide band exhibits non-Fermi-liquid behavior within the OSM phase, which is seen in the low-frequency behavior of the self-energy and also in the spectral function close to the Fermi edge. At low energies, the OSM phase is characterized by itinerant electrons in the wide band and quasi fully localized electrons in the narrow band, and is therefore closely related to the physics of the Falicov-Kimball model, which is known not only to exhibit non-Fermi-liquid behavior but also a second-order metal-insulator transition. The results of the analogy to the FK model, which was studied in the second part of this chapter, are summarized below.

It is also shown, that the high-frequency corrected QMC simulation, as developed

in chapter 2 of this thesis, gives very accurate solutions of the DMFT self-consistency equations also for multi-band systems [at half filling]. This is seen, e.g., in the comparison of the QMC estimates of the internal energy (energy per lattice site) at weak coupling with exact results, which were derived within second-order perturbation theory. The second transition of the wide band is further visible only in high-quality QMC data. This fact is clearly exposed by a comparison of the QMC data of this work with results of competing QMC methods used in the literature (Liebsch, 2004).

Another aspect of this chapter was the determination of the magnetic phase diagram of the J_z-model. The phase boundary between the paramagnetic high-temperature phase and the antiferromagnetically ordered ground state was determined within a QMC simulation. The vanishing of the inverse of the staggered magnetization χ_{st} [implying a second-order transition] served as criterion for the determination of the Néel temperature T_N. Other magnetically ordered phases, which would be signalled by the divergence of the associate susceptibility, were not found. These include ferromagnetic order, orbital order, combined ferromagnetic and orbital order and charge density waves. At weak coupling, the QMC estimates for T_N are found to agree well with the results of 2OPT (van Dongen, 2005), but differ substantially from first-order strong-coupling results (van Dongen, 2005) at large values of the interaction: The magnetic phase diagram seems to be governed by the thermodynamics of the narrow band. It is further found in a simulation allowing for AF order that the OSM phase is hidden deep inside the symmetry-broken phase of the J_z-model: The critical temperature $T_{c1} \approx 0.02$ is about a factor of 6 smaller than the Néel temperature at the same interaction. In addition, the MIT of the narrow band is shifted towards smaller values of the interactions compared to a decoupled band of equal width, which is clearly due to the additional interorbital interaction.

It was subsequently studied how the Néel temperature can be suppressed (partial frustration) upon variation of the interaction parameters. The results of 2OPT suggest that T_N cannot be diminished sufficiently by only varying the interaction parameters while keeping the scaling relation $U = U' + 2J$, which was imposed in order to demand rotational invariance of the Hamiltonian [which the OSMT compound $Ca_{2-x}Sr_xRuO_4$, in contrast, does not exhibit]. It is therefore expected, that the AF phase of the J_z-model can only be sufficiently suppressed by abandoning rotational invariance of the Hamiltonian and imposing additional frustration, which occurs, e.g., upon introduction of longer-range hopping or disorder, but also in lower dimensions.

In the second part of this chapter, a two-band Falicov-Kimball (FK) model with bandwidth ratio $W_2 = 2W_1$ was studied in the limit of infinite dimension on the Bethe lattice in the high-temperature phase. The considered FK model is a simplified version of the J_z-model in which only the spin down electrons of each orbital are allowed to hop [with hopping amplitudes $t_2 = 2t_1$] and where the spin up electrons are taken to be fully localized. In analogy to the J_z-model, the spins are conserved due to the absence of spin flip terms. When considering the full Hund's rule coupling, one has

to additionally include spin flip and pair exchange terms. In this case, the model maps within the DMFT to a Kondo impurity problem with a self-consistent conduction electron bath. The FK model can be solved within the exact mean-field theory as proposed by van Dongen and Vollhardt (1990), resulting in a self-consistency equation for the local Green functions. It turned out, that this self-consistency equation can be solved both numerically and analytically for vanishing hybridization V, but only numerically for $V \neq 0$. For $V = 0$, the Green functions of each band further scale with the ratio of the bandwidth, such that the problem effectively reduces to a single-band model. The main result, however, is the fact that the FK model exhibits an OSMT in the absence of hybridization. For the parameter set ($U' = \frac{U}{2}$, $V = 0$), the critical interactions are found to be $U_c \approx 1.49\,(2.99)$ for the narrow (wide) band. The metal-insulator transition is found to be of second order. In contrast to the single-band FK model, each of the bands split at the critical interaction U_c into four parts with semi-elliptical shape and equally distributed weights. Those parts retain their shape in the strong-coupling limit ($U \to \infty$) and are equally separated near $U = \pm\frac{1}{2}(U_{11} \pm U_{12})$ for the first orbital and near $U = \pm\frac{1}{2}(U_{21} \pm U_{22})$ for the second orbital.

It is also found, that the OSM phase ceases to exist when switching on a finite hybridization V [studied for parameters ($U' = \frac{U}{2}$, $V = \frac{U}{4}$)]. The single Mott transition takes then place at $U_c \approx 2.3$. The splitting of the upper and lower Hubbard shoulder now occurs at a slightly larger energy ($U_{c2} \approx 2.7$). Also, the spectral weight is not equally distributed anymore; the fraction of the DOS at lower energies accumulates more spectral weight than the one at higher energies. Also, the shape of the DOS differs significantly from the case without hybridization.

In summary, an important part of the low-energy physics of the OSM phase of the fully frustrated J_z-model is determined already by the physics of the Falicov-Kimball model in its high-temperature phase.

Chapter 4

The Attractive Hubbard Model at weak Coupling

In this chapter, we study the attractive (or negative-U) Hubbard model[1] away from half filling within second-order self-consistent (sc) perturbation theory in two spatial dimensions at weak coupling.

The negative-U Hubbard model[2] in $d = 2$ has been the subject of intense study (Micnas et al., 1990). At half filling, the ground state is an antiferromagnetic insulator (Hirsch, 1985; White et al., 1989); the spectrum is therefore gapped. As the Mermin-Wagner theorem excludes any long-range order at finite temperature, one expects the opening of a critical-fluctuation-induced pseudogap [or precursor pseudogap (Kampf and Schrieffer, 1990)] as the temperature is lowered. The existence of the precursor pseudogap, however, is still a matter of controversy, not only in the doped case but also at half filling (Moukouri et al., 2000; Huscroft et al., 2001; Sénéchal and Tremblay, 2004; Rohe and Metzner, 2005). The numerical analysis of perturbative (Inui and Littlewood, 1991) and nonperturbative results (Huscroft et al., 2001) concern mostly the half-filled case. Close to half filling, the Hubbard model exhibits complicated behavior due to the mutual interplay of singularities in the particle-particle and particle-hole channels. A systematic method for the study of this interplay, which cannot be captured by a simple resummation of Feynman diagrams, is given by the recently developed functional renormalization group for interacting Fermi systems (Salmhofer, 1998).

Analytical investigations of the Hubbard model in $d = 2$ were performed in the weak- (Schulz, 1990; Martín-Rodero and Flores, 1992) and strong-coupling limits

[1] The attractive Hubbard model is in particular relevant in the context of superconductivity where it represents one of the simplest phenomenological Hamiltonians for the study of superconductivity through local pairing (Micnas et al., 1990). Compare also Sec. 1.3 on page 8.

[2] Here, the results for the positive-U Hubbard model are also relevant for the negative-U model since they are connected by a special particle-hole transformation (Emery, 1976).

(van Dongen, 1994*c*). At strong coupling, the half-filled Hubbard model maps to an effective Heisenberg model, for which the estimates of the Néel temperature and the ground state energy are reliably known. Several methods have been proposed for the weak- to intermediate-coupling regime (Kakehashi and Hasegawa, 1988; Vilk et al., 1994; Cyrot and Kaga, 1996; Szczech et al., 1995), many of which also apply to $d = 3$. The estimates for the Néel temperature of these approaches in $d = 3$ all reduce to the Hartree-Fock result at weak-coupling. The Hartree-Fock approximation, however, overestimates the critical temperature (and similarly the order parameters) by a renormalization factor, as is known from DMFT-studies including $1/d$-corrections (van Dongen, 1991; van Dongen, 1994*a*) and the local approximation (Tahvildar-Zadeh et al., 1997). The precise value of this factor in $d = 3$ was calculated by Schauerte and van Dongen (2002) using self-consistent perturbation theory. The authors also found that sc perturbation theory diverges for the half-filled Hubbard model in $d \leq 2$. Asymptotically exact results in the weak-coupling limit for finite doping, however, are as yet unknown.

The main focus of this chapter is to study the broken-symmetry phase of the negative-U Hubbard model away from half filling and at weak-coupling beyond the mean-field approximation. As the Hubbard model is nonperturbative even at weak-coupling, one has to apply self-consistent theories. As sc perturbation theory breaks down exactly at half-filling (Schauerte and van Dongen, 2002; Kopietz, 1993), we focus especially on dopings which are not close to half-filling.

In a first step, we review the Hartree-Fock solution of the negative-U Hubbard model which is equivalent to first-order sc perturbation theory. We then calculate the second-order correction term. In particular, we present asymptotically exact results for the critical temperature and the superconducting order parameter. As a main result we find that the HF order parameter and HF critical temperature are renormalized by a factor q which is of the order of unity and depends explicitly on the chemical potential. In the limit of an empty system, we find that perturbation theory breaks down.

The calculations are actually performed for the positive-U Hubbard model (compare Sec. 1.3) at half filling subject to a uniform magnetic field, onto which the negative-U model away from half-filling can be mapped by a special particle-hole transformation (Robaszkiewicz et al., 1981*a*). The relation between these two models is most easily expressed in terms of the chemical potential μ and the magnetic field B. At half-filling, the chemical potential in the model ($U > 0, B > 0$) is exactly $\mu_> = U/2$. Then, $\mu_<$ in the model ($U < 0, B = 0$) reads (see Appendix A.1)

$$\mu_< = -\frac{U}{2} - B\,. \tag{4.1}$$

The correspondence of the physical quantities in the two models is summarized in table 4.1. There are various ways to impose self-consistency of the perturbation

	$(U<0, B=0, n\neq 1)$		$(U>0, B>0, n=1)$
μ	$-\frac{U}{2}-B$	$\Longleftrightarrow$	$\frac{U}{2}$
order type	$-2\chi_0=-\frac{2}{\mathcal{N}}\sum_{\boldsymbol{i}}\langle c^\dagger_{\boldsymbol{i}\uparrow}c^\dagger_{\boldsymbol{i}\downarrow}\rangle$ (superconducting order)	$\Longleftrightarrow$	$m_x=2(-1)^{\boldsymbol{i}}\langle c^\dagger_{\boldsymbol{i}\uparrow}c_{\boldsymbol{i}\downarrow}\rangle$ (staggered magnetization)
	$1-n$ (doping)	$\Longleftrightarrow$	$m_z=2\langle \boldsymbol{S}^z_{\boldsymbol{i}}\rangle$ (homogeneous magnetization)

Table 4.1: Correspondence between electronic orderings of the negative-U Hubbard model away from half filling, $(U<0, B=0, n\neq 1)$, and the attractive Hubbard model within a uniform magnetic field B at half filling , $(U>0, B>0, n=1)$.

expansion [compare Sec. 1.7]. In this chapter we use the self-consistent perturbation theory at fixed order parameter (PTFO) (Georges and Yedidia, 1991; van Dongen, 1994*a*).

The chapter is organized as follows. In Sec. 4.1 we solve the Hubbard model in a uniform magnetic field within first-order self-consistent perturbation theory. In subsection 4.1.3 we show that these results are equivalent to the HF approximation. The asymptotic results for small U are derived in Appendix D.2. The second-order corrections are subsequently calculated in Sec. 4.2. Many of the rather cumbersome calculations are included in Appendix D.3, D.4 and D.5. It is then shown in Sec. 4.3 that the second-order corrections lead to an renormalization of the HF results. The findings of this chapter are discussed in Sec. 4.4. Finally, a summary and outlook is given in Sec. 4.5.

4.1 First-order Perturbation Theory

We assume a homogeneous magnetization m_z in the z-direction and a staggered magnetization m_x in the x-direction. Then, the grand canonical Hamiltonian of the Hubbard model with two additional Lagrange parameters to keep m_z and m_x fixed has the form:

$$\begin{aligned} K =& H_t + H_U + H_B + \mu\Big[N - \sum_{\boldsymbol{i}\sigma} n_{\boldsymbol{i}\sigma}\Big] \\ &+ h^x(U)\Big[\mathcal{N}m_x - 2\sum_{\boldsymbol{i}}(-1)^{\boldsymbol{i}}\boldsymbol{S}^x_{\boldsymbol{i}}\Big] + h^z(U)\Big[\mathcal{N}m_z - 2\sum_{\boldsymbol{i}}\boldsymbol{S}^z_{\boldsymbol{i}}\Big], \end{aligned} \tag{4.2}$$

with the number of lattice sites $\mathcal{N}$ and the total number of particles N. At half filling we have $\mathcal{N} = N$. Here, H_t and H_U are defined in (1.1) and the term H_B introduces a homogeneous (Zeeman) magnetic field in the z-direction:

$$H_B = -B \sum_{\boldsymbol{i}\sigma} \sigma n_{\boldsymbol{i}\sigma} \,. \tag{4.3}$$

The fields $h^z(U)$ and $h^x(U)$ are the Lagrange multipliers for the homogenous and the staggered magnetization, respectively. Within PTFO, they are both expanded in powers of the interaction U, according to

$$\begin{aligned} h^x(U) &= h_0^x(m_z, m_x) + h_1^x(m_z, m_x)\, U + h_2^x(m_z, m_x)\, U^2 + \cdots \\ &\equiv h_0^x + h_1^x U + h_2^x U^2 + \cdots \,, \end{aligned} \tag{4.4}$$

and

$$\begin{aligned} B + h^z(U) &= h_0^z(m_z, m_x) + h_1^z(m_z, m_x) U + h_2^z(m_z, m_x) U^2 + \cdots \\ &\equiv h_0^z + h_1^z U + h_2^z U^2 + \cdots \,. \end{aligned} \tag{4.5}$$

As we focus on the half-filled band ($n = 1$), the chemical potential is exactly given by $\mu(U) = \frac{1}{2}U$, implying $\mu_0 = 0$. At half filling, we define the homogenous magnetization m_z by

$$\langle n_{\boldsymbol{i}\sigma} \rangle = \frac{1}{2}(1 + \sigma m_z) \,. \tag{4.6}$$

The staggered magnetization m_x in x-direction is given by

$$\langle \boldsymbol{S}_{\boldsymbol{i}}^x \rangle = \frac{1}{2}(-1)^{\boldsymbol{i}} m_x \equiv \frac{1}{2} \lambda_{\boldsymbol{i}} m_x \,. \tag{4.7}$$

Here,

$$\boldsymbol{S}_{\boldsymbol{i}}^{x,y,z} = \frac{1}{2} \sum_{\alpha\gamma} c_{\boldsymbol{i}\alpha}^\dagger \sigma_{\alpha\gamma}^{x,y,z} c_{\boldsymbol{i}\gamma} \tag{4.8}$$

are the spin operators with the Pauli matrices σ^x, σ^y and σ^z with spin index α and γ. Note, $m_z = 2\langle \boldsymbol{S}_{\boldsymbol{i}}^z \rangle$. In a first step, the Hamiltonian (4.2) is split up into an exactly solvable (U-independent) part K_0 and the perturbation K_1:

$$K = K_0 + K_1 \,, \tag{4.9}$$

with

$$K_0 = H_t + H_B + h_0^x \Big[\mathcal{N} m_x - 2 \sum_{\boldsymbol{i}} \lambda_{\boldsymbol{i}} \boldsymbol{S}_{\boldsymbol{i}}^x \Big] + h_0^z \Big[\mathcal{N} m_z - 2 \sum_{\boldsymbol{i}} \boldsymbol{S}_{\boldsymbol{i}}^z \Big] \,, \tag{4.10}$$

and

$$K_1 = H_U + \frac{U}{2}\Big[\mathcal{N} - \sum_{i\sigma} n_{i\sigma}\Big] + [h^x(U) - h_0^x]\Big[\mathcal{N}m_x - 2\sum_i \lambda_i \boldsymbol{S}_i^x\Big] + [h^z(U) - h_0^z]\Big[\mathcal{N}m_z - 2\sum_i \boldsymbol{S}_i^z\Big]\,. \tag{4.11}$$

In order to diagonalize K_0, we Fourier transform the c_j particles into momentum space, using the relation

$$c_{j\sigma} = \frac{1}{\sqrt{\mathcal{N}}}\sum_{\boldsymbol{k}} c_{\boldsymbol{k}\sigma} e^{i\boldsymbol{k}\cdot\boldsymbol{j}}\,, \tag{4.12}$$

where $\boldsymbol{k}$ is defined in the Brillouin zone. The resulting Hamiltonian is then diagonalized by a canonical transformation $c_{\boldsymbol{k}\sigma} \to d_{\boldsymbol{k}\sigma}$ of the form

$$c_{\boldsymbol{k}\sigma} = a_{\boldsymbol{k}\sigma} d_{\boldsymbol{k}\sigma} + b_{\boldsymbol{k}\sigma} d_{\boldsymbol{k}-\boldsymbol{Q},-\sigma}\,. \tag{4.13}$$

The real numbers $a_{\boldsymbol{k}\sigma}$ and $b_{\boldsymbol{k}\sigma}$ are given by

$$a_{\boldsymbol{k}\sigma} = \sqrt{\frac{\eta_{\boldsymbol{k}\sigma} + \epsilon_{\boldsymbol{k}\sigma}}{2\eta_{\boldsymbol{k}\sigma}}}\,, \quad b_{\boldsymbol{k}\sigma} = \mathrm{sign}(\epsilon_{\boldsymbol{k}\sigma})\sqrt{\frac{\eta_{\boldsymbol{k}\sigma} - \epsilon_{\boldsymbol{k}\sigma}}{2\eta_{\boldsymbol{k}\sigma}}}\,, \tag{4.14}$$

and

$$\eta_{\boldsymbol{k}\sigma} = \mathrm{sign}(\epsilon_{\boldsymbol{k}\sigma})\sqrt{\epsilon_{\boldsymbol{k}\sigma}^2 + h_0^{x\,2}}\,. \tag{4.15}$$

Here, $\epsilon_{\boldsymbol{k}\sigma} = \epsilon_{\boldsymbol{k}} - \sigma h_0 = \epsilon_{\boldsymbol{k}} - \sigma(B + h_0^z)$, with the dispersion of the square lattice in $d = 2$, $\epsilon_{\boldsymbol{k}} = -2t\sum_{l=1,2}\cos(k_l)$, for $U = 0$, and the nesting vector $\boldsymbol{Q} = (\pi, \pi)$. Finally, K_0 is diagonal in terms of the $d_{\boldsymbol{k}\sigma}$ operators:

$$K_0 = \sum_{\boldsymbol{k}\sigma} \eta_{\boldsymbol{k}\sigma}\nu_{\boldsymbol{k}\sigma} + \mathcal{N}(h_0^x m_x + h_0^z m_z)\,, \tag{4.16}$$

where $\nu_{\boldsymbol{k}\sigma} = d_{\boldsymbol{k}\sigma}^\dagger d_{\boldsymbol{k}\sigma}$ is the number operator of the new $d_{\boldsymbol{k}\sigma}$ particles.

4.1.1 Self-Consistency Relations and Green Functions

The self-consistency relations between the field h_0^z and the magnetization m_z, as well as between h_0^x and m_x, are obtained from

$$m_x = \frac{2}{\mathcal{N}}\sum_i \lambda_i \langle c_{i\uparrow}^\dagger c_{i\downarrow}\rangle = h_0^x \int_{-\infty}^{\infty} d\epsilon\, N_d(\epsilon)\frac{1}{\eta_{\epsilon_\uparrow}}\tanh\big(\tfrac{1}{2}\beta\eta_{\epsilon_\uparrow}\big)\,, \tag{4.17}$$

and

$$m_z = -2G_{\mathbf{0}\uparrow}(0) - 1 = -\int_{-\infty}^{\infty} d\epsilon\, N_d(\epsilon) \frac{\epsilon_\uparrow}{\eta_{\epsilon_\uparrow}} \tanh\left(\tfrac{1}{2}\beta\eta_{\epsilon_\uparrow}\right), \tag{4.18}$$

with $G_{\boldsymbol{i}\uparrow}(0) = -\langle n_{\boldsymbol{i}\uparrow}\rangle$ and $\epsilon_\uparrow = \epsilon - h_0$. As the above relations are valid for arbitrary dimension d, we supplement the density of states, N_d, with a suffix. Explicit expressions for the hypercubic density of states exist only in $d = 1, 2$ [see, Appendix D.1]. The Green function in (4.18) of the $c_{\boldsymbol{i}\sigma}$ particles (in position space) is defined by

$$G_{\boldsymbol{l}\sigma}(\tau - \tau') \equiv \langle T_\tau c_{\boldsymbol{j}+\boldsymbol{l},\sigma}(\tau) c^\dagger_{\boldsymbol{j}\sigma}(\tau')\rangle, \tag{4.19}$$

with the time ordering operator T_τ. It can be expressed in terms of the Green functions $g_{\boldsymbol{k}\sigma}(\tau)$ of the new particles $d_{\boldsymbol{k}\sigma}$, which is known because the Hamiltonian (4.16) is diagonal (Negele and Orland, 1987):

$$\langle T_\tau d_{\boldsymbol{k}\sigma}(\tau) d^\dagger_{\boldsymbol{k}'\sigma'}(\tau')\rangle = \delta_{\boldsymbol{k}\boldsymbol{k}'}\delta_{\sigma\sigma'} g_{\boldsymbol{k}\sigma}(\tau - \tau'), \tag{4.20}$$

where

$$g_{\boldsymbol{k}\sigma}(\tau) = e^{-\eta_{k\sigma}\tau}\left[\Theta(\tau - 0^+)(1 - \langle\nu_{\boldsymbol{k}\sigma}\rangle) - \Theta(0^+ - \tau)\langle\nu_{\boldsymbol{k}\sigma}\rangle\right] \tag{4.21}$$

and the step function Θ. One thus finds

$$G_{\boldsymbol{l}\sigma}(\tau) = \frac{1}{\mathcal{N}} \sum_{\boldsymbol{k}} e^{i\boldsymbol{k}\cdot\boldsymbol{l}} \left[a^2_{\boldsymbol{k}\sigma} g_{\boldsymbol{k}\sigma}(\tau) + b^2_{\boldsymbol{k}\sigma} g_{\boldsymbol{k}-\boldsymbol{Q},-\sigma}(\tau)\right], \tag{4.22}$$

resulting in the self-consistency relation (4.18). Eq. (4.17) is obtained along similar lines. In the limit $T \to 0$, the self-consistency equations simplify to

$$m_x(T = 0) = h_0^x \int_{-\infty}^{\infty} d\epsilon\, \frac{N_d(\epsilon)}{|\eta_{\epsilon_\uparrow}|}, \tag{4.23}$$

and

$$m_z(T = 0) = -\int_{-\infty}^{\infty} d\epsilon\, \frac{\epsilon_\uparrow N_d(\epsilon)}{|\eta_{\epsilon_\uparrow}|}. \tag{4.24}$$

4.1.2 Calculation of the Free Energy

The thermodynamic results to zeroth order in the interaction U immediately follow from the definition of the free energy f_0 per lattice site:

$$e^{-\mathcal{N}\beta f_0} = Z_0 = \operatorname{Tr} e^{-\beta K_0}, \tag{4.25}$$

where Z_0 is the non-interacting partition function. Using the average number of the $d_{\boldsymbol{k}\sigma}$ particles, $\langle \nu_{\boldsymbol{k}\sigma} \rangle = (e^{\beta\eta_{\boldsymbol{k}\sigma}} + 1)^{-1}$, one finds

$$\begin{aligned} f_0 &= h_0^x m_x + h_0^z m_z - \frac{1}{\mathcal{N}\beta} \sum_{\boldsymbol{k}\sigma} \ln\bigl(1 + e^{-\beta\eta_{\boldsymbol{k}\sigma}}\bigr) \\ &= h_0^x m_x + h_0^z m_z - \frac{2}{\beta} \int_{-\infty}^{\infty} d\epsilon \, N_d(\epsilon \pm h_0) \ln\bigl[2\cosh(\tfrac{1}{2}\beta\eta_\epsilon)\bigr] \,, \end{aligned} \tag{4.26}$$

where the sign in the density $N_d(\epsilon \pm h_0)$ can be chosen freely. We recall that η_ϵ is defined as $\eta_\epsilon = \mathrm{sign}(\epsilon)\sqrt{\epsilon^2 + h_0^{x\,2}}$. The optimization of f_0 obviously shows no magnetization, which is due to the fact that K_0 is a noninteracting system.

In order to calculate the first-order contribution to the free energy, f_1, the series expansions of the fields h_x and h_z [(4.4) and (4.5)] are truncated already after the first-order term:

$$K_1 = H_U + \frac{U}{2}\Bigl[\mathcal{N} - \sum_{i\sigma} n_{i\sigma}\Bigr] + h_1^x U\Bigl[\mathcal{N} m_x - 2\sum_{\boldsymbol{i}} \lambda^{\boldsymbol{i}} \boldsymbol{S}_{\boldsymbol{i}}^x\Bigr] + h_1^z U\Bigl[\mathcal{N} m_z - 2\sum_{\boldsymbol{i}} \boldsymbol{S}_{\boldsymbol{i}}^z\Bigr] \,. \tag{4.27}$$

Thus, f_1 is given by:

$$f_1 = \frac{1}{\beta\mathcal{N}} \int_0^{\infty} d\tau \, \langle K_1(\tau) \rangle_0^c \tag{4.28}$$

$$= \frac{U}{\beta\mathcal{N}} \int_0^{\infty} d\tau \, \sum_{\boldsymbol{i}} \langle c_{\boldsymbol{i}\uparrow}^\dagger c_{\boldsymbol{i}\uparrow} c_{\boldsymbol{i}\downarrow}^\dagger c_{\boldsymbol{i}\downarrow} \rangle_0^c \,. \tag{4.29}$$

Here, the index c signifies that the average is taken over all connected diagrams only, according to the linked cluster theorem (Negele and Orland, 1987). Using Wick's theorem one finds to first-order:

$$f_1 = \frac{U}{\mathcal{N}} \sum_{\boldsymbol{i}} \bigl\{ G_{\boldsymbol{i}\uparrow}(0) G_{\boldsymbol{i}\downarrow}(0) - \langle c_{\boldsymbol{i}\uparrow}^\dagger c_{\boldsymbol{i}\downarrow} \rangle_0 \langle c_{\boldsymbol{i}\downarrow}^\dagger c_{\boldsymbol{i}\uparrow} \rangle_0 \bigr\} \tag{4.30}$$

$$= \frac{U}{4}[1 - (m_z^2 + m_x^2)] \,. \tag{4.31}$$

Up to first order, we have for the free energy f:

$$\begin{aligned} f &= f_0 + f_1 \\ &= h_0^x m_x + h_0^z m_z - \frac{2}{\beta} \int_{-\infty}^{\infty} d\epsilon \, N_d(\epsilon \pm h_0) \ln\bigl[2\cosh(\tfrac{1}{2}\beta\eta_\epsilon)\bigr] + \frac{U}{4}[1 - (m_z^2 + m_x^2)] \,. \end{aligned} \tag{4.32}$$

The equilibrium value of the order parameter m_x is then determined by minimizing the free energy at fixed (U, T, m_z). The same holds for the order parameter m_z, but keeping (U, T, m_x) fixed, instead:

$$\begin{aligned} 0 \stackrel{!}{=} \frac{df}{dm_x} &= \frac{\partial f_0}{\partial m_x} + \frac{\partial f_1}{\partial m_x} + \frac{dh_0^x}{dm_x}\left(\frac{\partial f_0}{\partial h_0^x} + \frac{\partial f_1}{\partial h_0^x}\right) \\ &= h_0^x - \frac{1}{2}Um_x\,, \end{aligned} \tag{4.33}$$

and

$$\begin{aligned} 0 \stackrel{!}{=} \frac{df}{dm_z} &= \frac{\partial f_0}{\partial m_z} + \frac{\partial f_1}{\partial m_z} + \frac{dh_0^z}{dm_z}\left(\frac{\partial f_0}{\partial h_0^z} + \frac{\partial f_1}{\partial h_0^z}\right) \\ &= h_0^z - \frac{1}{2}Um_z\,, \end{aligned} \tag{4.34}$$

implying

$$h_0^x = \frac{1}{2}m_x U \tag{4.35}$$

$$h_0^z = \frac{1}{2}m_z U\,. \tag{4.36}$$

Here, the terms $\frac{\partial f_0}{\partial h_0^x}$ and $\frac{\partial f_0}{\partial h_0^z}$ vanish exactly, which follows from (4.18) and (4.17), respectively. Furthermore, $\frac{\partial f_1}{\partial h_0^x} = 0$ and $\frac{\partial f_1}{\partial h_0^z} = 0$, as can be inferred from (4.31). From (4.32) we also find the first order terms of the fields h^x and h^z by making use of the Maxwell relations (Georges and Yedidia, 1991):

$$h_x(m_z, m_x) = \left.\frac{\partial h_x}{\partial U}\right|_{U=0} = \left.\frac{\partial^2 f_1}{\partial U \partial m_x}\right|_{U=0} = -\frac{1}{2}m_x \tag{4.37}$$

$$h_z(m_z, m_x) = \left.\frac{\partial h_z}{\partial U}\right|_{U=0} = \left.\frac{\partial^2 f_1}{\partial U \partial m_z}\right|_{U=0} = -\frac{1}{2}m_z\,. \tag{4.38}$$

At this point, it is time to comment on the magnetic field B: The system becomes fully ferromagnetically ordered for a critical magnetic field $B_c(U)$, which is defined by $m_x = 0$ and $m_z = 1$. This corresponds to an empty system in the negative-U picture. At zero temperature, the condition for B_c is expressed by:

$$m_x = 0 \qquad \vee \qquad 1 = \frac{U}{2}\int_{-\infty}^{\infty} d\epsilon\, N_d(\epsilon)\frac{1}{|B_c + \frac{1}{2}U - \epsilon|}\,, \tag{4.39}$$

$$m_z = 1 \qquad \vee \qquad 1 = \int_{-\infty}^{\infty} d\epsilon\, N_d(\epsilon)\,\mathrm{sign}(B_c + \tfrac{1}{2}U - \epsilon)\,. \tag{4.40}$$

From (4.40) follows that $B_c \geq \epsilon_+ - \frac{1}{2}U$, with the band edge ϵ_+,[3] while equation

[3] For the square lattice in $d = 2$, the band edges are at $\epsilon_\pm = \pm 4t$ [see, e.g., Fig. D.1].

(4.39) is identical to the exact criterion for $B_c(U)$. Therefore, the evaluation of the results of this chapter for values of the magnetic field larger than B_c is pointless. It turns out in the remainder of this chapter, that self-consistent perturbation theory to second order is not applicable also right at B_c, but it is applicable for the whole range $0 < B < B_c$ [compare Sec. 4.4].

4.1.3 Hartree-Fock Approximation

The free energy of Eq. (4.32) can also be obtained within Hartree-Fock (HF) theory. To allow for a staggered magnetization m_x, the HF decoupling scheme takes the following form:

$$\begin{aligned} n_{\boldsymbol{i}\uparrow} n_{\boldsymbol{i}\downarrow} \quad \xrightarrow{\text{HF}} \quad & \langle n_{\boldsymbol{i}\uparrow}\rangle n_{\boldsymbol{i}\downarrow} + n_{\boldsymbol{i}\uparrow}\langle n_{\boldsymbol{i}\downarrow}\rangle - \langle n_{\boldsymbol{i}\uparrow}\rangle\langle n_{\boldsymbol{i}\downarrow}\rangle \\ & - c^\dagger_{\boldsymbol{i}\uparrow} c_{\boldsymbol{i}\downarrow}\langle c^\dagger_{\boldsymbol{i}\downarrow} c_{\boldsymbol{i}\uparrow}\rangle - \langle c^\dagger_{\boldsymbol{i}\uparrow} c_{\boldsymbol{i}\downarrow}\rangle c^\dagger_{\boldsymbol{i}\downarrow} c_{\boldsymbol{i}\uparrow} + \langle c^\dagger_{\boldsymbol{i}\uparrow} c_{\boldsymbol{i}\downarrow}\rangle\langle c^\dagger_{\boldsymbol{i}\downarrow} c_{\boldsymbol{i}\uparrow}\rangle \,. \end{aligned} \tag{4.41}$$

Applying this scheme to the grand canonical Hamiltonian of the Hubbard model $H = H_t + H_U + H_B + H_\mu$, with the contribution of the chemical potential $H_\mu = \frac{U}{2}\sum_{\boldsymbol{i}\sigma} n_{\boldsymbol{i}\sigma}$, we obtain (van Dongen, 2005):

$$K^{\text{HF}} = \sum_{\boldsymbol{k}\sigma} \epsilon_{\boldsymbol{k}\sigma} n_{\boldsymbol{k}\sigma} - U m_x \sum_{\boldsymbol{i}} (-1)^{|\boldsymbol{i}|} \boldsymbol{S}^x_{\boldsymbol{i}} + \frac{1}{4} U \mathcal{N}(m_x^2 + m_z^2 - 1) \,, \tag{4.42}$$

where $\eta_{\epsilon\sigma}$ is defined in (4.15) with $h_0^x = \frac{1}{2}Um_x$ and $\epsilon_{\boldsymbol{k}\sigma} = \epsilon_{\boldsymbol{k}} - \sigma(B + \frac{1}{2}Um_z)$. Here, $|\boldsymbol{i}|$ denotes the Manhattan distance on the hypercubic lattice. The Hartree-Fock Hamiltonian can then be diagonalized in the same manner as K_0. One finds for the ground state energy (van Dongen, 2005):

$$E_0(m_x, m_z) \equiv \frac{E}{\mathcal{N}} = -\int_{-\infty}^{\infty} d\epsilon \, N_d(\epsilon) |\eta_{\epsilon\uparrow}| + \frac{1}{4} U (m_x^2 + m_z^2 + 1) \,, \tag{4.43}$$

with $\eta_{\epsilon\sigma} = \text{sign}(\epsilon - \sigma h_0)\sqrt{(\epsilon - \sigma h_0)^2 + (\frac{1}{2}Um_x)^2}$ and $h_0 = B + \frac{1}{2}Um_z$. This result is equivalent to (4.32) in the limit $T \to 0$, showing that HF theory yields the same results as PTFO up to linear order in U.

The order parameters m_x and m_z can be calculated on the HF level from the self-consistency relations (4.17) and (4.18). One obtains two solutions: the trivial solutions $m_x = 0$ and $m_z = 0$ (which are the solutions of the high-temperature phase) as well as the nontrivial solutions $m_x^{\text{HF}} > 0$ and $m_z^{\text{HF}} > 0$, respectively, which have lower (Hartree) free energy. This is seen quickly, e.g., for m_x as follows: Within the HF approximation, the energy gain due to the symmetry breaking caused by m_x

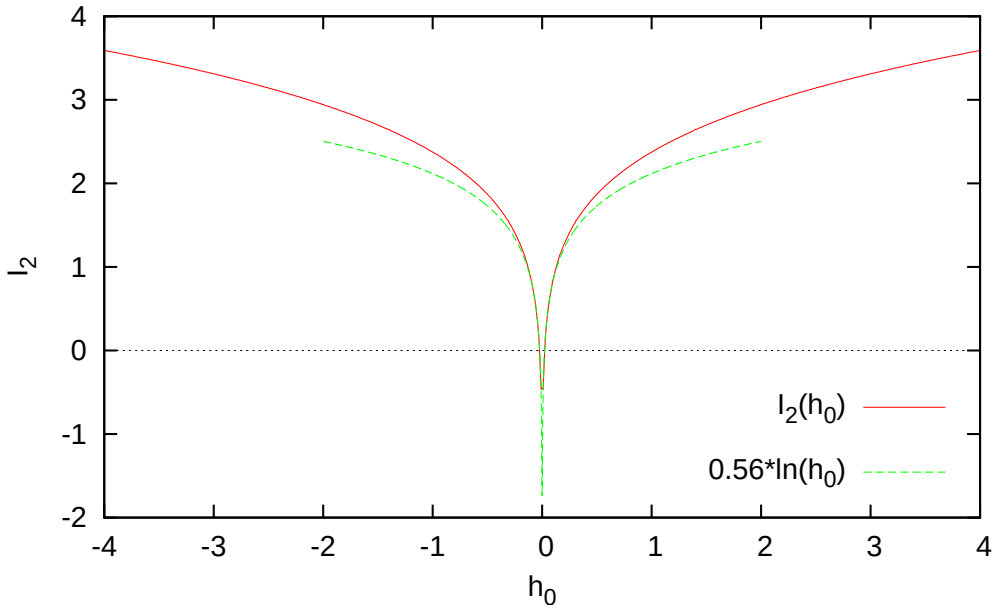

Figure 4.1: Value of I_2 for the DOS of the square lattice as a function of the field h_0. In the limit $h_0 \to 0$, I_d exhibits a logarithmic divergence.

at fixed magnetization $m_z > 0$ (i.e., at constant B with $0 < B < B_c$) is given by

$$E_0(m_x, m_z) - E_0(0, m_z) = \frac{1}{4} U m_x^2 - \int_{-\infty}^{\infty} d\epsilon \, N_d(\epsilon) \Big[\sqrt{(\epsilon - h_0)^2 + (U m_x/2)^2} - |\epsilon - h_0| \Big]$$
$$\sim \frac{1}{4} U m_x^2 \left[1 - U N_d(h_0) \, |\ln(U m_x)| \, \right] < 0 \qquad \text{for} \quad m_x \downarrow 0 \,. \tag{4.44}$$

It is therefore favorable to have $m_x > 0$ for all $B < B_c$.

In the following, we will summarize predictions of the Hartree-Fock theory concerning, amongst other things, the order parameters, the critical temperature and the gain in free energy due to the symmetry breaking in the limit $U \to 0$. Details of the calculations are presented in Appendix D.2. All quantities at HF level will be denoted by the superscript HF.

Let us start with the critical temperature $k_B T_c^{\mathrm{HF}} = (\beta_c^{\mathrm{HF}})^{-1}$ which is defined by setting $m_x(T_c) = 0$ in (4.17). In the limit $U \to 0$, the critical temperature is found

to be exponentially small:

$$k_B T_c^{\mathrm{HF}} \sim \exp\left(I_d - \frac{1}{U N_d(h_0)}\right), \tag{4.45}$$

with corrections of the order of $(k_B T_c)^2$. The function I_d is given by an integral that is difficult to calculate exactly in $d = 2$. The numerical solution of I_2 as a function of the field h_0 is plotted in Fig. 4.1. It reaches its maximum at the band edges $\epsilon_\pm$. In the limit $h_0 \to 0$, the function I_2 exhibits a logarithmic divergence: $I_2(h_0) \sim (0.557 \pm 0.003) \ln(h_0)$. In the limit of large dimensions, however, the integral I_d can be solved exactly (van Dongen, 1994*a*):

$$I_d = \tfrac{3}{2}\ln 2 + \tfrac{1}{2}\gamma - \ln\pi + \frac{1}{4d} + \mathcal{O}(\tfrac{1}{d^2}) \simeq 0.1836 + \frac{1}{4d}, \tag{4.46}$$

where the $\frac{1}{d}$-correction is included. Comparing the results in $d = \infty$ with $d = 2$ of Fig. 4.1 shows that the $\frac{1}{d^2}$-corrections in the $\frac{1}{d}$-expansion must be large.

Similarly, also the order parameter m_x is exponentially small:

$$m_x^{\mathrm{HF}} \;\propto\; \frac{4}{U}\sqrt{\epsilon_+^2 - B^2}\,\exp\left(-\tfrac{1}{UN(B)}\right). \tag{4.47}$$

The exact value at $T = 0$ can be expressed in terms of the critical temperature β_c:

$$m_x^{\mathrm{HF}}(T{=}0) = \frac{2\pi e^{-\gamma}}{U\beta_c}, \tag{4.48}$$

with Euler's constant $\gamma \approx 0.577$. The gap ratio $U m_x(0)/T_c^{\mathrm{HF}} = 2\pi e^{-\gamma}$ is therefore identical to the standard BCS gap ratio [compare, e.g., Ashcroft and Mermin (1976)]. Correction terms at low temperatures are exponentially small:

$$m_x^{\mathrm{HF}}(\theta) = m_x^{\mathrm{HF}}(T=0)\left[1 - \sqrt{\frac{\theta\pi}{\delta_0}}e^{-2\delta_0/\theta}\right], \tag{4.49}$$

with the rescaled temperature $\theta = T/T_c \ll 1$ and $\delta_0 = \frac{1}{2}\beta_c U m_x(T=0)$.

Finally, the gain in free energy per lattice site Ω^{HF} due to the symmetry breaking for $T \geq 0$ fixed value of m_z is given by

$$\Omega^{\mathrm{HF}} \sim -\frac{1}{4}U^2\left[m_x^{\mathrm{HF}}\right]^2 N_2(h_0)\,\Phi(\theta) \qquad (U \downarrow 0), \tag{4.50}$$

with the integral $\Phi(\theta)$:

$$\Phi(\theta) = \int_0^\infty dy\left\{\frac{2\theta}{\delta^2}\ln\left[\frac{\cosh(\sqrt{y^2+\delta^2}/\theta)}{\cosh(y/\theta)}\right] - \frac{\tanh(y)}{y}\right\}. \tag{4.51}$$

which converges for all $\theta \in \mathbb{R}^+$.

4.2 Second-Order Corrections

In this section, we calculate the second-order correction to the free energy. The contributions f_n for $n = 0, 1, 2$ are given by

$$f_0 = h_0^x m_x + h_0^z m_z - \frac{2}{\beta} \int_{-\infty}^{\infty} d\epsilon \, N_d(\epsilon \pm h_0) \ln\left[2\cosh(\tfrac{1}{2}\beta\eta_\epsilon)\right] \tag{4.52}$$

$$f_1 = \frac{U}{4}[1 - (m_z^2 + m_x^2)] \tag{4.53}$$

$$f_2 = -\frac{1}{2\beta\mathcal{N}} \int_0^\beta \int_0^\beta d\tau_1 \, d\tau_2 \, \langle K_1(\tau_1) K_1(\tau_2)\rangle_0^c \,. \tag{4.54}$$

In order to determine the perturbation K_1 in second order, we need to truncate the expansion of the fields h^x and h^z after the first order term. Employing the results for h_1^x and h_1^z from (4.37) and (4.38), respectively, K_1 can be written as

$$K_1 = \tilde{H}_U + \frac{1}{4} U\mathcal{N}(1 - m_x^2 - m_z^2) \,, \tag{4.55}$$

with

$$\tilde{H}_U \equiv H_U - H_U^{\mathrm{HF}}. \tag{4.56}$$

Here, H_U^{HF} denotes the Hartree Fock part of H_U, which can most easily be inferred from the Hartree Fock part of $(H_U - \frac{1}{2}U\sum_{\boldsymbol{i}\sigma} n_{\boldsymbol{i}\sigma})$, which is given by

$$\Big(H_U - \frac{1}{2}U\sum_{\boldsymbol{i}\sigma} n_{\boldsymbol{i}\sigma}\Big)^{\mathrm{HF}} = U\Big[m_z \sum_{\boldsymbol{i}} S_{\boldsymbol{i}}^z - m_x \sum_{\boldsymbol{i}} \lambda_{\boldsymbol{i}} S_{\boldsymbol{i}}^x - (1 - m_z^2 - m_x^2)\Big] \,. \tag{4.57}$$

Here, the advantage of subtracting the HF part from the interaction H_U is the fact that all direct (Hartree) diagrams and exchange (Fock) diagrams in the free energy are already taken account of and thus do not need to be calculated explicitely. The averages $\langle\cdots\rangle_0^c$ are calculated using Hartree Green functions with gap parameters h_0^x and h_0^z.

The second-order contribution to the free energy, f_2, is then transformed into momentum space, using (4.12):

$$\begin{aligned} f_2 = -\frac{U^2}{2\beta\mathcal{N}^3} \int_0^\beta \int_0^\beta d\tau_1 \, d\tau_2 \sum_{\boldsymbol{k}_1 \ldots \boldsymbol{k}_8} & \langle c_{\boldsymbol{k}_1\uparrow}^\dagger(\tau_1) c_{\boldsymbol{k}_3\uparrow}^\dagger(\tau_1) c_{\boldsymbol{k}_4\uparrow}(\tau_1) c_{\boldsymbol{k}_2\uparrow}(\tau_1) \\ & \times c_{\boldsymbol{k}_5\uparrow}^\dagger(\tau_2) c_{\boldsymbol{k}_7\uparrow}^\dagger(\tau_2) c_{\boldsymbol{k}_8\uparrow}(\tau_2) c_{\boldsymbol{k}_6\uparrow}(\tau_2)\rangle_0^c \, \delta^*_{\boldsymbol{k}_1+\boldsymbol{k}_3,\boldsymbol{k}_2+\boldsymbol{k}_4} \, \delta^*_{\boldsymbol{k}_5+\boldsymbol{k}_7,\boldsymbol{k}_6+\boldsymbol{k}_8} \,. \end{aligned} \tag{4.58}$$

Here, the function $\delta^*_{\boldsymbol{kp}}$ takes into account also Umklapp processes:

$$\delta^*_{\boldsymbol{kp}} = \frac{1}{\mathcal{N}} \sum_{\boldsymbol{j}} e^{i(\boldsymbol{k}-\boldsymbol{p})\cdot\boldsymbol{j}} = \sum_{\{\boldsymbol{K}\}} \delta_{\boldsymbol{k},\boldsymbol{p}+\boldsymbol{K}} \,, \tag{4.59}$$

where $\{\boldsymbol{K}\}$ are vectors of the reciprocal lattice and $\delta_{\boldsymbol{kp}}$ is the usual Kronecker δ.

The thermal average $\langle \cdots \rangle_0^c$ in (4.58) is evaluated using Wick's theorem (Negele and Orland, 1987) resulting in the following four contractions, which are expressed in terms of the HF Green functions: $G_{\boldsymbol{kk'}\sigma\sigma'}(\tau) \equiv \langle T_\tau c_{\boldsymbol{k}\sigma}(\tau) c^\dagger_{\boldsymbol{k'}\sigma'}(0)\rangle_0$. We then have:

$$f_2 = -\frac{U^2}{2\beta\mathcal{N}^3} \int_0^\beta \int_0^\beta d\tau_1 \, d\tau_2 \, I(\tau_{12}) \,, \tag{4.60}$$

with

$$\begin{aligned} I(\tau_{12}) \;=\; \sum_{\mathbf{1}\ldots\mathbf{8}} \big\{ & \; G_{\mathbf{61},\uparrow\uparrow}(-\tau_{12})\, G_{\mathbf{83},\downarrow\downarrow}(-\tau_{12})\, G_{\mathbf{47},\downarrow\downarrow}(\tau_{12})\, G_{\mathbf{25},\uparrow\uparrow}(\tau_{12}) \\ & + G_{\mathbf{81},\downarrow\uparrow}(-\tau_{12})\, G_{\mathbf{63},\uparrow\downarrow}(-\tau_{12})\, G_{\mathbf{45},\downarrow\uparrow}(\tau_{12})\, G_{\mathbf{27},\uparrow\downarrow}(\tau_{12}) \\ & - G_{\mathbf{81},\downarrow\uparrow}(-\tau_{12})\, G_{\mathbf{63},\uparrow\downarrow}(-\tau_{12})\, G_{\mathbf{47},\downarrow\downarrow}(\tau_{12})\, G_{\mathbf{25},\uparrow\uparrow}(\tau_{12}) \\ & - G_{\mathbf{61},\uparrow\uparrow}(-\tau_{12})\, G_{\mathbf{83},\downarrow\downarrow}(-\tau_{12})\, G_{\mathbf{45},\downarrow\uparrow}(\tau_{12})\, G_{\mathbf{27},\uparrow\downarrow}(\tau_{12}) \; \big\} \\ & \times \; \delta^*_{\mathbf{1}+\mathbf{3},\mathbf{2}+\mathbf{4}}\, \delta^*_{\mathbf{5}+\mathbf{7},\mathbf{6}+\mathbf{8}} \,, \end{aligned} \tag{4.61}$$

where $\tau_{12} = \tau_1 - \tau_2$. Here, $\mathbf{1}$ denotes $\boldsymbol{k}_1$ and so forth. By relabeling the indices $(\mathbf{1234}) \to (\mathbf{5678})$ one finds that $I(\tau)$ is symmetric $[I(\tau) = I(-\tau)]$ and periodic with period β. Therefore, the integrals in (4.60) simplify to

$$f_2 = -\frac{U^2}{\mathcal{N}^3} \int_0^{\beta/2} d\tau \, I(\tau) \,. \tag{4.62}$$

The Green functions $G_{\boldsymbol{kk'}\sigma\sigma'}(\tau)$ can be expressed in terms of the $d_{\boldsymbol{k}\sigma}$ particles, similar to (4.22):

$$G_{\boldsymbol{kk'}\sigma\sigma'}(\tau) = \delta_{\boldsymbol{kk'}}\, \delta_{\sigma\sigma'} A_{\boldsymbol{k}\sigma}(\tau) + \delta_{\boldsymbol{k},\boldsymbol{k'}-\boldsymbol{Q}}\, \delta_{\sigma,-\sigma'} B_{\boldsymbol{k}\sigma}(\tau) \,, \tag{4.63}$$

with

$$A_{\boldsymbol{k}\sigma}(\tau) = a^2_{\boldsymbol{k}\sigma} g_{\boldsymbol{k}\sigma}(\tau) + b^2_{\boldsymbol{k}\sigma} g_{\boldsymbol{k}-\boldsymbol{Q},-\sigma}(\tau) \tag{4.64}$$

$$B_{\boldsymbol{k}\sigma}(\tau) = a_{\boldsymbol{k}\sigma} b_{\boldsymbol{k}\sigma} [g_{\boldsymbol{k}-\boldsymbol{Q},-\sigma}(\tau) - g_{\boldsymbol{k}\sigma}(\tau)] \,, \tag{4.65}$$

and the Green functions $g_{\boldsymbol{k}\sigma}$ of the $d_{\boldsymbol{k}\sigma}$ particles, which are defined in (4.21). The following symmetry relations are useful for the further evaluation of f_2:

$$A_{\boldsymbol{k}\sigma}(-\tau) = -A_{\boldsymbol{k}-\boldsymbol{Q},-\sigma}(\tau) \tag{4.66}$$

$$B_{\boldsymbol{k}\sigma}(-\tau) = B_{\boldsymbol{k}-\boldsymbol{Q},-\sigma}(\tau) \tag{4.67}$$

$$B_{\boldsymbol{k}-\boldsymbol{Q},-\sigma}(\tau) = B_{\boldsymbol{k}\sigma}(\tau)\,. \tag{4.68}$$

For $\beta \to \infty$ the expressions $A_{\boldsymbol{k}\sigma}$ and $B_{\boldsymbol{k}\sigma}$ are given by

$$A_{\boldsymbol{k}\sigma}(\tau) = \frac{1}{2}\left(1 + \frac{\epsilon_{\boldsymbol{k}\sigma}}{|\eta_{\boldsymbol{k}\sigma}|}\right) e^{-|\eta_{\boldsymbol{k}\sigma}|\tau} \tag{4.69}$$

$$B_{\boldsymbol{k}\sigma}(\tau) = -\frac{h_0^x}{2|\eta_{\boldsymbol{k}\sigma}|} e^{-|\eta_{\boldsymbol{k}\sigma}|\tau}\,. \tag{4.70}$$

Inserting the expression of the Green function $G_{\boldsymbol{k}\boldsymbol{k}'}$ (4.63) into (4.61) one finds that one of the two δ^*-constraints is automatically fulfilled. Employing the expressions of A and B for the ground state, (4.69), and symmetrizing the resulting integrand with transformations of the form

$$\begin{aligned} (\mathbf{1},\mathbf{3}) &\to (\mathbf{3}-\boldsymbol{Q},\mathbf{1}-\boldsymbol{Q}) \\ (\mathbf{2},\mathbf{4}) &\to (\mathbf{4}-\boldsymbol{Q},\mathbf{2}-\boldsymbol{Q})\,, \end{aligned} \tag{4.71}$$

yields

$$f_2 = -\frac{U^2}{16} \iiiint\limits_{\text{1.BZ}} \frac{d\mathbf{1}\ldots d\mathbf{4}}{(2\pi)^{3d}} \delta^*(\mathbf{1}+\mathbf{3}-\mathbf{2}-\mathbf{4}) F(\eta_{\mathbf{1}\uparrow},\eta_{\mathbf{2}\uparrow},\eta_{\mathbf{3}\downarrow},\eta_{\mathbf{4}\downarrow};\epsilon_{\mathbf{1}\uparrow},\epsilon_{\mathbf{2}\uparrow},\epsilon_{\mathbf{3}\downarrow},\epsilon_{\mathbf{4}\downarrow};h_0^x)\,, \tag{4.72}$$

with

$$F(\ldots;\ldots;h_0^x) = \frac{\left[1+\frac{\epsilon_{\mathbf{1}\uparrow}\epsilon_{\mathbf{3}\downarrow}-(h_0^x)^2}{|\eta_{\mathbf{1}\uparrow}\eta_{\mathbf{3}\downarrow}|}\right]\left[1+\frac{\epsilon_{\mathbf{2}\uparrow}\epsilon_{\mathbf{4}\downarrow}-(h_0^x)^2}{|\eta_{\mathbf{2}\uparrow}\eta_{\mathbf{4}\downarrow}|}\right]}{\left(|\eta_{\mathbf{1}\uparrow}|+|\eta_{\mathbf{2}\uparrow}|+|\eta_{\mathbf{3}\downarrow}|+|\eta_{\mathbf{4}\downarrow}|\right)}\,, \tag{4.73}$$

where the sum over $\boldsymbol{k}$ in (4.61) is replaced by the integral over the 1st Brillouin zone, as indicated.

The self-consistency condition (1.53) for the order parameter implies that we do not need to calculate f_2, but only the derivative with respect to the order parameters,

$$\frac{1}{h_0^x}\frac{df_2}{dh_0^x} \quad \text{and} \quad \frac{1}{h_0^z}\frac{df_2}{dh_0^z}\,. \tag{4.74}$$

Hence, we need the derivatives of F with respect to h_0^x and h_0^z. Using transformations of the type (4.71) one finds:

$$\frac{df_2}{dh_0^x} = -\frac{U^2}{16} \iiiint\limits_{\text{1.BZ}} \frac{d\mathbf{1}\ldots d\mathbf{4}}{(2\pi)^{3d}}\, \delta^*(\mathbf{1}+\mathbf{3}-\mathbf{2}-\mathbf{4}) \left[4\frac{h_0^x}{|\eta_{\mathbf{1}\uparrow}|}\frac{\partial F}{\partial|\eta_{\mathbf{1}\uparrow}|} + 2h_0^x\frac{\partial F}{\partial(h_0^x)^2}\right] \tag{4.75}$$

For the further evaluation it is useful to consider the terms containing $\frac{\partial F}{\partial|\eta|}$ and $\frac{\partial F}{\partial(h_0^x)^2}$ separately. Some basic transformations, including the substitution $\boldsymbol{q}_1 = \mathbf{2} - \mathbf{1}$ and $\boldsymbol{q}_2 = \mathbf{3} - \mathbf{4}$ yields

$$\frac{df_2}{dh_0^x} = -\frac{U^2 h_0^x}{4}[T_\eta(h_0^x) + T_h(h_0^x)]\,, \tag{4.76}$$

with

$$\begin{aligned} T_h(h_0^x) = &\iiint\limits_{1.\mathrm{BZ}} \frac{d\mathbf{1}d\mathbf{4}d\boldsymbol{q}}{(2\pi)^{3d}} \frac{-1}{\big(|\eta_{\mathbf{1}\uparrow}| + |\eta_{\mathbf{1}+\boldsymbol{q},\uparrow}| + |\eta_{\mathbf{4}+\boldsymbol{q},\downarrow}| + |\eta_{\mathbf{4}\downarrow}|\big)|\eta_{\mathbf{1}\uparrow}\eta_{\mathbf{4}\downarrow}|} \\ &\times \left\{1 + \frac{\epsilon_{\mathbf{1}+\boldsymbol{q},\uparrow}\epsilon_{\mathbf{4}\downarrow}}{|\eta_{\mathbf{1}+\boldsymbol{q},\uparrow}\eta_{\mathbf{4}\downarrow}|} - \frac{(h_0^x)^2}{|\eta_{\mathbf{1}+\boldsymbol{q},\uparrow}\eta_{\mathbf{4}\downarrow}|}\right\} \qquad (4.77) \\ = &-(I_{h_1} + I_{h_3} - (h_0^x)^2 I_{h_2})\,, \qquad (4.78) \\ & \qquad (4.79) \end{aligned}$$

and

$$T_\eta(h_0^x) = \iiint\limits_{1.\mathrm{BZ}} \frac{d\mathbf{1}d\mathbf{4}d\boldsymbol{q}}{(2\pi)^{3d}} \frac{1}{|\eta_{\mathbf{1}\uparrow}|} \frac{\partial F}{\partial|\eta_{\mathbf{1}\uparrow}|}\,. \tag{4.80}$$

As second-order perturbation theory is only meaningful when its corrections are smaller than the Hartree-Fock results, one expects that h_0^x is exponentially small. We therefore need to know the behavior of df_2/dh_0^x for exponentially small h_0^x. One finds that the leading contribution in the limit $h_0^x \to 0$ is due to the integrals I_{h_1} and I_{h_3}, which are of the same order. For general values of the magnetic field B, with $h_0^x \ll B < B_c$, both integrals can be evaluated analytically to a certain extent. The calculation is shown in Appendix D.3. The divergences that appear in the remaining terms (including the terms that result from df_2/dh_0^z) are weaker and can therefore be neglected.

One finds that

$$I_{h_1} + I_{h_3} \;\sim\; 4\left[\ln\left(\frac{t}{h_0^x}\right)\right]^2 LS(h_0)\,, \tag{4.81}$$

where $LS(h_0)$ is a lattice sum that has to be evaluated numerically for generic values of the field h_0. The explicit expression of $LS(h_0)$ as well as the method used for its numerical computation are presented in Appendix D.4. One finds that the lattice sum $LS(h_0)$ can be computed in real space for values of the field h_0 for which the following relation holds: $h_0^x \ll h_0 < B_c$. The restriction to values of h_0 that are much larger than the symmetry breaking field h_0^x is due to the logarithmic van Hove singularity in the density of states $N_2(\epsilon)$ in $d = 2$ that appears at $\epsilon = 0$ [see Appendix D.1]. If $h_0 \sim \mathcal{O}(h_0^x)$, the logarithmic divergence of I_{h_1} becomes at least of the order of $\ln(h_0^x)^4$.

This is due to the energy integration in (D.29), which, in that case, becomes of the order of $\ln(h_0^x)^2$. This behavior is obvious, because the limit $h_0 \to 0$ corresponds to the Hubbard model without magnetic field B, for which it was shown explicitly that self-consistent perturbation theory diverges in the symmetry-broken phase for $d \leq 2$ (Schauerte and van Dongen, 2002). Next, the restriction of the field h_0 to values below the critical magnetic field $B_c = 4t$ is due to the fact that all lattice sites contribute almost equally to the lattice sum $LS(h_0)$ as $h_0 \to B_c$. This can be seen, e.g., in Fig. D.2. In the limit $h_0 \to B_c$, the integral I_{h_1} (and similarly I_{h_3}) is therefore most conveniently evaluated in momentum space. The analytical calculation in this limit is performed in Appendix D.5. As a result, one finds for the integral I_{h_1}:

$$I_{h_1} \sim \frac{1}{2^5(\pi\, t)^3} \ln\left(\frac{1}{b}\right) \left[\ln\left(\frac{t}{h_0^x}\right)\right]^2 , \tag{4.82}$$

with the parameter $b = (B_c - h_0)/t$. Thus, the leading order of the logarithmic divergence in h_0^x is unchanged, but one obtains an additional logarithmic divergence in b.

4.3 Renormalization of the Hartree Results

The order parameter in second-order perturbation theory can now be obtained by optimizing the free energy $f = f_0 + f_1 + f_2$, which is the sum of the Hartree contributions and the second-order corrections. The equilibrium equation for m_x is

$$\begin{aligned} 0 &= \frac{df}{dm_x} \\ &\sim h_0^x - \frac{1}{2} U m_x + \frac{df_2}{dh_0^x} \frac{dh_0^x}{dm_x} . \end{aligned} \tag{4.83}$$

The self-consistency equation (4.17) for the field h_0^x and the magnetization m_x for $T = 0$ implies $m_x \sim 2\, h_0^x\, N_2(h_0)\, \ln(1/h_0^x)$ for $h_0^x \downarrow 0$. Thus

$$\frac{dh_0^x}{dm_x} \sim \frac{1}{2 h_0^x N_2(h_0) \ln(1/h_0^x)} . \tag{4.84}$$

In both cases, in the limit $h_0 \to B_c$ (case 1) and for generic values of h_0 with $h_0^x \ll h_0 < B_c$ (case 2), the derivative df_2/dh_0^x can be expressed by

$$\frac{\partial f_2}{\partial h_0^x} \sim \frac{1}{4}\, h_0^x U^2\, (I_{h_1} + I_{h_3}) = h_0^x\, P U^2 \left[\ln\left(\frac{t}{h_0^x}\right)\right]^2 , \tag{4.85}$$

with

$$P = LS(h_0) \qquad \text{for} \quad h_0^x \ll h_0 < B_c \tag{4.86}$$

$$P \sim (4\pi t)^{-3} \ln\left(\frac{1}{b}\right) \qquad \text{for} \quad h_0 \to B_c\,, \qquad \text{with} \quad b = (B_c - h_0)/t\,. \tag{4.87}$$

When combining the results, equation (4.83) can be written as

$$\begin{aligned} h_0^x \;&\sim\; \frac{1}{2} U m_x \frac{1}{1+\xi U N(h_0)} \qquad && \text{with} \quad \xi = \frac{P}{2[N(h_0)]^3} \\ &=\; \frac{1}{2}\, a U m_x \qquad && \text{with} \quad a = \frac{1}{1+\xi U N(h_0)}\,. \end{aligned} \tag{4.88}$$

Inserting (4.88) into the self-consistency equation (4.17) and comparing with the Hartree result (D.13), shows that m_x has the same form as the staggered magnetization in Hartree approximation, m_x^{HF}, if one replaces $U \to aU$. Therefore, the symmetry-breaking field can be expressed in terms of the Hartree result times a renormalization factor:

$$h_0^x \sim q\, h_0^{x\mathrm{HF}}\,, \tag{4.89}$$

with

$$q = e^{-\xi} \qquad \text{for} \quad h_0^x \ll h_0 < B_c \tag{4.90}$$

$$q \sim \sqrt{b} \qquad \text{for} \quad h_0 \to B_c\,. \tag{4.91}$$

Note, that the q factor in (4.91) is correct only up to an unknown exponent of the order of unity, which is due to the approximation (D.60) in Appendix D.5. The identical replacement can be performed in the defining equation of the critical temperature T_c, (D.6), implying that the Hartree critical temperature T_c^{HF} is renormalized by the same factor q:

$$T_c \sim q\, T_c^{\mathrm{HF}} \qquad \text{for} \quad U \downarrow 0\,. \tag{4.92}$$

The self-consistency relation for the order parameter m_x, (D.15), can be treated in precisely the same manner, by redefining $\Theta \equiv T/T_c$ and $\delta = \frac{1}{2}\beta_c U m_x$. One finds that the order parameter is similarly renormalized by the factor q, evaluated at the temperature T/q:

$$m_x(T) \sim q\, m_x^{\mathrm{HF}}(T/q) \qquad \text{for} \quad U \downarrow 0\,. \tag{4.93}$$

The gain in free energy due to the symmetry breaking is directly inferred from (4.50):

$$\begin{aligned} \Omega \;&\sim\; -\frac{1}{4} U^2 \left[m_x(T)\right]^2 N_2(h_0)\, \Phi(\theta) \\ &\sim\; q^2\, \Omega^{\mathrm{HF}}(T/q)\,. \end{aligned} \tag{4.94}$$

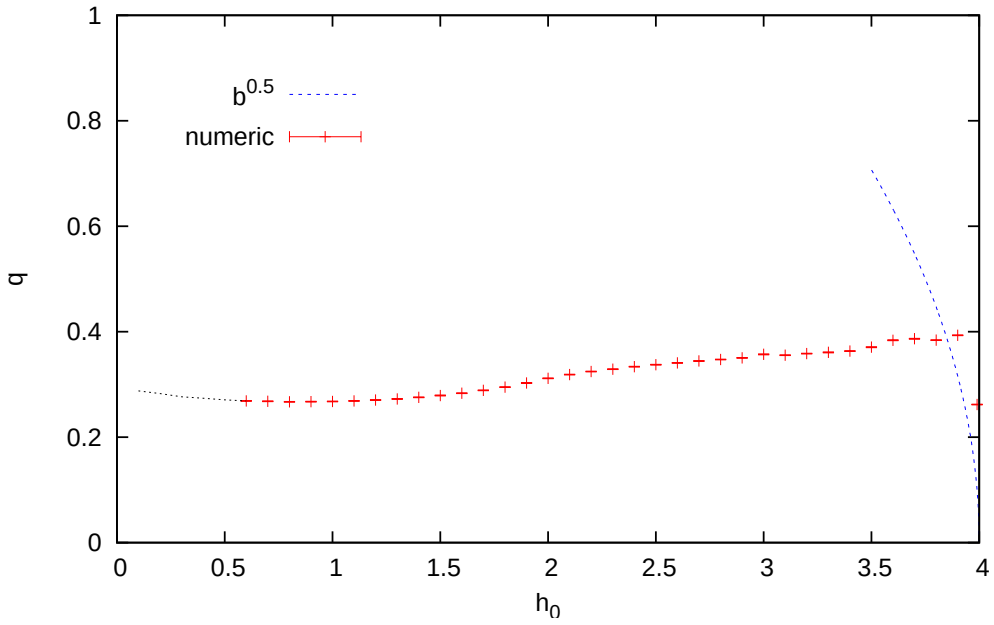

Figure 4.2: Renormalization factor q in $d = 2$ as a function of the magnetic field $h_0 = B + h_0^z$. For small values of h_0, the approximations performed in the derivation of q are not valid any more. This regime is indicated by the dotted (black) line. In the limit $h_0 \to B_c$, the q factor vanishes as $\sqrt{b}$, with $b = (B_c - h_0)/t$. This behavior is indicated by the dashed (blue) line. The vanishing of the q-factor is seen in the numerical data only for $h_0 \gtrsim 3.99$ (one data point).

Thus, since $\Omega < 0$ for $T < T_c$, the symmetry breaking is stable also within second-order perturbation theory, where fluctuations are taken into account.

The renormalization factor q in $d = 2$ is depicted in Fig. 4.2 as a function of the field h_0. For intermediate h_0 values, q is of the order of unity and only weakly dependent on the symmetry breaking field h_0. For these values, q reaches a minimum for $h_0 \approx 0.8$ with $q \simeq (0.2670 \pm 0.0007)$. In the limit $h_0 \to B_c$ (i.e., $b \to 0$), the renormalization factor q vanishes as $\sqrt{b}$, as is indicated by the dotted (blue) line. This drop in q is captured by the numerical estimates only for values of h_0, very close to B_c (compare, e.g., $h_0 = 3.99$). In this regime, the numerical evaluation of the lattice sum $LS(h_0)$ becomes unreasonably difficult because more and more lattice sites contribute almost equally to the lattice sum. This feature is illustrated in Fig. D.2. The behavior of q in the limit $h_0 \to 0$ is indicated by the dotted (blue) line in Fig. 4.2.

4.4 Discussion

In this chapter we studied the negative-U Hubbard model as a function of the chemical potential in second-order self-consistent perturbation theory in two spatial dimensions.

The above findings show that sc perturbation theory gives asymptotically exact results in $d = 2$ at finite doping. For generic values of the field h_0, with $h_0^x \ll h_0 < B_c$ (i.e., $0 < n < 1$ in the negative-U picture), the Hartree-Fock results are renormalized by a factor $q(h_0)$, which is positive and smaller than unity. Thus, the Hartree-Fock predictions are not only relevant for dimensions $d > 2$ but also in $d = 2$ if the system is doped. Quantitatively, however, the HF results are not a good approximation: Even for arbitrarily weak interaction ($U \to 0$), the HF results are rescaled by a factor of about $3 - 4$ for generic values of h_0. Consequently, the HF results are also renormalized at finite U. Higher order corrections are expected to be negligible in the limit $U \to 0$, on account of the results for $d \geq 3$ with $B = 0$ (van Dongen, 1991; van Dongen, 1994*a*). Exactly the same result, namely the renormalization of the HF results by factor of the order of unity, was found by van Dongen (1991) [compare also van Dongen (1994*a*)] for the extended Hubbard model in $d \gtrsim 3$ and by Schauerte and van Dongen (2002) for the Hubbard model in $d = 3$ (both at half-filling). In $d = 2$ and at finite doping, a renormalization of the HF results was obtained earlier by Martín-Rodero and Flores (1992), however, within an essentially uncontrolled expansion of the self-energy.[4] For a simplified[5] density of states and by approximating the second-order contribution of the self-energy by its local part, they found a (filling-independent) renormalization factor $q = \frac{1}{4}$.

It is instructive to consider the dependence of the renormalization factor on the symmetry breaking field h_0 in detail. For intermediate h_0 values (i.e. $h_0^x \ll h_0 < B_c$), the q factor is weakly increasing as a function of h_0. The numerical value ranges from $q(0.6) \simeq 0.268$ to $q(3.9) \simeq 0.393$. Here, the results can be compared directly to the renormalization occurring in the positive-U Hubbard model at half filling in $d \geq 3$, since it can be mapped on the negative-U Hubbard model by a particle-hole transformation. In $d = 3$, the Hartree results are renormalized by a factor $q \simeq 0.2599$ (Schauerte and van Dongen, 2002). The renormalization for intermediate h_0 values is therefore weaker than in $d = 3$ at half filling.[6]

[4] Here, the self-energy was assumed to be frequency independent.

[5] Here, the unperturbed density of states in $d = 2$ was approximated by $N_2(\epsilon) \sim 1/\epsilon$ for $|\epsilon| < \epsilon_+$ (Martín-Rodero and Flores, 1992).

[6] It is also interesting to note that the structure of the lattice sum in $d = 3$ differs from $LS(h_0)$ in our case: In $d = 3$, only lattice sites with an even distance $|\boldsymbol{j}|$ from a central site $\mathbf{0}$ contribute to the lattice sum due to a different symmetry of the Green function for even and odd values of $|\boldsymbol{j}|$ (Schauerte and van Dongen, 2002). At negative U and away from half filling, however, even and odd lattice sites both contribute significantly to the lattice sum.

Let us now focus on the case $h_0 \to B_c$ [which corresponds to the limit $n \to 0$ (empty band) in the negative-U picture]. In this limit, more and more lattice sites contribute significantly to the lattice sum $LS(h_0)$, as can be seen, e.g., in Fig. D.2. Here, the leading contribution to the integral I_{h_1} is due to a small region in momentum space, resulting in an additional logarithmic divergence $\ln(1/b)$. Consequently, the renormalization factor vanishes as $q \sim \sqrt{b}$ for $b \to 0$. This behavior is surprising at first sight: Taking the limit $b \to 0$, corresponds, in the negative-U picture, to the limit of an empty system, which one expects to be adequately described by a mean-field theory. Consequently one would expect that the renormalization factor becomes unity in this limit. In $d = 2$, however, the density of states displays a discontinuity right at the band edge $\epsilon = \pm\epsilon_+$. The occurrence of the discontinuity seems to be the reason for the inapplicability of sc perturbation theory in this limit. For dimensions $d \geq 2$, however, the DOS vanishes at the band edge (at least for hypercubic lattices). As a consequence, the exponent ξ in the definition of the renormalization factor q in (4.88) diverges,[7] implying $q \to 1$ in this limit. Sc perturbation theory yields therefore exact results in $d = 3$ for all fillings.

Next, let us consider the behavior of the renormalization factor as $h_0 \to 0$ [which corresponds to the limit $n \to 1$ (half-filled band) in the negative-U picture]. In this case, it is already known that sc perturbation theory diverges in dimensions $d \leq 2$ (Schauerte and van Dongen (2002); see also Kopietz (1993) for the second-order term in the expansion). Here, the quantum fluctuations completely destroy the mean-field results. The reason for the breakdown of sc perturbation theory in $d = 2$ is due to the logarithmic divergence of the DOS at the Fermi level, which gives an extra factor $\ln(h_0^x)$ to each energy integration in the expansion of the free energy. In our case, the approximations performed to derive the result (4.81) loose their validity. One expects that the logarithmic divergence in h_0^x of (4.81) is at least of the order of $\ln(h_0^x)^4$ due to the additional logarithmic divergence in the DOS.

Let us finally remark on the relevance of the above findings to superconductivity. The renormalization of the order parameters for the model ($U > 0, B > 0, n = 1$) implies that the superconducting transition temperature T_c^s and the superconducting order parameter χ_0 differ from the BCS predictions by the same factor. The exact gap ratio $Um_x(0)/k_BT_c$ is found to identical to the BCS gap ratio $2\pi e^{-\gamma} \simeq 3.5285$.

The most important conclusion of the above findings is the fact that Hartree-Fock theory (and thus also sc perturbation theory) is relevant for the description of the negative-U Hubbard model at finite doping. In the limits $h_0 \to 0$ and $h_0 \to B_c$, however, sc perturbation theory is not applicable.

[7] Here, the logarithmic divergence in b is retained, such that in $d = 3$, the integral I_{h_1} in (4.82) remains unchanged (except for the prefactors) and corresponds to the factor P in (4.88).

4.5 Summary and Outlook

In this section we have studied the negative-U Hubbard model away from half filling within self-consistent second-order perturbation theory on a hypercubic lattice in $d = 2$. The calculations were performed for the repulsive Hubbard model within a homogenous magnetic field B at half filling, to which the negative-U model can be mapped by a special particle-hole transformation. We found that the Hartree-Fock results for the critical temperature and the order parameter are not exact even in the limit $U \to 0$, but have to be renormalized by a factor of the order of unity. For finite doping n, with $0 < n < 1$, the renormalization factor can be expressed in terms of a lattice sum that explicitly depends on the doping. A numerical evaluation shows that the q values are within the range $q \approx 0.25 - 0.4$ at finite doping from not too close to 1. The Hartree-Fock results are therefore rescaled by a factor $2.5 - 4$. We also found that the exact gap ratio $Um_x(0)/k_BT_c$ in the limit $U \to 0$ is identical to the Hartree-Fock gap ratio $2\pi e^{-\gamma} \simeq 3.5285$. In the limit $n \to 0$ (i.e., $B \to B_c$), the renormalization factor can be calculated exactly and vanishes as $q \sim \sqrt{(B_c - B)/t}$. This implies that sc perturbation theory is not applicable in this limit. A similar result is known for the half-filled case ($n = 1$ or $B = 0$), for which Schauerte and van Dongen (2002) showed that sc perturbation theory diverges in $d \leq 2$. In summary, we have presented the first asymptotically exact results at weak-coupling for the negative-U Hubbard model in $d = 2$ for finite doping.

There are several possibilities to extend the results of this work. First of all, it would be interesting to investigate the region close to half-filling, which could shed light on the divergence of sc perturbation theory at half-filling. Another extension is to study the model for the occurrence of a finite temperature Kosterlitz-Thouless transition (Kosterlitz and Thouless, 1973), for which numerical evidence has been found already (Scalettar, Loh, Gubernatis, Moreo, White, Scalapino, Sugar and Dagotto, 1989; Moreo and Scalapino, 1991). Away from half-filling, such a transition is expected due to the symmetry breaking induced by the chemical potential μ (or the field B), which forces the spins to lie in the $x-y$ plane, but canted towards the z axis. The Hubbard model away from half filling and in $d = 2$ is thus in the XY-symmetry class of the Heisenberg model. Another direction of a generalization would be to include also nearest-neighbor Coulomb interactions V (extended Hubbard model), where V is negative [the case ($V > 0$, $d \gtrsim 3$) was treated by van Dongen (1994*a*)].

Summary

High-Frequency corrected QMC Simulations

In chapter 2 we developed a scheme that supplements the DMFT+QMC with high-frequency corrections (QMC+$\frac{1}{\omega}$). The method is based on a large-frequency expansion of the self-energy. The coefficients of the expansion, which can be derived rigorously from the moments of the spectral density, have to be determined self-consistently. We implemented the scheme into an existing multi-band code and subsequently demonstrated its applicability to the multi-orbital Hubbard model at half filling in a comparison with reference schemes. The QMC+$\frac{1}{\omega}$ scheme thereby reduces the error of the DMFT+QMC method to the inevitable Trotter error. The error associated with the discrete Fourier transformations, which are needed twice in the DMFT iteration cycle, is essentially eliminated. At large frequencies, the solutions of the self-energies are correct up to order $\frac{1}{\omega}$, the solutions of the Green functions up to order $\frac{1}{\omega^2}$. In a systematic study we showed that the solutions of the QMC+$\frac{1}{\omega}$ method can be optimized also at intermediate frequencies (in terms of oscillations around the large-frequency behavior). The QMC+$\frac{1}{\omega}$ scheme therefore allows for extremely precise solutions already for large values of the discretization $\Delta\tau$. A scheme with these properties is needed especially for the simulation of multi-orbital systems, where the numerical effort (which scales like $2^{2m(m-1)L^3}$, with $L = \beta/\Delta\tau$ and the number of orbitals m) is too large to allow for calculations at low temperatures or small values of $\Delta\tau$.

Orbital-Selective Mott Transitions

In chapter 3 we studied the anisotropic two-band Hubbard model (J_z-model) with bandwidth ratio $W_2/W_1 = 2$ and interaction parameters $U = U' + 2J_z$ within the DMFT+QMC in the fully frustrated phase at finite temperatures. Using the high-precision QMC algorithm developed in chapter 2, we found two successive metal-insulator transitions and thus corrected earlier QMC results from Liebsch (2004). We could therefore show that the additional spin-flip and pair-hopping terms that arise in the full J-model, which clearly exhibits an OSMT, are not a prerequisite for the OSMT scenario. We calculated estimates for the critical interactions of the

two transitions and for the critical temperature below which the narrow band exhibits a first-order transition. The second transition of the wide band is of second order for the examined temperatures. We also found that the OSM phase exhibits non-Fermi-liquid behavior. The QMC data was further compared to an expansion of the internal energy within weak-coupling perturbation theory. We determined the magnetic phase diagram of the J_z-model and compared it to results from weak- and strong-coupling expansions. Relevant microscopic mechanisms of frustration were discussed afterwards. The close connection of the physics of the J_z-model within the OSM phase to the spinless Falicov-Kimball (FK) model was subsequently investigated. For this purpose, we studied the solution of an exact mean-field theory of the FK model in the limit of infinite dimensions on a Bethe lattice. We found that the FK model exhibits an OSMT, where both transitions are of second-order. The analogy to the OSM phase was further revealed in a comparison of observables. Finally, we analyzed the influence of an additional hybridization to the FK Hamiltonian on the phase diagram.

Attractive Hubbard Model in d = 2

In chapter 4 we studied the negative-U Hubbard model on a square lattice in two spatial dimensions at weak-coupling within self-consistent second-order perturbation theory in the low-temperature limit at finite doping. First, we reviewed the Hartree-Fock results with special emphasis on the order parameter and the critical temperature in the limit of an asymptotically small interaction U. The calculation of the second-order corrections then revealed that the HF results are renormalized by a factor of the order of unity even at arbitrarily weak interaction ($U \to 0$). The renormalization factor was evaluated as a function of the chemical potential (or equivalently, the magnetic field B in the repulsive-U picture) for finite doping $1 - n$ (with $0 < n < 1$). We found that the renormalization factor can be calculated exactly in the limit $n \to 0$ (i.e., $B \to B_c$) and vanishes as $q \sim \sqrt{B_c - B}$, which implies that sc perturbation theory is not applicable in this limit. Furthermore, we observed, that the exact gap ratio $Um_x(0)/k_BT_c$ in the limit $U \to 0$ is identical to the BCS gap ratio $2\pi e^{-\gamma} \simeq 3.5285$. In summary, we have presented the first asymptotically exact results at weak-coupling for the negative-U Hubbard model in $d = 2$ at finite doping.

Appendix A

Auxiliary Calculations for Chapter 1

A.1 Particle-Hole Transformations of the Attractive Hubbard Model

In this section it is shown how the repulsive, half-filled Hubbard model in a magnetic field can be mapped onto the negative-U Hubbard model away from half filling. The mapping is based on a particle-hole transformation and is valid for bipartite lattices.

The Hamiltonian H^{R} of the repulsive Hubbard model in a homogeneous magnetic field B is given by:

$$H^{\mathrm{R}} = H_t + H_U + H_\mu + H_B \tag{A.1}$$

$$= H_t + H_U + H_\mu - B \sum_{i\sigma} \sigma n_{i\sigma} \,. \tag{A.2}$$

Using the particle-hole transformation that transforms electrons to holes and vice versa for both spin species on bipartite lattices,

$$\mathcal{T}_1 : \quad c^\dagger_{i\sigma} \;\mapsto\; (-1)^i \, c_{i\sigma} \,; \quad \sigma = \uparrow, \downarrow , \tag{A.3}$$

one can easily show that the band is half-filled at all temperatures for the chemical potential $\mu = \frac{U}{2}$. This also implies that the phase diagram is symmetric about half filling, $\langle n \rangle = 1$. The Hamiltonian (A.1) at half filling can then be mapped to the attractive Hubbard model (H^{A}) away from half filling, when restricting the transformation (A.3) only to one spin species, e.g., the spin up electrons:

$$\begin{aligned} \mathcal{T}_2 : \quad c^\dagger_{i\uparrow} \;&\mapsto\; (-1)^i \, c_{i\uparrow} \,, \\ c_{i\uparrow} \;&\mapsto\; (-1)^i \, c^\dagger_{i\uparrow} \,. \end{aligned} \tag{A.4}$$

This can be seen as follows. The operator of the kinetic energy, H_t, is invariant under the mapping $\mathcal{T}_2$:

$$H_t = -t \sum_{\langle ij\rangle\sigma} \big(c^\dagger_{i\sigma} c_{j\sigma} + \text{H.c.}\big) \;\mapsto\; -t \sum_{\langle ij\rangle} \big(-c_{i\uparrow} c^\dagger_{j\uparrow} + c^\dagger_{i\downarrow} c_{j\downarrow} + \text{H.c.}\big) = H_t \,. \tag{A.5}$$

The potential energy H_U is transformed according to:

$$H_U = U \sum_i n_{i\uparrow} n_{i\downarrow} \;\mapsto\; U \sum_i (1 - n_{i\uparrow}) n_{i\downarrow} \,. \tag{A.6}$$

The chemical potential of the Hubbard model in a magnetic field (1.8) at half filling is exactly given by $\mu = \frac{U}{2}$, thus

$$H_\mu = -\frac{U}{2} \sum_{i\sigma} n_{i\sigma} \;\mapsto\; -\frac{U}{2} \sum_{i\sigma} (1 - n_{i\uparrow} + n_{i\downarrow}) \,. \tag{A.7}$$

Finally, the contribution of the magnetic field, H_B, is transformed as:

$$H_B = -B \sum_{i\sigma} \sigma n_{i\sigma} \;\mapsto\; -B \sum_i (1 - n_{i\uparrow} - n_{i\downarrow}) \,. \tag{A.8}$$

Thus the Hamiltonian $H^{\mathrm{R}} = H_t + H_U + H_\mu + H_B$ of (1.8) is mapped onto the Hamiltonian H^{A} according to

$$\begin{aligned} H^{\mathrm{R}} \;\mapsto\; H^{\mathrm{A}} &= H_t - U \sum_i n_{i\uparrow} n_{i\downarrow} + \big(\tfrac{U}{2} + B\big) \sum_{i\sigma} n_{i\sigma} - \mathcal{N}\big(B + \tfrac{U}{2}\big) \\ &= H_{t'=t} + H_{U'=-U} + H_{\mu'=-(U/2+B)} + \text{const.} \end{aligned} \tag{A.9}$$

Hence, H^{A} corresponds to the negative-U Hubbard model away from half filling, with the chemical potential lowered by a constant $U+B$.

Assuming a homogeneous magnetization in the z-direction and a staggered magnetization in the x-direction, one can define the corresponding order parameters as follows:

$$\frac{1}{2}(1 + \sigma m_z) \equiv \langle n_{i\sigma} \rangle \tag{A.10}$$

$$\frac{1}{2}(-1)^i \, m_x \equiv \langle c^\dagger_{i\downarrow} c_{i\uparrow} \rangle \,, \tag{A.11}$$

where the definition in (A.11) is proper because the y-component of the staggered magnetization is assumed to vanish exactly. Employing $\mathcal{T}_2$ one finds that the order parameters are transformed according to

$$m_z = \langle n_{i\uparrow} \rangle - \langle n_{i\downarrow} \rangle \;\mapsto\; \langle 1 - n_{i\uparrow} - n_{i\downarrow} \rangle \equiv 1 - n \tag{A.12}$$

$$m_x \;\mapsto\; -2 \langle c^\dagger_{i\downarrow} c^\dagger_{i\uparrow} \rangle \equiv -2\chi_0 \,, \tag{A.13}$$

with the doping n and the singlet superconducting order parameter χ_0. Thus the homogenous magnetization in the z-direction of the Hamiltonian H^{R} corresponds to the doping (more explicitely, $1-n$) in the transformed Hamiltonian H^{A}. Similarly, the staggered magnetization in the XY plane of H^{R} corresponds to the singlet superconducting order parameter in the negative-U Hubbard model.

Appendix B

High-Frequency Expansion of the Self-Energy

In this part it is shown, how the coefficients of the high-frequency expansion of the self-energy can be computed analytically. This was done by Potthoff et al. (1997) for the single-band Hubbard model and by Oudovenko et al. (2005) and independently by Knecht (2002) for the multi-band model.

B.1 Single-Band Case

Starting point of the expansion of the self-energy is the single-impurity Anderson model (SIAM) which can be mapped onto the Hubbard model in the limit of infinite dimensionality. The Hamiltonian of the SIAM, which describes an impurity coupled to itinerant band-electrons, is given by:

$$\begin{aligned} H_{\mathrm{SIAM}} = &\sum_{k\sigma} (\epsilon_k - \mu) c^\dagger_{k\sigma} c_{k\sigma} + \sum_{\sigma} (\epsilon_d - \mu) d^\dagger_\sigma d_\sigma \\ &+ U n_{d\uparrow} n_{d-\downarrow} + \sum_{k\sigma} V_{kd} \left(d^\dagger_\sigma c_{k\sigma} + c^\dagger_{k\sigma} d_\sigma \right) . \end{aligned} \tag{B.1}$$

Here, $c^\dagger_{k\sigma}, c_{k\sigma}$ denote the creation and destruction operators of the itinerant electrons; $d^\dagger_\sigma, d_\sigma$ are the corresponding operators of the Wannier electrons of the d-orbital of the impurity. U is the on-site Coulomb interaction and V_{kd} is the hybridization-matrix of the itinerant electrons with the impurity. For the actual calculation, the hybridization appears only in the hybridization function:

$$\Delta(\omega) = \sum_k \frac{V^2_{kd}}{\omega - \epsilon_k} . \tag{B.2}$$

The self-consistency relation, which connects the SIAM in $d = \infty$ to the Hubbard model is given by (Jarrell, 1992; Georges and Kotliar, 1992):

$$\Delta_\sigma(\omega + \mu) = \omega - (\epsilon_d - \mu) - \Sigma_\sigma(\omega) - G_\sigma(\omega)^{-1} \,. \tag{B.3}$$

This relation allows to identify the Green function $G_{d\sigma}$ and the self-energy $\Sigma_{d\sigma}$ of the d-orbital of the SIAM with the corresponding Green function G_σ and self-energy Σ_σ of the Hubbard model.

For the high-frequency expansion, one needs the spectral function $A_{d\sigma}(\omega)$, which is connected to the Green function via:

$$A_{d\sigma}(\omega) = -\frac{1}{\pi}\mathrm{Im}G_{d\sigma}(\omega + i0^+) \,. \tag{B.4}$$

The Green function can also be expressed in terms of the spectral function:

$$G_{d\sigma}(\omega) = \int_{-\infty}^{\infty} \frac{A_{d\sigma}(\omega')}{\omega - \omega'} d\omega' \,. \tag{B.5}$$

Expanding the denominator of (B.5) in terms of $\frac{1}{\omega}$, one finds:

$$G_{d\sigma}(\omega) = \sum_{m=0}^{\infty} \frac{1}{\omega^{m+1}} M_{d\sigma}^{(m)} \,, \tag{B.6}$$

where $M_{d\sigma}^{(m)}$ denote the moments of the spectral density:

$$M_{d\sigma}^{(m)} = \int_{-\infty}^{\infty} \omega^m A_{d\sigma}(\omega) d\omega \,. \tag{B.7}$$

A similar expansion of the self-energy yields:

$$\Sigma_{d\sigma}(\omega) = \sum_{m=0}^{\infty} \frac{1}{\omega^m} C_{d\sigma}^{(m)} \,. \tag{B.8}$$

Here, $C_{d\sigma}^{(m)}$ are the coefficients of interest for the development of the model self-energy in chapter 2. When also expanding the hybridization function (B.2) in terms of $\frac{1}{\omega}$ one obtains the coefficients $C_{d\sigma}^{(m)}$ by comparison of coefficients using the Dyson equation (B.3). The coefficients $C_{d\sigma}^{(m)}$ are then dependent upon the spectral moments (B.7), for which a completely equivalent representation is given by:

$$M_{d\sigma}^{(m)} = \langle [\mathcal{L}^m d_\sigma, d_\sigma^\dagger]_+ \rangle, \tag{B.9}$$

where $\mathcal{L}\mathcal{O} \equiv [\mathcal{O}, H_{\mathrm{SIAM}}]_-$ labels the anticommutator of the operator $\mathcal{O}$ with the Hamiltonian, and $[\,,\,]_+$ labels the commutator. This representation of the spectral moments can be derived using the Heisenberg equation of motion for the time-dependent operators in the definition of the spectral density.

For the single-band Hubbard model, the first three moments of the spectral function are given by (Potthoff et al., 1997):

$$\begin{aligned}
M_{d\sigma}^{(0)} &= 1 \\
M_{d\sigma}^{(1)} &= \tilde{\epsilon}_d + U\langle n_{d-\sigma}\rangle \\
M_{d\sigma}^{(2)} &= \tilde{\epsilon}_d^2 + 2\tilde{\epsilon}_d U\langle n_{d-\sigma}\rangle + U^2\langle n_{d-\sigma}\rangle + \sum_k V_{kd}^2 \\
M_{d\sigma}^{(3)} &= \tilde{\epsilon}_d^3 + 3\tilde{\epsilon}_d^2 + \tilde{\epsilon}_d U^2\langle n_{d-\sigma}\rangle(2 + \langle n_{d-\sigma}\rangle) + U^3\langle n_{d-\sigma}\rangle \\
&\quad + \sum_k V_{kd}^2(\tilde{\epsilon}_k + 2\tilde{\epsilon}_d + 2U\langle n_{d-\sigma}\rangle) + U^2\langle n_{d-\sigma}\rangle(1 - \langle n_{d-\sigma}\rangle)\widetilde{B}_{d-\sigma}\,.
\end{aligned} \tag{B.10}$$

Here, $\tilde{\epsilon}_{d,k} = \epsilon_{d,k} - \mu$ and $\widetilde{B}_{d\sigma} = B_{d\sigma} - \mu$, with

$$\widetilde{B}_{d\sigma} = \tilde{\epsilon}_d + \frac{1}{\langle n_{d\sigma}\rangle(1 - \langle n_{d\sigma}\rangle)} \sum_k V_{kd}\langle c_{k\sigma}^\dagger d_\sigma(2n_{d-\sigma} - 1)\rangle\,. \tag{B.11}$$

Note, that the moments up to second order are dependent only upon one-particle expectation values. Higher-order correlation functions enter only for third order moments and higher.

The coefficients of the self-energy are then given by:

$$\begin{aligned}
C_{d\sigma}^{(0)} &= U\langle n_{d-\sigma}\rangle \\
C_{d\sigma}^{(1)} &= U^2\langle n_{d-\sigma}\rangle(1 - \langle n_{d-\sigma}\rangle) \\
C_{d\sigma}^{(2)} &= U^2\langle n_{d-\sigma}\rangle(1 - \langle n_{d-\sigma}\rangle)(\widetilde{B}_{d-\sigma} + U(1 - \langle n_{d-\sigma}\rangle))\,.
\end{aligned} \tag{B.12}$$

The high-frequency behavior of the self-energy is, therefore, determined by the coefficient $C_{d\sigma}^{(1)}$, which is a function of the on-site interaction U and the density, only.

B.2 Multi-Band Case

The high-frequency expansion of the self-energy for the multi-band case is performed analogously. The SIAM must be expanded to include multiple bands which are coupled in the same way as the bands in the multi-band Hubbard model. The Hamilto-

nian of such a multi-band SIAM is then given by:

$$\begin{aligned} H_{\mathrm{SIAM+}} = &\sum_{k\alpha}(\epsilon_{k\alpha}-\mu)c^\dagger_{k\alpha}c_{k\alpha} + \sum_{\alpha}(\epsilon_\alpha-\mu)d^\dagger_\alpha d_\alpha \\ &+ \frac{1}{2}\sum_{\alpha\neq\beta}U_{\alpha\beta}n_\alpha n_\beta + \sum_{k\alpha}V_{k\alpha}\left(d^\dagger_\alpha c_{k\alpha} + c^\dagger_{k\alpha}d_\alpha\right) , \end{aligned} \tag{B.13}$$

with multi-indices α, β combining spin σ and band m: $\alpha = m, \sigma$. The matrix $U_{\alpha\beta}$ is defined by:

$$U_{\alpha\beta} = \begin{pmatrix} 0 & U & U'-J_z & U' & U'-J_z & U' \\ U & 0 & U' & U'-J_z & U' & U'-J_z \\ U'-J_z & U' & 0 & U & U'-J_z & U' \\ U' & U'-J_z & U & 0 & U' & U'-J_z \\ U'-J_z & U' & U'-J_z & U' & 0 & U \\ U' & U'-J_z & U' & U'-J_z & U & 0 \end{pmatrix} . \tag{B.14}$$

A similar evaluation of the defining equation of the moments of the spectral density yields:

$$M^{(0)}_\gamma = 1 \tag{B.15}$$

$$M^{(1)}_\gamma = \tilde{\epsilon}_\gamma + \sum_{\alpha\neq\gamma}U_{\gamma\alpha}\langle n_\alpha\rangle \tag{B.16}$$

$$M^{(2)}_\gamma = \tilde{\epsilon}^2_\gamma + 2\tilde{\epsilon}_\gamma\sum_{\alpha\neq\gamma}U_{\gamma\alpha}\langle n_\alpha\rangle + \sum_{\alpha\neq\gamma}\sum_{\beta\neq\gamma}U_{\gamma\alpha}U_{\gamma\beta}\langle n_\alpha n_\beta\rangle + \sum_k V^2_{k\gamma} . \tag{B.17}$$

In contrast to the single-band case, two-particle correlation functions appear already in the second moment. For the coefficients of the self-energy one finds:

$$C^{(0)}_\gamma = \sum_{\beta\neq\gamma}U_{\beta\gamma}\langle n_\beta\rangle \tag{B.18}$$

$$C^{(1)}_\gamma = \sum_{\alpha\neq\gamma}\sum_{\beta\neq\gamma}U_{\alpha\gamma}U_{\beta\gamma}(\langle n_\alpha n_\beta\rangle - \langle n_\alpha\rangle\langle n_\beta\rangle) . \tag{B.19}$$

The correlation function $\langle n_\alpha n_\beta\rangle$ can be computed self-consistently within the DMFT+QMC algorithm.

Appendix C

Auxiliary Calculations for the Two-Band Falicov-Kimball Model

C.1 Symmetry Properties of the FK Hamiltonian

The Hamiltonian (3.46) of the two-band FK model at half filling implies symmetries that are used for the calculation of the Green function. It is shown here, that the hybridization $V \equiv V_{mm'}$ is a function of one variable, only.
Hermiticity of the Hamiltonian implies

$$V = V^\dagger \quad \Longleftrightarrow \quad V_{mm'} = V^*_{m'm}\,, \tag{C.1}$$

therefore, the matrix V can be written as

$$V = V_0\sigma_0 + V_1\sigma_1 + V_2\sigma_2 + V_3\sigma_3 \qquad (V_\alpha \in \mathbb{R}), \tag{C.2}$$

with σ_0 the unit matrix in 2 dimensions and the Pauli matrices $\sigma_{1,2,3}$.
Particle-hole symmetry under the transformation

$$d_{i1} \to d^\dagger_{i1}(-1)^i e^{i\alpha/2}, \quad d_{i2} \to d^\dagger_{i2}(-1)^i e^{-i\alpha/2}, \quad f_{im} \to f^\dagger_{im}(-1)^i, \qquad \alpha \in \mathbb{R}\,, \tag{C.3}$$

then gives the following equation for V:

$$\begin{aligned}\sum_{mm'} V_{mm'} d^\dagger_m d_{m'} &\stackrel{!}{=} V_{11} d_1 d_1^\dagger + V_{22} d_2 d_2^\dagger + V_{12} d_1 d_2^\dagger e^{-i\alpha} + V_{21} d_2 d_1^\dagger e^{i\alpha} \\ &= \mathrm{Tr}(V) - V_{11} d_1^\dagger d_1 - V_{22} d_2^\dagger d_2 - e^{-i\alpha} V_{12} d_2^\dagger d_1 - e^{i\alpha} V_{21} d_1^\dagger d_2\,,\end{aligned} \tag{C.4}$$

thus

$$\begin{aligned}&\mathrm{Tr}(V) = 0, \quad V_{11} = -V_{11}, \quad V_{22} = -V_{22}, \\ &\qquad\qquad V_{12} = -e^{i\alpha} V_{12}, \quad V_{21} = -e^{-i\alpha} V_{21}\,.\end{aligned} \tag{C.5}$$

The first three conditions imply $V_0 = V_3 = 0$.
The last two imply $-ie^{i\alpha/2}V_{21} = ie^{-i\alpha/2}V_{12} = (-ie^{i\alpha/2}V_{21})^*$, thus $v \equiv -ie^{i\alpha/2}V_{21} \in \mathbb{R}$. It follows that:

$$V_{12} = V_1 + iV_2 = ive^{-i\alpha/2} = v\left[\sin(\alpha/2) + i\cos(\alpha/2)\right], \tag{C.6}$$

hence:

$$V_1 = v\sin(\alpha/2), \quad V_2 = v\cos(\alpha/2), \quad V = v\left[\sin(\alpha/2)\sigma_1 + \cos(\alpha/2)\sigma_2\right]. \tag{C.7}$$

Note, that different choices for α are all canonically equivalent at half filling. Therefore, the sign of the hybridization is unimportant, since the model with parameter α is canonically equivalent to the model with parameter $\alpha' = \alpha + 2\pi$, which has a hybridization $v' = -v$. Since all choices for α are equivalent, one can choose $\alpha = \pi$ for simplicity, which corresponds to

$$V = v\sigma_1 = \begin{pmatrix} 0 & v \\ v & 0 \end{pmatrix} \qquad (v > 0). \tag{C.8}$$

Since the sign is unimportant one can choose $v > 0$.

C.2 Symmetry Properties of the Green Function

The defining equation of the Green function G, (3.60), implies important symmetries for G.

The following identity is proved here: If $G_V(z)$ is a solution, then $\sigma_3\left[G_V(-z^*)\right]^\dagger\sigma_3$ is also a solution:

$$\begin{aligned}
-\sigma_3\left[G_V(-z^*)\right]^\dagger\sigma_3 &= -\frac{1}{4}\sum_b \left\{\sigma_3\big[G_{0V}^{(b)}(-z^*)^\dagger\big]^{-1}\sigma_3 - \Theta\sigma_3 G_V(-z^*)^\dagger\sigma_3\Theta\right\}^{-1} \\
&= -\frac{1}{4}\sum_b \left\{-\sigma_3 G_{0,-V}^{(3-b)}(z)^{-1}\sigma_3 - \Theta\big(\sigma_3 G_V(-z^*)^\dagger\sigma_3\big)\Theta\right\}^{-1} \\
&= \frac{1}{4}\sum_b \left\{G_{0V}^{(3-b)}(z)^{-1} - \Theta\big(-\sigma_3 G_V(-z^*)^\dagger\sigma_3\big)\Theta\right\}^{-1} \\
&\overset{b\leftrightarrow(3-b)}{=} \frac{1}{4}\sum_b \left\{G_{0V}^{(b)}(z)^{-1} - \Theta\big(-\sigma_3 G_V(-z^*)^\dagger\sigma_3\big)\Theta\right\}^{-1}.
\end{aligned} \tag{C.9}$$

Since both solutions coincide for $\Theta = 0$, they are identical also for $\Theta \neq 0$. Thus

$$G_V(z) = \sigma_3\left[G_V(-z^*)\right]^\dagger\sigma_3. \tag{C.10}$$

This identity can then be used, e.g., to show that the DOS of both orbitals in the FK model is symmetric.

Appendix D

Auxiliary Calculations for Chapter 4

D.1 Density of States in d = 1, 2, 3

In the following, we briefly comment on the non-interacting density of states of the Hubbard model for the hypercubic lattice in $d = 1, 2$ and $d = 3$.

For $U = 0$, the energy dispersion in momentum space of the Hubbard model is given by

$$\epsilon_{\boldsymbol{k}} = -2t \sum_{l=1}^{d} \cos(k_l)\,. \tag{D.1}$$

The density of states is then obtained via its definition:

$$N(\epsilon) = (2\pi)^{-d} \int\limits_{1.\mathrm{BZ}} d\boldsymbol{k}\; \delta(\epsilon - \epsilon_{\boldsymbol{k}}) = \frac{1}{2\pi t} \int\limits_{0}^{\infty} dx\; \left[J_0(x)\right]^d \cos\left(\tfrac{\epsilon}{2t} x\right), \tag{D.2}$$

with the Bessel function of the first kind $J_0(x)$.

In $d = 1$, the integral can be evaluated exactly:

$$N_1(\epsilon) = \frac{1}{\pi} \frac{1}{\sqrt{(2t)^2 - \epsilon^2}} \Theta(2t - |\epsilon|) \tag{D.3}$$

with the step function Θ. Thus, the DOS has a square root divergence at the band edges $\epsilon_{\pm} = \pm 2t$.

In $d = 2$ one finds:

$$N_2(\epsilon) = \frac{1}{4\pi t}\, P_{-\frac{1}{2}}\left[\tfrac{1}{2}\left(\frac{\epsilon}{2t}\right)^2 - 1\right] \Theta(4t - |\epsilon|) \tag{D.4}$$

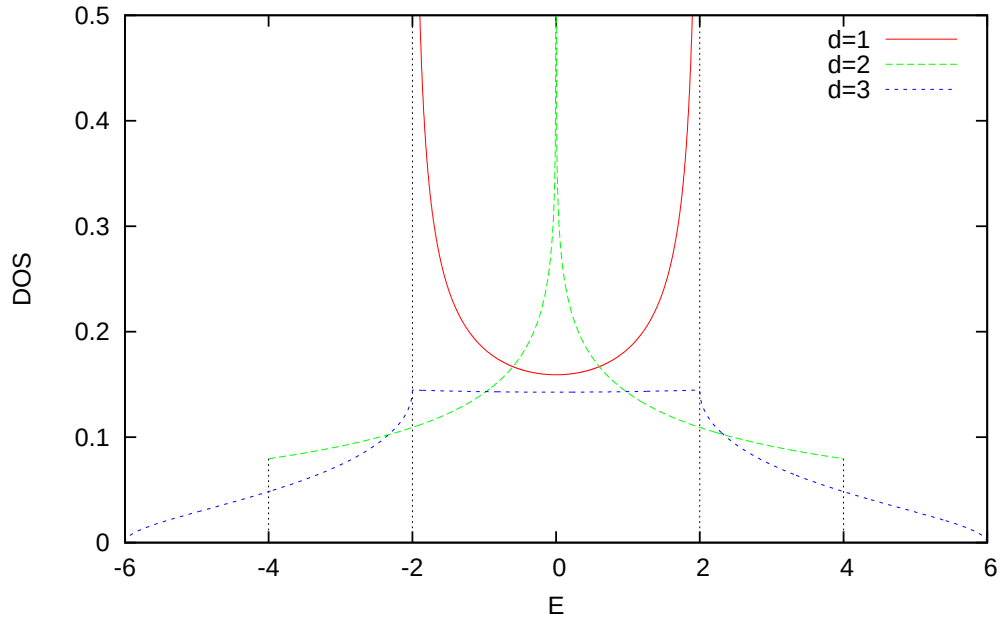

Figure D.1: Non-interacting density of states of the Hubbard model for the hypercubic lattice in dimensions $d = 1, 2, 3$.

where $P_n[x]$ denotes the Legendre functions of the first kind. Here, the DOS diverges logarithmically at the Fermi energy $\epsilon = 0$ according to

$$N(\epsilon) \sim \frac{1}{2\pi^2 t} \ln\left(\frac{4t}{|\epsilon|}\right) \qquad \text{for} \quad |\epsilon| \to 0\,. \tag{D.5}$$

The value at the band edges $\epsilon_\pm = \pm 4t$ is exactly $N_2(\epsilon_\pm) = 1/(4\pi)$.

In $d = 3$, the DOS has to be computed numerically for generic energies. Here, the band edges are at $\epsilon_\pm = \pm 6t$.

The non-interacting DOS for $d = 1, 2, 3$ are shown in Fig. D.1.

D.2 Asymptotic Results for small U

In this section, we calculate the asymptotic behavior of the critical temperature, the order parameter m_x as well as the energy gain due to symmetry breaking within the Hartree-Fock approximation.

The critical temperature $T_c = \beta_c^{-1}$ is determined by $m_x(T_c) = 0$ in (4.17), implying

$$\begin{aligned} 1 &= \frac{U}{2} \int_{-\infty}^{\infty} d\epsilon \, N(\epsilon) \, \frac{\tanh\left[\frac{1}{2}\beta_c(\epsilon - h_0)\right]}{\epsilon - h_0} \\ &= \frac{U}{2} J(\tfrac{1}{2}\beta_c) \, . \end{aligned} \tag{D.6}$$

Considering the function J for large arguments one finds (van Dongen, 1994*a*)[1]:

$$J(\gamma) = N_2'(0)[\ln(\gamma) + I_2 + \ln 2] + \mathcal{O}(\gamma^{-1}) \, , \tag{D.7}$$

with

$$I_2 = \int_0^{\infty} dy \, \frac{1}{y} \left[\tanh(y) - 1 + \frac{N_2'(y)}{N_2'(0)} \right] - \ln 2 \tag{D.8}$$

and

$$N_2'(\epsilon) = \tfrac{1}{2}[N_2(\epsilon + h_0) + N_2(h_0 - \epsilon)] \, . \tag{D.9}$$

The constant I_2 is difficult to calculate exactly for the square lattice in $d = 2$, but can be approached numerically. The numerical solution for I_d as a function of the field h_0 is shown in Fig. 4.1. In the limit $h_0 \to 0$, I_2 diverges logarithmically: $I_2(h_0) \sim 0.557 \ln(h_0) + 2.116$. The asymptotic standard error of both constants from a least square fit is 0.5%. Approximating the DOS by a square density of states, $N_s(\epsilon) = \frac{1}{2\epsilon_+}\Theta(\epsilon_+ - |\epsilon|)$, with the step function Θ, one finds for $B > 0$:

$$I_2 = \gamma + \ln \epsilon_+ \ln 2 - \ln \pi \simeq 1.51195 \, , \tag{D.10}$$

where $\gamma \simeq 0.577$ is Euler's constant and $\epsilon_+ = 4t$ the band edge. The constant can be calculated explicitly in high dimensions $d \gg 1$. Including corrections in $1/d$ one finds for the hypercubic lattice (van Dongen, 1994*a*):

$$I_d = \tfrac{3}{2} \ln 2 + \tfrac{1}{2}\gamma - \ln \pi + \frac{1}{4d} + \mathcal{O}(\tfrac{1}{d^2}) \simeq 0.1836 + \frac{1}{4d} \, . \tag{D.11}$$

It is interesting to note that the constant I_d including $1/d$ corrections is still a factor $\frac{0.3086}{1.51195} \simeq 0.2$ smaller than I_2 for the square density.

[1] Here, the calculation was performed for the extended Hubbard model in dimensions $d \geq 3$. The argumentation that leads to our result is identical when replacing the density of states with $N_2'(\epsilon)$. The essential observation is the fact that the leading contribution to the integration is due to energies $\epsilon \leq \mathcal{O}(\beta_c^{-1})$, such that $N_2'(\epsilon)$ can be replaced by $N_2'(0)$. The remaining integral can then be calculated explicitly by multiplying the integrand by a convergence factor $e^{-\kappa\epsilon}$ and taking the limit $\kappa \downarrow 0$.

Combining the above results for $U \to 0$, one finds that the critical temperature is exponentially small as a function of U:

$$k_B T_c^{\mathrm{HF}} \sim \exp\left(I_d - \frac{1}{U N_2(h_0)} \right). \tag{D.12}$$

Corrections to (D.12) are exponentially small and of order T_c^2, as can be inferred from (D.7).

Let us now consider the behavior of the order parameter m_x in the ground state ($T = 0$ or $\beta = \infty$) for small U and at fixed B with $0 < B < B_c$. In this case one expects that $\Delta m_z = 1 - m_z$ approaches a constant. From (4.17) follows that

$$\begin{aligned} \frac{2}{U} &= \int_{-\infty}^{\infty} d\epsilon\, N(\epsilon) \frac{1}{\sqrt{(\epsilon - h_0)^2 + (U m_x/2)^2}} \\ &\propto 2N(B) \ln\left[\frac{\sqrt{\epsilon_+^2 - B^2}}{U m_x/2} \right], \end{aligned} \tag{D.13}$$

implying

$$\frac{1}{2} U m_x^{\mathrm{HF}} \propto 2\sqrt{\epsilon_+^2 - B^2}\, \exp\left(-\tfrac{1}{UN(B)} \right). \tag{D.14}$$

This result shows that the staggered magnetization m_x is, indeed, exponentially small as $U \to 0$. The exact behavior of m_x, including the temperature dependence, can be determined by subtracting the defining equation of the critical temperature (D.6) from the consistency relation (4.17):

$$0 = \int_{-\infty}^{\infty} d\epsilon\, N(\epsilon) \left[\frac{\tanh(\frac{1}{2}\beta \eta_{\epsilon\uparrow})}{\eta_{\epsilon\uparrow}} - \frac{\tanh[\frac{1}{2}\beta_c(\epsilon - h_0)]}{\epsilon - h_0} \right] \tag{D.15}$$

$$= 2 \int_0^{\infty} N_2'(\epsilon) \left[\frac{\tanh(\frac{1}{2}\beta \eta_{\epsilon})}{\eta_{\epsilon}} - \frac{\tanh(\frac{1}{2}\beta_c \epsilon)}{\epsilon} \right], \tag{D.16}$$

with $\eta_\epsilon = \mathrm{sign}(\epsilon)\sqrt{\epsilon^2 + (U m_x/2)^2}$. Making use of the fact that the leading contribution to the integral (D.16) stems from the energy range $0 < \epsilon \lesssim \mathcal{O}(\beta_c^{-1})$, one finds (van Dongen, 1994*a*)[2]:

$$m_x^{\mathrm{HF}}(T = 0) = \frac{2\pi e^{-\gamma}}{U \beta_c}, \tag{D.17}$$

with Euler's constant $\gamma \approx 0.577$. The gap ratio $U m_x(T = 0)/T_c^{\mathrm{HF}} = 2\pi e^{-\gamma}$ is therefore identical to the standard BCS gap ratio [compare, e.g., Ashcroft and Mermin

[2] See footnote 1 on page 155.

(1976)]. Correction terms at low temperatures are exponentially small:

$$m_x^{\mathrm{HF}}(\theta) = m_x^{\mathrm{HF}}(T{=}0)\left[1 - \sqrt{\frac{\theta\pi}{\delta_0}}e^{-2\delta_0/\theta}\right], \tag{D.18}$$

with $\theta = T/T_c \ll 1$ and $\delta_0 = \frac{1}{2}\beta_c U m_x(T=0)$. Near T_c, the order parameter shows mean-field critical behavior,

$$\delta(\theta) \sim \sqrt{\frac{1-\theta}{Z}}\,, \tag{D.19}$$

where the constant Z is defined by

$$Z \equiv \int_0^\infty dy\, \frac{\sinh(2y) - 2y}{4y^3\cosh^2(y)} \simeq 0.4263\,. \tag{D.20}$$

Let us now calculated the gain in free energy per lattice site due to the symmetry breaking for $T \geq 0$ and fixed value of m_z. The calculation is performed in analogy to van Dongen (1994*a*). From the expression for the grand canonical potential we have:

$$\begin{aligned}
\Omega^{\mathrm{HF}} &\equiv \omega(T, m_z, m_x) - \omega(T, m_z, 0) \\
&= \frac{1}{4}Um_x^2 - \frac{4}{\beta}\int_0^\infty N_2'(\epsilon)\ln\left[\frac{\cosh(\frac{1}{2}\beta\eta_\epsilon)}{\cosh(\frac{1}{2}\beta\epsilon)}\right] \\
&= \frac{1}{4}Um_x^2\left\{1 - U\frac{2\theta}{\delta^2}\int_0^\infty dy\; N_2'(2y/\beta_c)\ln\left[\frac{\cosh(\sqrt{y^2+\delta^2}/\theta)}{\cosh(y/\theta)}\right]\right\},
\end{aligned} \tag{D.21}$$

Recall, $\eta_\epsilon = \mathrm{sign}(\epsilon)\sqrt{\epsilon^2 + h_0^{x\,2}}$. Inserting the criterion for the critical temperature T_c from (D.6) which can be rewritten similarly in the form

$$1 = U\int_0^\infty dy\; N_2'(2y/\beta_c)\frac{\tanh(y)}{y}\,, \tag{D.22}$$

one finds the following exact relation:

$$\Omega^{\mathrm{HF}} = -\frac{1}{4}U^2m_x^2\int_0^\infty dy\; N_2'(2y/\beta_c)\left\{\frac{2\theta}{\delta^2}\ln\left[\frac{\cosh(\sqrt{y^2+\delta^2}/\theta)}{\cosh(y/\theta)}\right] - \frac{\tanh(y)}{y}\right\}. \tag{D.23}$$

The leading contribution to the integral is due to y values of the order of unity, so that the factor $N_2'(2y/\beta_c)$ can be replaced by $N_2'(0)$ in the limit $U \downarrow 0$, or similarly

$\beta_c \to \infty$. One thus finds

$$\begin{aligned}\Omega^{\mathrm{HF}} &\sim -\frac{1}{4}U^2 \left[m_x^{\mathrm{HF}}\right]^2 N_2(h_0) \int\limits_0^\infty dy \left\{ \frac{2\theta}{\delta^2} \ln\left[\frac{\cosh(\sqrt{y^2+\delta^2}/\theta)}{\cosh(y/\theta)}\right] - \frac{\tanh(y)}{y} \right\} \\ &\equiv -\frac{1}{4}U^2 \left[m_x^{\mathrm{HF}}\right]^2 N_2(h_0)\, \Phi(\theta)\,. \end{aligned} \tag{D.24}$$

Here, the integral Φ is convergent for all values of θ. It approaches the value $\frac{1}{2}$ for $\theta \downarrow 0$ and vanishes for $\theta \uparrow 0$.

D.3 Evaluation of the Integrals $\mathbf{I_{h_1}}$ and $\mathbf{I_{h_3}}$ for $\mathbf{h_0^x \ll B < B_c}$

The leading contribution to the free energy derivative df_2/dh_0^x in the limit $h_0^x \to 0$ is due to the integrals I_{h_1} and I_{h_3}, which are evaluated in the following for generic values of the magnetic field B, with $h_0^x \ll B < B_c$. The constraints of the field h_0 will become clear in the remainder of this section. First, we consider the integral I_{h_1}; the integral I_{h_3} can then be evaluated in the same manner.

Substitution of $\mathbf{4}+\boldsymbol{q} \to \boldsymbol{q}$ in (4.79) leads to the following form of the integral I_{h_1}:

$$I_{h_1} = \iiint\limits_{1.\mathrm{BZ}} \frac{d\mathbf{1}d\mathbf{4}d\boldsymbol{q}}{(2\pi)^6} \frac{1}{\big(|\eta_{\mathbf{1}\uparrow}| + |\eta_{\mathbf{1}+\boldsymbol{q}-\mathbf{4},\uparrow}| + |\eta_{\boldsymbol{q},\downarrow}| + |\eta_{\mathbf{4}\downarrow}|\big)|\eta_{\mathbf{1}\uparrow}\eta_{\boldsymbol{q}\downarrow}|}\,, \tag{D.25}$$

where the integration extends over the first Brillouin zone and where $\mathbf{1}$ denotes $\boldsymbol{k}_1$ and so forth. The leading contribution to the integral is due to momenta for which both $\eta_{\mathbf{1}\uparrow}$ and $\eta_{\boldsymbol{q}\downarrow}$ become small. In the limit $h_0^x \to 0$ and with $|\eta_{\boldsymbol{k}\sigma}| = \sqrt{(\epsilon_{\boldsymbol{k}} - \sigma h_0)^2 + {h_0^x}^2}$ this is the case for $\boldsymbol{k}$ values close to the $\epsilon_{\boldsymbol{k}\sigma} = \sigma h_0$ surface. Thus for generic values of $\mathbf{4}$, the sum of the energy contributions in (D.25) is dominated by $\eta_{\mathbf{1}+\boldsymbol{q}-\mathbf{4},\uparrow}$ and $\eta_{\mathbf{4}\downarrow}$. The integral I_{h_1} can therefore be approximated by

$$I_{h_1} \sim \iiint\limits_{1.\mathrm{BZ}} \frac{d\mathbf{1}d\mathbf{4}d\boldsymbol{q}}{(2\pi)^6} \frac{1}{\big(|\eta_{\boldsymbol{q}-\mathbf{4}+\mathbf{1}\uparrow}| + |\eta_{\mathbf{4}\downarrow}|\big)|\eta_{\mathbf{1}\uparrow}\eta_{\boldsymbol{q}\downarrow}|}\,. \tag{D.26}$$

Employing the 2-particle density of states

$$\nu_d(\epsilon_4, \epsilon_2, \boldsymbol{q}) = \frac{1}{\mathcal{N}} \sum_{\boldsymbol{k}_4, \boldsymbol{k}_2} \delta(\epsilon_4 - \epsilon_{\boldsymbol{k}_4}) \delta(\epsilon_2 - \epsilon_{\boldsymbol{k}_2}) \delta_{\boldsymbol{k}_4, \boldsymbol{k}_2 + \boldsymbol{q}}\,, \tag{D.27}$$

where the sum is as usual over the first Brillouin zone, the integral I_{h_1} can be written as:

$$I_{h_1} \sim \frac{1}{4\pi^2} \iint d\epsilon_2 d\epsilon_4 \, \frac{1}{|\eta_{\epsilon_2\uparrow}| + |\eta_{\epsilon_4\downarrow}|} \int_{-\pi}^{\pi} d\boldsymbol{q} \; \nu_d(\epsilon_4, \epsilon_2, \boldsymbol{q}) \iint d\epsilon_1 d\epsilon_3 \, \frac{1}{|\eta_{\epsilon_1\uparrow}\eta_{\epsilon_3\uparrow}|} \nu_d(\epsilon_1, \epsilon_3, \boldsymbol{q}) \,. \tag{D.28}$$

The leading contribution to the ϵ_1 and ϵ_3 integrals on the right hand side of (D.28) is due to the region where both $\eta_{\epsilon_1\uparrow}$ and $\eta_{\epsilon_3\uparrow}$ become small. For $h_0 \gg h_0^x$ (recall, $h_0 = B + h_0^z$), the position of the logarithmic divergence of the density of states in $d = 2$ (which occurs at $\epsilon = 0$) does not coincide with the divergence of the energy denominator in (D.28). For small h_0^x, the integral then reduces to

$$\begin{aligned} \iint d\epsilon_1 d\epsilon_3 \, \frac{1}{|\eta_{\epsilon_1\uparrow}\eta_{\epsilon_3\uparrow}|} \nu_d(\epsilon_1, \epsilon_3, \boldsymbol{q}) \; &\sim \; 4\nu_d(h_0, -h_0, \boldsymbol{q}) \left[\int_0^{\epsilon_+} d\epsilon \, \frac{1}{\sqrt{\epsilon^2 + {h_0^x}^2}} \right]^2 \\ &= \; 4\nu_d(h_0, -h_0, \boldsymbol{q}) \left[\ln\left(\frac{\epsilon_+}{h_0^x} \right) \right]^2 , \end{aligned} \tag{D.29}$$

where $\epsilon_+ = 4t$ is the bandwidth in $d = 2$. Thus, to leading logarithmic order we have

$$I_{h_1} \sim 4 \left[\ln\left(\frac{t}{h_0^x} \right) \right]^2 \iint d\epsilon_2 d\epsilon_4 \, \frac{N_d(\epsilon_2, \epsilon_4, h_0)}{|\eta_{\epsilon_2\uparrow}| + |\eta_{\epsilon_4\downarrow}|} \,, \tag{D.30}$$

with

$$N_d(\epsilon_2, \epsilon_4, h_0) = \int_{-\pi}^{\pi} \frac{d\boldsymbol{q}}{4\pi^2} \; \nu_d(h_0, -h_0, \boldsymbol{q}) \, \nu_d(\epsilon_2, \epsilon_4, \boldsymbol{q}) \,. \tag{D.31}$$

The function $N_d(\epsilon_1, \epsilon_2, h_0)$ can now be expressed in terms of a lattice sum over integrals of Bessel functions $J_n(x)$:

$$N_d(\epsilon_1, \epsilon_2, h_0) = \sum_{\boldsymbol{j}} F_{\boldsymbol{j}}(h_0) F_{\boldsymbol{j}}(-h_0) F_{\boldsymbol{j}}(\epsilon_1) F_{\boldsymbol{j}}(\epsilon_2) \,, \tag{D.32}$$

with

$$F_{\boldsymbol{j}}(\epsilon) = \frac{1}{2\pi} \int_{-\infty}^{\infty} d\eta \; e^{-i\epsilon\eta} [\mathrm{sign}(z)]^{|\boldsymbol{j}|} \prod_{l=1}^{d} \; J_{|j_l|}(|z|) \,; \qquad z = -2t\eta \,. \tag{D.33}$$

Here, $|\boldsymbol{j}|$ denotes the Manhattan distance on the square lattice. A close examination shows that $F_{\boldsymbol{j}}(\epsilon)$ exhibits an integrable logarithmic divergence at $\epsilon = 0$ for even $|\boldsymbol{j}|$ in

$d = 2$. The energy integrals on the right hand side of (D.30) are therefore convergent for $h_0 \gg h_0^x$. They contribute a finite, h_0 dependent coefficient P:

$$P(h_0) = \iint d\epsilon_1 d\epsilon_2 \, \frac{N_d(\epsilon_1, \epsilon_2, h_0)}{|\eta_{\epsilon_{2\uparrow}}| + |\eta_{\epsilon_{4\downarrow}}|} \; < \; |\infty| \, . \tag{D.34}$$

At this point, it is important to note that the requirement $h_0 \gg h_0^x$ is essential for the validity of (D.34). For $h_0 \to h_0^x$, one has to take into account the logarithmic divergence of the density of states at $\epsilon = 0$, which results in a logarithmic divergence of the order of $\ln(t/h_0^x)^6$ for I_{h_1}. This, in turn, results in the breakdown of perturbation theory for the Hubbard model (without magnetic field) in $d = 2$ (Schauerte and van Dongen, 2002; Kopietz, 1993).

For the further evaluation of the integral I_{h_1} it is useful to distinguish between lattice sites with even and odd values of $|\boldsymbol{j}|$. Inserting (D.32) into (D.34) yields

$$P = \sum_{|\boldsymbol{j}| \text{ even}} [F_{\boldsymbol{j}}(h_0)]^2 \int_0^\infty d\tau [\hat{F}_{\boldsymbol{j}}(\tau)]^2 + \sum_{|\boldsymbol{j}| \text{ odd}} [F_{\boldsymbol{j}}(h_0)]^2 \int_0^\infty d\tau [\hat{F}_{\boldsymbol{j}}(\tau)]^2 \, , \tag{D.35}$$

with

$$\hat{F}_{\boldsymbol{j}}(\tau) = \int_{-\infty}^{\infty} d\epsilon \; F_{\boldsymbol{j}}(\epsilon) e^{-\tau|\epsilon + h_0|} \, . \tag{D.36}$$

For even $|\boldsymbol{j}|$ we have:

$$\hat{F}_{\boldsymbol{j}}(\tau) = \hat{F}^e_{\boldsymbol{j}}(\tau) = \frac{2}{\pi} \int_0^\infty dz \; \cos[h_0 z/(2t)] \frac{2t\tau}{(2t\tau)^2 + z^2} \; \prod_{l=1}^{d} \; J_{|j_l|}(z) \, , \tag{D.37}$$

for odd $|\boldsymbol{j}|$:

$$\hat{F}_{\boldsymbol{j}}(\tau) = \hat{F}^o_{\boldsymbol{j}}(\tau) = -i \, \frac{2}{\pi} \int_0^\infty dz \; \sin[h_0 z/(2t)] \frac{2t\tau}{(2t\tau)^2 + z^2} \; \prod_{l=1}^{d} \; J_{|j_l|}(z) \, . \tag{D.38}$$

The τ integration in (D.35) can be performed explicitly, resulting in integrals of the form

$$\int_0^\infty d\tau \; [\hat{F}^e_{\boldsymbol{j}}(\tau)]^2 = \frac{1}{\pi t} \int_0^\infty \int_0^\infty dz_1 dz_2 \; \frac{\cos[h_0 z_1/(2t)] \cos[h_0 z_2/(2t)]}{z_1 + z_2} \; \prod_{l=1}^{d} \; J_{|j_l|}(z_1) J_{|j_l|}(z_2) \, , \tag{D.39}$$

where $|\boldsymbol{j}|$ is even. For odd $|\boldsymbol{j}|$, one has to replace the cosine functions by sine functions.

Hence, to leading logarithmic order in h_0^x, the integral I_{h_1} reads

$$I_{h_1} \sim 4\left[\ln\left(\frac{t}{h_0^x}\right)\right]^2 \left\{ \sum_{|\boldsymbol{j}| \text{ even}} [F_{\boldsymbol{j}}(h_0)]^2 \int_0^\infty d\tau [\hat{F}^e_{\boldsymbol{j}}(\tau)]^2 + \sum_{|\boldsymbol{j}| \text{ odd}} [F_{\boldsymbol{j}}(h_0)]^2 \int_0^\infty d\tau [\hat{F}^o_{\boldsymbol{j}}(\tau)]^2 \right\}. \tag{D.40}$$

The integral I_{h_3}, with

$$I_{h_3} = \iiint\limits_{1.\mathrm{BZ}} \frac{d\mathbf{1} d\mathbf{4} d\boldsymbol{q}}{(2\pi)^6} \frac{\epsilon_{1+q,\uparrow}\epsilon_{4\downarrow}}{\big(|\eta_{1\uparrow}| + |\eta_{1+q,\uparrow}| + |\eta_{4+q,\downarrow}| + |\eta_{4\downarrow}|\big)|\eta_{1\uparrow}\eta_{1+q\uparrow}\eta_{4+q\downarrow}\eta_{4\downarrow}|}, \tag{D.41}$$

gives the following contribution:

$$I_{h_3} \sim 4\left[\ln\left(\frac{t}{h_0^x}\right)\right]^2 \left\{ - \sum_{|\boldsymbol{j}| \text{ even}} [F_{\boldsymbol{j}}(h_0)]^2 \int_0^\infty d\tau [\check{F}^e_{\boldsymbol{j}}(\tau)]^2 - \sum_{|\boldsymbol{j}| \text{ odd}} [F_{\boldsymbol{j}}(h_0)]^2 \int_0^\infty d\tau [\check{F}^o_{\boldsymbol{j}}(\tau)]^2 \right\}, \tag{D.42}$$

where $\check{F}$ for even $|\boldsymbol{j}|$ is given by

$$\check{F}_{\boldsymbol{j}}(\tau) = \check{F}^e_{\boldsymbol{j}}(\tau) = -\frac{2}{\pi} \int_0^\infty dz\, \sin[h_0 z/(2t)] \frac{z}{(2t\tau)^2 + z^2} \prod_{l=1}^{d} J_{|j_l|}(z), \tag{D.43}$$

and for odd $|\boldsymbol{j}|$ by

$$\check{F}_{\boldsymbol{j}}(\tau) = \check{F}^o_{\boldsymbol{j}}(\tau) = i\,\frac{2}{\pi} \int_0^\infty dz\, \cos[h_0 z/(2t)] \frac{z}{(2t\tau)^2 + z^2} \prod_{l=1}^{d} J_{|j_l|}(z). \tag{D.44}$$

Combining the integrals I_{h_1} and I_{h_3} and simplifying the trigonometric function yields

$$\begin{aligned} I_{h_1} + I_{h_3} \;&\sim\; 4\left[\ln\left(\frac{t}{h_0^x}\right)\right]^2 \sum_{|\boldsymbol{j}|} [F_{\boldsymbol{j}}(h_0)]^2 \left(FT^e_{\boldsymbol{j}} + FT^o_{\boldsymbol{j}}\right) && \text{(D.45)} \\ &\equiv\; 4\left[\ln\left(\frac{t}{h_0^x}\right)\right]^2 LS(h_0), && \text{(D.46)} \end{aligned}$$

with

$$\begin{aligned} FT^e_{\boldsymbol{j}} &= \int_0^\infty d\tau\, [\hat{F}^e_{\boldsymbol{j}}(\tau)]^2 = -\int_0^\infty d\tau\, [\check{F}^o_{\boldsymbol{j}}(\tau)]^2, \\ FT^o_{\boldsymbol{j}} &= \int_0^\infty d\tau\, [\hat{F}^o_{\boldsymbol{j}}(\tau)]^2 = -\int_0^\infty d\tau\, [\check{F}^e_{\boldsymbol{j}}(\tau)]^2. \end{aligned} \tag{D.47}$$

Note that the functions $FT^e_{\boldsymbol{j}}$ and $FT^o_{\boldsymbol{j}}$ in the lattice sum on the right hand side of (D.45) are evaluated for both even and odd values of $|\boldsymbol{j}|$. The lattice sum LS in (D.46) is still too complicated to be calculated exactly but can be approximated numerically.

D.4 Numerical Evaluation of the Integral $\mathbf{I_{h_1}}$ for $\mathbf{h_0^x \ll B < B_c}$

In the following we discuss the numerical evaluation of the integral I_{h_1}. For this purpose, we first simplify the lattice sum in (D.45) according to

$$LS(h_0) = \sum_{|\boldsymbol{j}| \text{ even}} [F_{\boldsymbol{j}}(h_0)]^2 FT_{\boldsymbol{j}} + \sum_{|\boldsymbol{j}| \text{ odd}} [F_{\boldsymbol{j}}(h_0)]^2 FT_{\boldsymbol{j}} \,, \tag{D.48}$$

with

$$FT_{\boldsymbol{j}}(h_0) = FT^e_{\boldsymbol{j}} + FT^o_{\boldsymbol{j}} = \frac{1}{\pi t} \int_0^\infty \int_0^\infty dx\, dy\, \frac{\cos[\frac{h_0}{2t}(x+y)]}{x+y} \prod_{l=1}^{d} J_{|j_l|}(x) J_{|j_l|}(y) \,. \tag{D.49}$$

The integrals $F_{\boldsymbol{j}}(h_0)$ and $FT_{\boldsymbol{j}}(h_0)$ are evaluated numerically using Romberg's integration method (Press et al., 1992). Here, the integration of $F_{\boldsymbol{j}}(h_0)$ is straightforward for generic values of h_0. The convergence of the integral $FT_{\boldsymbol{j}}(h_0)$, however, is very slow as $h_0 \to B_c$. The two-dimensional integral is therefore evaluated numerically as a function of the upper integration limits, m; the results are then extrapolated to the limit $m \to \infty$. For large values of m, the functional dependence is well described by $a + b/(m + c)$. The extrapolation is performed by a least square fit. The lattice sum over $|\boldsymbol{j}|$ can be simplified due to the symmetry-property of the components: $F_{\boldsymbol{j}} \equiv F_{j_1,j_2} = F_{j_2,j_1}$ (the same holds for $FT_{\boldsymbol{j}}$). Thus, for $|\boldsymbol{j}| = j_1 + j_2$, constant, one has to sum only over $|\boldsymbol{j}|/2+1$ (integer division) different configurations of (j_1, j_2). The numerical effort is therefore only linear in $|\boldsymbol{j}|$.

Figure D.2 shows the numerical results of addends to the lattice sum $LS(h_0)$ as a function of $|\boldsymbol{j}|$ for different values of the field h_0. For intermediate values of the field h_0, i.e. for $h_0^x \ll h_0 < B_c$, the main contribution to the lattice sum is due to the central site $\mathbf{0}$. In this regime, the lattice sum is easily evaluated in real space. As the field approaches the critical value B_c, however, the contribution of the central site vanishes and the value of $LS(h_0)$ is determined by a larger and larger region in real space. This behavior suggests, that I_{h_1} is better evaluated in momentum space in the limit $h_0 \to B_c$. Also, the numerical effort increases rapidly in real space as $h_0 \to B_c$.

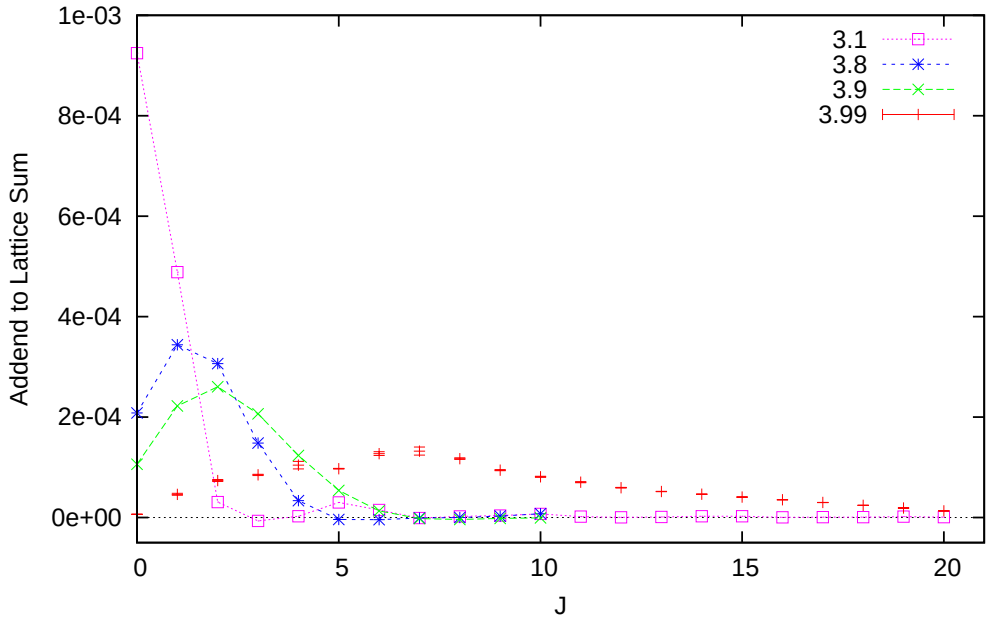

Figure D.2: Contributions to the lattice sum $LS(h_0)$ stemming from sites at a Manhattan distance $J = |\boldsymbol{j}|$ from a central site $\mathbf{0}$ on the square lattice in $d = 2$ for various values of the field h_0. Errors are of the order of 1% for values of the field $h_0 \neq 3.99$. Lines are guides to the eye only.

D.5 Analytical Evaluation of the Integral $\mathbf{I_{h_1}}$ for $\mathbf{B \to B_c}$

In this section we evaluate the integral I_{h_1} analytically in the limit $h_0 \to B_c$.

From (D.25) we have:

$$I_{h_1} = \iiint\limits_{1.\mathrm{BZ}} \frac{d\mathbf{1}d\mathbf{4}d\boldsymbol{q}}{(2\pi)^6} \frac{1}{\big(|\eta_{\mathbf{1}\uparrow}| + |\eta_{\mathbf{1}+\boldsymbol{q}-\mathbf{4},\uparrow}| + |\eta_{\boldsymbol{q},\downarrow}| + |\eta_{\mathbf{4}\downarrow}|\big)|\eta_{\mathbf{1}\uparrow}\eta_{\boldsymbol{q}\downarrow}|} \,. \tag{D.50}$$

Similar to the general case of $h_0 \gg h_0^x$ which was regarded in Appendix D.3, the leading contribution to the integral for $h_0^x \to 0$ is determined by the regimes for which all the energy denominators become small. Now, in the limit $h_0 \to B_c$, the energy $\eta_{\boldsymbol{k}\sigma}$ becomes of the order of h_0^x for the following $\boldsymbol{k} = (k_1, k_2)$ values:

$$\begin{aligned} \sigma = \uparrow\!: \quad & k_1 = (2n+1)\,\pi \quad ; \quad k_2 = (2n'+1)\,\pi \\ \sigma = \downarrow\!: \quad & k_1 = k_2 = 2n''\pi \qquad\qquad\qquad \text{with} \quad n, n', n'' \in \mathbb{Z}\,. \end{aligned} \tag{D.51}$$

Thus the main contribution to the integral (D.50) comes from $\boldsymbol{q} \simeq \mathbf{0}$ and $\mathbf{1} \simeq (\pi, \pi)$ (compare also Fig. D.3). Thus performing the transformation $\mathbf{1} \to \mathbf{1} + (\pi, \pi)$ we obtain:

$$I_{h_1} \sim \iiint\limits_{\{|\boldsymbol{q}|,|\mathbf{1}|,|\mathbf{4}|\leq\delta\}} \frac{d\mathbf{1}d\mathbf{4}d\boldsymbol{q}}{(2\pi)^6} \frac{1}{\big(\tilde{\eta}_{\mathbf{1}\uparrow} + \tilde{\eta}_{\mathbf{1}+\boldsymbol{q}-\mathbf{4},\uparrow} + \tilde{\eta}_{\boldsymbol{q},\downarrow} + \tilde{\eta}_{\mathbf{4}\downarrow}\big)\tilde{\eta}_{\mathbf{1}\uparrow}\tilde{\eta}_{\boldsymbol{q}\downarrow}}\,, \tag{D.52}$$

where δ is some finite fraction of the size of the first Brillouin zone: $\delta = \epsilon\pi$ with $0 < \epsilon \ll 1$ fixed. For $|\boldsymbol{k}| \leq \delta$, the energy dispersion $\tilde{\eta}_{\boldsymbol{k}\uparrow}$ can be approximated by

$$\tilde{\eta}_{\boldsymbol{k}\uparrow} = \sqrt{\big(-2t[\cos(\pi + k_1) + cos(\pi + k_2)] - h_0\big)^2 + h_0^{x\,2}} \tag{D.53}$$

$$\sim t\sqrt{(|\boldsymbol{k}|^2 - b)^2 + (\bar{h}_0^x)^2} = t\,\bar{\eta}_{\boldsymbol{k}\uparrow}\,, \tag{D.54}$$

with $\boldsymbol{k} = (k_1, k_2)$ and $\bar{h}_0^x = h_0^x/t$. Here we have introduced the parameter b, which controls the limit $h_0 \to B_c$:

$$b = \frac{B_c - h_0}{t}\,. \tag{D.55}$$

Exactly the same approximation holds for $\tilde{\eta}_{\boldsymbol{k}\downarrow}$:

$$\tilde{\eta}_{\boldsymbol{k}\downarrow} = \sqrt{\big(-2t[\cos(k_1) + cos(k_2)] + h_0\big)^2 + h_0^{x\,2}} \tag{D.56}$$

$$\sim t\sqrt{(|\boldsymbol{k}|^2 - b)^2 + (\bar{h}_0^x)^2} = t\,\bar{\eta}_{\boldsymbol{k}\downarrow}\,. \tag{D.57}$$

Thus, for small b, we have $\tilde{\eta}_{\boldsymbol{k}\downarrow} = \tilde{\eta}_{\boldsymbol{k}\uparrow}$. For the further evaluation of I_{h_1} let us consider the $\mathbf{4}$ integration of the right hand side of (D.52) only:

$$\begin{aligned}
&\frac{1}{t}\int\limits_{\{|\mathbf{4}|\leq\delta\}} d\mathbf{4}\,\frac{1}{\bar{\eta}_{\mathbf{1}\uparrow} + \bar{\eta}_{\boldsymbol{q},\downarrow} + \bar{\eta}_{\mathbf{1}+\boldsymbol{q}-\mathbf{4},\uparrow} + \bar{\eta}_{\mathbf{4}\downarrow}} \\
=&\frac{1}{t}\int\limits_{\{|\mathbf{4}|\leq\delta\}} d\mathbf{4}\,\frac{1}{\bar{\eta}_{\mathbf{1}\uparrow} + \bar{\eta}_{\boldsymbol{q},\downarrow} + \sqrt{(|\mathbf{4}|^2 - b)^2 + \big(\bar{h}_0^x\big)^2} + \sqrt{(|\mathbf{4} - \mathbf{1} - \boldsymbol{q}|^2 - b)^2 + \big(\bar{h}_0^x\big)^2}}\,.
\end{aligned} \tag{D.58}$$

Now, for values of the momentum $\mathbf{1}$, for which $(|\mathbf{1}|^2 - b) \sim \mathcal{O}(h_0^x)$, one has $\bar{\eta}_{\mathbf{1}\uparrow} \sim \mathcal{O}(h_0^x)$. The same relation holds for the momentum $\boldsymbol{q}$ and the energy $\bar{\eta}_{\boldsymbol{q}\downarrow}$. Similarly, if $|\mathbf{4}|^2 \sim \mathcal{O}(b)$, the energy $\bar{\eta}_{\mathbf{4}\downarrow}$ is of the order of h_0^x. The second essential observation is that for almost all $(\mathbf{1}, \boldsymbol{q}, \mathbf{4})$-values for which $(|\mathbf{1}|^2, |\boldsymbol{q}|^2, |\mathbf{4}|^2) \sim \mathcal{O}(b)$, the sum $|\mathbf{4}-\mathbf{1}-\boldsymbol{q}|^2$ is not close to b, implying $[|\mathbf{4} - \mathbf{1} - \boldsymbol{q}|^2 - b] \sim \mathcal{O}(b)$. Thus for $h_0^x \ll b < \delta$ the denominator in (D.58) can be approximated by

$$\sqrt{(|\mathbf{4}|^2 - b)^2} + b \qquad \text{for} \quad |\mathbf{4}|^2 \lesssim \mathcal{O}(b) \tag{D.59}$$

$$2\sqrt{(|\mathbf{4}|^2 - b)^2} \qquad \text{for} \quad |\mathbf{4}|^2 > \mathcal{O}(b)\,. \tag{D.60}$$

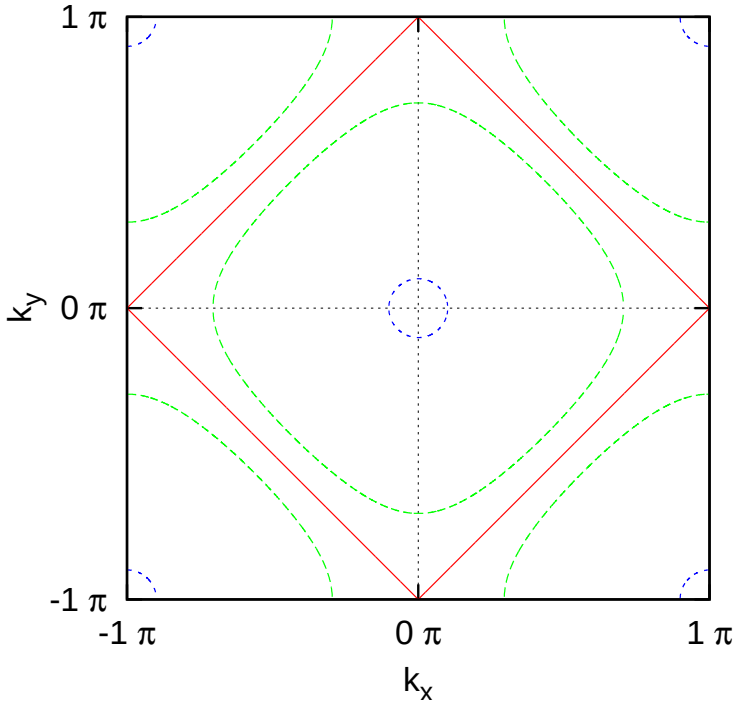

Figure D.3: The Fermi surface of the noninteracting Hubbard model ($t = 1$) in $d = 2$ for various choices of the chemical potential μ. The Fermi surface at half filling is indicated by the solid (red) line. Here, the regime close to the four edges $\boldsymbol{k} \simeq (\pi, 0), (0, \pi), \cdots$, is responsible for the logarithmic divergence of the density of states.

The leading contribution of the **4** integral in the limit $b \to 0$ is due to (D.60). The integration is simple and yields

$$\frac{\pi}{2t} \ln\left(\frac{\delta^2 - b}{b}\right) \sim \frac{\pi}{2t} \ln\left(\frac{1}{b}\right) . \tag{D.61}$$

The integral I_{h_1} is thus to leading logarithmic order in $1/b$ given by

$$I_{h_1} \sim \frac{\pi}{2t^3 (2\pi)^6} \ln\left(\frac{1}{b}\right) \left[\int\limits_{\{|\boldsymbol{q}| \leq \delta\}} dq \, \frac{1}{\bar{\eta}_{\boldsymbol{q}\uparrow}} \right]^2 . \tag{D.62}$$

The $\boldsymbol{q}$ integration of (D.62) is straightforward:

$$\begin{aligned}
\frac{1}{t}\int\limits_{\{|\boldsymbol{q}|\le\delta\}} d\boldsymbol{q}\,\frac{1}{\sqrt{(|\boldsymbol{q}|^2-b)^2+\left(\bar{h}_0^x\right)^2}} &\sim \frac{\pi}{t}\left\{\int\limits_{\bar{h}_0^x}^{b}+\int\limits_{\bar{h}_0^x}^{\delta^2-b}\right\} dr\,\frac{1}{r} \\
&\sim \frac{\pi}{t}\left\{\ln\left(\frac{b}{\bar{h}_0^x}\right)+\ln\left(\frac{\delta^2-b}{\bar{h}_0^x}\right)\right\} \\
&\sim \frac{2\pi}{t}\ln\left(\frac{t}{h_0^x}\right).
\end{aligned} \tag{D.63}$$

Thus, in the limit $b\to 0$, the integral I_{h_1} has the following form:

$$I_{h_1} \sim \frac{1}{2^5(\pi\,t)^3}\ln\left(\frac{1}{b}\right)\left[\ln\left(\frac{t}{h_0^x}\right)\right]^2. \tag{D.64}$$

The same expression also holds for the integral I_{h_3}.

Bibliography

Anderson, P. W., 1958, Phys. Rev. **109**, 1492.

Anderson, P. W., 1959, Phys. Rev. **115**, 2.

Anderson, P. W., 1963, in *Solid State Physics*, edited by D. Turnball, and F. Seitz, Vol. 14 (Academic Press, New York), p. 99.

Anderson, P. W., 1975, Phys. Rev. Lett. **34**, 953.

Anderson, P. W., 1987, Science **235**, 1196.

Anisimov, V., I. Nekrasov, D. Kondakov, T. Rice, and M. Sigrist, 2002, Eur. Phys. J. B **25**, 191.

Arita, R., and K. Held, 2005, Phys. Rev. B **72**, 201102(R).

Aryanpour, K., T. A. Maier, and M. Jarrell, 2005, Phys. Rev. B **71**, 037101.

Ashcroft, N. W., and N. D. Mermin, 1976, *Solid State Physics* (Holt-Saunders, Philadelphia).

Bardeen, J., L. N. Cooper, and J. R. Schrieffer, 1957, Phys. Rev. **108**, 1175.

Baym, G., 1962, Phys. Rev. **127**, 1391.

Baym, G., and L. P. Kadanoff, 1961, Phys. Rev. **124**, 287.

Bednorz, J. G., and K. A. Müller, 1986, Z. Phys. B **64**, 189.

Bickers, N. E., and D. J. Scalapino, 1989, Ann. Physik **193**, 206.

Bickers, N. E., and S. R. White, 1991, Phys. Rev. B **43**, 8044.

Biermann, S., L. de' Medici, and A. Georges, 2005, Phys. Rev. Lett. **95**, 206401.

Biroli, G., and G. Kotliar, 2002, Phys. Rev. B **65**, 155112.

Blankenbecler, R., D. J. Scalapino, and R. L. Sugar, 1981, Phys. Rev. D **24**, 2278.

Blümer, N., 2002, *Mott-Hubbard Metal-Insulator Transition and Optical Conductivity in High Dimensions* (Shaker Verlag, Aachen).

Blümer, N., and E. Kalinowski, 2005, Phys. Rev. B **71**, 195102.

Blümer, N., and K. Požgajčić, 2005. private communication.

Brandt, U., and C. Mielsch, 1989, Z. Phys. B **75**, 365.

Brandt, U., and R. Schmidt, 1986, Z. Phys. B **63**, 45.

Brandt, U., and R. Schmidt, 1987, Z. Phys. B **67**, 43.

Brinkman, W. F., and T. M. Rice, 1970, Phys. Rev. B **2**, 4302.

Brout, R., 1960, Phys. Rev. **118**, 1009.

Brout, R., and H. Thomas, 1967, Physics **3**, 317.

Bryan, R. K., 1990, Eur. Biophys. J **18**, 165.

Caffarel, M., and W. Krauth, 1994, Phys. Rev. Lett. **72**, 1545.

Castellani, C., C. R. Natoli, and J. Ranninger, 1978, Phys. Rev. B **18**, 4945.

Cyrot, M., and H. Kaga, 1996, Phys. Rev. Lett. **77**, 5134.

Dagotto, E., 1994, Rev. Mod. Phys. **66**, 763.

Damascelli, A., Z. Hussain, and Z. Shen, 2003, Rev. Mod. Phys. **75**, 473.

Daré, A. M., and G. Albinet, 2000, Phys. Rev. B **61**, 4567.

de' Medici, L., A. Georges, and S. Biermann, 2005, Phys. Rev. B.

Doniach, S., and E. H. Sondheimer, 1998, *Green's functions for solid state physicists* (Imperial College Press, London).

Economou, E. N., 1979, *Green's Functions in Quantum Physics* (Springer Verlag, Berlin).

Elliott, R. J., J. A. Krumhansl, and P. L. Leath, 1974, Rev. Mod. Phys. **46**, 465.

Emery, V. J., 1976, Phys. Rev. B **14**, 2989.

Essler, F. H. L., V. L. Korepin, and K. Schoutens, 1992, Nucl. Phys. B **384**, 431.

Evertz, H. G., 2003, Adv. Phys. **52**, 1–66.

Falicov, L. M., and J. C. Kimball, 1969, Phys. Rev. Lett. **22**, 997.

Fang, Z., and K. Terakura, 2001, Phys. Rev. B **64**, 020509(R).

Fang, Z., N. Nagaosa, and K. Terakura, 2004, Phys. Rev. B **69**, 045116.

Feldbacher, M., K. Held, and F. F. Assaad, 2004, Phys. Rev. Lett. **93**, 136405.

Ferrero, M., F. Becca, M. Fabrizio, and M. Capone, 2005, Phys. Rev. B **72**, 205126.

Fetter, A. L., and J. D. Walecka, 1971, *Quantum Theory of Many-Particle Systems* (McGraw-Hill, New York).

Freericks, J. K., B. K. Nikolic, and P. Miller, 2001, Phys. Rev. B **64**, 054511.

Freericks, K., and V. Zlatic, 2003, Rev. Mod. Phys. **75**, 1333.

Gebhard, F., 1997, *The Mott Metal-Insulator Transition* (Springer-Verlag, Berlin).

Georges, A., and G. Kotliar, 1992, Phys. Rev. B **45**, 6479.

Georges, A., and J. S. Yedidia, 1991, Phys. Rev. B **43**, 3475.

Georges, A., and W. Krauth, 1992, Phys. Rev. Lett. **69**, 1240.

Georges, A., and W. Krauth, 1993, Phys. Rev. B **48**, 7167.

Georges, A., G. Kotliar, W. Krauth, and M. Rozenberg, 1996, Rev. Mod. Phys. **68**, 13.

Gill, W., and D. J. Scalapino, 1987, Phys. Rev. B **35**, 215.

Gros, C., and R. Valenti, 1994, Ann. Phys. (Leipzig) **3**, 460.

Gubernatis, J. E., M. Jarrell, R. N. Silver, and D. S. Sivia, 1991, Phys. Rev. B **44**, 6011.

Guillou, J. C. L., and J. Zinn-Justin, 1990, in *Current Physics Sources and Comments*, edited by J. C. L. Guillou, and J. Zinn-Justin, Vol. 7 (North-Holland, Amsterdam).

Gutzwiller, M. C., 1963, Phys. Rev. Lett. **10**, 159.

Halboth, C. J., and W. Metzner, 2000, Phys. Rev. B **61**, 7364.

Hanisch, T., G. S. Uhrig, and E. Müller-Hartmann, 1997, Phys. Rev. B **56**, 13960.

Held, K., 1999, Ph.D. Thesis, Universität Augsburg.

Held, K., and D. Vollhardt, 1998, Eur. Phys. J. B **5**, 473.

Held, K., G. Keller, V. Eyert, D. Vollhardt, and V. Anisimov, 2001, Phys. Rev. Lett. **86**, 5345.

Held, K., I. A. Nekrasov, N. Blümer, V. I. Anisimov, and D. Vollhardt, 2001, Int. J. Mod. Phys. B **15**, 2611.

Hettler, M., A. N. Tahvildar-Zadeh, M. Jarrell, T. Pruschke, and H. R. Krishnamurthy, 1998, Phys. Rev. B **58**, R7475.

Hettler, M., A. N. Tahvildar-Zadeh, M. Jarrell, T. Pruschke, and H. R. Krishnamurthy, 2000, Phys. Rev. B **61**, 12739.

Hirsch, J. E., 1983, Phys. Rev. B **28**, 4059.

Hirsch, J. E., 1985, Phys. Rev. B **31**, 4403.

Hirsch, J. E., 1987, Phys. Rev. B **35**, 1851.

Hirsch, J. E., 1997, Phys. Rev. B **56**, 11022.

Hirsch, J. E., and D. J. Scalapino, 1985, Phys. Rev. B **32**, 117.

Hirsch, J. E., and R. M. Fye, 1986, Phys. Rev. Lett. **56**, 2521.

Honerkamp, C., and M. Salmhofer, 2001, Phys. Rev. Lett. **87**, 187004.

Hubbard, J., 1963, Proc. Roy. Soc. London A **276**, 238.

Huscroft, C., M. Jarrell, T. Maier, S. Moukouri, and A. N. Tahvildarzadeh, 2001, Phys. Rev. Lett. **86**, 4415.

Imada, M., A. Fujimori, and Y. Tokura, 1998, Rev. Mod. Phys. **70**, 1039.

Inaba, K., A. Koga, S. Suga, and N. Kawakami, 2005, J. Phys. Soc. Jap. **74**, 2393.

Inui, M., and P. B. Littlewood, 1991, Phys. Rev. B **44**, 4415.

Ishida, K., H. Mukuda, Y. Kitaoka, K. Asayama, Z. Q. Mao, Y. Mori, and Y. Maeno, 1998, Nature (London) **396**, 658.

Janiš, V., and D. Vollhardt, 1992, Int. J. Mod. Phys. B **6**, 731.

Jarrell, M., 1992, Phys. Rev. Lett. **69**, 168.

Jarrell, M., and J. E. Gubernatis, 1996, Physics Reports **269**, 133.

Jin, S., M. McCormack, T. H. Tiefel, and R. Ramesh, 1994, J. Appl. Phys. **76**, 6929.

Joo, J., and V. Oudovenko, 2001, Phys. Rev. B **64**, 193102.

Kakehashi, Y., and H. Hasegawa, 1988, Phys. Rev. B **7777**, 37.

Kampf, A., and J. R. Schrieffer, 1990, Phys. Rev. B **41**, 6399.

Kanamori, J., 1963, Prog. Theor. Phys. **30**, 275.

Keiter, H., and J. C. Kimball, 1970, Phys. Rev. Lett. **25**, 672.

Kennedy, T., and E. H. Lieb, 1986, Physica A **138**, 320.

Knecht, C., 2002, Diploma Thesis, Universität Mainz.

Knecht, C., N. Blümer, and P. G. J. van Dongen, 2005, Phys. Rev. B **72**, 081103(R).

Kobayashi, K. I., T. Kimura, H. Sawada, K. Terakura, and Y. Tokura, 1998, Nature (London) **395**, 677.

Koga, A., N. Kawakami, T. Rice, and M. Sigrist, 2004, Phys. Rev. Lett. **92**, 216402.

Koga, A., N. Kawakami, T. Rice, and M. Sigrist, 2005*a*, Physica B **359-361**, 1366.

Koga, A., N. Kawakami, T. Rice, and M. Sigrist, 2005*b*, Phys. Rev. B **72**, 045128.

Kopietz, P., 1993, Phys. Rev. B **48**, 13789.

Kosterlitz, J. M., and D. J. Thouless, 1973, J. Phys. C **6**, 1181.

Kotliar, G., S. Y. Savrasov, and G. Pálsson, 2001, Phys. Rev. Lett. **87**, 186401.

Kuei, J., and R. T. Scalettar, 1997, Phys. Rev. B **55**, 14968.

Langer, W., M. Plischke, and D. Mattis, 1969, Phys. Rev. Lett. **23**, 1448.

Lee, J. S., Y. S. Lee, T. W. Noh, S.-J. Oh, J. Yu, S. Nakatsuji, H. Fukazawa, and Y. Maeno, 2002, Phys. Rev. Lett. **89**, 257402.

Lee, P. A., and N. Nagaosa, 1992, Phys. Rev. B **46**, 5621.

Lee, P. A., and T. V. Ramakrishnan, 1985, Rev. Mod. Phys. **57**, 287.

Lieb, E., 1986, Physica A **140A**, 240.

Lieb, E. H., 1989, Phys. Rev. Lett. **62**, 1201.

Lieb, E. H., and D. Mattis, 1962, Phys. Rev. **125**, 164.

Lieb, E. H., and F. Y. Wu, 1968, Phys. Rev. Lett. **20**, 1445.

Liebsch, A., 2003*a*, Europhys. Lett. **63**, 97.

Liebsch, A., 2003*b*, Phys. Rev. Lett. **91**, 226401.

Liebsch, A., 2004, Phys. Rev. B **70**, 165103.

Liebsch, A., 2005, Phys. Rev. Lett. **95**, 116402.

Little, W. A., 1964, Phys. Rev. **134**, A1416.

Luttinger, J. M., and J. C. Ward, 1960, Phys. Rev. **118**, 1417.

Mackenzie, A. P., S. R. Julian, A. J. Diver, G. J. McMullan, M. P. Ray, G. G. Lonzarich, Y. Maeno, S. Nishizaki, and T. Fujita, 1996, Phys. Rev. Lett. **76**, 3786.

Maeno, Y., H. Hashimoto, K. Yoshida, S. Nishizaki, T. Fujita, J. G. Bednorz, and F. Lichtenberg, 1994, Nature (London) **372**, 532.

Maier, T., M. Jarrell, T. Pruschke, and M. H. Hettler, 2005, Rev. Mod. Phys. **77**, 1027.

Martín-Rodero, A., and F. Flores, 1992, Phys. Rev. B **45**, 13008.

Mermin, N. D., and H. Wagner, 1966, Phys. Rev. Lett. **17**, 1133.

Metropolis, N., A. Rosenbluth, M. Rosenbluth, A. Teller, and E. Teller, 1953, J. Chem. Phys. **21**, 1087.

Metzner, W., and D. Vollhardt, 1989, Phys. Rev. Lett. **62**, 324.

Micnas, R., J. Ranninger, and S. Robaszkiewicz, 1990, Rev. Mod. Phys. **62**, 113.

Micnas, R., S. Robaszkiewicz, and K. A. Chao, 1984, Phys. Rev. B **29**, 2784.

Mielke, A., 1991, J. Phys. A **24**, 3311.

Mielke, A., and H. Tasaki, 1993, Commun. Math. Phys. **158**, 341.

Moreo, A., and D. J. Scalapino, 1991, Phys. Rev. Lett. p. 946.

Mott, N. F., 1968, Rev. Mod. Phys. **40**, 677.

Moukouri, S., S. Allen, F. Lemay, B. Kyung, D. Poulin, Y. M. Vilk, and A.-M. S. Tremblay, 2000, Phys. Rev. B **61**, 7887.

Müller-Hartmann, E., 1989, Z. Phys. B **74**, 507.

Müller-Hartmann, E., 1995, J. Low Temp. Phys. **99**, 349.

Nagaoka, Y., 1965, Solid State Commun. **3**, 409.

Nakatsuji, S., and Y. Maeno, 2000*a*, Phys. Rev. Lett. **84**, 2666.

Nakatsuji, S., and Y. Maeno, 2000*b*, Phys. Rev. B **62**, 6458.

Negele, W., and H. Orland, 1987, *Quantum Many-Particle Systems* (Addison-Wesley, New York).

Ng, K. K., and M. Sigrist, 2000, Europhys. Lett. **49**, 473.

Nozières, P., and S. Schmitt-Rink, 1985, J. Low Temp. Phys. **59**, 195.

Oguchi, T., 1995, Phys. Rev. B **51**, 1385.

Onsager, L., 1936, J. Am. Chem. Soc. **58**, 1486.

Oudovenko, V. S., K. Haule, S. Savrasov, D. Villani, and G. Kotliar, 2005, Phys. Rev. B **71**, 115117.

Pairault, S., D. Sénéchal, and A.-M. S. Tremblay, 1998, Phys. Rev. Lett. **80**, 5389.

Pairault, S., D. Sénéchal, and A.-M. S. Tremblay, 2000, Eur. Phys. J. B **16**, 85.

Penn, R. G., 1966, Phys. Rev. **142**, 350.

Petrone, P., and A. A. Aligia, 2002, Phys. Rev. B **66**, 104418.

Potthoff, M., 2003, Eur. Phys. J. B **32**, 429.

Potthoff, M., T. Wegner, and W. Nolting, 1997, Phys. Rev. B **55**, 16132.

Press, W. H., S. A. Teukolsky, W. T. Vetterling, and B. P. Flannery, 1992, *Numerical Recipes in C* (Cambridge University Press, Cambridge).

Pruschke, T., D. L. Cox, and M. Jarrell, 1993, Phys. Rev. B **47**, 3553.

Rice, T. M., and D. B. McWhan, 1970, IBM J. Res. Develop. p. 251.

Rice, T. M., and L. Sneddon, 1970, Phys. Rev. Lett. **47**, 689.

Robaszkiewicz, S., R. Micnas, and J. Ranninger, 1987, Phys. Rev. B **36**, 180.

Robaszkiewicz, S., R. Micnas, and K. A. Chao, 1981*a*, Phys. Rev. B **23**, 1447.

Robaszkiewicz, S., R. Micnas, and K. A. Chao, 1981*b*, Phys. Rev. B **24**, 1579.

Robaszkiewicz, S., R. Micnas, and K. A. Chao, 1981*c*, Phys. Rev. B **24**, 4018.

Robaszkiewicz, S., R. Micnas, and K. A. Chao, 1982, Phys. Rev. B **26**, 3915.

Rohe, D., and W. Metzner, 2005, Phys. Rev. B **71**, 115116.

Rombouts, S. M. A., K. Heyde, and N. Jachowicz, 1999, Phys. Rev. Lett. **82**, 4155.

Rozenberg, M. J., 1997, Phys. Rev. B **55**, 4855.

Rozenberg, M. J., R. Chitra, and G. Kotliar, 1999, Phys. Rev. Lett. **83**, 3498.

Rozenberg, M. J., X. Y. Zhang, and G. Kotliar, 1992, Phys. Rev. Lett. **69**, 1236.

Rubtsov, A. N., V. V. Savkin, and A. I. Lichtenstein, 2005, Phys. Rev. B **72**, 35122.

Salmhofer, M., 1998, *Renormalization* (Springer, Berlin).

Sandvik, A. W., and D. J. Scalapino, 1995, Phys. Rev. B **51**, 9403.

Scalettar, R. T., D. J. Scalapino, R. L. Sugar, and D. Toussaint, 1989, Phys. Rev. B **39**, 4711.

Scalettar, R. T., E. Y. Loh, J. E. Gubernatis, A. Moreo, S. R. White, D. J. Scalapino, R. L. Sugar, and E. Dagotto, 1989, Phys. Rev. Lett. **62**, 1407.

Schauerte, T., and P. G. J. van Dongen, 2002, Phys. Rev. B **65**, 081105(R).

Schlipf, J., 1998, Ph.D. Thesis, Universität Augsburg.

Schulz, H. J., 1990, Phys. Rev. Lett. **64**, 1445.

Sénéchal, D., and A.-M. S. Tremblay, 2004, Phys. Rev. Lett. **92**, 126401.

Shen, S., and Z. Qiu, 1993, Phys. Rev. Lett. **71**, 4238.

Shiba, H., 1972, Prog. Theor. Phys. **48**, 2171.

Si, Q., G. Kotliar, and A. Georges, 1992, Phys. Rev. B **46**, 1261.

Sigrist, M., and M. Troyer, 2004, Eur. J. Phys. B **39**, 207.

Silver, R. N., D. S. Sivia, and J. E. Gubernatis, 1990, Phys. Rev. B **41**, 2380.

Singer, J. M., M. H. Pedersen, T. Schneider, H. Beck, and H.-G. Matuttis, 1996, Phys. Rev. B **54**, 1286.

Singh, D. J., 1995, Phys. Rev. B **52**, 1385.

Slater, J. C., 1936, Phys. Rev. **49**, 537.

Soven, P., 1967, Phys. Rev. **156**, 809.

Staudt, R., M. Dzierzawa, and A. Muramatsu, 2000, Eur. Phys. J. B **17**, 411.

Suzuki, M., 1976, Prog. Theor. Phys. **56**, 1454.

Szczech, Y., M. A. Tusch, and D. E. Logan, 1995, Phys. Rev. Lett. **74**, 2804.

Tahvildar-Zadeh, A. N., J. K. Freericks, and M. Jarrell, 1997, Phys. Rev. B **55**, 3332.

Tasaki, H., 1998*a*, Prog. Theor. Phys. **99**, 489.

Tasaki, H., 1998*b*, J. Phys. Cond. Matter **10**, 4353.

Taylor, D. W., 1967, Phys. Rev. **156**, 1017.

Trotter, H. F., 1959, Proc. Am. Math. Soc. **10**, 545.

Ulmke, M., 1995, Ph.D. Thesis, KFA Jülich.

Ulmke, M., 1998, Eur. Phys. J. B **1**, 301.

Ulmke, M., P. J. H. Denteneer, V. Janiš, R. T. Scalettar, A. Singh, D. Vollhardt, and G. Zimanyi, 1999, Advances In Solid State Physics **38**, 369.

Ulmke, M., R. T. Scalettar, A. Nazarenko, and E. Dagotto, 1996, Phys. Rev. B **54**, 16523.

Ulmke, M., V. Janiš, and D. Vollhardt, 1995, Phys. Rev. B **51**, 10411.

van Dongen, P. G. J., 1991, Phys. Rev. Lett. **67**, 757.

van Dongen, P. G. J., 1992, Phys. Rev. B **45**, 2267.

van Dongen, P. G. J., 1994*a*, Phys. Rev. B **50**, 14016.

van Dongen, P. G. J., 1994*b*, Phys. Rev. Lett. **72**, 3258.

van Dongen, P. G. J., 1994*c*, Phys. Rev. B **49**, 7904.

van Dongen, P. G. J., 1995, Phys. Rev. Lett. **74**, 182.

van Dongen, P. G. J., 1996, Phys. Rev. B **54**, 1584.

van Dongen, P. G. J., 2005, private communication.

van Dongen, P. G. J., and C. Leinung, 1997, Adv. Phys. **6**, 45.

van Dongen, P. G. J., and D. Vollhardt, 1990, Phys. Rev. Lett. **65**, 1633.

van Vleck, J. H., 1953, Rev. Mod. Phys. **25**, 220.

Vilk, Y. M., L. Chen, and A.-M. S. Tremblay, 1994, Phys. Rev. B **49**, 13267.

Visscher, P. B., 1974, Phys. Rev. B **10**, 943.

Wahle, J., N. Blümer, J. Schlipf, K. Held, and D. Vollhardt, 1998, Phys. Rev. B **58**, 12749.

White, S. R., D. J. Scalapino, and R. L. Sugar, 1989, Phys. Rev. Lett. **63**, 1523.

Wilson, K. G., 1975, Rev. Mod. Phys. **47**, 773.

Zaitsev, R. O., and M. I. Dushenat, 1983, Sov. Phys. Solid-State **25**, 1979.

Zhang, F. C., and T. M. Rice, 1988, Phys. Rev. B **37**, 3759.

List of Publications

Parts of this thesis were published in the following articles:

C. Knecht, N. Blümer, P. G. J. van Dongen, "*Orbital-selective Mott transitions in the anisotropic two-band Hubbard model at finite temperatures*", Phys. Rev. B **72**, 081103(R) (2005).

P. G. J. van Dongen, C. Knecht, N. Blümer, "*Orbital-selective Mott transitions in the 2-band J_z-model: a high-precision quantum Monte Carlo study*", Phys. Stat. Sol. (b) **243**, 116 (2005).

The accuracy of our multi-band QMC algorithm as compared to previous work was explicitly demonstrated in:

C. Knecht, N. Blümer, P. G. J. van Dongen, Reply to a Comment on "*Orbital-selective Mott transitions in the anisotropic two-band Hubbard model at finite temperatures*", cond-mat 0506450